2D materials for improved membrane technology

A thesis submitted to The University of Manchester for the degree of

Doctor of Philosophy

in the Faculty of Science and Engineering

2018

Monica Raquel Pedrosa Alberto

School of Chemical engineering and Analytical Science

List Content

Word count: 48681

List of Figures

List of tables

List of abbreviations

ABE	Acetone-Butanol-Ethanol
AFM	Atomic force microscope
ATR-FTIR	Attenuated Total Reflectance – Fourier Transform Infrared Spectroscopy
BET	Brunauer-Emmett-Teller
CMS	Carbon molecular sieve
CNT	Carbon nanotube
CPF	Capillary flow porometry
CVD	Chemical vapor deposition
DCM	Dichloromethane
DI	Deionised
DMAc	Dimethylacetamide
DTG	Derivative thermos-gravimetric
EA	Elemental analysis
EtOH	Ethanol
FID	Flame ionization detector
GC	Gas chromatography
GHG	Greenhouse gas
GO	Graphene oxide
GO-ODA	functionalized graphene oxide with octadecylamine
GPC	Gel permeation chromatography
GS	Gas Separation
IUPAC	International Union of Pure and Applied Chemistry
LbL	Layer-by-Layer
MF	Microfiltration
MFP	Mean Flow Pore
MMM	Mixed matrix membrane
MOF	Metal organic framework
***n*-BtOH**	*n*-Butanol
NF	Nanofiltration

NMR	Nuclear magnetic resonance
OA	Octylamine
ODA	Octadecylamine
OSN	Organic solvent nanofiltration
PC	Polycarbonate
PDMS	Polydimethylsiloxane
PEBA	Polyether block amide
PES	Polyethersulfone
PIM	Polymer of intrinsic microporosity
PPU	PoraPLOT U
PSA	Pressure swing adsorption
PSF	Polysulfone
PSI	Pervaporation separation index
PTFE	Polytetrafluoroethylene
PTMS	*n*-propyltrimethoxysilane
PTMSP	poly[1-(trimethylsilyl)-1-propyne]
PV	Pervaporation
PVDF	Polyvinylidene fluoride
rGO-OA	Functionalized reduced graphene oxide with octylamine
rGO-ODA	Functionalized reduced graphene oxide with octadecylamine
RO	Reverse osmosis
SEM	Scanning Electron Microscope
STEM	Scanning transmission electron microscope
SU	Solvent uptake
TEM	Transmission electron microscopy
TFC	Thin Film Composite
TFN	Thin Film Nanocomposite
TGA	Thermogravimetric Analysis
UF	Ultrafiltration
UV-Vis	Ultraviolet-visible
XPS	X-ray Photoelectron Specstroscopy

ZIF   Zeolitic imidazolate framework

ZSM   Zeolite Socony Mobil

Variables

A	Effective membrane area (m^2)
D	Diffusion coefficient (cm^2 s^{-1})
Đ	Polydispersity
J	Flux (kg m^{-2} h^{-1})
l	Membrane thickness (m)
m	Mass (kg)
M_n	Number average molecular weight (g mol^{-1})
M_w	Weight-average molar mass (g mol^{-1})
P	Permeability (Barrer, 1 Barrer = 10^{-10} cm^3 (STP) cm cm^{-2} s^{-1} $cmHg^{-1}$)
Q	Gas flow rate (cm^3(STP) s^{-1})
S	Solubility coefficient (cm^3(STD) cm^{-3} $cmHg^{-1}$)
t	Time (s)
X	Mole fraction of bioalcohol in the feed
Y	Mole fraction of bioalcohol in the permeate
α	Selectivity
β	Separation factor
Δp	Pressure difference (cmHg)

Abstract

In this work membranes containing 2D materials, namely graphene-like materials, and the most representative polymer of intrinsic microporosity (PIM), PIM-1, were developed for their use in bioalcohol recovery and CO_2 gas separation. Graphene-like materials resulting from the alkyl-functionalization of graphene oxide (GO) using octylamine (OA) and octadecylamine (ODA), and their further chemical reduced forms were used as fillers for both applications. The incorporation of graphene-based fillers in freestanding membranes enhanced the separation performance for n-butanol (n-BtOH)/water separation and an average separation factor of 32.9 for n-BtOH/water was obtained with mixed matrix membranes (MMMs) containing 0.1 wt.% reduced alkyl-functionalized GO (OA functionalization), while pristine PIM-1 membranes presented an average separation factor of 13.

In order to improve the productivity of the aforementioned membranes, thin film nanocomposite (TFN) membranes were fabricated via dip-coating. Herein, porous polyvinylidene fluoride (PVDF) membranes were used as support layers. The addition graphene-like materials with lateral sizes in the nanometer-range improved the separation performance, in comparison with pristine PIM-1 thin film composite (TFC) membranes. As expected, their fluxes were greater than that for freestanding membranes. Besides that, the incorporation of nanometer-sized fillers also enhanced the total flux of TFN membranes in approximately 40% when compared to PIM-1 TFC membranes.

Finally, the addition of graphene-like materials into freestanding PIM-1 polymer matrices and their effect on the physical aging was studied. After 155 days, pristine PIM-1 membranes presented a CO_2 permeability of $(2.0 \pm 0.7) \times 10^3$ Barrer, corresponding to a reduction in 68% from their initial value. The addition of graphene-based fillers proved to be an efficient way to retard the physical aging of PIM-1; after the same period of 155 days, MMMs containing 0.05 wt.% reduced OA-functionalized GO membranes showed a CO_2 permeability of $(3.5 \pm 0.6) \times 10^3$ Barrer, i.e., a reduction of 39% relatively to day 0.

16

Declaration

No portion of the work referred to in the thesis has been submitted in support of an application for another degree or qualification of this or any other university or other institute of learning.

Copyright Statement

i. The author of this thesis (including any appendices and/or schedules to this thesis) owns certain copyright or related rights in it (the "Copyright") and she has given The University of Manchester certain rights to use such Copyright, including for administrative purposes.

ii. Copies of this thesis, either in full or in extracts and whether in hard or electronic copy, may be made only in accordance with the Copyright, Designs and Patents Act 1988 (as amended) and regulations issued under it or, where appropriate, in accordance with licensing agreements which the University has from time to time. This page must form part of any such copies made.

iii. The ownership of certain Copyright, patents, designs, trademarks and other intellectual property (the "Intellectual Property") and any reproductions of copyright works in the thesis, for example graphs and tables ("Reproductions"), which may be described in this thesis, may not be owned by the author and may be owned by third parties. Such Intellectual Property and Reproductions cannot and must not be made available for use without the prior written permission of the owner(s) of the relevant Intellectual Property and/or Reproductions.

iv. Further information on the conditions under which disclosure, publication and commercialisation of this thesis, the Copyright and any Intellectual Property and/or Reproductions described in it may take place is available in the University IP Policy (see http://documents.manchester.ac.uk/DocuInfo.aspx?DocID=2442 0), in any relevant Thesis restriction declarations deposited in the University Library, The University Library's regulations (see http://www.library.manchester.ac.uk/about/regulations/) and in The University's policy on Presentation of Theses.

Acknowledgements

Achievements

Publications:

1. Sebastian Leaper, Ahmed Abdel-Karim, Bilal Faki, Jose Miguel Luque-Alled, Monica Alberto, Aravind Vijayaraghavan, Stuart M Holmes, Gyorgy Szekely, Mohamed I Badawy, Nima Shokri, Patricia Gorgojo, *Flux-enhanced PVDF mixed matrix membranes incorporating APTS-functionalized graphene oxide for membrane distillation*, In Journal of Membrane Science, Volume 554, 2018, Pages 309-323, ISSN 0376-7388, https://doi.org/10.1016/j.memsci.2018.03.013.

2. Ahmed Abdel-Karim, Sebastian Leaper, Monica Alberto, Aravind Vijayaraghavan, Xiaolei Fan, Stuart M. Holmes, Eglal R. Souaya, Mohamed I. Badawy, Patricia Gorgojo, *High flux and fouling resistant flat sheet polyethersulfone membranes incorporated with graphene oxide for ultrafiltration applications*, In Chemical Engineering Journal, Volume 334, 2018, Pages 789-799, ISSN 1385-8947, https://doi.org/10.1016/j.cej.2017.10.069.

3. Lei Gao, Monica Alberto, Patricia Gorgojo, Gyorgy Szekely, Peter M. Budd, *High-flux PIM-1/PVDF thin film composite membranes for 1-butanol/water pervaporation*, In Journal of Membrane Science, Volume 529, 2017, Pages 207-214, ISSN 0376-7388, https://doi.org/10.1016/j.memsci.2017.02.008

4. Monica Alberto, Jose Miguel Luque-Alled, Lei Gao, Maria Iliut, Eric Prestat, Leon Newman, Sarah J. Haigh, Aravind Vijayaraghavan, Peter M. Budd, Patricia Gorgojo, *Enhanced organophilic separations with mixed matrix membranes of polymers of intrinsic microporosity and graphene-like fillers*, In Journal of Membrane Science, Volume 526, 2017, Pages 437-449, ISSN 0376-7388, https://doi.org/10.1016/j.memsci.2016.12.061.

Submitted papers:

1. <u>Monica Alberto</u>, Rupesh Bhavsar, Jose Miguel Luque-Alled, Aravind Vijayaraghavan, Peter M. Budd, Patricia Gorgojo, *Impeded physical aging in PIM-1 membranes containing graphene-like fillers*, submitted to Journal of Membrane Science.

2. <u>Monica Alberto</u>, Rupesh Bhavsar, Jose Miguel Luque-Alled, Eric Prestat, Lei Gao, Peter M. Budd, Aravind Vijayaraghavan, Gyorgy Szekely, Stuart M. Holmes, Patricia Gorgojo, *Study on the formation of thin film nanocomposite (TFN) membranes of polymers of intrinsic microporosity and graphene-like fillers: effect of lateral flake size and chemical functionalization,* submitted to Journal of Membrane Science.

Presentations:

1. 5th International Scientific Conference on Pervaporation, Vapor Permeation and Membrane Distillation (June 2017) - *Efficient Butanol Recovery Using Graphene-Based Composite Membranes via Pervaporation* (Oral presentation), Torun, Poland.

2. CEAS Postgraduate Conference, The University of Manchester (May, 2017) - *Pervaporation graphene-based membranes for bioalcohol recovery* (Oral presentation), Manchester, UK.

3. *15th Network Young Membrains* (September, 2015) - *Novel graphene-based membranes for molecular separations* (Oral presentation), Aachen, Germany.

4. *Graphene Week 2015* (June 2015) – *Graphene-based composite membranes for alcohol/water separation* (Poster), Manchester, UK

5. *ChemEngDayUK 2015* (April, 2015) - *Graphene-based composite membranes for alcohol/water separation* (Poster), Sheffield, UK.

Awards:

1. Travel grant from the European Membrane Society (May, 2017).

2. Best Oral Presentation at the CEAS Postgraduate Conference (May, 2017).

3. PhD Scholarship from Chemical Engineering and Analytical Science, The University of Manchester (2014).

Chapter 1 - Research motivation, objectives and thesis structure

1.1.   Context

The world currently faces a number of challenges caused by economic, technological and social development. High energy consumption, especially energy generated from fossil fuels, has led to worldwide environmental concerns. The emerging need to replace fossil fuels by sustainable alternative energy sources and the need to mitigate climate change have been promoted worldwide. Biofuels and biogas are examples of renewable energy sources that have been investigated to replace fossil fuels.

Bioethanol and biobutanol are example of biofuels. Both of them can be produced from acetone-butanol-ethanol (ABE) fermentation; however, their yield is low due to end-product inhibition caused by the alcohol toxicity on bacteria. Regarding biogas, it can be produced from anaerobic fermentation of organic matter, and it is mainly composed of methane (CH_4) and carbon dioxide (CO_2). Herein, the presence of CO_2 not only reduces the calorific value of the gas but also causes pipeline corrosion, making its transport and storage difficult.

In order to use these two forms of renewable energy, the target compounds (i.e. bioalcohol and methane gas) need to be recovered and purified from other species formed in their production processes, thus, cost-effective separation technologies are required. Distillation is the process traditionally used in industry for separating the bioalcohols from fermentation broths. On the other hand, cryogenic separation and pressure swing adsorption (PSA) are examples of technologies currently used for CO_2/CH_4 separation in the production of biogas. Yet, all these three routes are high energy-intensive and alternatives are required.

Over the years, the development of both membranes and membrane-based separation processes have led to an increase in their use in industry, competing hand in hand with well-established technologies. Currently, membrane-based separation processes can be found in an ever-increasing wide range of different applications, as seen in Figure 1.
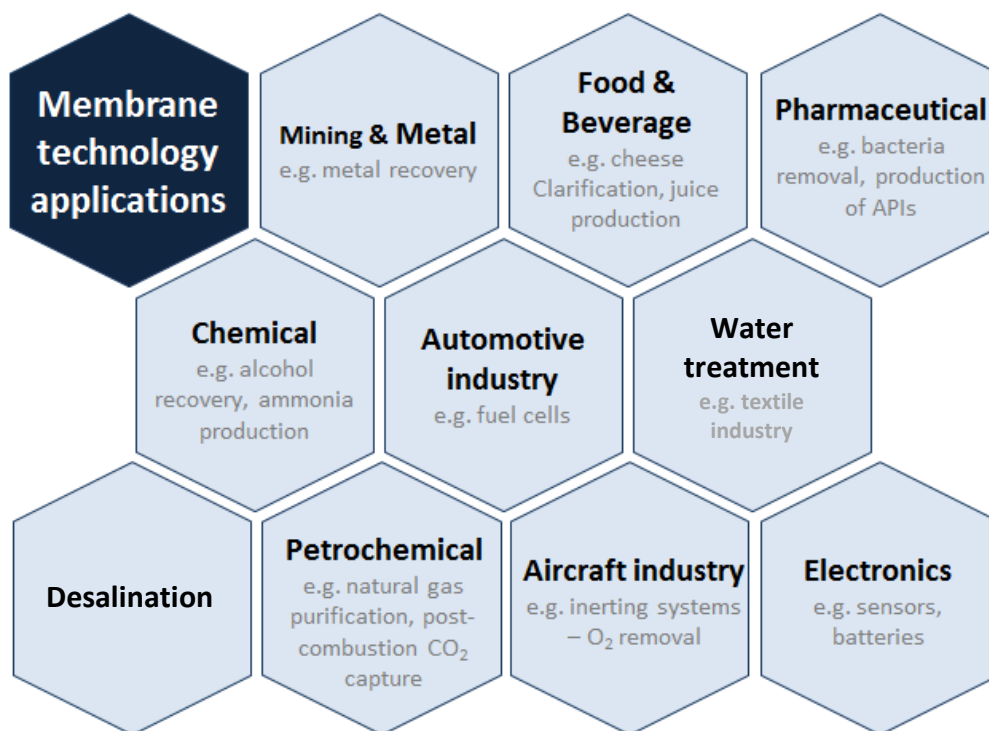
Figure 1: Membrane technology applications (API: Active Pharmaceutical Ingredients).

Polymers are by far the most used materials for membrane fabrication. Currently, poly(dimethyl-siloxane (PDMS), also known as silicone rubber, is a commercialized membrane material for bioalcohol recovery. This material is characterized by its high hydrophobicity degree and excellent chemical stability. Its low flux, as it is prepared from crosslinking processes, and its excessive swelling are its main drawbacks [1]. With regard to CO_2 separation, polysulfone (PSF), cellulose acetate (CA) and polyimides are commercialized membrane materials currently used for such application. Even though they can withstand high operating pressure and exhibit high CO_2 selectivity, all these materials present low free volume and consequently low permeability.

For these two particular applications polymers of intrinsic microporosity (PIMs) can be used. PIMs consist of a new class of microporous materials introduced by Budd et al. in 2004, where PIM-1 is the most commonly used for membrane fabrication [2]. PIM-1 is characterized by its organophilic nature and its high free volume, which allows the separation of organics over water at a relatively high yield, and therefore makes it suitable for bioalcohol recovery via pervaporation (PV) [3, 4]. The high free volume of PIM-1 explains its very high permeability, not only in PV application, but

also in other application such as gas separation (GS). Additionally, PIM-1 presents very high CO_2 solubility compared to other gases, which leads to high CO_2 permeability and moderate selectivity. Thus, this makes PIM-1 an attractive material for CO_2/CH_4 separation [5]. Despite the fact that PIM-1 exhibits great potential as a membrane material, it still faces limitations; PIM-1 suffers from physical aging due to its high free volume, which compromises its long-term stability, and swells excessively in the presence of alcohols, which affect the overall membrane performance [4].

Over the years, mixed matrix membranes (MMMs), comprising PIM-1 and different fillers, have been investigated and have shown potential to overcome the abovementioned disadvantages inherent to a neat polymer membrane. Graphene-like fillers such as mechanically exfoliated graphene nanoplatelets and functionalised graphene oxide (GO) nanosheets are examples of fillers that can be used for such purpose. The incorporation of non-porous graphene nanosheets into the polymer structure may increase the diffusion path of the penetrants due to the tortuosity, affect the packing and mobility of the polymer chains, and hence reduce the swelling and physical aging of the membranes. Besides that, the hydrophobic nature of this type of fillers might improve the affinity of the membrane towards the organic phase in the production of bioalcohol.

Given the nature of PIM-1 and the potential use of graphene-like nanosheets, PIM-1/graphene membranes represent an opportunity for improved membrane technology, opening a door for sustainable energy sources. In this work two different membrane-based applications were investigated: (i) bioalcohol recovery from aqueous solutions to explore the effect of graphene on the reduction of swelling and higher affinity for the organic, and (ii) separation of carbon dioxide from methane to explore the retardation of physical aging by the addition of graphene.

1.2. Objectives

The aim of this Thesis is to study how the incorporation of graphene-like materials into a PIM-1 polymer matrix to improve the performance of pristine PIM-1 for the recovery of alcohol from water mixtures via PV and the separation of CO_2 from gas mixtures. Such PIM-1/graphene-like hybrids are produced as freestanding membranes. A further objective is to prepare thin film membranes supported on porous substrates to enhance their productivity.

The following tasks have been carried out in order to achieve the aim of this work:

1. Synthesis and characterization of graphene-like materials that can be dispersed in chloroform. This solvent is one of the few that can solubilise PIM-1, allowing the casting of membranes.

2. Preparation and characterization of freestanding MMMs prepared with fillers from task 1 and PIM-1 for ethanol (EtOH) and *n*-butanol (*n*-BtOH) recovery from aqueous solutions via PV, as well as the study of the effect of the filler loading on the membrane performance.

3. Fabrication and characterisation of thin film nanocomposite (TFN) membranes with the materials used for the preparation of freestanding membranes in task 2.

4. Study on the effect of filler size, operating temperature and feed composition on the overall membrane performance of TFNs for PV of alcohol/water mixtures.

5. Preparation and characterization of freestanding MMMs with graphene-like fillers for CO_2 separation.

6. Investigate physical aging of membranes from task 5 by measuring the CO_2 and CH_4 permeabilities as a function of time.

1.3.   Thesis structure

This dissertation is organized into 7 chapters as follows:

Chapter 1 gives a brief introduction to membrane technology, its applications and the motivation behind this work. In addition, this chapter describes the objectives and provides the outline of the thesis.

Chapter 2 presents an overview of membrane science and technology, highlighting PV and GS membrane processes. It also includes a brief review of graphene and its application on membrane technology.

Chapter 3 covers the synthesis and characterization of all materials used in this work – PIM-1 and graphene-like materials.

Chapter 4 presents the fabrication and characterization of freestanding MMMs for EtOH and *n*-BtOH recovery from aqueous solutions. The effect of the fillers loading on the overall performance was investigated and the results are presented in this chapter.

Chapter 5 focuses on the fabrication and characterisation of membranes with higher flux yield for *n*-BtOH recovery from aqueous solutions. TFN membranes were prepared through dip-coating. The effect of the filler size and loading on the overall membrane performance was investigated. In addition, a detailed study of the effect of the operating temperature and feed composition was conducted and results are also presented in this chapter.

Chapter 6 contains the study on the physical aging of MMMs made of PIM-1 and graphene-like materials with different filler loadings. Physical aging studies were based on CO_2 and CH_4 permeability measurements.

Chapter 7 presents the overall conclusions of this work as well as recommendations for future work.

Chapter 2 – Background

2.1. Overview of membrane science and technology

2.1.1. Definition of membrane

A membrane is defined as a permeable and selective interface that moderates the mass transfer of chemical species across it, as represented in Figure 2 [6]. The transport across the membrane is aided by a driving force, such as gradients of concentration, pressure, temperature and electrical potential [7]. Herein, the chemical species that permeate the membrane form the so-called permeate, while others are left behind, forming the retentate.
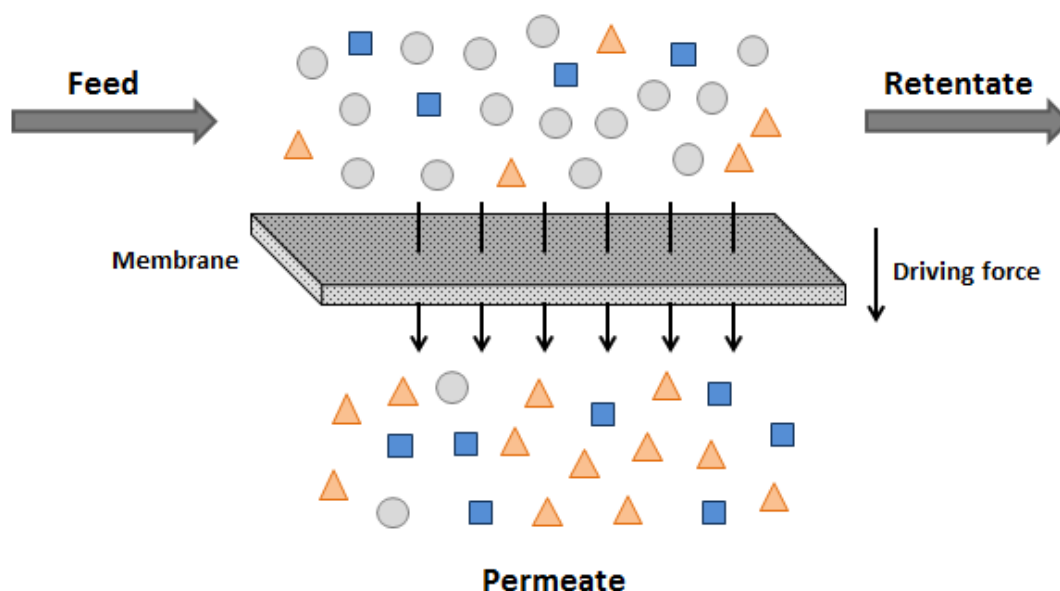
Figure 2: Schematic diagram of a two-phase system separated by a membrane. ΔC: concentration gradient, ΔP: pressure gradient, ΔT: temperature gradient and ΔE: electrical potential gradient (adapted from [8]).

2.1.2. Membrane classification

Membranes can be classified into various categories according to their nature, structure, configuration or application (more detail on this in section 2.1.4.) [9, 10]. Table 1 shows a schematic representation of some of the most common categories for classifying membranes.

In terms of nature, they can be divided into two main groups: natural, including biological and non-biological membranes, and synthetic ones - organic, inorganic,

hybrid and liquid membranes. Based on the physical structure, membranes may present either a symmetric (isotropic) or asymmetric (anisotropic) structure. Symmetric membranes can be either porous or dense, whereas asymmetric membranes can be integrally skinned asymmetric (ISA), also known as Loeb-Sourirajan membrane, and thin film composite (TFC) membranes. Finally, membranes can adopt different configurations such as flat sheets, tubular, spiral wound and hallow fibre.

Table 1: Classification of membranes according to their nature, structure and configuration (adapted from [10] and [9]).
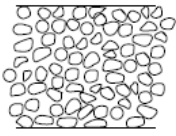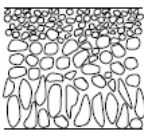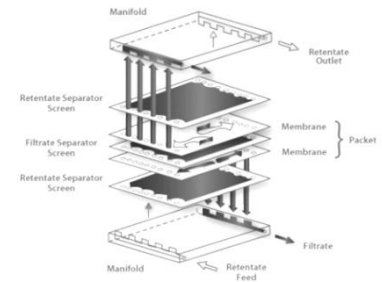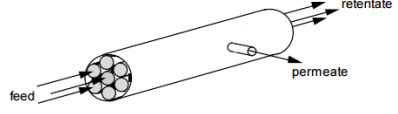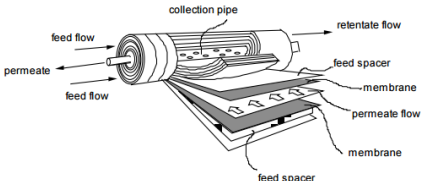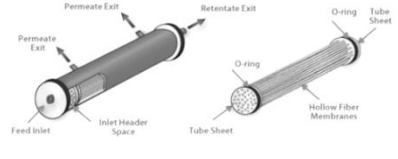
Nature	Synthetic	Organic
		Inorganic
		Hybrid
		Liquid
	Natural	Biological
		Non-biological

Structure	Symmetric	Porous	Dense
	Asymmetric	Integral asymmetric	Composite structure

Configuration	Flat sheet	Tubular
	Spiral wound	Hollow fibre

Table 2 shows the advantages and disadvantages of the different membrane configurations.

Table 2: Advantages and disadvantages of the different membrane configurations.

Membrane configuration	Advantages	Disadvantages
Flat sheet	Process high solids loading Easy detection of membrane defects Easy membrane replacement	Low packing density
Tubular	Easy to clean High tolerance for suspended solids Low fouling tendency	Low membrane density Highest energy consumption
Spiral wound	High packing density	Dead end are difficult to clean Small channels are susceptible to fouling
Hollow fiber	Highest packing density Low hold up volume	Pre-treatment required Easy breakage Difficult to detect membrane defects Difficult to clean

2.1.3. Mass transport across membranes

The mass transfer across a membrane consists of the movement of one or more components from the upstream side to the downstream side of the membrane. There are two models used to describe the permeation mechanism: pore-flow model and solution-diffusion model. The transition between pore-flow and solution-diffusion models occurs in the range of 5 -10 Å diameter pore size [9].

2.1.3.1. Pore-flow model

In pore-flow model, the transport of permeating species occurs through tiny pores via pressure-driven convective flow. This model is applied to ultrafiltration (UF), microfiltration (MF) liquid separation processes, and microporous Knudsen diffusion gas separation membrane if the pore diameter is larger than approximately 100 nm [9].

MF membranes often present pore diameter 10 times larger than the smallest permeating components. These membrane are usually symmetric (isotropic) and are considered depth filters as the separation is performed within its structure. [9]

UF membranes are typically asymmetric (anisotropic), having a surface layer, with small pores, on a much thick and open microporous support. Herein, the separation and permeation performance of UF filtration is determined by the surface layer, and therefore they can be classified as screen filters. [9]

Dense polymer membranes are usually used in industrial gas separation processes. In microporous membranes (pore radius (r) larger than 50 nm), normal convective flow dominates the transport across the membrane (Figure 3a) [11]. When the pore radius is smaller than the mean free path (λ) of the diffusing molecules, Knudsen diffusion takes place (Figure 3b) [12]. Herein, the diffusion of gas molecules is based on their collision with the pore wall rather than with other gas molecules seen in normal convective flow. In terms of r/λ ratio, normal convective flow predominates when r/λ is greater than 1, whereas Knudsen diffusion predominates for r/λ ratio smaller than 1. [9]

Molecular sieving transport (Figure 3c) occurs when the pore diameter of the membrane decreases to the 0.5-1 nm range, being 1-5 larger than the diameter size of the transported species [12, 13].
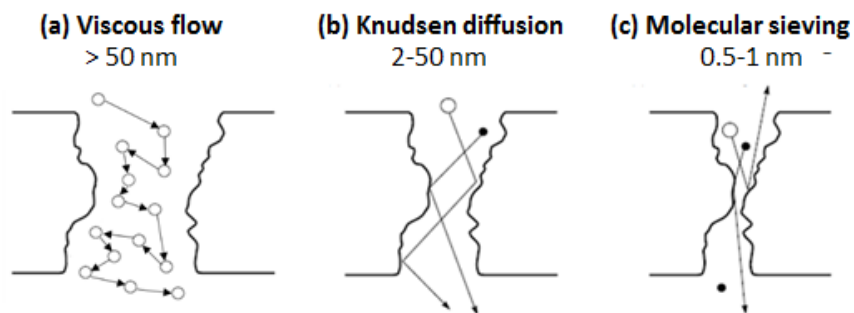
Figure 3: Mass transport mechanism across porous gas separation membranes: (a) viscous flow, (b) Knudsen diffusion and (c) molecular sieving and the respective pore size range (adapted from [14]).

Additionally, surface diffusion and capillary condensation are mass transport mechanisms that can also contribute to gas permeation in microporous membranes.

2.1.3.2.   Solution-diffusion model

The solution-diffusion model is a mass transport mechanism generally accepted for non-porous membranes. This model is based on the differences in solubility and

diffusivity of the chemical species with the membrane material. The permeability of the permeating chemical species, P (cm³(STD) cm cm^{-2} s^{-1} cmHg^{-1}), is given by Equation (1) as follows [15]:

$$P = S \times D \tag{1}$$

Where, S (cm³(STD) cm^{-3} cmHg^{-1}) and D (cm² s^{-1}) correspond to the solubility and diffusivity coefficients, respectively. The permeability coefficient is defined as the flux of the permeating species, per unit of driving force gradient across the membrane per unit membrane thickness. The diffusion coefficient is a kinetic parameter and refers to the mobility of the permeating species through the membrane material. Solubility is a thermodynamic parameters and it is an indicator of the concentration of the permeating species dissolved in the membrane at a given temperature and pressure.

Figure 4 shows a schematic diagram of the solution-diffusion transport mechanism. This transport mass mechanism involves the following three consecutive steps: (1) sorption of components onto upstream membrane surface, (2) diffusion of the absorbed components through bulk membrane material and (3) desorption from the membrane into the downstream side of the membrane [16].

Solubility depends on the interactions between the membranes material and the penetrant molecules. Diffusion is mainly dependent on the mobility of the polymer chains and free volume of polymer bulk. Solubility and diffusivity selectivities favour the most soluble and smallest molecules, respectively. As long as these differences are significant, molecules with similar molecular weight, size and shape can be separated.
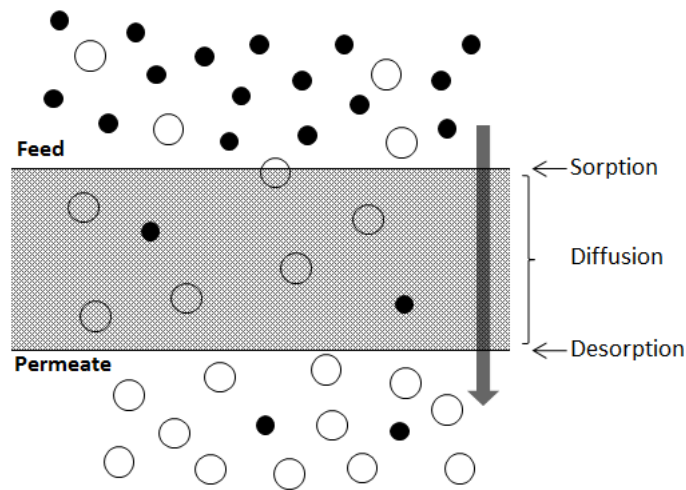
Figure 4: Solution-diffusion transport mechanism in dense or non-porous membranes.

The solution-diffusion model is used for dense polymeric membranes for pervaporation (PV), reverse osmosis (RO) and gas separation. Polymer membranes are typically divided into two categories – glasses and rubbers. Glassy polymers are defined as rigid and tough where the rotation of the polymer segments is prohibited due to the steric hindrance along their backbone. For this reason, glassy polymers possess large fractional free volume (up to 35%). On the other hand, rubbery polymers are characterized by the freely motion of segments of polymer chains. Their free volume is approximately around 10-15%.[9] In membranes of glassy polymer the separation performance is usually governed by the mobility selectivity (smaller molecules diffuse faster than larger molecules). In rubbery polymers, the separation process is based on solubility selectivity, which allows the faster permeation of larger molecules than smaller ones due to higher solubility coefficients. [17]

2.1.4. Membrane applications

Membranes have been developed for an extensive and still growing range of different applications including microfiltration (MF), ultrafiltration (UF), nanofiltration (NF), reverse osmosis (RO), pervaporation (PV), gas separation (GS), dialysis, electrodialysis and membrane distillation (MD) [8]. Table 3 shows the relevant characteristics and applications of the various membrane separation processes mentioned above.

Table 3: Relevant characteristics of the various separation processes (L- liquid phase, G – gas phase) [8].

Separation process	Phase 1	Phase 2	Driving force	Material pore size	Applications
Microfiltration (MF)	L	L	Pressure 0.1 -2 bar	0.1-10 µm	Clarification and sterilization of solutions Concentration of cells
Ultrafiltration (UF)	L	L	Pressure 1–5 bar	5-100 nm	Fractionation and concentration on solutions Recovery of oils and pigments
Nanofiltration (NF)	L	L	Pressure 1.5-40 bar	1-5 nm	Purification of proteins Separation of organic compounds and salts
Reverse Osmosis (RO)	L	L	Pressure 10-100 bar	< 2nm	Desalination
Dialysis	L	L	Concentration	< 2nm	Haemodialysis Separation on salts
Liquid membranes	L/G	L/G	Concentration	10-100 nm	Gas separation, waste water treatment
Electrodialysis	L	L	Electrical potential	< 2nm	Separation of ions from water
Gas separation	G	G	Pressure Concentration	<1 nm	CO2/CH$_4$ separation H$_2$ recovery
Pervaporation (PV)	L	G	Concentration	< 1nm	Volatile separation

2.1.5. Membrane materials

Membranes have been successfully made from a large number of different materials including polymers, inorganic, metals, glass and liquids [10]. The choice of the materials should be tailored in order to meet the required specifications. Among all, polymers are the most commonly used materials in membrane technology for diverse applications. Polymers are flexible, inexpensive and easy to process [18, 19]. With regards to the recovery of bioalcohol through PV, polydimethylsiloxane (PDMS), also known as silicone rubber, is the material most commonly used for the production of commercial membranes. It is characterized by its high degree of hydrophobicity and excellent chemical stability. With respect to gas separation, cellulose acetate (CA), polysulfone (PSF) and polyimides are the most representative polymers currently used in industry. More recently, polymers of intrinsic microporosity (PIMs) have been successfully synthetized as promising membrane materials. The most representative PIMs, PIM-1, presents intrinsic characteristics that make it suitable for both bioalcohol recovery and CO_2 separations; PIM-1 is an organophilic polymer and has high solubility towards CO_2.

Since PIM-1 is the polymer material used in this work, a more detailed discussion on PIM-1 is given in section 2.1.5.1.

Despite the advantages of polymer membranes, they have drawbacks including low thermal and chemical stability, swelling and change in performance over time. Thus, the development of mixed matrix membranes (MMMs) has emerged as potential membrane morphologies to overcome such disadvantages. They are composed by a filler, which can be organic, inorganic or hybrid, embedded in a polymer phase. MMMs have been developed in order to benefit from the advantages of both phases, aiming to enhance the overall performance of the membrane, regardless of their application.

In organophilic PV, MMMs have been fabricated in order to reduce the membrane swelling, improve separation performance and increase the productivity of the membrane. Carbon nanotubes (CNTs) [20], zeolitic imidazolate frameworks (eg. ZIF-71 [21]) and silicalite-1 [20, 22] are examples of fillers used for such purpose. With regard to gas separation membranes, the incorporation of fillers may help in the retardation of the physical aging as well as lead towards an improvement in the selectivity and permeability properties of the membranes. In addition, the fabrication of MMMs has been also reported in other membrane applications including UF [23], NF [24], RO [25] and fuel cells [26]. Enhancement of anti-fouling properties, flux, and rejection are examples of properties that have been enhanced by using different fillers in MMMs for those applications.

Despite their promising features, MMMs still present a challenge when trying to achieve a homogeneous and stable dispersion of the filler into the polymeric dope solutions to prepare defect-free membranes [27]. Figure 5 shows different interfacial morphologies in MMMs. The creation of voids, rigidified polymer chain and plugged sieves are examples of defects that might happen in MMMs [27-29]. The lack of compatibility between the filler particles and the polymeric matrix can result in the formation of non-selective voids, which, in turn, leads to membranes with increased permeability and with loss of selectivity. Rigidification occurs when polymer chains are densely packed around the filler particles, and normally leads to

an improvement in selectivity with a loss of flux. Finally, plugged sieves is caused by the clogging of the pores, when remaining processing solvents and/or polymer chain block partially or completely the pores, resulting in reduced permeability, with variation in selectivity depending on the extent of pore blockage and permeant molecular sizes. [27] The formation of agglomerates is another issue when designing MMMs, since it can cause the formation of gaps between the two phases resulting in defective membranes. In thin films, the presence of agglomerates is even more relevant since they can span the entire thickness of the membrane creating a nonselective path across it. [27] Besides that, the size of the filler has a significant impact on the overall membranes performance, especially in TFC membranes [30-36].

Ideal morphology   **Voids**   **Rigidified polymer chain**   **Plugged sieves**
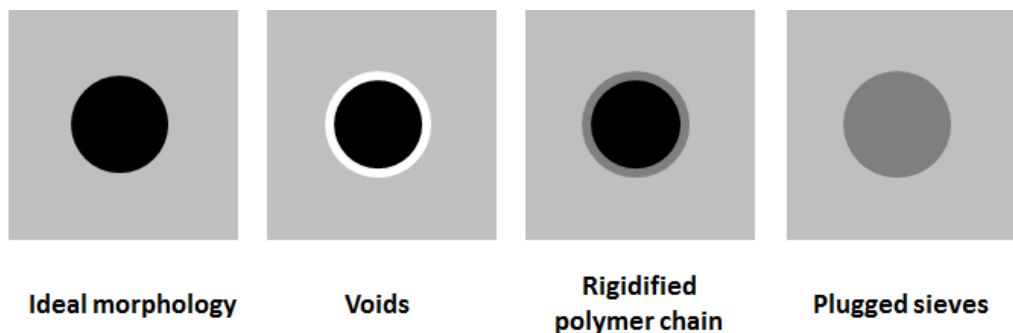
Figure 5: Interfacial morphologies in MMMs (adapted from [27]).

2.1.5.1.   Polymers of intrinsic microporosity

In 2004, Budd *et al*. [3] introduced a new class of porous materials named polymers of intrinsic microporosity. Intrinsic microporosity in polymers is defined as *"a continuous network of interconnected intermolecular voids, which forms as a direct consequence of the shape and rigidity of the component macromolecules "* [37]. In a PIM, conformational freedom of polymeric chains is restricted due to the absence of single bonds along the polymer backbone, affecting their packing and thus the free volume distribution. PIMs present a fractional free volume above 20% [38].

Among all PIMs, PIM-1 is the most commonly used for membrane formation. According to the International Union of Pure and Applied Chemistry (IUPAC), PIM-1 is classified as a microporous material since it has a pore size of 2 nm. In PIM-1, the intrinsic microporosity results from the frustrating packing of polymer chains due to

a spiro-centre (i.e. a single tetrahedral C atom shared by two rings) of contortion in the rigid ladder polymer chain which causes a random contorted structure [17, 39, 40]. Thus, free volume at molecular dimension in solid state is created as result of poor molecular packing. Figure 6 shows the chemical structure and a molecular model of PIM-1.

PIM-1 is soluble in few common organic solvents such as chloroform and tetrahydrofuran, which allows the fabrication of membranes through solution-process techniques including solvent evaporation, dip-coating, spin coating and phase inversion. In addition, PIM-1 features good chemical, mechanical and thermal stability [39].

PIM-1 has been subject of study for various membrane-based applications such as GS [17, 41, 42], hydrogen storage [43], organic solvent nanofiltration (OSN) [44, 45] and PV applications [3, 4, 46, 47]. PIM-1 is an organophilic polymer, thus, selective towards organic compounds from aqueous solutions [3, 4, 46, 47]. Moreover, PIM-1 possesses higher solubility coefficients than other polymers [17, 48], especially for CO_2, which make it a promising material for CO_2 separation over other gases such as CH_4 and N_2 [49]. However, despite the extensive work on the use of PIM-1 for membrane development, the first commercial PIM-1 application is an end-use life sensor used for organic vapour absorbing cartridge developed by 3M, which benefits from the strong affinity of the polymer to organic vapours. [50]

(a)   **(b)**
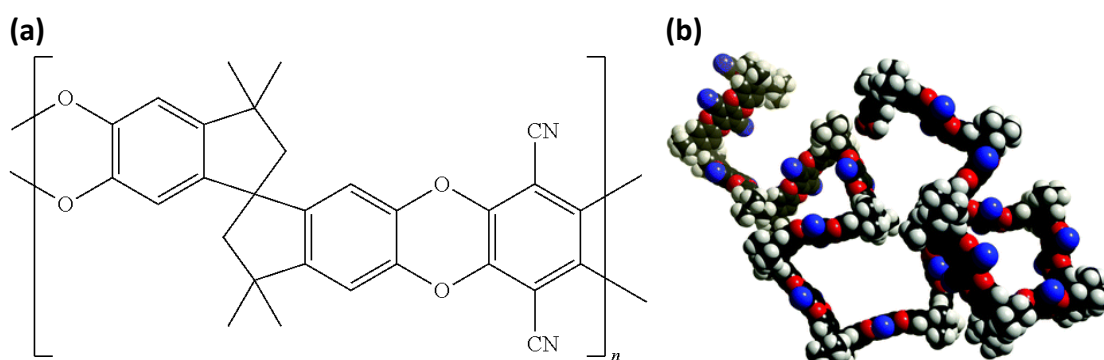
Figure 6: (a) Structure of PIM-1 and (b) molecular model of a small fragment of PIM-a showing its rigid and contorted structure (adapted from reference [43]).

2.1.6. Membrane fabrication

This Thesis contains results from membranes prepared via solvent evaporation, phase inversion and dip coating techniques. Therefore brief descriptions of their principles are included in the following subsections. It is worth mentioning that these fabrication techniques can be carried out for the fabrication of purely polymeric membranes and mixed matrix membranes containing a variety of fillers in polymer matrices.

2.1.6.1. Solvent evaporation

Solvent evaporation is a straightforward technique used to prepare dense homogenous polymer membranes. A dope solution is cast on a suitable substrate (e.g. flat petri dish) followed by the slow evaporation of the solvent at a given temperature. This leads to the precipitation of the polymer and dense homogenous polymer membrane is formed. Freestanding PIM-1 membranes and MMMs studied in this Thesis were prepared following this method.

2.1.6.2. Non-solvent induced phase inversion

Non-solvent induced phase inversion is a technique that is commonly used in the preparation of polymer MF [51], UF [52] and NF [53] asymmetric membranes. Besides that, these porous polymer membranes can be used as support layers for the fabrication of composite membranes, providing mechanical support to the thin top layer without additional transport resistance [44]; this method was employed in this Thesis to fabricate membrane supports for such purpose. It is worth mentioning that very recently, hollow fibre PIM-1 membranes have been successfully fabricated using this technique for their application in GS [54].

In this procedure (Figure 7), a polymer solution is poured into either a glass slide or on a non-woven fabric and is spread on top of it by means of a casting knife. Then, the cast polymer solution is immersed into a coagulation bath (e.g. water), and the mass exchange between the solvent and the non-solvent occurs [55]. A dense layer, also called skin layer, on the surface of the membrane can be achieved by using a non-solvent with low mutual affinity to the solvent. This dense layer is formed when a high ratio between the solvent outflow and the non-solvent inflow is

registered, resulting in delayed demixing and increase in polymer concentration on the surface of the membrane. [8, 56]
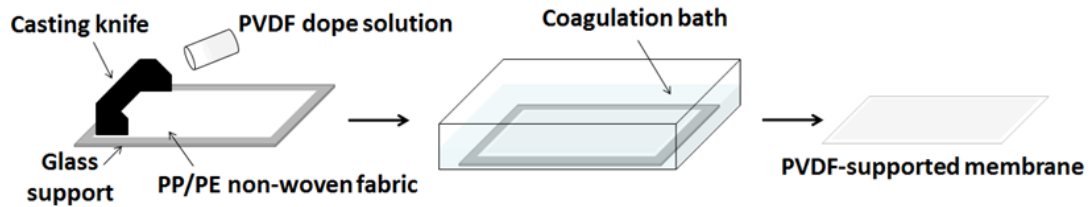
Figure 7: Non-solvent induced phase inversion.

2.1.6.3.   *Composite membranes through dip coating*

Dip-coating is a fabrication technique commonly used for the preparation of TFC membranes. Thus, this technique was selected for the work on thin films in this Thesis. This process involves the immersion of a porous substrate into a coating solution and its subsequent removal at a controlled speed. The solvent in the polymeric coating solution evaporates leading to the formation of a thin film on top of it. The morphology of the final membrane depends on the support and the operating coating parameters. With regard to the support, controlled surface pore size and porosity of the substrate are desired. Generally, smaller surface pore sizes lead to the formation of defect-free coatings of the substrate, and the membrane effective area is maximised with increasing surface porosity.[47] The formation of the active layer is also affected by operating parameters such as the concentration of the dope solution and withdrawal speed. The increase in concentration of the dope solution and consequent increase of its viscosity leads to a formation of thicker membranes as observed by Gao *et al.* [47]. Regarding the withdrawal speed, there is no linear relationship between the coating thickness and the withdrawal speed [57]. It is noteworthy that the total thickness of the dip-coated membrane is difficult to be measured, as the penetration of the dope solution into the pores of the substrate is likely to occur.

2.1.7. Membrane market

The global market for membrane technology is forecasted to increase worldwide [58, 59]. In 2014, Asia-Pacific had the largest membrane technology market share of 32.21%. In this region, China was registered as the largest consumer. In the same year, North America accounted for the second largest global market share of 27.08%, where USA represents 87.04% of that consumption. In Europe, Germany and France are the largest market shareholders, accounting for 36.41% of the total European membrane market in 2014.[58] A maximum growth of 7.9%/year in membrane market is predicted between 2015 and 2020 [60, 61].

MF, RO and UF technologies are processes that together accounted for 78.36% of the membrane market in 2014. Amongst these, NF is expected to experience the fastest growth rate from 2015 to 2020 which in turn is attributed to the rapid growth of water and wastewater treatment membranes, and pharmaceutical and biomedical applications.[58, 62]

Similar to industry, there is an obvious rapid growth in the number of membrane-related publications over time, as shown in Figure 8. The increase in membrane-related publications shows the academic and industrial interest and the importance of these processes. The number of publications on some of the most studied membrane-based separation processes was obtained on *ISI web of knowledge* between years 2000 and 2017.
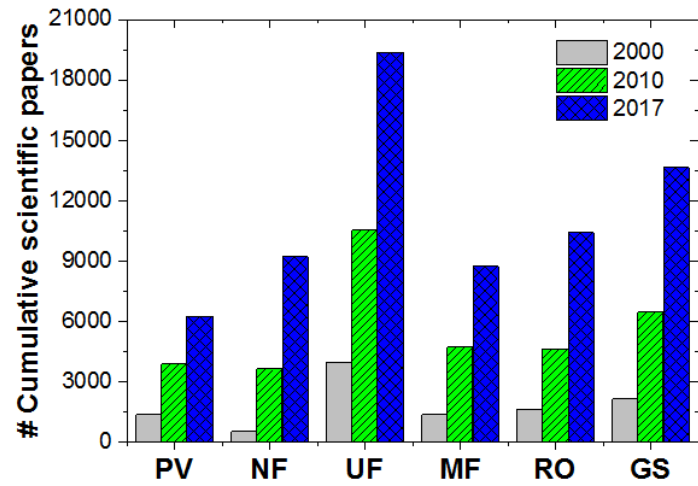
Figure 8: Cumulative number of publications in various membrane-based processes – pervaporation (PV), nanofiltration (NF), ultrafiltration (UF), microfiltration (MF), reverse osmosis (RO) and gas separation(GS). Data taken from *ISI web of knowledge*.

2.2. Pervaporation for bioalcohol recovery

2.2.1. Overview

Technological growth and social development have been the major driving forces to the increase in energy consumption, which has turned to be one of the greatest concerns worldwide. Currently, the transportation sector consumes approximately 20% of all global energy, and according to British Petroleum (BP), an increase in transportation consumption of approximately 1 Billion toe by 2035 is predicted as shown in Figure 9a [63]. Currently, petroleum dominates as the preferred transportation energy source and a continuing global rise is expected (Figure 9b) [64].

(a)

Billion toe

(b)

Quadrillion Btu
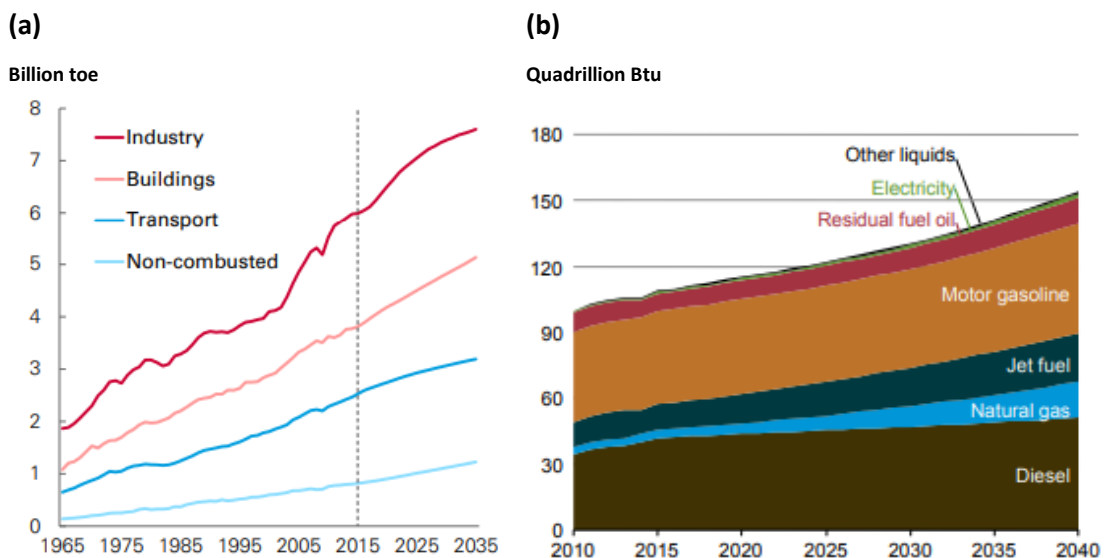
Figure 9: (a) consumption of energy by sector [63] and (b) transportation sector energy consumption by fuel (other liquid fuels include natural gas plant liquids, biofuels, gas-to-liquids and coal-to-liquids) (Btu – British thermal unit, toe – Tonne of oil equivalent) [64].

Besides being a finite source of energy (i.e. reserves will run out sooner or later), fossil fuels present risks associated with the emission of greenhouse gases (GHG) into the atmosphere when they are burnt. The replacement of these fuels by sustainable alternative sources of energy has been promoted worldwide alongside with environmental awareness in order to mitigate climate change. Moreover, there is a target in achieving at least 10% share of renewable energy sources for vehicles by 2020 according to the 2020 Climate and Energy Package [65].

Biofuels are seen as part of this solution as they are potential contributors to reduce carbon dioxide (CO_2) emissions by completing the carbon cycle. Apart from that, the providing of the security of energy supplier is another feature that make biofuels more attractive over fossil fuels. On the other hand, there are social, economic and environmental aspects that may compromise their sustainability. Increase in land demand, competition with food production systems and water use with consequent food prices rise are real issues regarding the production of biofuels. Land ownerships, human and labour rights are examples of social concerns related to biofuels production.[66]

Bioethanol and biobutanol are both potential biofuels; however, biobutanol presents higher energy content [67-69]. Both bioalcohols can be produced through acetone-butanol-ethanol (ABE) fermentation process, typically at an average weight ratio of 3:6:1, respectively [70]. Maximum biobutanol content on the fermentation broth is usually not higher than 20 g/L in aqueous solution. This low yield is caused by end-product inhibition due to the alcohol toxicity on bacteria [67]. The high-energy demand required for the recovery of ABE products from the fermentation broth is preventing a wider use of such biofules, with separation process accounting for 60-80 % of the operation costs [71].

Distillation is the traditional method used for this application; however, it is an energy-intensive process [72]. Over the past years, the study of alternative processes has been attracting the attention of the scientific community. Among all, pervaporation (PV) has emerged as a potential alternative as it allows a continuous recovery of bioalcohol, hence reducing the alcohol toxicity on bacteria and increasing the productivity of the process. However, research studies have reported the non-economically feasibility of PV as a separation process on its own due to low permeate fluxes, where huge areas are required, and the difficulty in achieving products of high purity [73-75]. On the other hand, PV processes integrated with distillation require less energy than pure distillation as PV membranes can be used to increase the biobutanol concentration that feeds the distillation column [76, 77]. As an example, the energy required to reach a final product purity of 99.9 wt% *n*-butanol (*n*-BtOH), when a feed composition of 0.5wt% *n*-BtOH was used is 79.5

MJ/kg (roughly two times the energy content in 1 kg of *n*-BtOH [78], when distillation is used alone [76]). On the other hand, when an hybrid PV-distillation is used, only 7.4 MJ/kg are required [76].

2.2.2. Definition of pervaporation

The term *pervaporation* results from the combination of the words *permeation* and *evaporation* (Figure 10). It is based on the affinity of a membrane by preferential sorption, diffusion and desorption of some components and is previously described by the so-called solution-diffusion model (section 2.1.3.2.) [15, 79]. The chemical species in the liquid feed solution are partially absorbed on the upstream side of the membrane, permeate through it, being then released on the downstream side of the membrane as vapour. This process can be aided by a driving force such as vacuum, sweep gas or difference in temperature. This separation process is particularly interesting for azeotrope mixtures (liquid and vapour phases have the same composition), close-boiling point components and removal of diluted compounds [9, 70]; it is an energetically favourable process for the extraction or recovery of diluted species from a liquid mixture as only a small part of the feed mixture has to be vaporised.
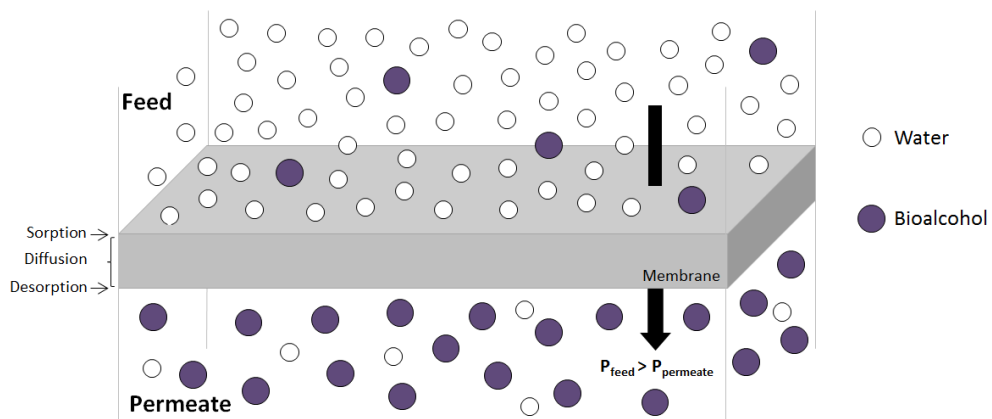
Figure 10: Schematic diagram of bioalcohol recovery from water by pervaporation.

2.2.3. Parameters in pervaporation membrane performance

The performance of a PV membrane is determined by mainly two parameters, namely, the total permeation flux, *J*, and separation factor for a given component, *β*, as defined by equations (2) and (3), respectively:

$$J = \frac{m}{A\,t} \tag{2}$$

$$\beta = \frac{Y/(1-Y)}{X/(1-X)} \tag{3}$$

Where *m* is the weight (kg) of the permeate, *A* (m^2) is the effective membrane area in contact with the feed solution, *t* is the permeate collection time (h), and finally, *Y* and *X* are the concentrations of component *i* in the permeate and feed side, respectively.

The overall PV performance of the membrane can be evaluated by the PV separation index (PSI) which is defined as follows (Equation (4)) [15]:

$$PSI = J(\beta - 1) \tag{4}$$

The membrane performance depends not only on the nature of the membrane but also on the feed temperature, feed concentration, membrane thickness and downstream pressure. The increase in feed concentration of the desired compound enhances the difference in transmembrane partial pressure, favouring the increase in membrane flux [28, 80]. Similarly, higher fluxes are also registered when lowering the partial pressure of the permeants, due to the enhancement of the transmembrane pressure as driving force [81]. Moreover, the overall mass transfer across the membrane is inversely proportional to the membrane thickness, i.e., thin membranes favour the total flux [82, 83]. The operating temperature is another parameter that affects the overall performance of the membrane; since the feed supplies the heat of vaporisation required for the phase change, a temperature loss between the feed and the retentate takes place and the membrane acts as a heat exchanger barrier. Both solubility and diffusivity coefficients of all permeants are affected by the operating temperature. In general, the diffusivity coefficient

increases with increasing temperature, whereas the solubility coefficient decreases with temperature [84]. The diffusion coefficient measures the rate at which molecules move from one position to another. The increase in temperature leads to an increase in the kinetic energy of the gas molecules, and therefore they will move faster and consequently the diffusion occurs quicker. The solubility coefficient can be defined by the Henry's law that states the concentration of the sorbed compound inside the membrane is proportional to the equilibrium partial pressure of the compound around the membrane. Increased temperature leads to an increase in kinetic energy of the gas molecules that breaks the intermolecular bonds between them, making their escape from the inside of the membrane easier. Generally, the increase in operating temperature increases the total flux and usually has a minor impact on the separation performance of the membrane.

2.2.4. Membrane materials for bioalcohol recovery through pervaporation

Polydimethylsiloxane (PDMS) is a rubber polymer extensively studied for membranes for bioalcohol recovery due to its hydrophobicity, good chemical, thermal and mechanical properties as well as ease and economic fabrication process [80, 85, 86]. PERVAP 4060 (DeltaMem AG, Switzerland), PDMS (Pervatech, the Netherlands), PolyAn (Polyan GmbH, Germany) and GFT 1060 (Deutsche Carbone AG, Germany) are example of PDMS membranes commercially available. Since PDMS-based membranes are prepared through crosslinking processes, these membranes present relatively low fluxes [1]. Therefore, other organophilic polymers with higher free volume have been studied for the same purpose including poly[1-(trimethylsilyl)-1- propyne] (PTMSP) [87-91] and PIM-1 [4, 46, 47]. From these two polymers, PIM-1 seems to be the most promising membrane material due to its better stability in terms of flux over time [46, 92].

The homogeneous dispersion of hydrophobic fillers into polymeric membranes is an effective way to improve membrane performance for recovery of alcohols from aqueous solutions. A wide variety of inorganic fillers have been incorporated into polymer matrices, including carbon nanotubes (CNT) [20], zeolites [22, 80, 88, 93-95] and silica [89]. Table 4 and Table 5 show the PV performance of polymeric lab-

scale membranes and MMMs used for BtOH and ethanol (EtOH) recovery, respectively.

Improvements in performance can be due to different factors including enhancement of hydrophobicity of the membrane surface [93], reduction of membrane swelling [93, 94, 96], better mechanical properties [93] as well as enhanced affinity towards the alcohols over water [95-97]. In addition, the yield (i.e. flux) can be greatly enhanced by reducing the thickness of the membrane active layer [47, 89].

Table 4: Performance of PV membranes for the separation of *n*-BtOH from water.

Membrane	Temp. (°C)	BtOH$_{Feed}$ (wt.%)	Separation factor, β	Flux, J (kg m^{-2} h^{-1})	Ref.
10 wt.% CNT/PDMS	80	0.8	32.9	0.244	[20]
25 wt.% ZIF-71/PEBA	40	1	22.3	0.085	[21]
PEBA 2533	60	0.4	32	0.400	[97]
PDMS	70	1	48.66	0.350	[85]
60 wt.% Silicalite-1/PDMS-	70	1	93	0.607	[85]
PIM-1	50	2	2.8	0.107	[4]
PDMS/PVDF	30	3	44	0.331	[98]
PDMS/PVDF-Fe(II)	30	3	42	0.233	[98]
PEBA	60	1	21	4.196	[99]
PIM-1	65	5	18.5	5.640	[47]
25 wt.% silica/PTMSP	50	5	104	9.500	[89]
PTMSP	70	1.5	70	1.030	[90]

Table 5: Performance of PV membranes for the separation of EtOH from water.

Membrane	Temp. (°C)	EtOH$_{Feed}$ (wt.%)	Separation factor, β	Flux, J (kg m^{-2} h^{-1})	Ref.
PDMS	50	5	~6	~0.100	[80]
40 wt.% Silicatie-1(F)/PDMS	50	5	23.8	~0.160	[80]
PTMSP	50	10	17	0.800	[87]
PIM-1	60	5	3.25	0.704	[22]
silicalite-1/PIM-1	60	5	5.68	0.758	[22]
1.5 wt.% Silicalite-1 PTMSP	50	10	12 ± 2	3.5 ± 0.3	[88]
PIM-1	30	10	10.7	0.470	[46]
30 wt.%HF etched ZSM-5/PDMS	50	5	17	0.125	[93]
2 wt.% POSS/Pebax	65	5	5.7	0.427	[96]

2.3. Gas Separation

2.3.1. Overview

Supressing the release of carbon dioxide (CO_2) and other greenhouse gases (GHGs) into the atmosphere in order to mitigate climate change has been the subject of intense research work. A recent report released by the World Meteorological Organization identified the atmospheric CO_2 concentration as the highest in 800,000 years, having reached a concentration of 403.3 parts per million in 2015 [100]. These high levels of CO_2 emissions are linked to population growth, economic development, deforestation and agriculture; and they are expected to keep increasing in the coming years due to the worldwide growing energy demand [100, 101].

In order to address this situation, the Paris Agreement was signed, and the use of renewable energy sources is now a priority to decrease the CO_2 emissions. Biogas is a sustainable alternative candidate to replace fossil fuels. It is produced from anaerobic digestion of organic matter that, by completing the carbon cycle, reduces CO_2 emissions. Biogas is mainly composed of methane (CH_4) and CO_2 and traces of hydrogen sulphide. Similar to natural gas, the presence of CO_2 reduces the calorific value and together with other acid gases originates pipeline corrosion, which in turn make the gas handling, transport and storage difficult and expensive [102, 103].

The development of economic and effective techniques to separate CO_2 from other gases such as CH_4 has attracted great interest over the past few years. Cryogenic separation and amine scrubbing are conventional technologies used for such purpose. However, these processes feature high energy consumption, and require complex equipment, high capital investment and operation costs [102, 104]. For this reason, the development of sustainable alternatives, such as membrane-based processes, has been explored. Their use can reduce the energy demand and maintenance cost, and membranes are well known for their ease of operation and scale-up [102].

2.3.2. Gas separation mechanism

A simplified diagram of a membrane-based gas separation (GS) process is shown in Figure 11. A pressurized feed stream (single gas or a mixture of gases) contacts one side of the membrane and it is separated into two streams: permeate and retentate. The permeate corresponds to the gas or gases that passes through the membrane and the retentate refers to the part of the feed that does not travel across the membrane. A sweep gas is typically used on the downstream side of the membrane as a carrier for analysis at lab-scale. The driving force for this process is the difference in pressure across the membrane. While the feed gas is maintained at high pressure by compression, the permeate streams are usually at atmospheric pressure. Separation is achieved by the difference in the transmembrane transport rates of the feed gases. The gas transport mechanism in PIM-1 membranes is based on the solution-diffusion mechanism.
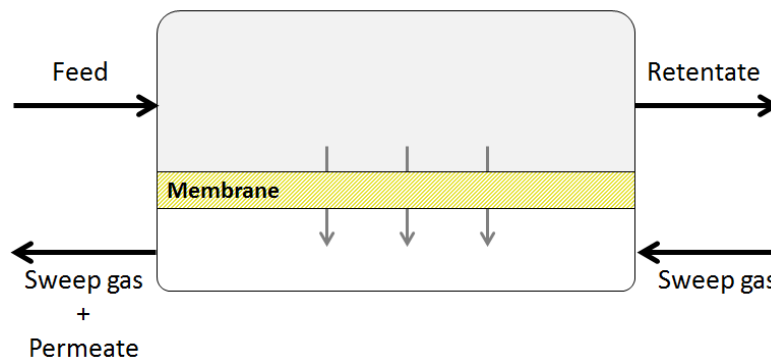
Figure 11: Simplified diagram of a membrane-based gas separation process.

2.3.3. Parameters in gas separation membrane performance

Permeability, permeance and selectivity are the common parameters to assess the effectiveness of a gas separation membrane.

The permeability coefficient of a gas, *P*, is defined by Equation (5), where *l* (cm) is the membrane thickness, *Q* (cm³ s⁻¹, STP) is the gas flow rate, *Δp* (cmHg) is the transmembrane pressure and *A* (cm²) represents the membrane area.

$$P_i = \frac{Q\,l}{A\,\Delta p} \tag{5}$$

The permeability coefficient is commonly given in Barrer, where 1 Barrer = 10^{-10} cm^3 (STP) cm cm^{-2} s^{-1} $cmHg^{-1}$ (SI units: mol m^{-1} s^{-1} Pa^{-1}, 1 Barrer = 3.3×10^{-16} mol m^{-1} s^{-1} Pa^{-1}). Gas permeance is used in asymmetric membranes and corresponds to flux of gas per unit area per unit pressure. It is commonly expressed in gas permeation units (GPU), where 1 GPU = 10^{-6} cm^3 (STP) cm^{-2} s^{-1} $cmHg^{-1}$ = 3.3×10^{-1} mol m^{-2} s^{-1} Pa^{-1}.

The selectivity, α, describes the ability of a membrane to separate gas A from gas B and is defined in Equation (6) as follows:

$$\alpha_{AB} = \frac{P_A}{P_B} \qquad (6)$$

Where P_A and P_B are the permeability coefficients of the gases A and B, respectively, being A the more permeable gas.

The economic viability of a membrane-based separation process is strongly influenced by the permeability of the membranes. The higher permeability, the less membrane area is required, which in turn reduces the operation and capital investment costs. [105-107] On the other hand, the increase in membrane selectivity is generally translated in an increase in overall costs. The higher the membrane selectivity, the higher the concentration of permeant species in the permeate and consequently the lower their concentration in the retentate. This leads to a reduction in the driving force and therefore, the permeability is reduced. In order to keep up with the required recovery of the permeant species, the membrane area needs to increase, resulting in higher overall costs. [107]

Generally, membrane separation processes are still uncompetitive compared to traditional ones due to the low pressure ratio. Therefore, hybrid systems have been considered in order to improve the economic viability of the overall process, such as the use of membranes with cryogenic separation. Herein, the decrease of the overall cost is registered mainly due to the reduction in the size of the cryogenic separation stage. [107]

2.3.4. Membranes materials for CO_2/CH_4 separation

Most of the membranes currently available in the market are manufactured from polymer materials and are found in different configurations (Table 6).

Table 6: Suppliers of commercial membranes for CO_2/CH_4 separation [108, 109].

Company	Product name	Membrane material	Membrane configuration
UOP (USA)	Separex™	Cellulose acetate (CA)	Spiral-wound
MTR (USA)	Ztop	Perfluoro composite	Spiral-wound
	Cytop		-
Airrane	Meritair	Silicone-coated polysulfone	Hollow fibre
NATCO (USA)	Cynara®	Cellulose triacetate	Hollow fibre
Air Products (USA)	Prism®	Polysulfone	Hollow fibre
Air Liquid (USA)	Medal	Polyimide	Hollow fibre
Kvaerner	Grace	Cellulose Acetate	Spiral wound
Ube Industries		Polyimide	Hollow fibre
Praxair	IMS	Polyimide	Hollow fibre

Apart from the polymers shown in Table 6, other materials have been investigated for CO_2/CH_4 separation including polyethersulfone (PES) [110], polycarbonate (PC) [111], poly(trimethylsilyl propyne) (PTSMP) [112] and PIM-1 [17, 41, 42, 48, 113]. Despite their numerous advantages such as their flexibility, ease of fabrication and reduced cost, polymers normally suffer from a general trade-off between permeability and selectivity. It was represented by Roberson for the first time in 1991 (Robeson upper bound) [114] and revisited by the same author in 2008 [115] (Figure 12a). Roberson's diagrams are log-log plots of selectivity versus permeability of the more permeable gas for common binary gas mixtures. On the other hand, the performances of inorganic membranes lay far beyond the 2008 Roberson upper bound (Figure 12b). Their major drawbacks are the high cost, brittleness and difficulty in membrane fabrication.

Similarly to PV, MMMs have been proposed to combine the advantages of both polymer and inorganic membranes for gas separation applications and potentially surpass the upper-bound limit. Both porous and nonporous fillers have been used in MMMs for CO_2/CH_4 separation. Porous fillers include zeolites [111, 116-118], carbon molecular sirves (CMS) [119-121], metal-organic framework (MOFs) [113, 122-125], carbon nanotubes (CNTs) [126-129]. Graphene [112], silica [42, 130],

metal oxide particles [110] are example of nonporous fillers embedded in MMMs. Table 7 compares the CO_2/CH_4 separation performance of polymer membranes and MMMs composed of different polymers and fillers. Polyimide (PI) membranes, such as 2,2'-bis (3,4'dicarboxyphenyl) hexafluoropropane dianhydride (6FDA) and Matrimid® are examples of polymer matrices that have been intensively studied for CO_2/CH_4 separation. Besides showing an interesting performance and stability, their productivity is relatively low. In this respect, poly[1-(trimethylsilyl)-1-propyne] (PTMSP) shows the highest permeabilities due to its high free volume; however, it has poor selectivity. The success of MMMs depends on different factors including the compatibility between the polymer matrix and filler [125, 127], filler size [32, 131], morphology [30, 33] and loading [125, 130, 132]. Chen *et al.* showed that better membrane performances were obtained by functionalizing the filler, improving their dispersion in the polymer matrix and therefore, minimizing the defects in the membranes such as those caused by sedimentation [125]. In addition, a good dispersion of the filler inside the polymer matrix allows the use of higher filler loading in order to take the most of the advantages of the properties of the filler [125]. The addition of a filler can also modify the molecular packing of the polymer chains, increasing the free volume, and therefore enhancing the membrane performance as shown by Zornoza *et al.* [130].

In addition to MMMs, other strategies have been adopted to improve the membrane performance in purely polymeric ones including polymer blending [133], polymer cross-linking [134] and thermal annealing [135].
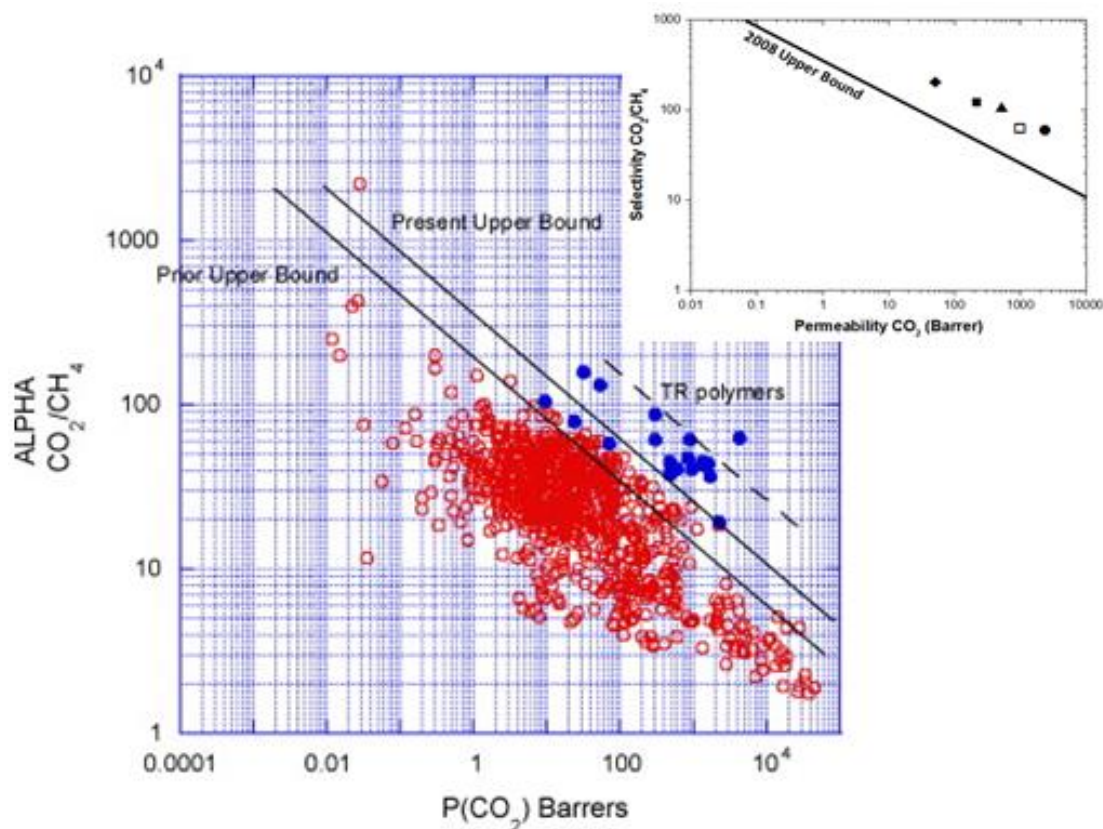
Figure 12: 1991 and 2008 Upper bound correlation for CO_2/CH_4 separation plotted on a log-log plot scale [115] and inorganic membranes shown in the inset: ● [136], ■ and ▲ [137], □ and ◆[138] (TR: thermally rearranged).

An important requirement for membrane commercialization is the long term stability, which is often adversely affected by the physical aging of the polymer. Physical aging refers to the loss of free volume as a function of time due to the rearrangement of the polymer segments approaching an equilibrium state [139, 140]. This leads to a decline in gas permeability that represents a potential obstacle for their application in industry. This phenomenon is more evident in high-free volume polymers, including PTMSP and PIM-1, being the later one the polymer studied in this Thesis. Several strategies have been shown as effective ways to retard the physical aging, including the addition of fillers [49, 141-143], UV-treatment [144], UV photo-oxidation [145], surface modification [146] and cross-linking [145, 147]. It is noteworthy that physical aging is more pronounced in thin films, as the free volume diffuses faster towards the surface of the polymer membrane in thin films [148]. Apart from that, aging temperature [149], storage conditions (e.g. temperature, atmosphere and pressure) [150] and membrane treatment [39, 48, 49, 151, 152] also affect the physical aging of membranes.

Moreover, Pilnáček *et al.* reported that different results are obtained when different experimental testing methodologies (continuous or momentary) are chosen [153]. Amongst all, only the effect of the addition of different fillers into the polymer matrix on the physical aging was a subject of our study.

Plasticization is another issue that affects PIM-1 membranes. CO_2, acting as a plasticizer, swells the polymer, hence increasing the mobility of polymer chains and free volume. As a consequence, the permeability of all gases is enhanced and the selectivities are reduced.[154] This phenomenon occurs when membrane are exposed to high operational pressures and is more evident in thin films compared to thick films. Tiwari *et al.* reported an up to 4-fold increase in CO_2 permeability when thin PIM-1 membranes were under 32.4 bar [155].

Table 7: CO_2/CH_4 separation performance of polymer membranes and MMMs.

Membrane	Pressure (bar)	Temp. (ºC)	CO_2 permeability/ permeance		Selectivity (CO_2/CH_4)	Test type[b] (CO_2 vol.%)[c]	Ref.
			Value	Units[a]			
6FDA-BAPAF	30	21	24.60	GPU	22.78	S	[156]
6FDA-DAP	30	21	38.57	GPU	77.82	S	[156]
6FDA-DABA	30	21	26.30	GPU	46.96	S	[156]
PDMS	2-4	23	3800	Barrer	3.17	S	[157]
Matrimid®	15	20	11	GPU	67	M (20%)	[158]
Pebax®1657	3.75-7.5	20	287	GPU	14	S	[122]
34 wt.% ZIF-7/Pebax®1657	3.75-7.5	20	39	GPU	44	S	[122]
Matrimid®	5	35	10	GPU	17	M (35%)	[123]
30 wt.% ZIF-8/Matrimid®	5	35	23	GPU	20	M (35%)	[123]
6FDA-durene	3.5	30	468	Barrer	7	S	[118]
1 wt% Zeolite T/6FDA-durene	3.5	30	858	Barrer	18	S	[118]
Matrimid®	3	35	6.20	Barrer	28.2	S	[124]
15 wt% MIL-53/Matrimid®	3	35	12.43	Barrer	51.8	S	[124]
6FDA-ODA	10.3	35	14.4	Barrer	47.1	M (50%)	[125]
25 wt.% Al-MIL-53/6FDA-ODA	10.3	35	20.9	Barrer	44.9	M (50%)	[125]
25 wt.% Al-MIL-53-NH$_2$/6FDA-ODA	10.3	35	14.4	Barrer	64.2	M (50%)	[125]
PIM-1	1	20-22	4390	Barrer	14.2	S	[41]
36 vol.% ZIF-8/PIM-1	1	20-22	6820	Barrer	13.4	S	[41]
PIM-1		30	2300	Barrer	18.4	S	[17]
PIM-1		25	4390	Barrer	14.2	S	[48]
PC	3.7	25	8.8	Barrer	23.6	S	[111]
20 wt% Zeolite 4A/PC	3.7	25	78	Barrer	32.5	S	[111]

[a]1 GPU = 10^{-6} cm³(STP) cm^{-2} s^{-1} cmHg^{-1}; 1 Barrer = 10^{-10} cm³ (STP) cm cm^{-2} s^{-1} cmHg^{-1}
[b]Test type: Single gas experiment (S) and mixed gas experiment (M).

Continued from Table 7.

Membrane	Pressure (bar)	Temp. (°C)	CO_2 permeability/ permeance		Selectivity (CO_2/CH_4)	Test type[b] (CO_2 vol.%)[c]	Ref.
			Value	Units[a]			
PI	1	15	2.31	Barrer	10.04	S	[126]
3 wt.% MWCNT/PI	1	15	5.44	Barrer	15.54	S	[126]
PES	10	29	1.33	GPU	7.6	S	[133]
3 wt.% ESPU/PES	10	29	1.89	GPU	5.3	S	[133]
3 wt.% ETPU/PES	10	29	1.92	GPU	3.7	S	[133]
PIM-1	2	30	4506	Barrer	12.5	S	[113]
20 wt.% ZIF-67/PIM-1	2	30	5182	Barrer	16.8	S	[113]
PTMSP		30	21900	Barrer	2.4	S	[112]
GO/PTMSP		30	23800	Barrer	2.4	S	[112]

[a]1 GPU = 10^{-6} cm^3(STP) cm^{-2} s^{-1} cmHg^{-1}; 1 Barrer = 10^{-10} cm^3 (STP) cm cm^{-2} s^{-1} cmHg^{-1}

[b]Test type: Single gas experiment (S) and mixed gas experiment (M).

2.4. Graphene in membrane technology

2.4.1. Background

Graphene is defined as a two-dimensional nanomaterial where carbon atoms are arranged into a hexagonal honeycomb structure [159]. It is one atom thick and features remarkable properties including high thermal and electrical conductivity [160-162], mechanical strength, flexibility and transparency [163]. Graphene is the basic compound of all other dimensionalities of carbon materials as 0D buckyballs, 1D nanotube or 3D graphite [159], as seen in Figure 13.
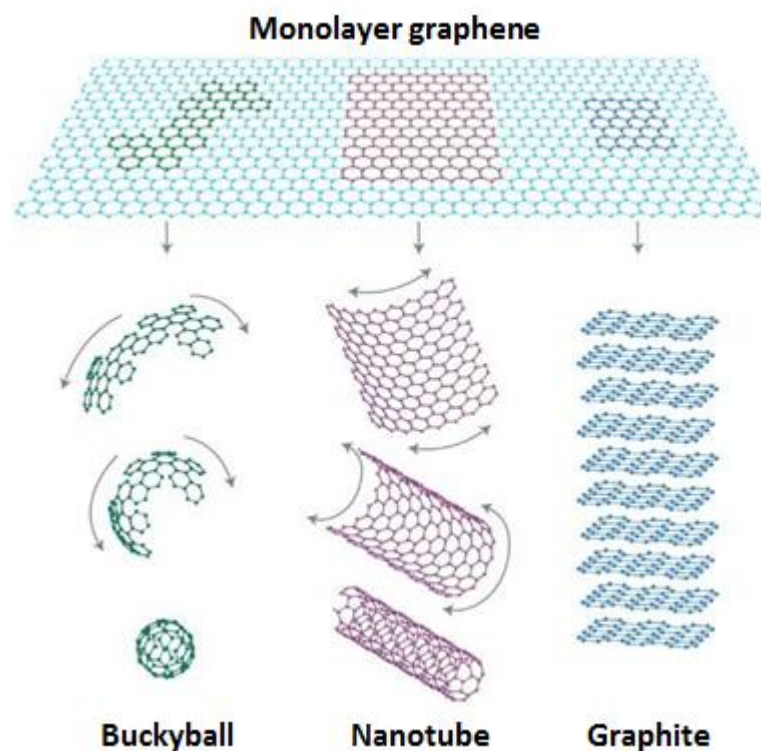
Figure 13: Different dimensionalities of carbon materials having graphene as the basic building block (adapted from [159]).

Graphene was isolated for the first time in 2003 by Novoselov *et al.* by repeatedly peeling off layers of graphite block until a monolayer was reached by means of a scotch tape [164]. This breakthrough in science distinguished Andre Geim and Kostya Novoselov with the Nobel Prize in Physics in 2010. All the outstanding properties combined in one material have enabled its use for a wide range of different applications, including transistors [165], energy storage [166], flexible

electronics [167] and composite materials [168]. This is evidenced by the increasing number of scientific publications over the past years, as shown in Figure 14.
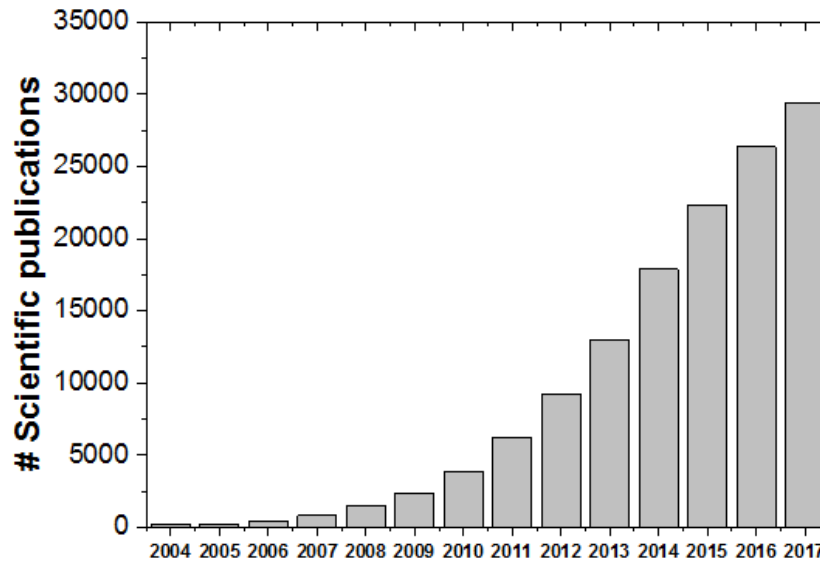
Figure 14: Graphene-related scientific publications. Data was obtained on ISI web of knowledge between 2004 and 2017.

2.4.2. *Fabrication of graphene*

Graphene fabrication methods can be divided into two different categories: bottom-up and top-down methods. Bottom-up methods involve the growth of graphene on different substrates and commonly include epitaxial growth using silicon carbide and chemical vapour deposition (CVD). On the other hand, top-down approaches are based on the exfoliation of bulk graphite including micromechanical cleavage ("scotch tape" method), chemical exfoliation and chemical synthesis. [169] Large scale synthesis of pristine graphene suitable for all applications still remains a challenge to the scientific community. Moreover, each abovementioned fabrication method results in graphene that differs in terms of quality, size, price and quantity. Since there is not a single method to produce graphene that suits all applications, the choice of fabrication method should be based on the requirements for a particular application. [170] Figure 15 presents several methods and their position in terms of the quality of graphene synthetized and its price when mass-produced.
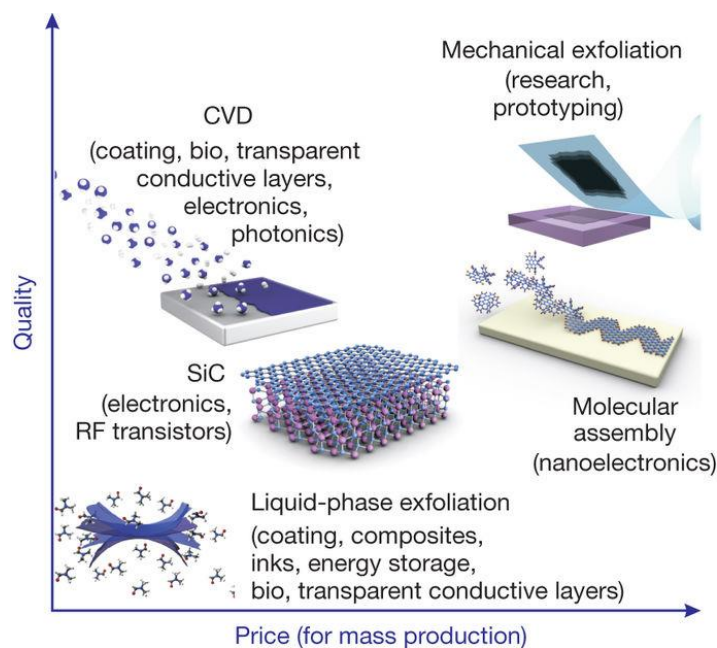
Figure 15: Fabrication methods of mass-production of graphene, and their relationship between quality and price for any particular application (Reprinted from [171], with permission from Springer Nature).

2.4.3. Graphene-based membranes

Since its discovery, graphene has received the attention of the scientific community for a wide variety of applications, including membrane separation technology. Graphene is an attractive material to membrane applications due to its atomic thickness, mechanical strength and flexibility. In 2008, Bunch *et al.* demonstrated the impermeability of a defect-free graphene sheet to all gases and liquids [172]. Therefore, the creation of controlled pore sizes (nanoholes), together with the one atom-thickness feature, make graphene a potential membrane material. This has been confirmed by theoretical studies which have predicted very high permeabilities and selectivities [173-175]. However, highly permeable membranes are expected to register a gradual built-up in concentration of the less permeating species on the upstream side of the membrane, creating a boundary layer. As a consequence, the flux and selectivity decrease because the concentration gradient across the membrane is reduced. This phenomenon is known as concentration polarization. Few experimental attempts have been devoted to the fabrication of such membranes; techniques including ultraviolet-induced oxidative etching [176] and electron beam exposure[177] have been used. However, the need for high and

uniform pores density with controlled pore sizes in larger areas, and the scale-up of the fabrication techniques still remain a challenge.

Alternatively, graphene derivatives have been investigated for membrane-based separations. Amongst all, graphene oxide (GO) has been getting great attention for such purpose. This material consists of a monolayer of graphite oxide, which results from the exfoliation of highly oxidised graphite. GO is rich in oxygen-containing functional groups (epoxy, hydroxyl and carboxyl) located on its basal planes and edges. For this reason, GO features highly aqueous processability, possibility of further functionalization, low cost and large scale production [178].

The breakthrough discovery was made by Nair *et al.* [179], reporting vacuum-assisted self-assembled GO membranes that are only permeable to water, whereas gases (hydrogen (H_2), nitrogen (N_2) and argon (Ar)) and organic molecules (ethanol, hexane acetone, decane and propanol) are left behind. Herein, the mass transport in such membranes occurs along the interlayer spacing, *d*-spacing, between two-dimensional GO sheets (Figure 16a). Following Nair's discovery, a large number of studies on GO membranes have been reported, including separation of organics over water [180, 181]. Over the years, both freestanding and supported onto a porous layer (e.g. alumina) GO membranes have been investigated and different fabrication methods have arisen including vacuum and pressure filtration [182-184], coating [185] and layer-by-layer (LbL) [186]. More recently, Abraham *et al.* tailored the *d*-spacing of GO membranes by changing the humidity of the surroundings and the separation was performed for the first time along the GO planes, as shown in Figure 16b [187].
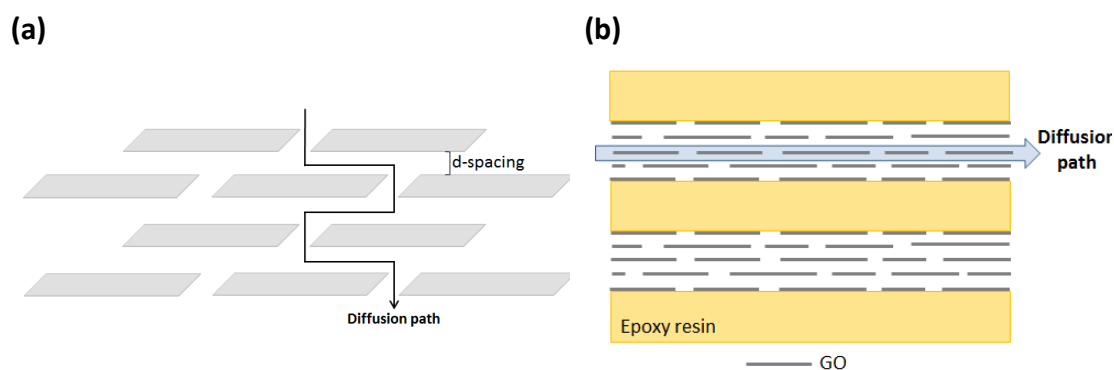
Figure 16: Graphene oxide membranes: (a) transport perpendicular to GO nanosheets and (b) transport along the GO nanosheets.

Reduced graphene oxide (rGO), a graphene–like material that results from the reduction of GO, has also been investigated as a potential membrane material. Following that rational, Su *et al.* reported rGO membranes, obtained from the chemical reduction of GO flakes, that were highly impermeable to all gases and liquids due to its high degree of graphitization [188]. Ultraviolet (UV) reduction has also been demonstrated as an effective way to prepare rGO membranes from GO flakes; Sun *et al.* prepared hybrid membranes intercalating monolayer titania nanosheets into GO flakes that were then subject to UV radiation. These membranes showed impressive overall water desalination performance. [189] Other graphene-like materials, resulting from the functionalization of GO flakes, have been used for the fabrication of graphene-based membranes. The functionalization endows the required properties including making it dispersible in organic solvents and enhancing the interaction between the membranes and the target permeating molecules. With regards to that, Pei *et al* reported high water permeation and salt rejection of graphene-based membranes containing dopamine-functionalized GO flakes [190].

Graphene-based membranes have been also investigated in gas separation (GS), which is an important part of this Thesis. Although defects are undesirable in electronic applications, they might provide an opportunity in membrane technology since they can provide more and shorter transport pathways through the stacked GO nanosheets. Following this rational, Li *et al.* prepared ultra-thin GO membranes highly permeable to H_2 and extremely high H_2/CO_2 (3400) and H_2/N_2 (900)

selectivities [191]. Moreover, the functionalization of those materials can enhance both the solubility and diffusivity parameters. Several studies have been reported with regard to this matter including mixed matrix membranes (MMMs) made of acid-functionalized GO nanosheets in sulfonated poly(ether ether ketone) (SPEEK) matrix [192], MMMs with polyethylene glycol- and polyethylenimine functionalized GO nanosheets incorporated into Pebax 1657 matrix [193] and MMMs made with CNTs and GO into Matrimid® matrix [194]. CO_2 permeability of MMMs made of graphene and PIM-1 have been studied by Althumayri *et al.* [195]; an increase in CO_2 permeability is observed at some extent (graphene content of 0.05 vol.%, 12700 Barrer) that might be due to changes in packing of the polymer chains. At higher graphene loadings, the CO_2 permeabilities decrease possibly due to the impermeability of graphene.

Regarding pervaporation (PV), several studies emphaticizing the use of GO and graphene-like materials either on their own or as a filler, have been reported on dehydration of alcohols. Cao *et al.* demonstrated an enhancement of both swelling resistance and mechanical stability in MMMs containing either GO or rGO in a sodium alginate matrix when used for ethanol (EtOH) dehydration [196]. Yeh *et al.* reported a superior performance of GO thin film composite (TFC) membranes for EtOH dehydration when compared to commercial membranes [197]. Relatively to freestanding membranes, it has been reported that the packing density of GO membranes is affected by the pressure at which the membranes are fabricated, which in turn, has an impact on their PV performance [180]. Higher pressures lead to faster filtration processes and consequently to the formation of non-orderly assembled GO membranes. Tang *et al.* showed an optimal fabrication pressure of 5 bar for GO membranes used in EtOH dehydration [180]. Additionally, Wang *et al.* studied the performance of a GO/Poly(vinyl alcohol) (PVA) membrane for toluene/*n*-heptane separation [198]. Their results showed a reduction in membrane swelling as well as an improvement in separation performance towards the aromatic compounds due to their preferential affinity to the membrane. To the best of our knowledge, the work in this Thesis presented in Chapter 4 and already

published in *Journal of Membrane Science*, is the very first work on graphene-based

membranes for alcohol recovery from aqueous solutions through pervaporation.

Chapter 3 - Synthesis and characterization of base materials for membrane preparation: PIM-1 and graphene-like nanosheets

This chapter includes the synthesis and detailed characterization of PIM-1 and the graphene-like materials used in the subsequent chapters. Synthesis methods and some characterization results of the polymer and the graphene-like fillers are included in the publication by Alberto, M., *et al.*, J. Membr. Sci., 536 (2017), 437-449.

3.1. Materials

3.1.1. Materials used for the synthesis of PIM-1

Tetrafluorophthalonitrile (TFTPN, 98%), N,N-dimethyl formamide (DMAc), toluene, methanol, chloroform, 1,4-dioxane and dichloromethane (DCM) were purchased from Sigma Aldrich (UK). 5,5',6,6'-tetrahydroxy-3,3,3',3'-tetramethyl-1,1'-spirobisindane (TTSBI, 98%) were acquired from Aesar (UK). Anhydrous potassium carbonate (K_2CO_3) was purchased from Fisher (UK) was kept in an oven overnight at 100 °C before use. TFTPN was purified through sublimation at approximately 150 °C and then collected without vacuum. TTSBI was dissolved in methanol and reprecipitated in DCM before use. Apart from TTSBI and TFTPN, all chemicals were without further purification.

3.1.2. Materials used for the synthesis of graphene-like materials

Chloroform, octadecylamine (ODA), octylamine (OA), ethanol (EtOH), hydrazine monohydrate (~80 vol% in H_2O), hydrogen peroxide (H_2O_2), potassium nitrate (KNO_3) and sulphuric acid (H_2SO_4) were purchased from Sigma Aldrich (UK). Graphite was purchased from NGS Naturegraphit GmbH (Germany). Potassium permanganate ($KMnO_4$) was acquired from Aesar (UK). Ammonia was procured from Acros Organics (United Kingdom). All the other chemicals were used as obtained without any purification.

3.2. Synthesis of PIM-1

The two monomers, TFTPN (0.05 mol, 10.00 g) and TTSBI (0.05 mol, 17.29 g), and anhydrous K_2CO_3 (0.15 mol, 20.73 g) DMAc (100 mL) and toluene (50 mL) were added to a round flask and were magnetically stirred under a nitrogen atmosphere (Figure 17). The reaction was set at 160 °C for 40 min under reflux. At the end of the reaction, a highly viscous solution was obtained, which was then poured into methanol and the crude product was collected through vacuum filtration. The polymer was dissolved in chloroform, re-precipitated in methanol and washed using fresh solvent. After recovering the precipitate through vacuum filtration, the precipitate was refluxed overnight in deionised (DI) water (1L) at 100 °C. Following this, the crude yellow product was filtrated and washed with water and then with acetone. From that, the crude product was dissolved in 1,4-dioxane being after washed with acetone and methanol. The solid product was left in a beaker with methanol for about 2h and washed methanol again. The final product was put into a beaker and left to dry overnight in a vacuum oven at 110 °C. Two batches of PIM-1 were synthetized using the abovementioned procedure and were identified as Batch 1 and Batch 2.
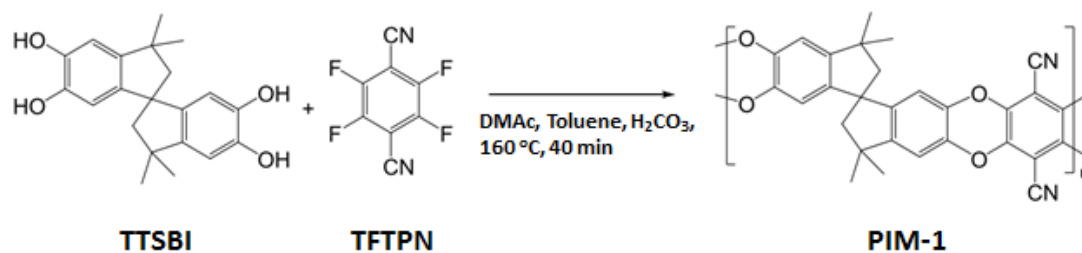
Figure 17: Synthesis of PIM-1.

3.3. Synthesis of graphene-like materials

3.3.1. Graphene oxide

GO was prepared through the modified Hummers' method described by Rourke et. al. [199]. In summary, KNO_3 (4.5 g) was dissolved in H_2SO_4 (169 mL). Natural flake graphite (5 g) was added under continuous stirring for 2 h. The mixture was cooled down and kept cold by means of an ice bath while 22.5 g $KMnO_4$ was added over 70

min. The mixture was left to stir for 3 days and was left thereafter for 4 more days without stirring. After that, 550 mL 5 wt% H_2SO_4 in water was added over approximately 1 h and left stirring for another 3 h. H_2O_2 (15 g, 30% vol.) was added drop by drop with considerable effervescence and stirred for 24 h. 550 mL of 3 wt% H_2SO_4/0.5 wt% H_2O_2 was added and the mixture was stirred for 3 days. The previous mixture was further centrifuged at 8000 rpm for 20 min and the supernatant was discarded. The pellet, a thick dark yellow liquid, was then dispersed with 500 mL of 3 wt% H_2SO_4/0.5 wt% H_2O_2 and shaken in order to fully disperse the pellets. This last step was repeated twelve times until a characteristic glittery colour was not visible. After that, the mixture was washed 5 times with DI water –500 mL of DI water was added in each washing cycle. GO was further dried under vacuum at room temperature.

3.3.2. Functionalized graphene oxide

Alkyl-functionalized graphene oxides were synthesised based on the procedure followed by Hou *et al.* [200]. Ammonia was added to an aqueous solution containing 120 mg GO (1 mg mL^{-1}) until it reached a pH of 10. A solution containing either 8-carbon chain alkylamine (OA) or 18-carbon chain alkylamine (ODA) was gradually added into the GO solution under stirring for approximately 24 h at 60 °C. The ratio of GO to alkylamine (OA or ODA) was fixed at 1.0 mg of GO to 0.01 mol of alkylamine so the alkylamine was dissolved in EtOH up to a concentration of 5 mg mL^{-1}. . After the reaction for 24 h, the suspensions were washed with EtOH first to remove unreacted alkylamine, filtered and then washed with EtOH and chloroform. The final products were labelled as GO-OA and GO-ODA for alkyl-functionalized GO using OA and ODA, respectively. GO-ODA was further dispersed in chloroform, whereas GO-OA was dispersed in EtOH due to its low degree of dispersion in chloroform. Due to this fact, GO-OA could not be used for membrane preparation.

3.3.3. Reduced functionalized graphene oxide

Reduction of alkyl-functionalized graphene oxide solutions was carried out by adding hydrazine monohydrate (0.12 mL, 80% vol.) to 1 mg mL^{-1} GO-OA and GO-ODA solutions, prepared as described in the previous section, and stirring for 2 h at

90 °C. These solutions were filtered and washed with EtOH and chloroform. The filtered solids were collected and dispersed in chloroform and labelled as rGO-OA and rGO-ODA for reduced alkyl-functionalized GO using OA and ODA, respectively. Figure 18 shows a schematic diagram of the synthesis of graphene-like materials.
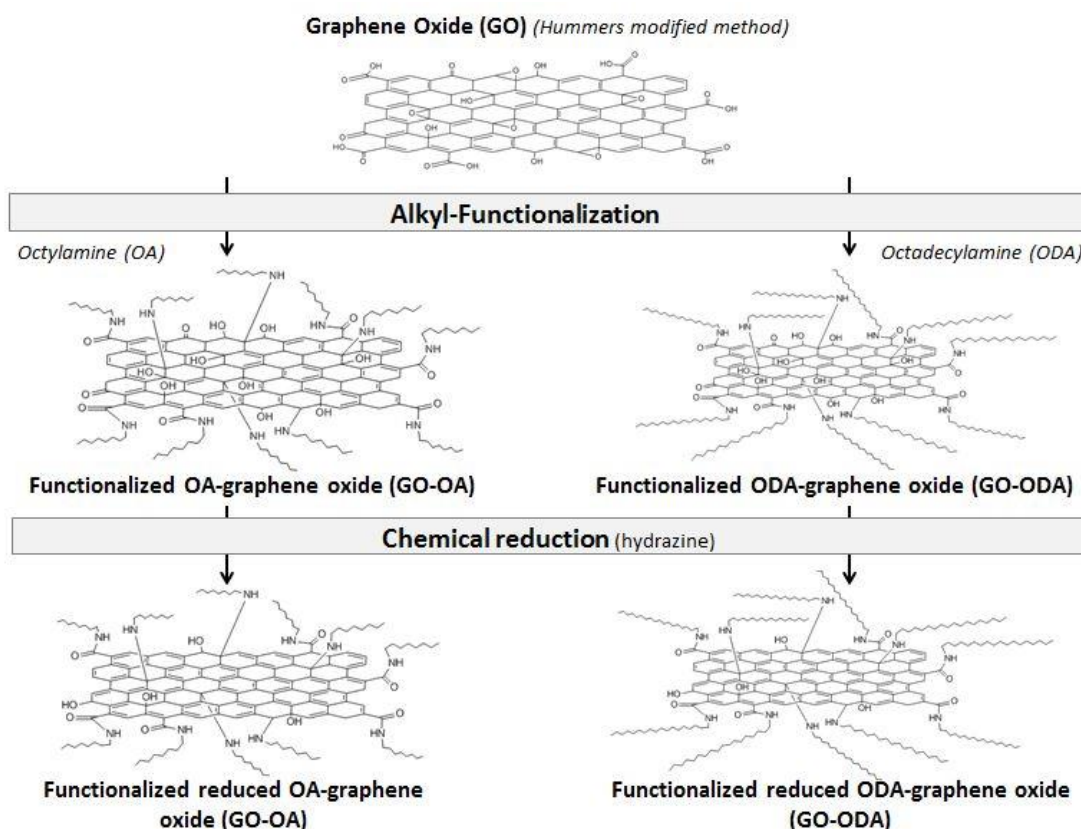
Figure 18: Schematic diagram of the synthesis of graphene-like materials.

3.4. Characterization

3.4.1. PIM-1

PIM-1 was characterized using a range of techniques including gel permeation chromatography (GPC), elemental analysis (EA), gas sorption analysis using the Brunauer–Emmett–Teller (BET) method, thermogravimetric analysis (TGA), elemental analysis (EA), attenuated total reflectance-Fourier transform infrared (ATR-FTIR) and nuclear magnetic resonance (NMR). PIM-1 samples from Batch 1 and Batch 2 were analysed.

Weight-average molar mass of the resulted polymers were determined through GPC, performed on a multi-detector Viscotek GCPmax VE 2001 gel chromatograph (Malvern, UK) equipped with two PLgel mixed-B columns and Viscotek TDA302 tripe detector array. Analysis was performed in chloroform at a flow rate of 1 mL min^{-1}. OmniSEC software (Malvern, UK) was used to analyze the data. The polymer was dissolved in chloroform at a concentration of 1 mg mL^{-1}.

EA was performed by using a Carlo Erba Instruments EA1108 elemental analyser.

Surface area and pore distribution of the two batches of PIM-1 were determined from nitrogen adsorption and desorption isotherms obtained by Brunauer–Emmett–Teller (BET) method. These measurements were performed at 77.3 K using a Micromeritics ASAP 2020 volumetric adsorption analyser.

TGA was conducted under nitrogen (N_2) atmosphere at a heating rate of 10 °C min^{-1} from room temperature to 800 °C (Q5000, TA Instruments, USA).

An iDS Nicolet iS5 FTIR spectrometer, equipped with an attenuated total reflectance (ATR) (Thermo Scientific, United Kingdom) was used to characterize qualitatively the chemical bonds present in PIM-1. PIM-1 samples were vacuum dried at 110 °C overnight prior to analysis.

The chemical structure of PIM-1 was confirmed by ^{1}H NMR using a Bruker Avance II 500 MHz instrument. PIM-1 was dissolved in deuterated chloroform ($CDCl_3$) for NMR analysis.

3.4.2. Graphene-like materials

The graphene-like materials that were used as fillers in MMMs were synthesised and characterized prior to incorporating them in the polymer matrices using ATR-FTIR, scanning electron microscopy (SEM), X-ray photoelectron spectroscopy (XPS), Raman spectroscopy, atomic force microscopy (AFM) and TGA.

ATR-FTIR was carried out with an iDS Nicolet iS5 spectrometer (Thermo Scientific, UK), using a Ge crystal as a background over a wavenumber range of 500–4000 cm^{-1}, and a step size of 0.5 cm^{-1}. Samples were dried at room temperature under

vacuum prior to analysis. Samples were placed onto the ATR crystal and the spectra were collected.

The initial flake sizes of GO-ODA, rGO-ODA and rGO-OA were determined using a SEM FEI Quanta 250 FEG-SEM (FEI, USA). For that, the different graphene materials were dispersed in chloroform and then sprayed-coated onto silicon oxide wafer.

XPS was carried out to obtain the elemental composition and to identify the chemical bonds present in GO and functionalized GO materials. XPS measurements were performed with an Axis Ultra spectrometer (Kratos Analytical Limited, Manchester, UK) using a monochromatic Al Kβ source (1486.7 eV). All the XPS spectra were analysed using CasaXPS software. GO, GO-ODA, rGO-ODA, GO-OA and rGO-OA dispersions were drop cast onto silicon substrates at a sufficient concentration to allow complete coverage of the surface and dried at room temperature under vacuum before the analysis.

Raman spectra were obtained using a Renishaw Raman imaging microscope (inVia) equipped with a Leica microscope and a CCD detector. Samples were excited at 532 nm (Cobolt sambaTM continuous wave diode-pumped solid-state laser, 20 mW), and laser power kept below 10 mW in order to avoid thermal degradation. 3–4 mappings/points were analysed for each sample. Samples were prepared by depositing the dispersions on glass slides, which were left to dry under vacuum at room temperature.

AFM was carried out using a Fastscan microscope (Bruker, USA). The measurements were conducted using tapping mode at room temperature under air atmosphere. Samples were prepared by spray coating of GO-ODA, rGO-ODA and rGO-OA dispersions (0.08 mg mL^{-1}) onto silicon substrates. GO samples were prepared by spin coating GO aqueous solution (0.1 mg mL^{-1}) onto silicon substrates at 1000 rpm. The spin coater was a SPIN150, SPS-Europe, The Netherlands.

Thermal stability and hygroscopic behaviour of the prepared materials were assessed by TGA. A TA Q5000 thermogravimetric analyser (TA instruments, USA)

was used and the measurements were conducted under air atmosphere at a heating rate of 10 °C min^{-1} from 30 to 650 °C.

3.5. Results and Discussion

3.5.1. PIM-1

Figure 19 shows a picture of the polymer PIM-1 from Batch 1.

Figure 19: Polymer of intrinsic microporosity (Batch 1).

3.5.1.1. Gel Permeation chromatography

Results from the GPC analysis of purified PIM-1 from both batches is shown in Table 8. The weight-average molar masses of PIM-1 obtained in the two batches are within the range of the values found in literature [3, 39, 49]. The values obtained for polydispersi**ty** are slightly higher than the ones reported, which can be due to the presence of oligomers [3].

Table 8: GPG analysis of PIM-1 from both batches synthetized (M_n: number average molecular mass and M_w: weight average molecular mass).

Sample of PIM-1	M_n (g mol^{-1})	M_w (g mol^{-1})	Polydispersity ($Đ$)
Batch 1	41636	137 400	3.3
Batch 2	39968	123 410	3.1

3.5.1.2. Elemental Analysis

Table 9 contains the elemental analysis for carbon, hydrogen, nitrogen and oxygen for the PIM-1 powders from Batch 1 and Batch 2. These results confirm that the polymer was successfully synthetized. A maximum deviation from the ideal calculated elemental C, H and N masses of 1.91 %, 0.69 % and 3.37 %, respectively, was observed. The content of oxygen in the sample was calculated theoretically, as

the EA analysis was conducted under an oxygen (O_2) atmosphere. The deviation obtained from the theoretical values might be due to the presence of trap molecules in its highly porous polymer structure [201] as well as incomplete combustion of the sample during analysis.

Table 9: Elemental analysis of the two PIM-1 batches synthetized used in our experiments.

Element	Theoretical, %	PIM-1 (Batch 1), %	PIM-1 (Batch 2), %
Carbon	75.64	74.00	74.38
Hydrogen	4.37	4.32	4.36
Nitrogen	6.08	5.88	5.87
Oxygen*	13.91	15.8	15.39

*Calculated theoretically.

3.5.1.3.   Gas Sorption Analysis

The surface areas of PIM-1 from batches 1 and 2 are 681.6 ± 6.8 and 705.6 ± 5.9 m^2 g^{-1}, respectively. The values obtained are similar to the values reported in the literature [49, 202]. The isotherm adsorption of PIM-1, a glassy polymer, results from the combination of two distinctive processes – Langmuir and Henry adsorption modes. Henry-type adsorption corresponds to the gas adsorbed in the equilibrium free volume of the material, where the gas solubility increases linearly with pressure. This phenomenon is seen in gas absorption in rubbery polymers and liquids. Langmuir-type adsorption refers to gas adsorbed in the excess of free volume present in glassy polymers caused by the non-equilibrium packing of the polymer segments. Since this free volume is limited, gas adsorption will cease when all adsorption sites are filled. Therefore, glassy polymers exhibit both adsorption processes and it can be described as dual-sorption model. [7, 203] Figure 20 shows the N_2 adsorption-desorption isotherms. The large N_2 uptake at low relative pressures is an indicator of the microporosity where the N_2 is absorbed by the smallest pores due to multiwall interactions. As the relative pressure increases, the larger pores are progressively filled, and typically above 2 nm the filling of the pores occurs due to the condensation of the N_2 from the walls to the centre. The hysteresis, lying above the respective absorption curves are observed in both PIM-1 samples. This is believed to be due to the swelling of the polymer matrix caused by the absorbed N_2, which prevents the complete desorption of N_2 [204].
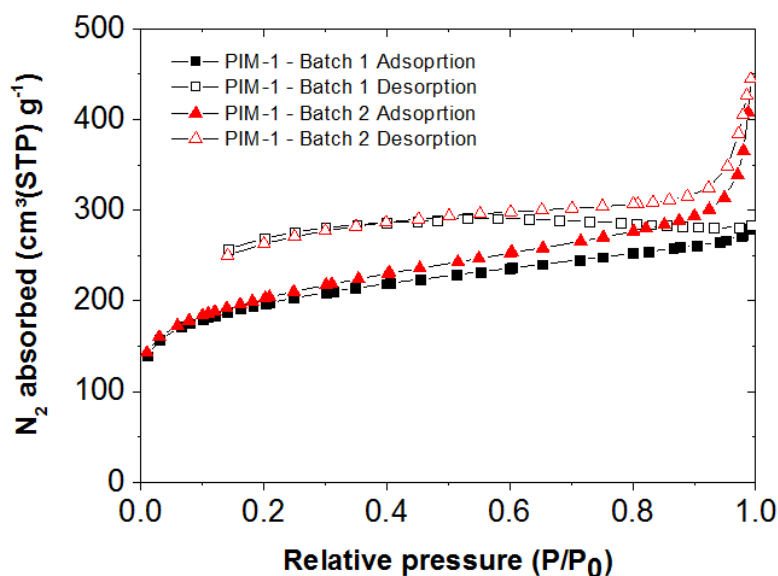
Figure 20: Nitrogen adsorption and desorption isotherms (77 K) of PIM-1 synthetized from two different batches (P_0 is the saturation pressure).

3.5.1.4. Thermogravimetric Analysis

TGA and derivative thermo-gravimetric (DTG) curves of the two batches of PIM-1 synthetized are shown in Figure 21. The initial weight loss experienced by both samples up to approximately 200 °C may be due to entrapped solvent or water present in the sample, from the polymer synthesis. As it can be seen, PIM-1 is thermally stable up to approximately 500 °C, experiencing the greatest weight loss at this temperature [5, 144, 205]. In both cases, a loss in mass of 50-55% of the original value at 800 °C indicates that carbonization occurs under a N_2 atmosphere.
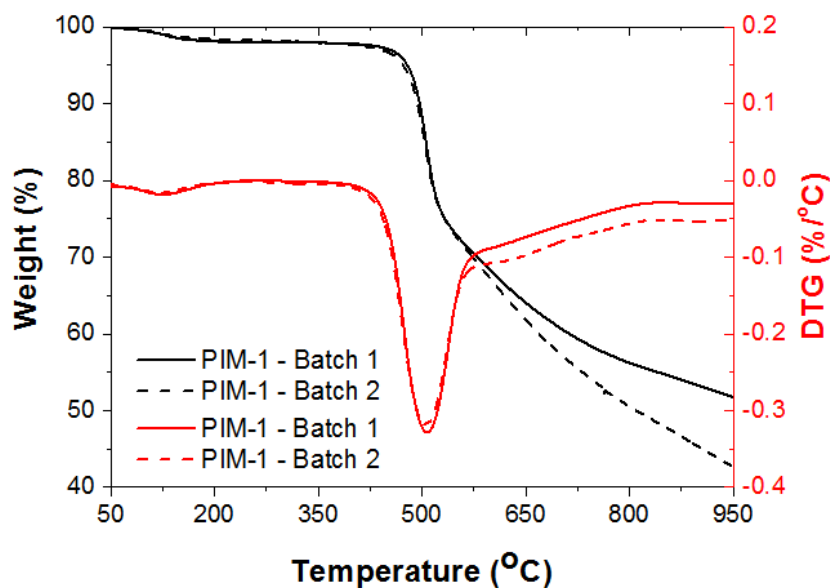
Figure 21: TGA and DTG curves of the two batches of PIM-1 synthetized.

3.5.1.5. Attenuated total reflection - Fourier transform infrared spectroscopy

FTIR-ATR was employed to study qualitatively the chemical structure of PIM-1 of the two different batches used in the experiments. Figure 22 shows the FTIR-ATR spectra of the two batches of PIM-1 used. PIM-1 presents characteristics peaks for nitrile (C≡N, ~2240/2238 cm^{-1}), aliphatic and aromatic C-H stretching (~2800-3010 cm^{-1}), C=C aromatic bending (~1607 cm^{-1}) and C-O stretching (~1000-1300 cm^{-1}) [206, 207].
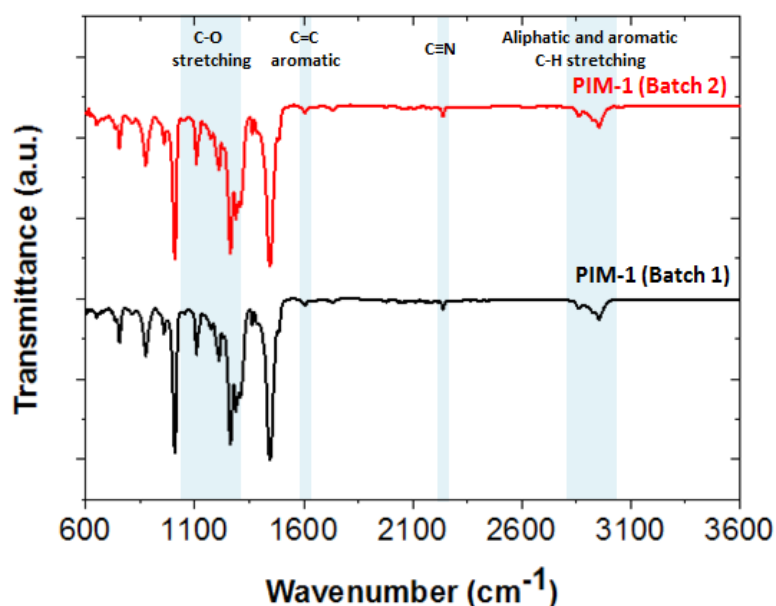
Figure 22: FTIR-ATR spectra of the two batches of PIM-1 used in the experiments.

3.5.1.6. ^{1}H Nuclear Magnetic Resonance

From the molecular structure of PIM-1, four different proton environments can be identified, which are labelled from 1 to 4 (Figure 23a). Figure 23b shows the ^{1}H NMR spectra of PIM-1 from both batches and the respective correspondence of the peaks to the type of proton environment. The proton environment labelled as 1 corresponds to the hydrogen on the methyl group. The peak possesses a chemical shift between approximately 1.2 and 1.3 ppm. The peak labelled 2 corresponds to the hydrogens on methylene group. The chemical shifts of these two peaks are from approximately 2.1 to 2.3 ppm. The aromatic hydrogens are represented as number 3 and 4, with a chemical shift of 6.3 and 6.7, respectively. Apart from those ones, two more peaks can be identified: water and CDCl$_3$ at approximately 1.5 and 7.3 ppm. Similar values can be found in the literature [49, 208].

Following the conventional way to present the information from ^{1}H NMR spectra, the data obtained from both batches of PIM-1 can be written as follows:

PIM-1 – Batch 1: ^{1}H NMR (500 MHz, CDCl3, δ, ppm): 6.74 (2H, s), 6.35 (2H, s), 2.26–2.08 (4H, dd), 1.29–1.23 (broad, 12H).

PIM-1 – Batch 2: ^{1}H NMR (500 MHz, CDCl3, δ, ppm): 6.74 (2H, s), 6.35 (2H, s), 2.25–2.08 (4H, dd), 1.29–1.24 (broad, 12H).

(a)   **(b)**
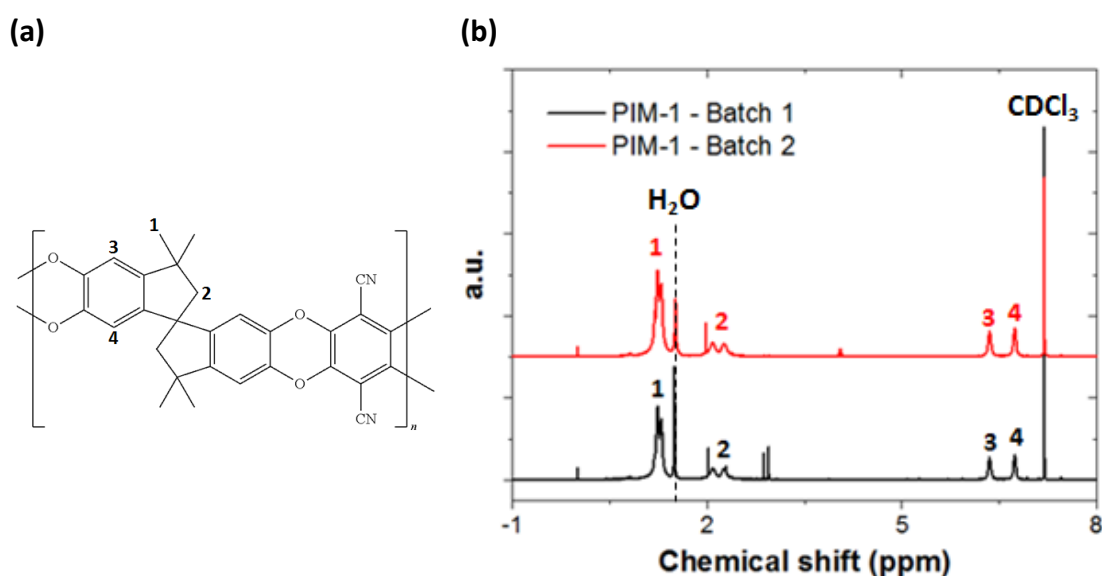
Figure 23: (a) Molecular structure and (b) ^{1}H NMR spectra of PIM-1 from two different batches.

3.5.2. Graphene-like materials

3.5.2.1.   Attenuated total reflection- Fourier transform infrared spectroscopy

The FTIR spectra of GO, GO-ODA, rGO-ODA, GO-OA and rGO-OA samples shown in Figure 24 confirm the success in the alkyl-functionalization of GO. The spectrum of GO exhibits representative peaks at ~1050 cm^{-1}, 1220 cm^{-1}, ~1600 cm^{-1}, 1715 cm^{-1} and ~3300 cm^{-1}, which correspond to alkoxy C-O stretching vibrations, epoxy C–O stretching vibrations, C=C stretching in the aromatic ring, C=O carboxyl stretching and O-H stretching, respectively [209]. After alkyl-functionalization some new peaks appear; two peaks at ~2920 cm^{-1} and ~2850 cm^{-1} which correspond to the C-H stretching in the −CH2 present in the ODA and OA chains, and two peaks at approximately 1470 cm^{-1} and 1580 cm^{-1} due to the formation of covalent bonds (C-

N-C) between the alkylamines and GO, N-H stretching vibration and C-N stretch, respectively [210]. It is worth mentioning that even after chemical reduction of functionalized GO with ODA and OA (rGO-ODA and rGO-OA in Figure 24) the peaks at ~2920 cm−1 and ~2850 cm−1 remain, which indicates the grafting of the ODA and OA chains onto GO sheets. However, it is noticeable that the intensity of these peaks for the reduced samples decreases as compared to non-reduced samples, which could indicate the loss of some alkylamine upon treatment with hydrazine. It is worth mentioning that, as expected, after the reduction step for both functionalized GO samples, the absorption peak at 1715 cm^{-1} which corresponds to C=O stretch disappears and the intensity of the OH stretching at ~3300 cm^{-1} decreases considerably.
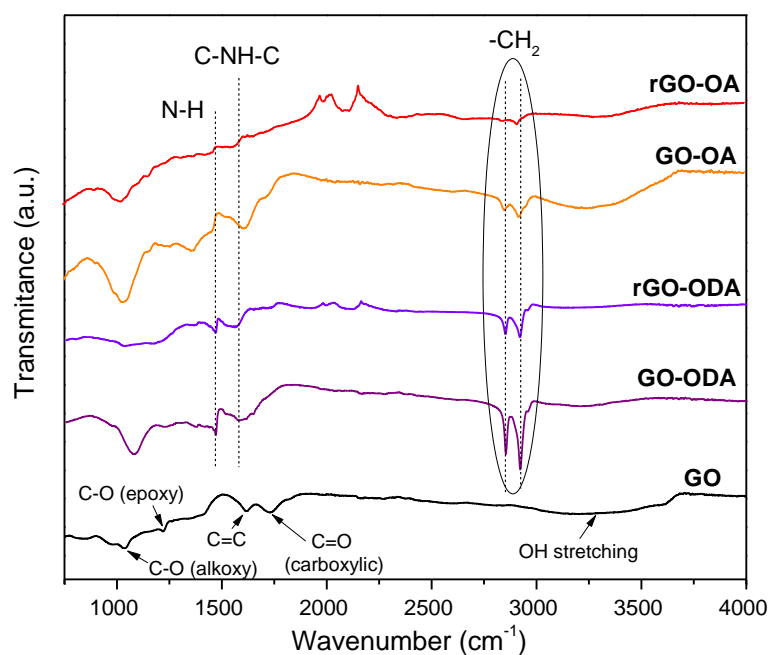
Figure 24: ATR-FTIR spectra of GO, GO-ODA, rGO-ODA, GO-OA, and rGO-OA.

3.5.2.2. Scanning Electron Microscope

The lateral flake size of GO-ODA, rGO-ODA and rGO-OA was measured from SEM images (Figure 25). According to the obtained micrographs, the average flake size of GO-ODA, rGO-ODA and rGO-OA were 4.9 ± 3.4 μm, 4.0 ± 2.3 μm and 4.6 ± 2.8 μm, respectively.
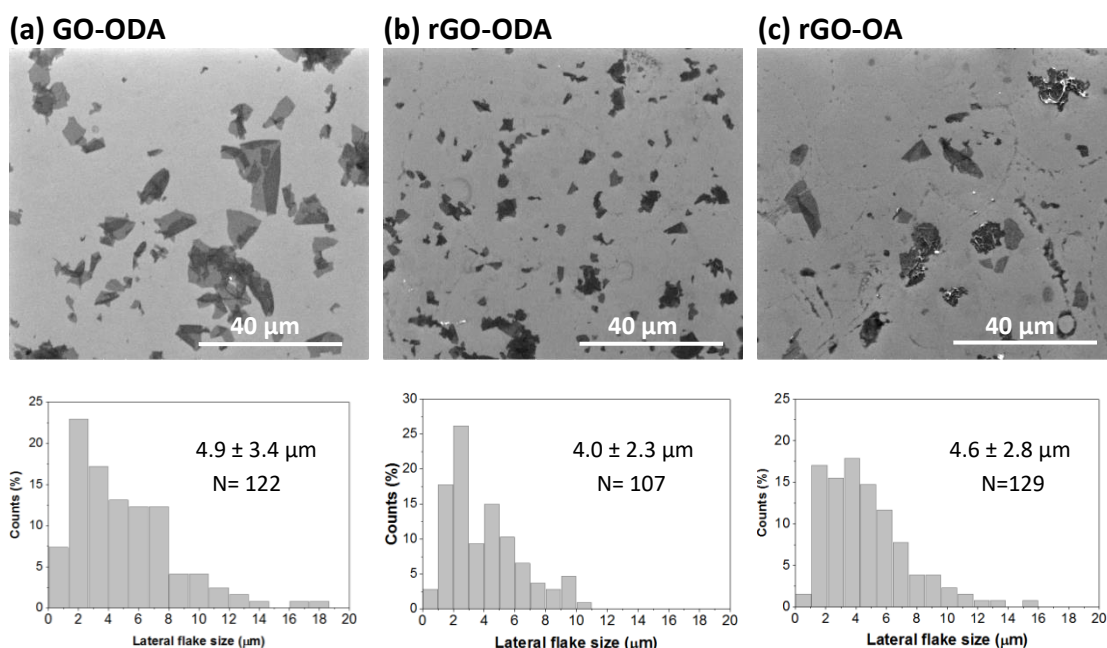
Figure 25: SEM images and Lateral flakes size of (a) GO-ODA, (b) rGO-ODA and (c) rGO-OA.

3.5.2.3. Atomic force microscope

AFM was carried out on the samples to confirm the presence of monolayer flakes in the starting material (i.e. GO) and to characterize the graphene-like fillers used for the preparation of membranes (i.e. GO-ODA, rGO-ODA and rGO-OA). Micrographs of GO sheets such as that depicted in Figure 26a and others that are not shown here reveal that the lateral dimensions of GO sheets are in the expected range with flakes of sizes ranging from few tens of nanometers to few micrometers. The thickness of the GO flake was inferred from the height profile of the AFM image as shown in the inset of Figure 26a; a value of approximately 1 nm was obtained, which indicates a good exfoliation of graphite oxide into single-layer GO sheets, in good agreement with values reported elsewhere [211]. Figure 26b, c and d show AFM images of GO-ODA, rGO-ODA, and rGO-OA flakes, respectively. Their corresponding height profiles, which are shown as insets in the corresponding micrographs, reveal similar thicknesses to GO in the range of 1–2 nm, suggesting monolayer and few-layered structures. Moreover, all the alkyl-functionalized flakes present vivid wrinkles and overlaps that could be due to the uncontrolled dewetting inherent to the sample preparation process (i.e. spray coating) in contrast to the GO sample which was prepared via spin coating of aqueous dispersions.
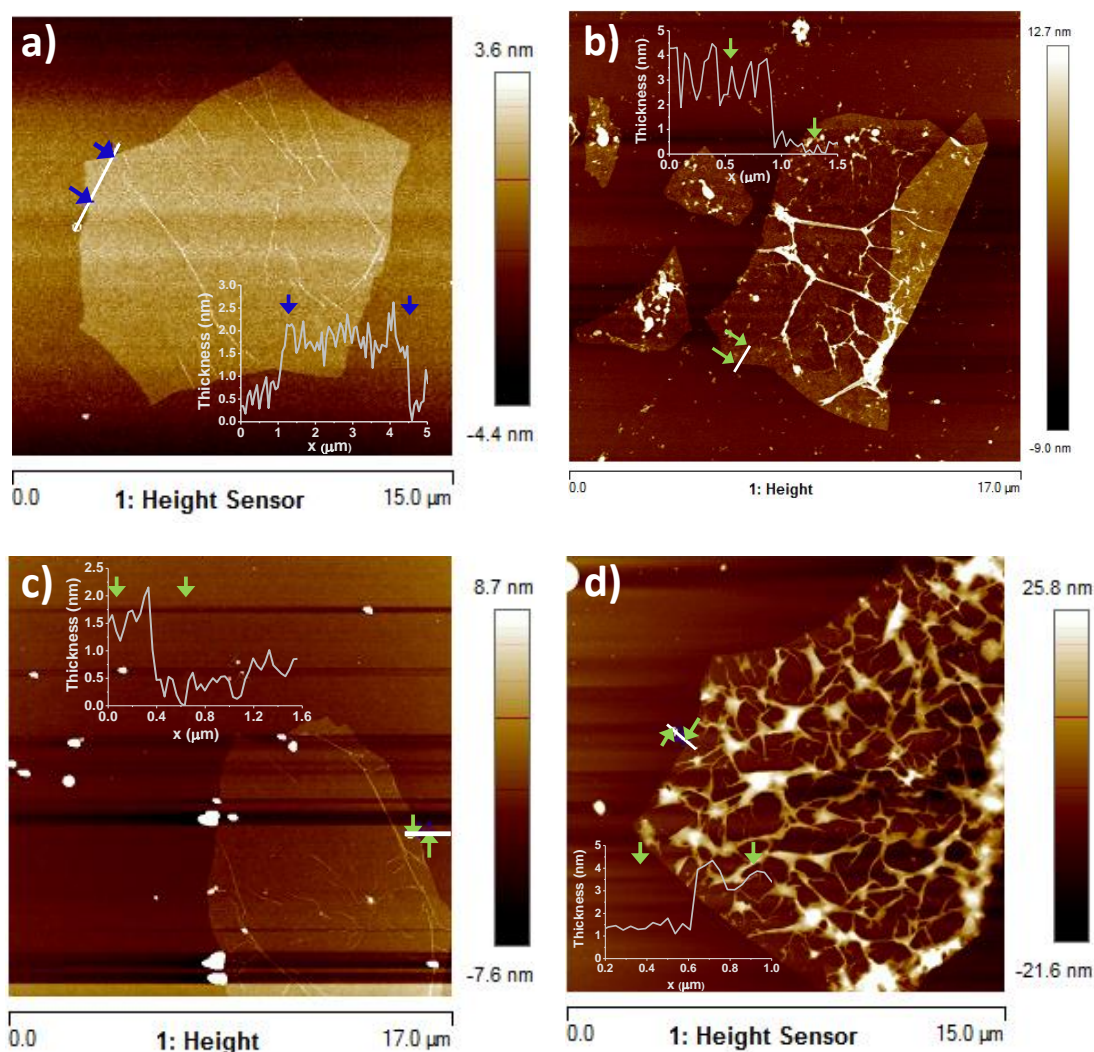
Figure 26: AFM images and height profiles of a) a GO flake, b) a GO-ODA flake, c) a rGO-ODA flake and d) a rGO-OA flake.

3.5.2.4. X-ray photoelectron spectroscopy

In general, GO has a range of carbon groups that can be characterized through XPS analysis. This technique is useful to confirm the oxidation degree of the samples, and in this case, also the grafting of alkylamines onto the flakes and the extent of the functionalization. Figure 27 shows the deconvoluted XPS C1s spectra of GO and functionalized GO samples before (GO-ODA and GO-OA) and after chemical reduction (rGO-ODA and rGO-OA). The C1s GO spectrum show a peak at 284.6 eV that is assigned to sp2 and sp3-hybridized carbons. Oxygen-containing functional groups C-O and C=O are observed at 286.8 eV and 288.4 eV, respectively. GO is predominantly oxidized with epoxide and hydroxyl groups as is evidenced by the

great peak corresponding to C-O bonds in Figure 27a. After functionalization using OA and ODA, the intensity of that peak significantly decreases (see Figure 27b and Figure 27c) which indicates that the functionalization occurs mainly on these oxygen functional groups. Furthermore, a peak corresponding to C-N (285.6 eV), was found in all the functionalized GO samples (Figure 27b, Figure 27c, Figure 27d and Figure 27e) but with a higher intensity as compared to GO (Figure 27a). This finding further confirms the successful alkyl-functionalization to epoxy and hydroxyl groups to produce the C-NH(CH2)x functional group. The reduction in the intensity of the peaks corresponding to C-N and C-O after reduction (Figure 27d and Figure 27e) would indicate the removal of hydroxyl and epoxy groups and possibly detachment of some alkylamines upon treatment with hydrazine. As expected, the intensity C=O decreased after functionalization and decreased even more after further reduction for both OA and ODA. A table at the top right hand side of Figure 27 shows the C:O ratio for all five samples. The increase in C:O ratio after functionalization from 1.74 to 13.8 and 3.8 for GO-ODA and GO-OA, respectively, which corresponds to an increase of 693% and 176%, indicates the effective addition of the alkylamines on the graphene oxide flakes. The higher C:O ratio corresponds to the sample functionalized with the alkylamine that has the longer chain (i.e. has more carbon atoms) as anticipated. Nonetheless, upon chemical reduction it is observed that, contrary to what is expected, the C:O ratio decreases; a small reduction of 6.52% and 20.83% for rGO-ODA and rGO-OA, respectively, is obtained, which could be attributed to a small portion of the grafted alkyl chains being removed. Moreover, the decrease of nitrogen content in the fillers observed by XPS after chemical reduction, 9% and 28% for rGO-ODA and rGO-OA, respectively, confirms the loss. This is in agreement with the results from FTIR spectrometry that show a slight decrease of the intensity of the peaks attributed to the binding of amines for the two samples after reduction.
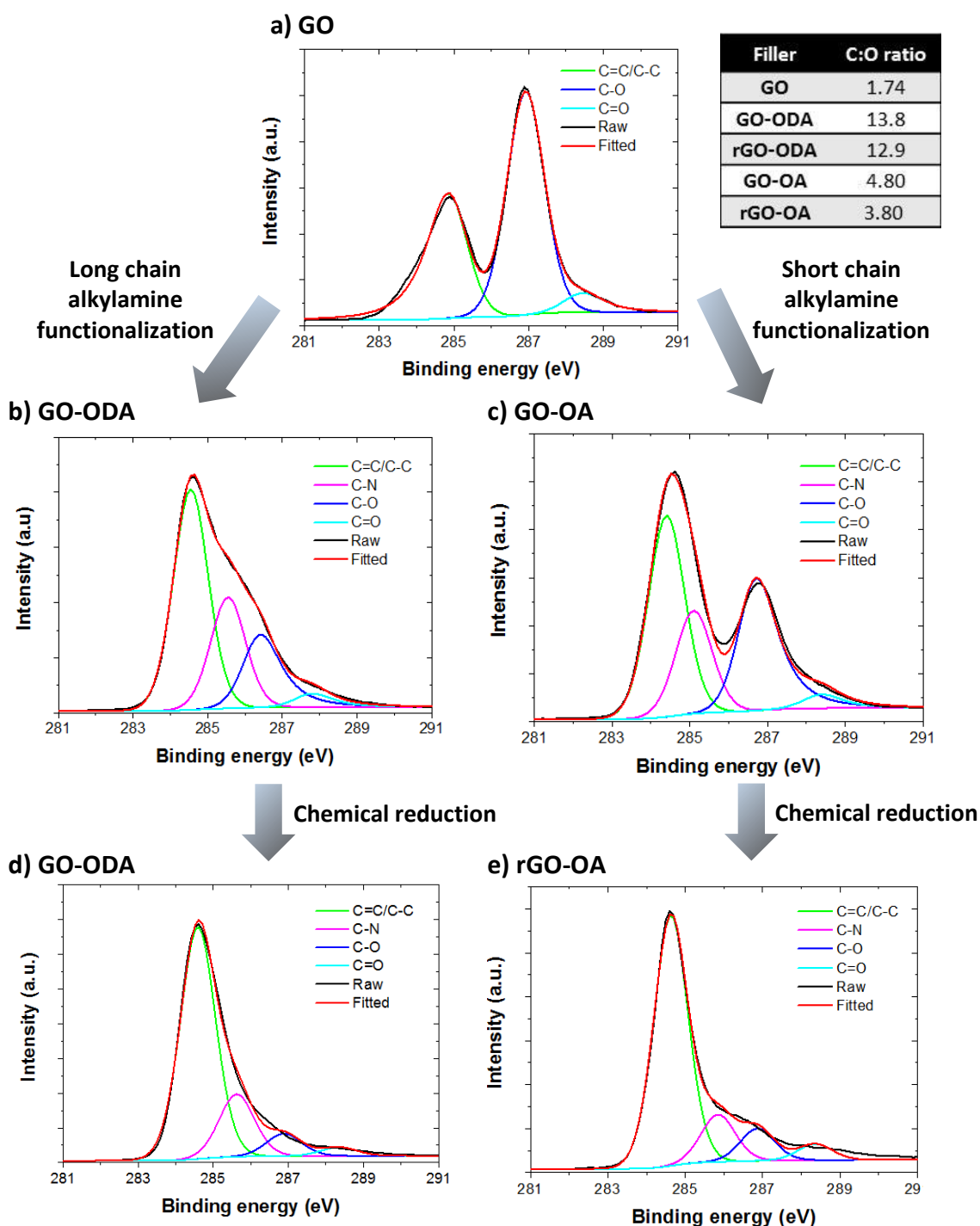
Figure 27: C 1*s* XPS spectra of a) GO, b) GO-ODA, c) GO-OA, d) rGO-ODA, and e) rGO-OA. Top right hand side of the figure shows the obtained C:O ratio from elemental analysis for all the materials. (For interpretation of the references to color in this figure, the reader is referred to the web version of this article.).

3.5.2.5. *Raman Spectroscopy*

Raman spectroscopy, which is normally used to characterize the symmetry and disorder in the sp^2 in carbon materials, was performed on GO and GO samples after

alkyl-functionalization and chemical reduction. Raman spectra of all the samples are represented in

Figure **28** and show two prominent peaks at ~1340 cm^{-1} and 1580 cm^{-1}, designed as band D and band G, respectively. The ratio between the intensities of the band D and G, I_D/I_G, is used to follow structural changes in graphene based materials [212]. According to Cancado *et al.* [213], the I_D/I_G can be used to evaluate the distance between two defects; this ratio increases for a distance between two defects up to 3 nm and decreases for a distance larger than 3 nm when analysed under a laser wavelength of 532 nm. The intensity ratio I_D/I_G obtained for GO in this work is 0.86 and increases to 0.88, 0.97, 0.92 and 1.07, for GO-OA, rGO-ODA, GO-ODA, rGO-OA, respectively. This increase in I_D/I_G upon functionalization and even a further increase upon reduction suggests an increase in the number of sp^2 domains in the graphene oxide structure [213]. Lucchese *et al.* suggested that the D peak results from the contribution of both structurally-disordered regions, and "activated areas" that correspond to the preserved graphene lattice around the defect. The later regions are the ones that contribute the most for the D band. According to this study, the intensity of the D peak reaches a maximum with increasing defect concentration and then it starts decreasing with further increase in defect density as the defects overlap and the D band becomes dominated by structurally-disordered areas [213].
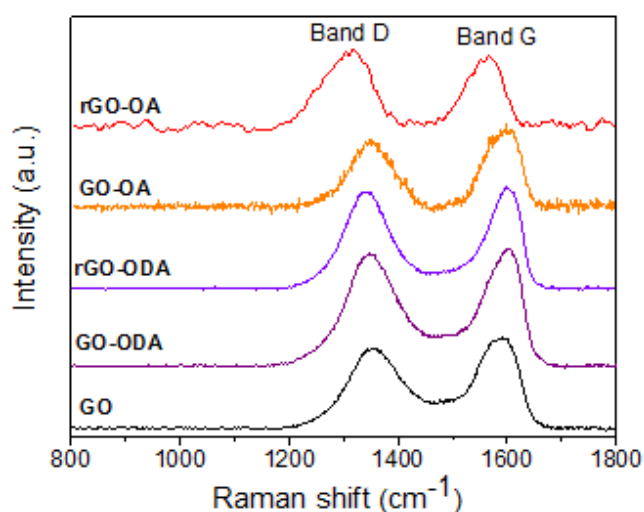
Figure 28: Raman spectra of GO, GO-ODA, rGO-ODA and rGO-OA with an excitation laser wavelength of 532 nm.

3.5.2.6.   Thermogravimetric Analysis

Thermal stability of the synthesized graphene-like materials was examined by means of TGA, the obtained weight loss curves are represented in Figure 29. Below 130 °C the weight loss is due to the evaporation of water adsorbed on the sample, with values for GO, GO-ODA, rGO-ODA and rGO-OA of 11.1%, 4.9%, 1.8% and 6.7%, respectively. These results indicate an enhancement in the hydrophobicity degree of starting material GO in this order: rGO-ODA > GO-ODA > rGO-OA. For GO there are three weight losses; up to 130 °C the first stage due the aforementioned water adsorbed on the sheets, between 130 °C and 500 °C the loss (48.5%) is due to the decomposition of labile oxygen-functional groups [214], and from 500 to 650 °C a loss of an extra 35.4% is due to the combustion of the carbon skeleton. For the ODA-functionalized GO sample, according to previous work by Lin *et al.* [214], there are two distinct losses of ODA: physically bonded molecules (150–180 °C) and covalently bonded molecules (200–500 °C). The weight loss of GO-ODA between 130 °C and 500 °C is 53.4%, which is about 5% higher than that of non-functionalized graphene oxide in the same temperature range. From the TGA curves it is obvious that most of the weight loss in GO takes place at up to 250 °C and is due to the decomposition of oxygen-functional groups created during the oxidation of graphite. However, in GO-ODA the loss takes place at a slower pace throughout the whole range (130–500 °C), supporting the presence of both physically adsorbed and chemically bonded ODA to the GO flakes, and remaining oxygen-containing functional groups that have not reacted with ODA. Both curves of functionalized GO samples after reduction confirm that hydrazine treatment has removed remaining un-reacted oxygen-containing functional groups and a portion of the ODA that was attached to GO, as evidenced by the smaller weight losses in the range 130–500 °C, of 48.2% and 34.1% for rGO ODA and rGO-OA, respectively. The higher weight loss for rGO-ODA as compared to rGO-OA is in agreement with ODA chains containing more atoms and therefore having larger mass.
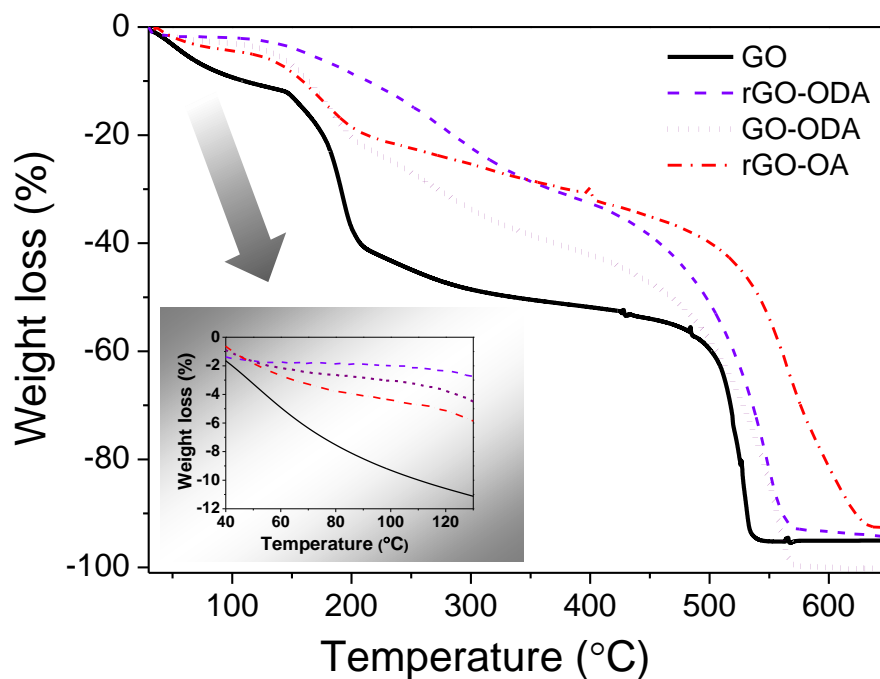
Figure 29: TGA curves for GO, rGO-ODA, GO-ODA and rGO-OA up to 650 °C under N_2 atmosphere.

3.6. Conclusions

This chapter contains detailed information about the synthesis and characterization of all materials required for the preparation of membranes which are presented in the subsequent chapters.

PIM-1 was successfully synthetized and characterized using a wide range of different techniques. Two different batches of PIM-1 were used and their weight-average molar mass obtained through GPC, ranged from 123 410 to 137 400 g mol^{-1}, with polydispersability index from 3.1 to 3.3. Moreover, both batches showed similar thermal stability, being stable to temperatures up to approximately 450 °C. The chemical structure of PIM-1 was comfirmed by ^{1}H NMR spectroscopy and ATR-FTIR spectroscopy. Finally, the surface area of PIM-1, obtained through the BET method, was roughly 700 m^2 g^{-1}, which is in satisfactory agreement with the previously reported data.

Graphene-like materials were successfully synthetized and fully characterized. The qualitative information on the chemical structure of all graphene-like materials was obtained through ATR-FTIR. Moreover, the elemental composition and chemical bonds in GO and alkyl-functionalized GO materials was assessed through XPS. These

measurements successfully proved the grafting of the alkyl chains to the GO nanosheets and their resulting chemical reduction when reacted with hydrazine. AFM indicated the presence of mono-layer and few-layer graphene-like nanosheets. Raman spectroscopy was also conducted to investigate the chemical structure of all graphene-like materials. Finally, these materials were also characterized in terms of thermal stability by means of TGA.

Chapter 4 - Enhanced organophilic separations with membranes of polymers of intrinsic microporosity and graphene-like fillers

Monica Alberto[a], Jose Miguel Luque-Alled[a], Lei Gao[b], Maria Iliut[c], Eric Prestat[c], Leon Newman[d,e], Sarah J .Haigh[c], Aravind Vijayaraghavan[c], Peter M. Budd[b], Patricia Gorgojo[a]

[a]School of Chemical Engineering and Analytical Science, The University of Manchester, United Kingdom

[b]School of Chemistry, The University of Manchester, United Kingdom

[c]School of Materials, The University of Manchester, United Kingdom

[d]Nanomedicine Lab, Faculty of Biology, Medicine & Health, The University of Manchester, United Kingdom

[e]National Graphene Institute, The University of Manchester, United Kingdom

4.1. Motivation

This work aimed to take advantage of the properties of both PIM-1 and graphene for organophilic pervaporation. The organophilic character of PIM-1 makes it a promising material for such application. With regard to graphene, its hydrophobic nature might favour the bioalcohol transport of water when incorporated into the polymer matrix, leading to an enhancement of the overall performance of the membrane. Additionally, the presence of graphene might help control the membrane swelling by restricting the mobility of the polymer chains.

Therefore, this chapter studies the effect on the overall performance of the addition of graphene-like materials into the polymer matrix of the membranes for alcohol recovery from aqueous solutions.

This work has been already published in Alberto, M., *et al*., J. Membr. Sci., 536 (2017), 437-449. The sample preparation for Scanning Transmission Electron Microscopy (STEM) was conducted by Leon Newman. Dr Eric Prestat performed the analysis and wrote the conditions at which the analysis was performed as well as the discussion of the results obtained.

4.2. Highlights

- Alkyl-functionalized GO that could be dispersed in chloroform was prepared.
- Free-standing MMMs were prepared with PIM-1 and these graphene-like materials.
- The MMMs were tested for ethanol and butanol recovery from water via pervaporation.
- 0.1 wt.% of filler showed the highest improvement in selectivity towards butanol

4.3. Abstract

Organophilic mixed matrix membranes (MMMs) have been fabricated with the polymer of intrinsic microporosity PIM-1 and graphene oxide (GO) derivatives for the recovery of *n*-butanol (*n*-BtOH) and ethanol (EtOH) from aqueous solutions via pervaporation (PV). Graphene oxide (GO) has been synthesized in solution through a modified Hummers' method, functionalized with alkylamines, and further reduced. The use of two alkylamines with chains of different lengths, octylamine (OA) and octadecylamine (ODA) −8 and 18 carbons, respectively - has been evaluated and the functionalized GO materials have been used as fillers in MMMs. The membranes have been prepared by casting-solvent evaporation of PIM-1/GO derivative solutions at room temperature, and a range of characterization techniques have been used to interpret their structure and relate it to their separation performance. Electron microscopy has been carried out to determine

the morphology of the membranes and the dispersion of the functionalized GO flakes in the polymer matrix. Moreover, the membranes have been characterized by Fourier transform infrared spectroscopy (FTIR), thermogravimetric analysis (TGA), and contact angle. Separation of alcohol from two binary mixtures composed of EtOH/water and *n*-BtOH/water, containing 5 wt% of alcohol, have been performed. Under these conditions, the incorporation of graphene-like fillers at relatively low concentrations shows an increase in average separation factor for *n*-BtOH ($\beta_{n\text{-BtOH/H2O}}$) from 13.5 for pure PIM-1 membranes to, in some cases, more than double for the MMMs; with the addition of 0.1 wt% of reduced amine-functionalized GO $\beta_{n\text{-BtOH/H2O}}$ reaches 32.9 and 26.9 for the short-chain (OA) and the long-chain (ODA) alkylamines, respectively.

4.4. Graphical abstract

Figure 30 shows the graphical abstract that summarizes the main findings in this work.
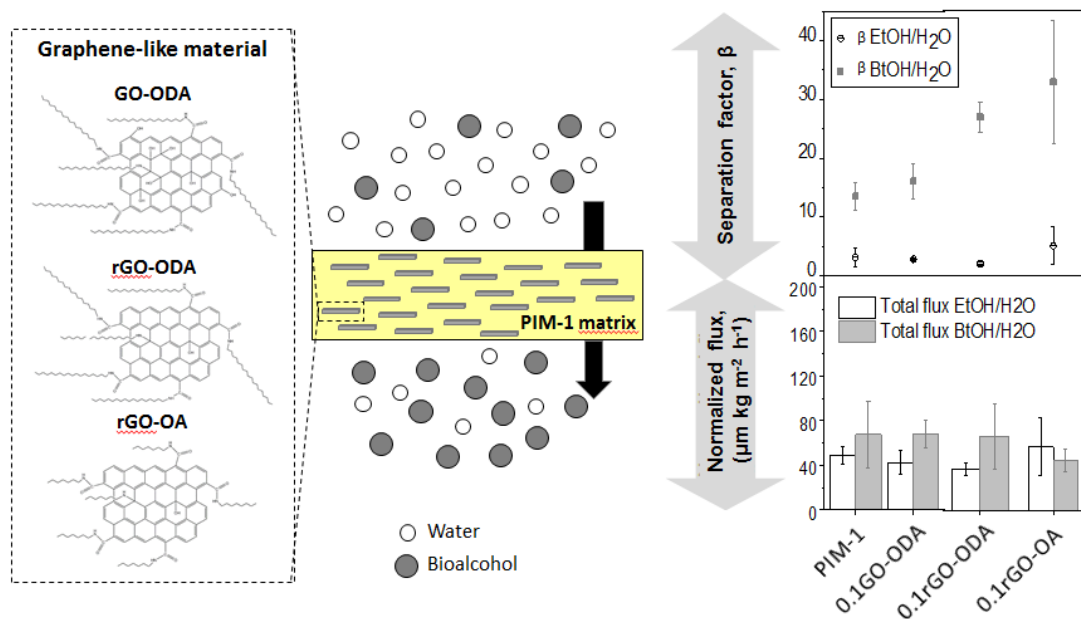
Figure 30: Graphical abstract.

4.5. Introduction

Over the last few decades, global concern on climate change has led to a growth of public environmental awareness of the need to reduce greenhouse gases (GHG). In this context the scientific community is exploring alternative sustainable energy

sources, such as biofuels, to replace conventional fossil fuels in sectors such as transportation. Bioethanol and biobutanol are particularly interesting although the latter, with higher energy density, lower volatility and lower flammability, is expected to attract greater attention [67, 69]. Biobutanol and bioethanol can be produced from biomass through the acetone-butanol-ethanol (ABE) fermentation process, typically at an average weight ratio of 3:6:1, respectively [70]. However, production costs are extremely high due to the amount of energy required to recover the alcohol from the broth. The fermentation process leads to a concentration of less than 2% of bioalcohol that is typically purified by a series of conventional distillation columns; 60–80% of the operating costs of the whole biofuel production come just from the purification steps [215]. End-product inhibition caused by the alcohol toxicity on bacteria during the fermentation alongside the required aforementioned high energy-intensive separation processes are still critical issues that hinder a more rapid implementation of this technology. In order to solve this drawback an alternative approach to distillation where membranes can selectively recover the alcohol from the broth in situ has been proposed in recent years. This on-line alcohol separation process can be done via pervaporation (PV) and is mainly based on the affinity of the membranes for alcohol over water by preferential sorption, diffusion and desorption. PV is a reasonable alternative to distillation in terms of economic viability; the alcohol is the component that preferentially permeates through the membrane and is present at low concentration in the feed side of the membrane. However, a major limitation with regards to the butanol recovery via PV is the lack of membranes with higher butanol selectivity, higher permeation fluxes, and better thermal stability [4]. Vane published a review on PV for the recovery of biofuels from fermentation processes where energy efficiency, capital cost, integration design with the fermentor, and further purification of the biofuel (dehydration) via PV is discussed in detail [215].

Research on butanol and ethanol recovery via PV has focused on the use of organophilic membranes, including polydimethylsiloxane (PDMS) [67, 68, 85, 86], poly[1-(trimethylsilyl)−1- propyne] (PTMSP) [89], polyether block amide (PEBA) [69,

86

97], polytetrafluoroethylene (PTFE) [216], and mixed matrix membranes (MMMS) prepared with some of these polymers and a range of fillers [20, 28, 69, 88, 217, 218]. A good number of materials have been proven to be promising fillers for the preparation of MMMs for alcohol recovery. For instance, the addition of metal organic frameworks (MOFs) within the polymer matrix aims to improve the overall performance of the membranes by reducing the swelling degree of the polymeric matrix as well as to favour the transport of a preferential compound through the membrane due to preferential sorption and diffusion [219]. However, improvements have been achieved for relatively high loadings of fillers, and compatibility between the inorganic filler and the organic phase, chain rigidification and pore obstruction are still critical issues limiting the preparation of defect-free membranes [28, 218]. Other fillers including zeolitic imidazolate frameworks (ZIFs) (ZIF-90 [220], ZIF-71 [218], ZIF-7 [28]), zeolites (ZSM-5 [69, 221], silicalite-1 [67, 80]), and carbon nanotubes (CNTs) [20, 222] have been used.

Furthermore, layered nanomaterials have been attracting attention over the past years in a number of membrane-based separations, due to their high aspect ratio, small thickness and high specific surface area [223, 224]. Some layered nanomaterials used in the fabrication of MMMs include layered aluminophosphate (AlPO) [225], crystalline layered silicate AMH-3 [226], titanosilicate JDF-L1 [223], layered zeolite Nu-6(2) [227], and copper 1,4-benzenedicarboxylate (Cu BDC) MOF [33], and have likely paved the way for graphene use in this area. Since the discovery of graphene in 2003 by Novoselo, *et al.* [164], graphene became one of the most attractive 2D materials for multiple applications, with its chemical derivative graphene oxide (GO) revolutionising membrane-based separation processes. Cohen-Tanugi and Grossman demonstrated theoretically that a single-layer graphene membrane could be used for desalination purposes [228]. Moreover, Nair *et al.* showed experimentally that a defect-free GO membrane is permeable to water vapour, whereas it blocks the permeation of all gases including helium [179]. In addition, graphene and GO have been incorporated into polymers forming MMMs for various applications including gas separation (GS) [131, 192-

194], PV (dehydration of isopropanol and ethanol) [229, 230] and desalination [231, 232].

A new class of polymers, so-called polymers of intrinsic microporosity (PIMs), have attracted widespread interest in fields such as gas separation [17, 41, 42, 145], hydrogen storage [43], organic solvent filtration [44, 45] and PV [4, 46, 233]. PIM-1 is an organophilic polymer with intrinsic microporosity that is selective towards organic compounds. It is formed by a sequence of rings along its backbone and a spiro-centre (i.e., a single tetrahedral C atom shared by two rings) which makes the chain twist and turn, resulting in a randomly contorted structure with limited rotational freedom; high free volume is created as a result of the poor molecular packing, which leads to higher permeability values as compared to conventional glassy polymers used for molecular separations [43]. Despite being a promising material, PIM-1 suffers from physical ageing which compromises its long-term stability [4]. Previous reports have shown that physical aging in glassy polymers is dependent on the membrane thickness, being much more rapid in thin films than in thicker films [234-236]. Moreover, PIM-1 polymer suffers from excessive swelling in the presence of alcohols which can limit its performance in PV and organic solvent nanofiltration (OSN) [45].

A wide range of fillers have also been used in combination with PIMs to improve their separation performance including silicalite 1 [22], silica nanoparticles [42, 237, 238], MOFs [41, 206, 239], CNTs [240] and few-layered graphene [195]. A theoretical study reported by Gonciaruk *et al.* [241] shows that the incorporation of graphene into PIM-1 affects the packing and can potentially prevent the swelling of the membrane, hence enhancing its performance. This improvement might be due to the parallel alignment of the PIM-1 chain fragments with the graphene sheets that lead to a decrease in their mobility and therefore to a decrease in swelling. The same study also predicts a good interfacial compatibility between the polymer and graphene sheets, which in turn might facilitate the dispersion of graphene in the polymeric solution. Consequently, driven by these results, in this experimental work a range of graphene oxide (GO) derivatives have been incorporated into PIM-1 membranes to study their performance for ethanol (EtOH) and *n*-BtOH separation

from aqueous solutions via pervaporation. In order to obtain a homogeneous and well dispersed phase in the polymer matrix, exfoliated GO flakes have been alkyl-functionalized and further reduced. The effect of loading and length of alkylamine chains on the membrane morphology, wettability and separation performance have been examined.

4.6. Experimental

4.6.1. Materials

Chloroform, ethanol (EtOH), *n*-butanol (*n*-BtOH) were purchased from Sigma Aldrich (UK).

4.6.2. Synthesis of PIM-1

The synthesis of PIM-1 is described in section 3.2. PIM-1 from Batch 1 was used in this study.

4.6.3. Synthesis of graphene-like materials

The synthesis of graphene-like materials used in this work is described in section 3.3 and includes alkyl-functionalized graphene oxide with octadecylamine (GO-ODA), alkyl-functionalized reduced graphene oxide with octadecylamine (rGO-ODA), and alkyl-functionalized reduced graphene oxide with Octylamine (rGO-OA).

4.6.4. Preparation of mixed matrix membranes

Polymeric solutions with 5 wt% of PIM-1 and different contents of GO-ODA, rGO-ODA and rGO-OA, were used to prepare free-standing membranes. In addition, pure PIM-1 membranes without fillers were also prepared as controls. The dope solutions were prepared by adding the polymer to a chloroform solution where the fillers had been dispersed and left stirring overnight. After that, the solutions were left to degas without stirring for 30 min and then poured in Steriplan® petri dishes that were immediately covered and put into a drying cabinet. Subsequently they were left to dry for approximately 3 days at room temperature in the cabinet with continuous flow of N_2. The dried films were then exposed to DI water in order to

remove them from the petri dish. Table 10 shows the estimated graphene content for the prepared membranes (solvent-free films) that is based on the compositions of the prepared casting solutions. The filler loading in the composite membrane is defined by Equation (7).

$$Filler\ loading = \frac{m_{\text{filler}}}{m_{\text{filler}} + m_{\text{PIM}-1}} \times 100\% \qquad (7)$$

Where m_{filler} is the weight of graphene-based fillers and $m_{\text{PIM-1}}$ is the weight of the polymer in the membrane. The filler loadings in the present study were predetermined at 0.01, 0.1, 0.5, and 1 wt% which express 0.01/99.99 (w/w) filler/PIM-1, 0.1/99.9 (w/w) filler/PIM-1, 0.5/99.5 (w/w) filler/PIM-1, and 1/99 (w/w) filler/PIM-1, respectively. A digital micrometer screw gauge with an accuracy of ±0.5 μm (Mitutoyo IP65 Coolant Proof, United Kingdom) was used to measure the thicknesses of the membranes; at least 10 measurements were performed on each membrane to obtain an average thickness, which was in some cases also verified by scanning electron microscopy. Membranes were used without any further treatment.

Table 10: PIM-1-based membranes. At least three membranes of each type were prepared to assess reproducibility. The concentration values obtained from UV correspond to one of the three repeats that were fabricated.

Membrane code	Filler	wt% of filler Values from the preparation of casting solutions	wt% of filler Values from UV of re-dissolved membranes	Membrane Thickness (μm)*
PIM-1	-	-	-	60 ± 9.1
0.01GO-ODA	GO-ODA	0.01	0.040 ± 0.008	54 ± 6.5
0.1GO-ODA		0.1	0.197 ± 0.024	65 ± 4.2
0.5GO-ODA		0.5	0.601 ± 0.045	57 ± 2.2
1GO-ODA		1	1.340 ± 0.316	51 ± 8.8
0.01rGO-ODA	rGO-ODA	0.01	0.018 ± 0.003	59 ± 6.2
0.1 rGO-ODA		0.1	0.065 ± 0.012	56 ± 2.4
0.5rGO-ODA		0.5	0.316 ± 0.078	68 ± 7.6
1rGO-ODA		1	0.704 ± 0.207	52 ± 6.9
0.01rGO-OA	rGO-OA	0.01	0.031 ± 0.006	48 ± 3.9
0.1rGO-OA		0.1	0.125 ± 0.094	51 ± 2.1
0.5rGO-OA		0.5	0.487 ± 0.085	54 ± 6.3
1rGO-OA		1	0.972 ± 0.097	59 ± 6.1

(*) Average of thickness of at least 3 membranes of each type of membrane. 10 measurements were performed for each membrane with a screw gauge in different areas of the membrane.

4.6.5. Characterisation

4.6.5.1. Membranes

The concentration of graphene-based fillers present in the membranes was determined through ultraviolet-visible (UV–Vis) spectroscopy. Pieces of the membranes were dried under vacuum at room temperature in order to remove all the moisture that could be present after their use in pervaporation. Subsequently, the dried samples were redissolved in chloroform; typically pieces of membranes with a weight from 0.004 to 0.013 g were dissolved in 2 mL of chloroform, and the absorbance under UV–Vis at 660 nm was recorded. Four samples of each set of membranes were measured. The measurements were carried out using a Genesys 10 S UV–Vis spectrophotometer (Thermo Scientific, United Kingdom). The Beer–Lambert law was used to estimate the concentration of the filler in the membrane. Extinction coefficients were determined by preparing solutions with known concentrations.

Scanning electron microscopy (SEM) images of cross-sections were taken on a FEI Quanta 200 SEM (FEI, USA), under an accelerating voltage of 15 kV. Cross section samples were prepared by immersion of pieces of membranes in EtOH for about 30 s, and subsequent immersion in liquid nitrogen where they were fractured. Samples were coated with a 6–8 nm Platinum layer using an MTM 10 Thickness Monitor (Cressington, USA).

Scanning Transmission Electron Microscopy (STEM) data were collected using a FEI Titan 80–200 equipped with a Chemistem EDX detector, probe-side aberration corrector and an X-FEG electron source operating at 200 kV. In STEM mode, the microscope was set at a beam current of 150 pA, a convergence angle of 21 mrad and collection angles of 22–84 mrad. For TEM specimen preparation, the membranes were embedded in TAAB 812 epoxy resin (TAAB Laboratories, UK) that was allowed to polymerize at 60 °C for 48 h. Ultrathin sections (70 nm) were then obtained using an ultracut E ultramicrotome (Reichert-Jung, USA). The face of the membrane was positioned perpendicular to the edge of the diamond knife (DiATOME, Switzerland) allowing cross sections of the specimen to be acquired,

which were collected onto copper S 7/2 Quantifoil Grids (Electron microscopy Sciences, USA).

Membrane wettability was determined by measurements of contact angle with DI water, EtOH and n-BtOH on the top surface of the membranes. The experiments were conducted at room temperature with an optical tensiometer Attension Theta (Biolin Scientific, UK) using the sessile drop method. A drop of DI water was dropped onto the membrane surface by means of a microsyringe with a stainless steel needle. The software was set to record 30 fps for 20 s, and the water contact angle was recorded 10 s after the water droplet had touched the sample surface. An average value of at least three measurements from different locations on each membrane was calculated. The same procedure was followed for EtOH and n-BtOH contact angles with a maximum of two measurements from the same sample.

A solvent uptake (SU) test was conducted on the membranes using pure solvents (water, n-BtOH and EtOH) at room temperature. Firstly, the membranes were cut into pieces and their weights were recorded. Each piece was completely immersed into a solvent for 3 days, after which the membrane was removed, wiped out to remove the excess of solvent from their surface, and rapidly weighed. The solvent uptake, SU, was calculated with Equation (8) as follows:

$$SU = \frac{m_f - m_i}{m_i} \times 100\%$$ (8)

where m_f and m_i are the final and initial mass of the polymer, respectively. Two samples of each membrane were analysed to assess reproducibility.

The PV apparatus used to determine the separation performance of EtOH and n-BtOH over water is represented in Figure 31. The experiments were carried out with approximately 100 g of a feed mixture of alcohol/water (5 wt% alcohol). The same membrane was tested for both mixtures with the separation of EtOH/water carried out always first. The feed was constantly stirred and kept at a constant temperature of 65 °C by means of a recirculating water bath. Permeates were collected in cold traps chilled by liquid nitrogen which were allowed to warm up to ambient

temperature for analysis. Vacuum was set at a pressure of 10 mbar and the effective area of the membranes was 2.54 cm^2.
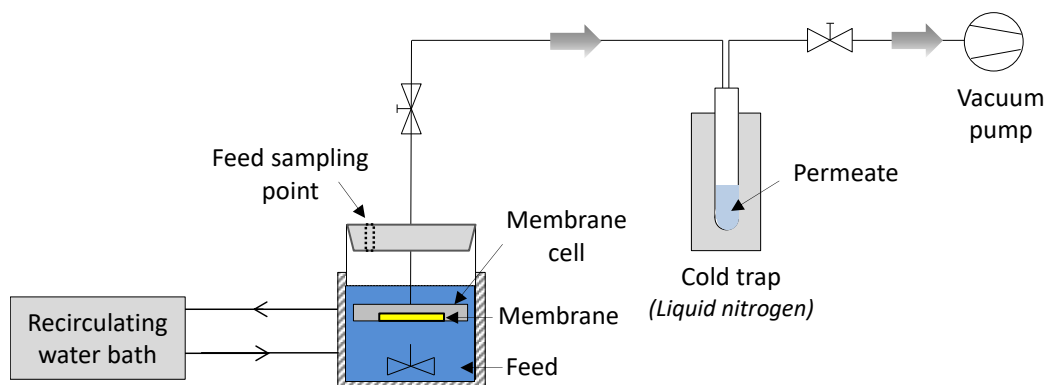
Figure 31: Schematic diagram of the pervaporation apparatus used to test the separation performance of prepared MMMs.

The performance of a membrane in pervaporation is usually expressed in terms of the total permeation flux, *J* (Equation (9) and the separation factor for a component, *α*, which for a binary mixture is defined by Equation (10).

$$J = \frac{m}{A\,t} \tag{9}$$

$$\beta = \frac{Y/(1-Y)}{X/(1-X)} \tag{10}$$

Where *m* is the weight of the permeate (kg), *A* is the effective membrane area (m^2) in contact with the feed solution, *t* is the permeate collection time (*h*). *Y* and *X* are the mole fractions of the component in the permeate and feed side, respectively.

Alcohol concentrations were determined by gas chromatography (GC). EtOH-water samples were diluted with water prior to analysis, whereas *n*-BtOH-water ones were diluted with acetone to form a single liquid phase. The feed concentration was also analysed by GC. Analyses were performed using an Agilent 7820 A gas chromatography-flame ionization detector (GC-FID) equipped with a PoraPLOT Q-HT column (10 mx0.32 mmx20 μm). Helium was used as carrier gas with a constant flow rate of 1.2 mL min^{-1}. The ion source was set at 190 °C. The oven temperature was programmed as follows: initial temperature of 175 °C kept isothermal for 2 min, ramped at 15 °C min^{-1} up to 200 °C, and isothermal again at this temperature

for 2.5 min. The injection volume was 2 µL applying a split ratio of 60:1. The scanning time was 6.1 min.

4.7. Results and discussion

4.7.1. Ultraviolet–visible Spectroscopy

As described in section 4.6.5.1., UV–Vis absorption spectrometry was carried out in order to determine the amount of filler in the membranes and to compare these values against the initial values from the preparation of casting solutions (Table 10). Linear relationships between the concentration of rGO-ODA, GO-ODA and rGO-OA dispersions in chloroform and the absorbance values at 660 nm were obtained. The extinction coefficients of GO-ODA, rGO-ODA, and rGO-OA were calculated to be 4.939, 15.256, and 7.556 mL mg^{-1} cm^{-1} (Appendix A, Figure A1), respectively, and obtained concentrations of fillers of re-dissolved membranes are shown in Table 10. These values are close to those from the preparation of casting solutions, with small differences that could be due to the level of accuracy in measuring the weight of the membrane pieces, which in some cases was as low as 4 mg (scale precision of 0.5 mg).

4.7.2. Scanning electron microscopy

Cross-sectional morphologies of pristine PIM-1 membranes and MMMs were determined by SEM. Figure 32a shows a micrograph of a PIM-1 membrane of ~ 60 µm in thickness that was prepared without any filler. It is clear that a dense and defect free film was formed. The rest of the SEM images, all cross sections of MMMs (Figure 32b, c, d, e and f), also reveal dense films of about the same thickness. Moreover, SEM images also suggest that the incorporation of graphene-like fillers has influenced the packing of PIM-1 at the microscale as evidenced by their change in morphology; however, SEM analysis cannot provide detailed information regarding the packing of polymer chains at the molecular level. Large agglomerates are not observed which suggests a homogeneous distribution of the fillers throughout the polymer matrices.
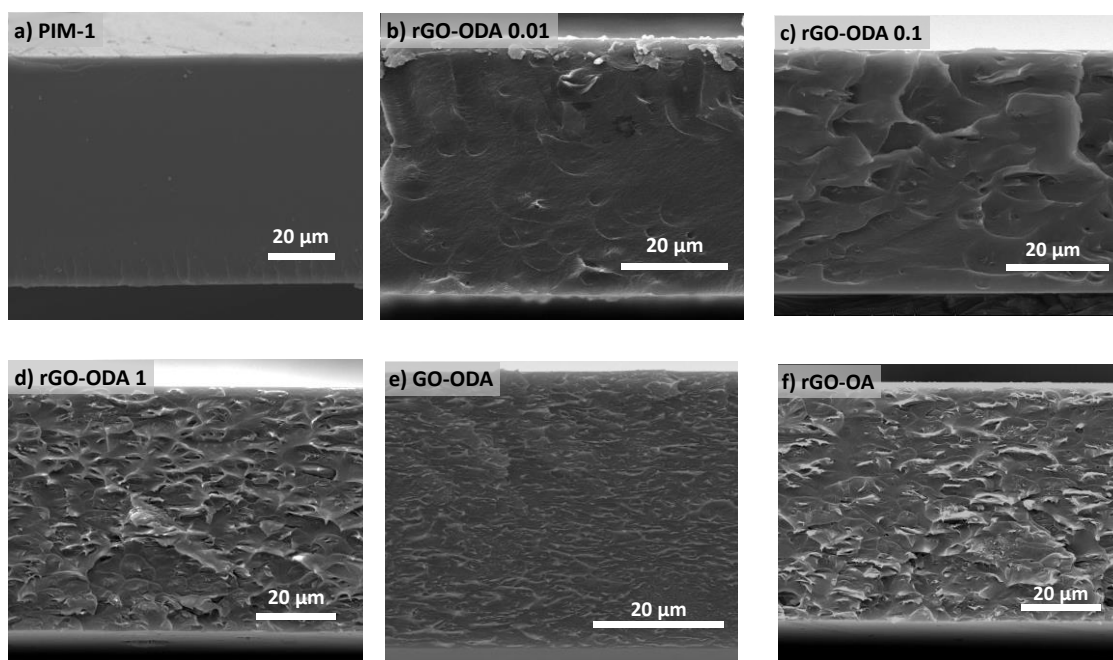
Figure 32: SEM images of the cross section of (a) pure PIM-1 membrane, (b) 0.01rGO-ODA, (c) 0.1rGO-ODA, (d) 1rGO-ODA, (e) 1GO-ODA and (f) 1rGO-OA.

4.7.3. Transmission Electron Microscopy

Due to the limitations of scanning electron microscopy that do not allow the visualization of individual flakes, STEM and selected area electron diffraction (SAED) were used to investigate the presence of thin graphene flakes in the PIM-1 based membranes. Figure 33a shows a low angle annular dark field (LAADF-) STEM of graphene flakes in the polymeric matrix of a 0.1rGO-ODA membrane (sample obtained via ultramicrotomy), where the presence of graphene flakes is demonstrated by the SAED shown in Figure 33b. The radial profile of areas containing PIM-graphene (dash red line) and PIM only (solid blue line), corresponding to the areas labelled 1 and 2 in Figure 33a, are plotted in Figure 33b. The measured diffraction signal from graphene is very weak and diffuse, because of its very low signal-to-background. Indeed the diffraction comes mainly from the polymer membranes, which overlaps with the weak graphene contribution. In Figure 33b, the small intensity increase at 4.7 nm^{-1} and 8.2 nm^{-1} is attributed to the [1010] and [1120] lattice reflection of graphene, therefore demonstrating that the features observed in Figure 33a are graphene flakes.
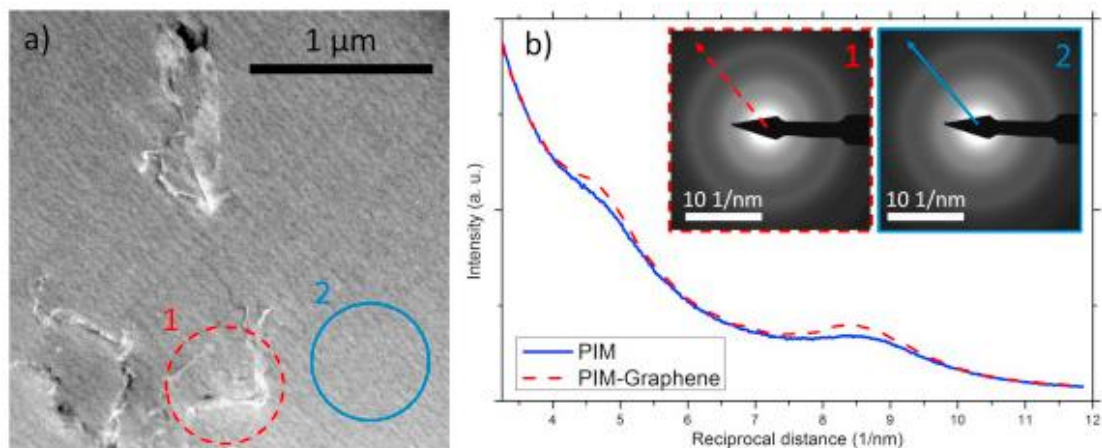
Figure 33: (a) LAADF-STEM images showing the presence of rGO-ODA in PIM-1 mixed matrix membranes (sample obtained via ultramicrotomy of a 0.1rGO-ODA membrane). (b) Intensity profiles of electron diffraction of areas containing PIM-graphene (dash red line) and PIM only (solid blue line). The sampled areas are displayed by the two circles in (a) labelled 1 and 2, respectively, and the profiles have been measured in the SAED patterns shown in the inset.

4.7.4. Contact angle

Separation performance in pervaporation highly depends on the nature of the membrane. In this particular application, where an alcohol is removed from an aqueous solution, hydrophobic membranes are desired. One way of assessing the hydrophobic nature of a material is by measuring its water contact angle, hence, contact angle measurements on all the membranes were performed, and obtained values are plotted in the graph in Figure 34. PIM-1 membranes have a water contact angle of 88 ° ± 3°, which is in accordance with the values reported in the literature [207]. From the water contact angle of MMMs it is inferred that the addition of graphene-like fillers into the polymeric matrix do not change significantly the surface properties of the membrane. All the values ranged from 80 to 90°, which could indicate that the fillers are completely covered by PIM-1 with no significant change in surface roughness. Similar conclusions can be drawn from EtOH and *n*-BtOH contact angle measurements carried out on the membranes; values obtained for MMMs were quite close to those of bare polymer membranes. The EtOH contact angles varied between 10° and 15° (13° ± 2° for PIM-1), whereas *n*-BtOH contact angles varied between 8° and 10° (9° ± 1° for PIM-1). As expected for organophilic PIM-1 polymer, low values for alcohol contact angle indicates

larger affinity of the membranes towards alcohols, and therefore preferential permeation over water.
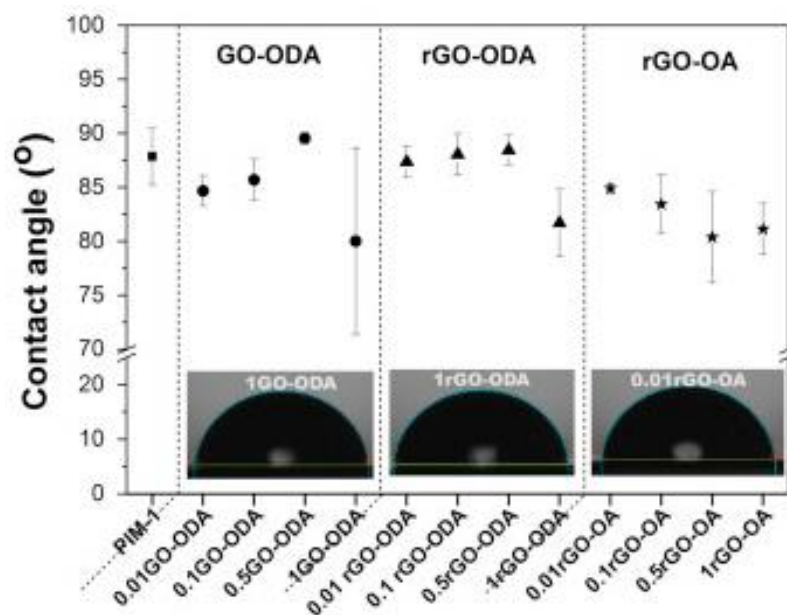
Figure 34: Water contact angle values for PIM-1 membranes. At least 3 measurements on different locations for each membrane were performed. Insets show some images of the measurements performed.

4.7.5. Solvent uptake

SU in EtOH, *n*-BtOH and water of PIM-1 membranes and MMMs prepared with relatively low concentrations of graphene-like fillers (0.1 wt% in the dried membranes calculated from the preparation of casting solutions) was investigated. The results are summarized in Figure 35 and according to them the addition of non-reduced and reduced GO-ODA, and rGO-OA increased the SU for both *n*-BtOH and EtOH, which indicates an increase in the affinity of the membrane towards these solvents. The membrane containing rGO-ODA shows the lowest SU in water (1.6 ± 1.2) when compared with the other fillers (4.6 ± 0.1 for rGO-OA and 8.5 ± 3.7 for GO-ODA), which shows it has the lowest affinity to water, as previously observed from the TGA results in Section 3.4.6. (weight loss due to moisture of 1.8%). The next membrane with less affinity towards water is the one with reduced OA-functionalized GO as filler, which is also consistent with the TGA results and demonstrates the hydrophobic nature of reduced GO samples. Furthermore, the average SU in water of the MMM that contains GO-ODA is higher (8.5 ± 3.7) than the average SU of the pristine PIM-1 membrane in the same fluid (6±4.1), which

suggests that a relatively hydrophilic filler inside a hydrophobic polymer matrix can increase the uptake of water even when it is added at very low concentrations. Moreover, the changes in the SU might be a good indication of changes in the chain polymer packing caused by the addition of the fillers. In summary, it can be concluded that i) all the membranes show preferential sorption as follows: *n*-BtOH > EtOH > water, ii) graphene-based fillers improve in all cases the sorption towards alcohols and, iii) chemically reduced samples hinder the sorption of water.
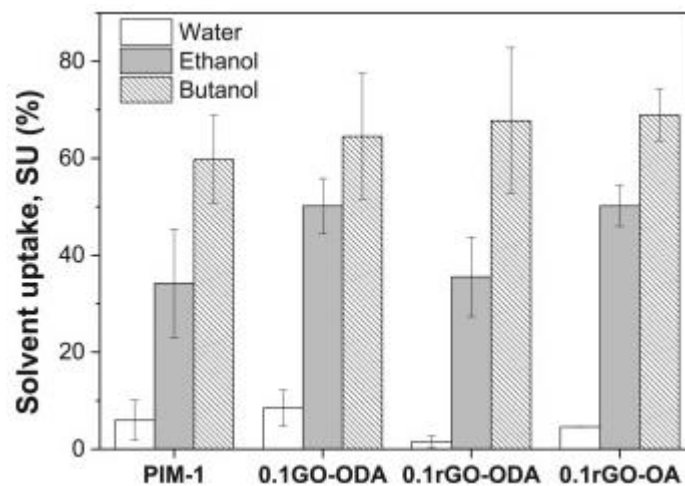
Figure 35: Solvent uptake of PIM-1, 0.1GO-ODA, 0.1rGO-ODA, and 0.1rGO-OA membranes in water, EtOH and *n*-BtOH after 3 days. Two samples from the same membrane were tested for each solvent. The error bar for SU in water of 0.1rGO-OA has a value of±0.07 which is not visible.

4.7.6. Membrane performance

To evaluate the separation performance of prepared membranes, pervaporation of binary aqueous solutions containing either EtOH or *n*-BtOH was carried out. Their performance relies on their preferential permeation of the alcohol over water and therefore, the higher the separation factor ($\beta_{alcohol/water}$) the higher the concentration of alcohol recovered in the permeate for a given feed composition. Figure 36 depicts the obtained separation factors ($\beta_{alcohol/water}$) and total fluxes for all the prepared membranes. Fluxes have been normalized with thickness to allow for a better comparison. *n*-BtOH and EtOH flux, and separation factors for each type of membrane are gathered in Table 11. In agreement with the fact that all membranes suggest to have higher affinity for *n*-BtOH regardless of their

composition as demonstrated by SU and contact angle experiments, separation factors for n-BtOH are higher than those for EtOH i.e. $\beta_{n\text{-BtOH/water}} > \beta_{EtOH/water}$. The highest $\beta_{n\text{-BtOH/water}}$ is achieved when reduced alkyl-functionalized GO fillers are introduced into PIM-1, reaching a maximum average of 32.9 for MMM 0.1rGO-OA (calculated loading from UV of 0.125 ± 0.094 wt%). The average separation factor for n-BtOH of the membrane that comprises reduced GO functionalized with the longer alkyl chain at approximately the same concentration (0.1rGO-ODA, 0.197±0.024 wt% from UV data) is 26.9. This value is slightly lower than that of 0.1rGO-OA but still higher than that of pristine PIM-1. On the other hand, membranes containing GO-ODA show an average n-BtOH separation factor similar to pristine PIM-1; despite the fact that the addition of GO-ODA suggests an increase of solvent uptake in n-BtOH, their average SU in water is also increased. Moreover, at higher loadings (~1 wt%), the average separation factors of GO-ODA and rGO-OA filled membranes decrease, possibly due to the agglomeration of the graphene flakes as observed from SEM images. For membranes containing 1 wt% of rGO-OA the total flux increases up to 126.3 μm kg m^2 h^{-1} from 67.9 μm kg m^{-2} h^{-1} for pure PIM-1 which is almost double, and the selectivity decreases ($\beta_{n\text{-BtOH/water}}$ =11.5). This result suggests that non-selective interfaces between aggregated filler particles dominate the mass transport across the membrane when the highest filler concentration of 1 wt% is used [20]. Previous work at the University of Manchester revealed strong re-agglomeration of initially exfoliated graphene when forming PIM-1 composites from solutions of 6 mg mL^{-1} [242]. During the solvent evaporation stage in the membrane formation filler concentrations largely exceed this value and can be responsible for the observed behaviour. In the case of GO-ODA filled membranes, the lower average separation factor at a concentration of 1 wt.% is due to a reduction by almost a factor of 5 of the n-BtOH flux from 25.5 μm kg m^{-2} h^{-1} for a pure PIM-1 membrane down to 5.6 μm kg m^{-2} h^{-1} for the MMM (reduction from 32.4 down to 9.7 μm kg m^{-2} h^{-1} if averaged values from Table 11 are considered); the water flux through this membrane (31.4 μm kg m^{-2} h^{-1}) is also lower, although the decrease is not as significant (water flux for pure PIM-1 of 42.4 μm kg m^{-2} h^{-1}). This phenomenon cannot be explained by aggregation at higher loadings, but it could be attributed to blockage of porosity in the polymer matrix

around the GO-ODA flakes as a consequence of strong interactions between PIM-1 and ODA molecules or other functionalities introduced during the oxidation of graphite. The SEM image of the cross section of this membrane depicted in Figure 32e shows fewer agglomerates and a more intimate adherence of the polymer around the filler as compared to MMMs of reduced functionalized GO at a concentration of 1 wt% (Figure 32d and f). In addition to blockage of pores, the higher average reduction in *n*-BtOH flux as compared to water flux suggests a higher degree of hydrophilicity in the composite material that can be attributed to the remaining oxygen-containing functional groups of non-reduced GO-ODA. Concentration polarization, which predominantly affects highly permeable membranes, could be responsible for the decrease in *n*-BtOH flux, and therefore the decrease of total flux in MMMs. However it is extremely difficult to demonstrate this effect for membranes of similar thicknesses that have been tested under the same conditions (same effective membrane area, same degree of feed agitation, temperature and pressure difference).
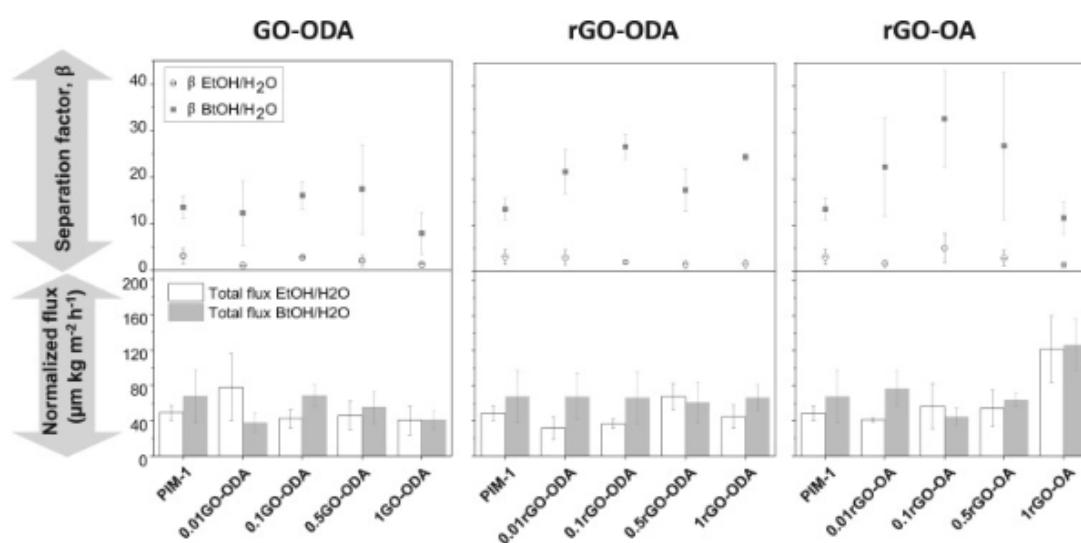
Figure 36: Pervaporation performance of PIM-1 membranes and MMMs composed of PIM-1 and graphene-like fillers. The preferential permeation of alcohol though the membranes was investigated with aqueous feed solutions at 65 °C containing 5 wt% of alcohol under a downstream pressure of 10 mbar. Top graphs display the separation factor for EtOH and *n*-BtOH over water. Bottom graphs show the total flux (alcohol plus water) permeating through the membranes normalized with thickness. At least 3 membranes with an effective area of 1.54 cm^2 were tested for each composition.

Table 11: Pervaporation performance results for EtOH and *n*-BtOH separations of prepared membranes.

Membrane code	wt% of filler (*)	Membrane Thickness (μm)**	J_{EtOH} (g m^{-2}h^{-1})	$\beta_{EtOH/H2O}$	$J_{n\text{-}BtOH}$ (g m^{-2}h^{-1})	$B_{n\text{-}BtOH/H2O}$
PIM-1	-	60 ± 9	98.2 ± 43.2	3.1 ± 1.7	540.3 ± 161.4	13.5 ± 2.3
0.01GO-ODA	0.01	54 ± 6	57.5 ± 27.1	1.1 ±0.5	316.1 ± 125.2	12.2 ± 6.9
0.1GO-ODA	0.1	65 ± 4	84.2 ± 12.1	3.1 ± 0.6	462.0 ± 122.5	16.1 ± 3.0
0.5GO-ODA	0.5	57 ± 2	65.8 ± 4.6	2.1 ± 1.2	389.2 ± 100.6	17.4 ± 9.7
1GO-ODA	1	51 ± 8	53.5 ± 32.0	1.3 ± 0.5	189.8 ± 74.8	7.9 ± 4.5
0.01rGO-ODA	0.01	59 ± 6	62.5 ± 28.7	3.0 ± 1.6	585.1 ± 209.9	21.5 ± 4.8
0.1 rGO-ODA	0.1	56 ± 2	57.3 ± 13.2	2.0 ± 0.4	411.5 ± 7.9	26.9 ± 2.6
0.5rGO-ODA	0.5	68 ± 8	73.7 ± 5.9	1.5 ± 0.8	453.5 ± 265.5	17.6 ± 4.6
1rGO-ODA	1	52 ± 7	57.2 ± 34.4	1.7 ± 0.9	890.0 ± 149.5	24.7 ± 0.7
0.01rGO-OA	0.01	48 ± 4	79.5 ± 21.2	1.8 ± 0.8	914.2 ± 411.1	22.6 ± 0.6
0.1rGO-OA	0.1	51 ± 2	187.2 ± 88.6	5.1 ± 3.2	541.4 ± 88.0	32.9 ± 10.4
0.5rGO-OA	0.5	54 ± 6	126.0 ± 82.5	2.9 ± 1.6	649.7 ± 193.9	27.1 ± 15.9
1rGO-OA	1	59 ± 6	298.5 ± 84.0	1.4 ± 0.3	774.1 ± 159.9	11.6± 3.5

* Values from the preparation of casting solutions.
** Average of the thickness of at least 3 membranes for each type of membrane.

According to the work carried out by Gonciaruk *et al*. [241], the incorporation of graphene into a PIM-1 matrix would lead to either a potential disruption of the packing of polymer chains and subsequent increasing in free volume or the creation of voids at the filler/polymer interface. Higher free volume and voids are associated with higher fluxes in membranes; this effect has been recognized for 1rGO-OA membranes as a consequence of the aforementioned high loading of filler. Nonetheless, the rest of the prepared MMMs, despite having some of the microporosity blocked by graphene, and vapour molecules permeating through the membrane encountering more tortuous paths, have a total flux similar to that of PIM-1 membranes and increased separation factors. This enhancement can be due to the presence of graphene-like materials that can hinder the permeation of water, as depicted in Figure 37a, down to a minimum value that corresponds to an optimum loading of filler of 0.1 wt%. The optimum loading is quite low as compared to concentrations required in other MMMs reported in the literature with other types of fillers, such as CNTs (10 wt%) [20], silicalite-1 (60 wt%) [85], or ZIF-71 (25 wt%) [218]. The high area/volume aspect ratio of graphene flakes, similarly to other layered materials [226, 227], allow the use of smaller filler loadings to achieve exceptional improvements on the bulk structural properties of the polymer,

provided agglomeration does not take place as it has been shown in this case by SEM and TEM characterization.

For comparison, a summary of performance for different membranes used for *n*-BtOH recovery is presented in Figure 37b. The flux of the membranes developed by our group are among the highest values reported in the literature and present similar separation factors, with the clear exception of reported PDMS membranes filled with 60% of silicalite-1 that have a remarkable *n*-BtOH separation factor of 93 [85], and reported PDMS membranes filled with 40 wt.% of ZIF-7 (separation factor of 66) [28]. The improvement achieved in this work for *n*-BtOH separation with loadings as low as 0.1 wt%, as compared to very high loadings used in previously mentioned works, demonstrates the potential of these new hybrids. It is also worth mentioning that the flux could be further enhanced by reducing the effective thickness of PIM-1 down to few hundreds of nanometers via the preparation of composite membranes supported on highly porous substrates. Examples of flux enhancement via thin film composite membrane configurations can be found in the literature: a PEBA film coated on a ceramic hollow fibre [99] or the Pervatech PAN-PV [243] with total fluxes as high 4196 and 4350 g m^{-2} h^{-1}, respectively.

(a)   **(b)**
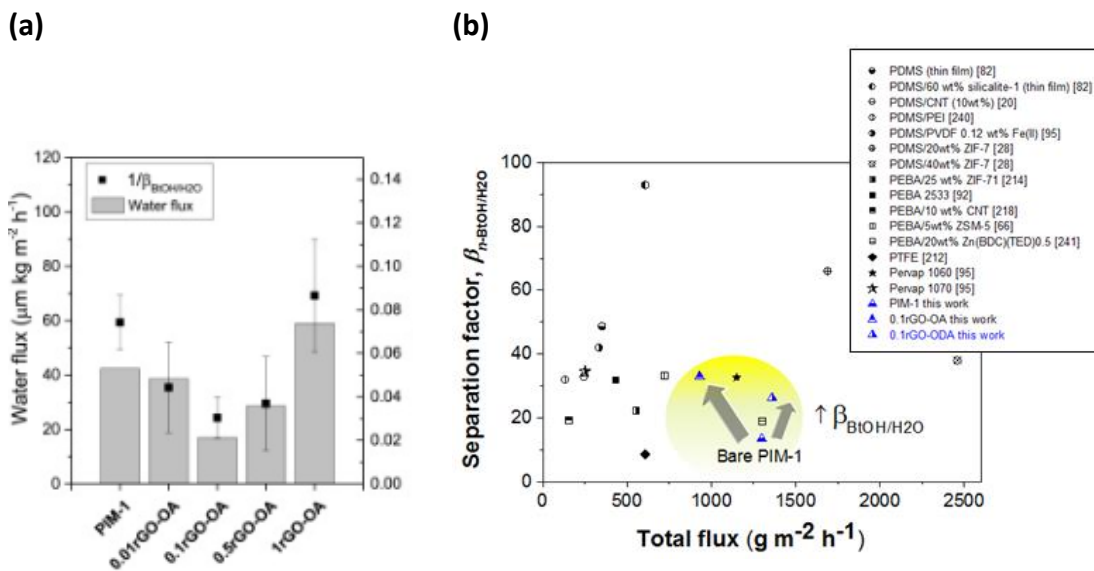
Figure 37: Water flux and inverse of separation factor for *n*-BtOH in rGO-OA based MMMs and b) Performance of prepared MMMs and other reported organophilic membranes; separation factor of BtOH vs total flux (not normalized with thickness) [98, 244, 245].

4.8. Conclusions

Novel mixed matrix membranes comprising PIM-1 and graphene-based filler have been developed and successfully used for the separation of alcohols from binary aqueous solutions. Herein, it has been shown that the choice of suitable hydrophobic fillers with high surface area to volume ratio is an effective way of improving the performance of PV membranes for butanol recovery at very low concentrations; just 0.1 wt.% of alkyl-functionalized GO is needed to double the selectivity towards n-BtOH, maintaining a total flux in the range of 930–1360 g m^{-2} h^{-1} (normalized flux 40–60 µm kg m^{-2} h^{-1}). The incorporation of reduced graphene oxide derivatives in PIM-1 enhances the membrane affinity towards n-BtOH and decreases the affinity towards water, which results in a much lower flux of water permeating through the membrane and an increase in average separation factor for n-BtOH ($\beta_{n\text{-BtOH/H2O}}$) from 13.5 for pure PIM-1 membranes to values of 32.9 and 26.9, for membranes containing flakes functionalized with the short-chain (OA) and the long-chain (ODA) alkylamines, respectively.

For EtOH separations there is not a significant improvement; with solubility and diffusivity coefficients for EtOH in PIM-1 closer to those of water, the obtained separation factors are lower than those for other organophilic polymers such as PTMPS and PDMS.

In summary, in this work freestanding membranes of several tens of micrometers have been fabricated with a polymer of intrinsic microporosity and tested, achieving total flux values for n-BtOH separation via PV which are the highest among those found in the literature. These results could potentially be enhanced even further by the reduction of the effective thickness as in thin film composite membranes. However, aging studies in thinner films should be carried out, and the addition of nanosheets of graphene derivatives evaluated.

Chapter 5 – Study on the formation of thin film nanocomposite (TFN) membranes of polymers of intrinsic microporosity and graphene-like fillers: effect of lateral flake size and chemical functionalization

Monica Alberto[a], Rupesh Bhavsar[b], Jose Miguel Luque-Alled[a], Eric Prestat[c,d], Lei Gao[b], Peter M. Budd[b], Aravind Vijayaraghavan[c], Gyorgy Szekely[a], Stuart M. Holmes[a], Patricia Gorgojo[a]

[a] School of Chemical Engineering and Analytical Science, The University of Manchester, Manchester, M13 9PL, UK.

[b] School of Chemistry, The University of Manchester, Oxford Road, Manchester, M13 9PL, UK.

[c] School of Materials, The University of Manchester, Oxford Road, Manchester, M13 9PL, UK.

[d] SuperSTEM Laboratory, SciTech Daresbury Campus, WA4 4AD Warrington, UK.

5.1. Motivation

As seen in our previous study, the separation performance can be enhanced by adding graphene-like fillers into PIM-1 polymer matrices. In order to improve the productivity of those membranes in terms of flux yield, thin film nanocomposite (TFN) membranes, containing PIM-1 and graphene-like materials, were developed and are presented in this chapter.

The work developed in this chapter is, in part, a continuation of the work presented in the previous chapter and the work conducted by Lei Gao _et al_. at the School of Chemistry in Prof. Budd's group [47], who prepared thin film composite (TFC) PIM-1 membranes for _n_-butanol (_n_-BtOH) recovery from aqueous solutions. Gao _et al._

optimized the preparation of PVDF membrane supports through phase inversion, using phosphoric acid as an addictive to control the porosity and surface pore size.. TFC membranes were prepared via dip coating, and using different PIM-1 concentrations (2 to 4 wt.%) in the dope solutions. Total fluxes in the range between 2.76 ± 0.20 and 9.08 ± 0.42 kg m^{-2} h^{-1} were achieved, and the separation factor ranged from 7.5 to 18.5. A trade-off between the separation factor and membrane productivity was observed in these membranes.. From the results obtained in that work, PVDF support containing a concentration of phosphoric acid of 3wt.%, 18 wt.% of PVDF in DMAc and dope solutions containing 4 wt.% gave the best performance. Thus, the same preparation conditions were selected for the preparation of supports for the TFN membranes in this Thesis.

The results obtained here have been submitted to *Journal of Membrane Science*. The sample preparation for Scanning Transmission Electron Microscopy (STEM) was conducted by Jose Miguel Luque-Alled. Dr Eric Prestat performed the analysis and wrote the conditions at which the analysis was performed as well as the discussion the results obtained.

5.1. Abstract

Thin film nanocomposite (TFN) membranes of polymer of intrinsic microporosity PIM-1 incorporating graphene oxide (GO) nanosheets of different sizes and chemistries are presented. These membranes show an improved separation performance for the recovery of *n*-butanol (*n*-BtOH) from aqueous solutions through pervaporation; an improvement of *ca.* a third of the value achieved for pristine PIM-1 thin films is obtained for TFN membranes filled with nanometer-sized reduced octyl-functionalized GO. In addition, these nanometer-sized fillers lead to a maximum increase in total flux of approximately 40%. The thickness of the supported films produced are in the range 1 - 1.5 µm, and fillers used are micrometer- and nanometer-sized alkyl-functionalized GO nanosheets and their chemically reduced counterparts. As evidenced by a superior overall membrane performance, the interfacial interaction between the filler and the polymer matrix is enhanced for those whose lateral size is in the nanometer range. Moreover, an

enhancement in the separation performance and productivity of such membranes is observed for higher operating temperatures and higher contents of *n*-BtOH in the feed.

5.2. Introduction

Pervaporation (PV) is a membrane-based technology that can potentially replace energy-intensive distillation processes currently used for industrial separation such as the recovery of bioalcohols from fermentation broths. Bioalcohols are established as sustainable alternatives to fossil fuels, but there are hurdles to be overcome in the development of effective membrane materials for their separation. For instance, polymer membranes show a trade-off between permeability and selectivity and typically undergo swelling when exposed to organic solvents. Inorganic membranes, on the other hand, are brittle and can get damaged more easily. In addition, other considerations regarding the economic viability of the technology need to be made; polymers are inexpensive to process, whereas the cost of processing inorganic materials is high but they stand out for their high thermal and chemical stability, and higher selectivity.[18, 19]

The flux through a membrane is directly proportional to the reciprocal of the membrane thickness. Therefore, in recent years extensive research has been geared towards the preparation of extremely thin layers with molecular separation properties, using 2-dimensional inorganic materials: high-aspect-ratio zeolites,[246] carbon materials such as diamond-like carbon nanosheets,[247] graphene oxide (GO) [182, 248-253] and reduced graphene oxide (rGO).[254-257] However, large-scale preparation of such membranes is a challenge.

Mixed matrix membranes (MMMs), composed of particles of diverse nature incorporated in polymeric matrices, seem to be good candidates to benefit from the advantageous properties of both types of material. Porous materials (zeolites, [35, 80] metal-organic frameworks (MOFs)[218, 258] and carbon nanotubes (CNTs) [20, 259]) and non-porous materials (graphene[260]) have been used as fillers in MMMs. However, large loadings are often needed in order to achieve noticeable improvements in the separation performance as compared to the pristine

106

polymers, which increases the cost and gives rise to problems of agglomeration and formation of non-selective voids. Moreover, most of the research on MMMs deals with freestanding membranes that are several tens of microns thick, which are unviable for industrial applications.[30, 32, 35]

Whether it is a purely polymeric membrane or a MMM, it should be produced as a thin dense selective layer supported on a much cheaper and thicker porous substrate, so as to maximize the flux of permeate and minimize the area required to process large-scale streams.[261] This arrangement also brings down the cost of the membrane, since the amount of active material can be considerably reduced. The dense thin layer can be a few tens or hundreds of nanometers in thickness, and when separately formed on top of the porous support (tens of microns thick) the combination is referred to as a thin film composite (TFC) membrane. When nanoparticles are embedded in the polymer thin layer, the configuration is known as a thin film nanocomposite (TFN) membrane. Both TFC and TFN membranes are typically produced via techniques such as coating or interfacial polymerization.

Polyamide TFC membranes used for reverse osmosis and for nanofiltration in organic liquids are produced via interfacial polymerization (IP) and comprise an active polyamide layer of about 200 nm in thickness. Recently, this thickness has been lowered down to a sub-10 nm film by controlling the interfacial reaction, and the resulting membranes have shown permeance values two orders of magnitude higher than commercial ones.[262] Similarly, ultrathin polyarylate nanofilms with thicknesses down to 20 nm have been synthesized via IP.[263] Other successful attempts to increase the flux through thin film polyamide membranes include the addition of porous MOF nanoparticles in the polyamide layer during the IP reaction.[264-266] Graphene-like materials have also been introduced into thin film polyamide membranes to enhance their separation performance and provide them with anti-fouling properties.[267-269] Polyamide films are hydrophilic and can be used for the dehydration of alcohols.[270, 271] However, for the recovery of alcohols from fermentation broths, where the alcohol concentration can be as low as 2 wt%,[272] organophilic membranes are required.

Polymers of intrinsic microporosity (PIMs) are a class of organophilic material with exceptional separation properties, not just in terms of selectivity but also in terms of permeability (i.e. flux normalized for the driving force and the membrane thickness). The first membrane-forming PIM to be synthesized, PIM-1, has been used for gas separation,[49, 141, 206] pervaporation[3, 46] and organic solvent nanofiltration.[44] To date, thin films of PIM-1 have been prepared on porous supports via dip coating [260, 273] and spin coating/transferal.[44] Very recently integrally skinned asymmetric (ISA) PIM-1 hollow fibers have been reported for the first time.[54] ISA membranes, like TFC membranes, comprise a thin dense separation layer supported on a highly porous structure, produced in this case via immersion precipitation. Thus, the dense and the porous structures are both produced in a single step from the same polymer solution, which makes the structure more stable as compared to a TFC. However, large amounts of expensive PIM-1 are needed for producing ISA membranes, as compared to supported TFCs.[274]

Freestanding PIM-1 membranes several tens of microns thick have been investigated for n-BtOH recovery from aqueous solutions.[4, 260] In our previous study, the separation performance of PIM-1 freestanding membranes (~ 60 μm in thickness) was greatly improved by adding alkyl-functionalized graphene oxide into the polymer matrix. The best membrane showed a 144 % increase in the separation factor for n-BtOH with a total flux of 1.2 kg m^{-2} h^{-1}, but that is still low, as expected for freestanding membranes.[260] Furthermore, polyvinylidine fluoride (PVDF) porous supports were investigated for the preparation of TFC membranes via dip coating (thickness of pristine PIM-1 active layer in the range 1.0–2.9 μm) and flux values of up to 9.08 kg m^{-2} h^{-1} were reported.[47] Herein, thin film nanocomposite (TFN) membranes made with PIM-1 incorporated with alkyl-functionalized GO nanosheets are prepared on PVDF supports for n-BtOH/water separation. Considering that contradicting results on MMMs have been reported in the literature,[30-35] the effect of the filler size and loading on the membrane performance is investigated in this study. In addition, the effect of operating temperature and feed composition on the PV performance of the membranes with

optimal fillers is also analyzed. Optimizing the size and concentration of fillers in TFN membranes is essential for achieving good separation performance and therefore, positioning them as candidates for the next generation of commercial membranes, where high flux and separation performance are critical.

5.3. Experimental

5.3.1. Materials

Polyvinylidene fluoride (PVDF, Mw ~5.34×105 g mol^{-1}), dimethylacetamide (DMAc), chloroform, *n*-butanol (*n*-BtOH) and phosphoric acid were purchased from Sigma Aldrich (UK). Non-woven fabric (2471 Polypropylene/Polyethylene (PP/PE)) was purchased from Freudenberg-Filter, Germany. All chemicals were used as obtained without any purification. Commercial PERVAP 4060 membranes were kindly supplied by DeltaMem AG, Switzerland.

5.3.2. Synthesis of PIM-1

The synthesis of PIM-1 is described in section 3.2. PIM-1 from Batch 2 was used in this study.

5.3.3. Synthesis of graphene-like materials

The synthesis of graphene-like materials used in this work is described in section 3.3 and includes alkyl-functionalized graphene oxide with octadecylamine (GO-ODA), alkyl-functionalized reduced graphene oxide with octadecylamine (rGO-ODA), and alkyl-functionalized reduced graphene oxide with Octylamine (rGO-OA).

5.3.4. Preparation of PVDF membrane supports

PVDF supports were prepared by phase inversion technique as described in the work by Gao *et al.*[47] with the casting solution containing 18 wt% PVDF, 3 wt% phosphoric acid and 79 wt% DMAc and using an automatic film applicator (Sheen 1133N, UK). The viscosity of the PVDF dope solution was measured using an Elcometer 2300 Rotational Viscometer (Elcometer Limited, UK), using a TL7 spindle

and a spindle speed of 6 rpm. The measurement was done at a humidity and temperature of 65% and 20.3 °C, respectively, and gave a value of 5390 mPa s.

5.3.5. Preparation of dip-coated thin film nanocomposite membranes

TFN membranes supported on porous PVDF were prepared through a dip-coating technique using an in-house built system. The polymer content used in all coating solutions was 4 wt% in chloroform; whereas the filler loading ranged from 0.01 to 0.25 wt.% with regards to the weight of the polymer. PVDF membrane supports were dried at room temperature overnight before use and cut into a rectangular shape (~ 3cm × 10cm). TFN membranes were prepared by putting the PVDF supports in contact with the coating solutions for 0.7 s, as schematized in Figure 38.
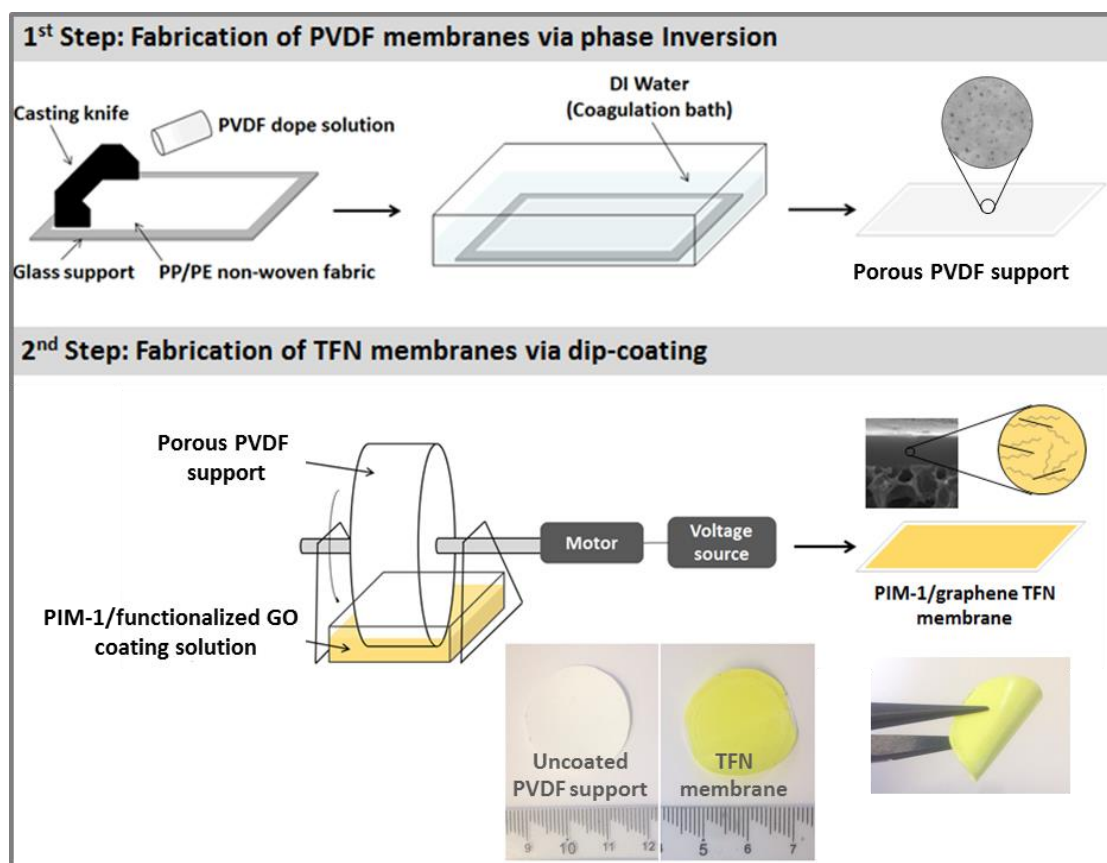
Figure 38: Schematic representation of the fabrication process of the thin film nanocomposite (TFN) membranes. It includes a first step of fabrication of porous supports via phase inversion, and a second step of coating such supports with PIM-1 solutions containing alkyl-functionalized graphene oxide nanosheets. Pictures of an uncoated PVDF support disc and a TFN membrane disc are displayed; the scale bar is in cm.

5.3.6. Characterization

5.3.6.1. Lateral size of alkyl-functionalized graphene oxide nanosheets

The lateral flake size of the nanosheets was analysed by scanning electron microscopy (SEM) using a SEM FEI Quanta 250 FEG-SEM (FEI, USA). Foe that, graphene-like materials were dispersed in chloroform and then sprayed-coated onto a silicon dioxide wafer.

5.3.6.2. Membranes

A Porolux 1000 (Porometer, Belgium) capillary flow porometer was used in this study to measure the bubble point size, smallest pore size, mean flow pore (MFP) and pore size distribution of the PVDF flat sheet membranes. In this technique, nitrogen was used to pressurise the sample chamber and displace the wetting liquid from the membrane structure. The pore diameter, D, is determined using the Young-Laplace equation (11) as follows:

$$D = \frac{4\gamma \cos\theta}{P} \tag{11}$$

Where γ is the surface tension of the wetting liquid, θ is the contact angle between the sample and the wetting liquid and P is the difference in pressure across the membrane. Membrane samples with a diameter of 2.5 cm (effective area of 2.9 cm^2) were immersed into a wetting liquid (Porefil, surface tension of 0.0159 N m^{-1}) before testing. They were characterized using the "dry-up-wet-up" method. Software provided by Porometer (Belgium) was used to analyze the data. Three different discs of PVDF membranes were tested. Bubble point pore size, the largest pore size, was determined taking into account the pressure required to achieve a downstream 100 mL min^{-1} flow rate. MFP size was calculated though the pressure at which the wet and half dry curves meet. Finally, the pressure at which the dry and wet curves meet allowed determination of the minimum pore diameter.

Surface morphology of PVDF membranes were examined by AFM, carried out using a Fastscan microscope (Bruker, USA). The measurements were conducted using tapping mode at room temperature under an air atmosphere. Nanoscope Analysis

software was used to generate 2D surface scanning images as well as to compute automatically the roughness parameters of the membranes.

A Quanta 250FEG-SEM (FEI, USA) was used to observe cross sections and surfaces of PVDF and the TFN membranes. The samples were immersed firstly in EtOH for about 30 s and then in liquid nitrogen for another 30 s where they were fractured. Subsequently, they were coated with a conductive layer of sputtered Platinum. ImageJ (NIH) open-source software was used to determine the mean pore size and surface porosity of the PVDF membranes from the SEM images, as well as to determine the thickness of the TFN dense layer formed on top of the PVDF membrane supports.

The water contact angle values of PVDF and TFN membranes were measured using an Attension Theta optical tensiometer (Biolin Scientific, UK) via the sessile drop method. Measurements were conducted at room temperature and DI water used as a probe liquid. Water droplets (3 uL) were generated using a microsyringe. OneAttension software (Biolin Scientific, UK) was set to record 17 frames per second for 20 s. The water contact angle values were taken 10 s after the water droplet had touched the membrane surface. The final water contact angles resulted from the average of at least three points of each membrane.

Scanning Transmission Electron Microscopy (STEM) and Electron Diffraction (ED) data were collected using a FEI Titan 80–200 equipped with a Chemistem EDX detector, probe-side aberration corrector and an X-FEG electron source operating at 200 kV. In STEM mode, the microscope was set at a beam current of 100 pA, and a convergence angle of 21 mrad and collection angles ranging from 0 to 14 mrad for the bright field detector. Electron diffraction pattern were acquired over an area of 0.2 μm^2 using the smallest condenser aperture (50 um diameter) of the microscope. For TEM specimen preparation, the membranes were embedded in TAAB 812 epoxy resin (TAAB Laboratories, UK) that was allowed to polymerize at 60 °C for 24 h. Ultrathin sections (80 nm) were then obtained using an ultracut E ultramicrotome (Reichert-Jung, USA). The face of the membrane was positioned perpendicular to the edge of the diamond knife (DiATOME, Switzerland) allowing

cross sections of the specimen to be acquired, which were collected on to copper Lacey carbon film (Agar Scientific Ltd, UK).

Ultraviolet visible (UV-Vis) spectroscopy was used to determine the filler concentration in the PIM-1/graphene coating solutions. Part of the solution used for dip coating was dried at room temperature and subsequently placed in the vacuum oven in order to remove any residual solvent. Afterwards, dried samples were weighed and redissolved in chloroform (4 mL). At least three samples of each coating solution were measured. The absorbance at 660 nm was recorded using a Genesys 10 S UV–Vis spectrophotometer (Thermo Scientific, United Kingdom), using avquartz cuvette with a 1 cm optical path at room temperature. The extinction coefficients obtained in our previous work [260] were used; 4.939, 15.256, and 7.556 mL mg^{-1} cm^{-1} for GO-ODA, rGO-ODA, and rGO-OA, respectively (Appendix A, Figure A1).

PV was carried out as described in our previous work on freestanding membranes (section 4.6.5.1.).[260] The effect of the temperature and composition of the feed solution on the separation performance was investigated. The temperature was varied from 35 to 65 $^{\circ}$C and the n-BtOH composition from 2 to 5 wt.% at a constant temperature of 65 °C. The effective area of the membranes was 2.54 cm^2. The permeate flux, J, (kg m^{-2} h^{-1}) was determined using equation (12):

$$J = \frac{m}{A\,t} \tag{12}$$

where m is the weight of the permeate (kg), A is the effective membrane area (m^2) in contact with the feed solution and t is the permeate collection time (h). The separation factor, β, was determined as in equation (13):

$$\beta = \frac{Y_{n-\text{butanol}}/Y_{\text{water}}}{X_{n-\text{butanol}}/X_{\text{water}}} \tag{13}$$

where $Y_{n\text{-BtOH}}/Y_{\text{water}}$ is the weight ratio of n-BtOH to water in the permeate and $X_{n\text{-BtOH}}/X_{\text{water}}$ is the corresponding ratio in the feed.

Commercial PERVAP 4060 membranes were also tested for *n*-BtOH recovery from aqueous solutions under the same conditions.

5.4. Results and discussion

TFN membranes were prepared via dip coating of alkyl-functionalized GO nanosheets dispersed in a solution of PIM-1 in chloroform (nanosheet concentrations of 0.01-0.25 wt.% with regards to the mass of PIM-1) onto tailored porous PVDF supports, with active layer thicknesses as low as 1 μm, as schematized in Figure 38. Dip coating was the selected technique as it can produce reasonable defect-free thin layers than can be scaled up for the production of larger amounts of membranes for industrial applications. However, some challenges were encountered when moving from a freestanding configuration (such as that previously reported[260]) to a much thinner supported membrane: (i) appropriate porous substrates onto which the thin films are fabricated were tailored (high surface porosity and small pore size) and (ii) nanosheets with suitable sizes had to be selected in order to avoid inhomogeneity and defects within the selective thin film. In this work three different fillers were used for the preparation of TFN membranes: GO functionalized using octadecylamine (GO-ODA) and its chemically reduced form (rGO-ODA), and GO functionalized using octylamine then chemically reduced (rGO-OA). The lateral size of the flakes was reduced via sonication and its effect on the membrane performance was studied.

5.4.1. Lateral size of alkyl-functionalized graphene oxide nanosheets

Samples of GO-ODA, rGO-ODA and rGO-OA were dispersed in chloroform and probe sonicated at different times, 10 min and 8 h, in order to obtain flakes with different lateral sizes. The size distribution of the nanosheets was characterized via direct image analysis from SEM images. Figure 39 shows micrographs of the fillers and their lateral flake size distributions, which were derived from between 70 and 147 flakes. Gaussian curve-fitting was used to determine the mean value for each individual sample. According to these results, after probe sonicating for 10 min, the average lateral flake sizes of GO-ODA, rGO-ODA and rGO-OA were 0.74 ± 0.40 μm, 1.26 ± 0.75 μm and 1.35 ± 0.73 μm, respectively. After a longer probe sonication of

8 h the average lateral flake size decreased to 0.25 ± 0.16 µm, 0.25 ± 010 µm and 0.26 ± 0.16 µm for GO-ODA, rGO-ODA and rGO-OA, respectively.
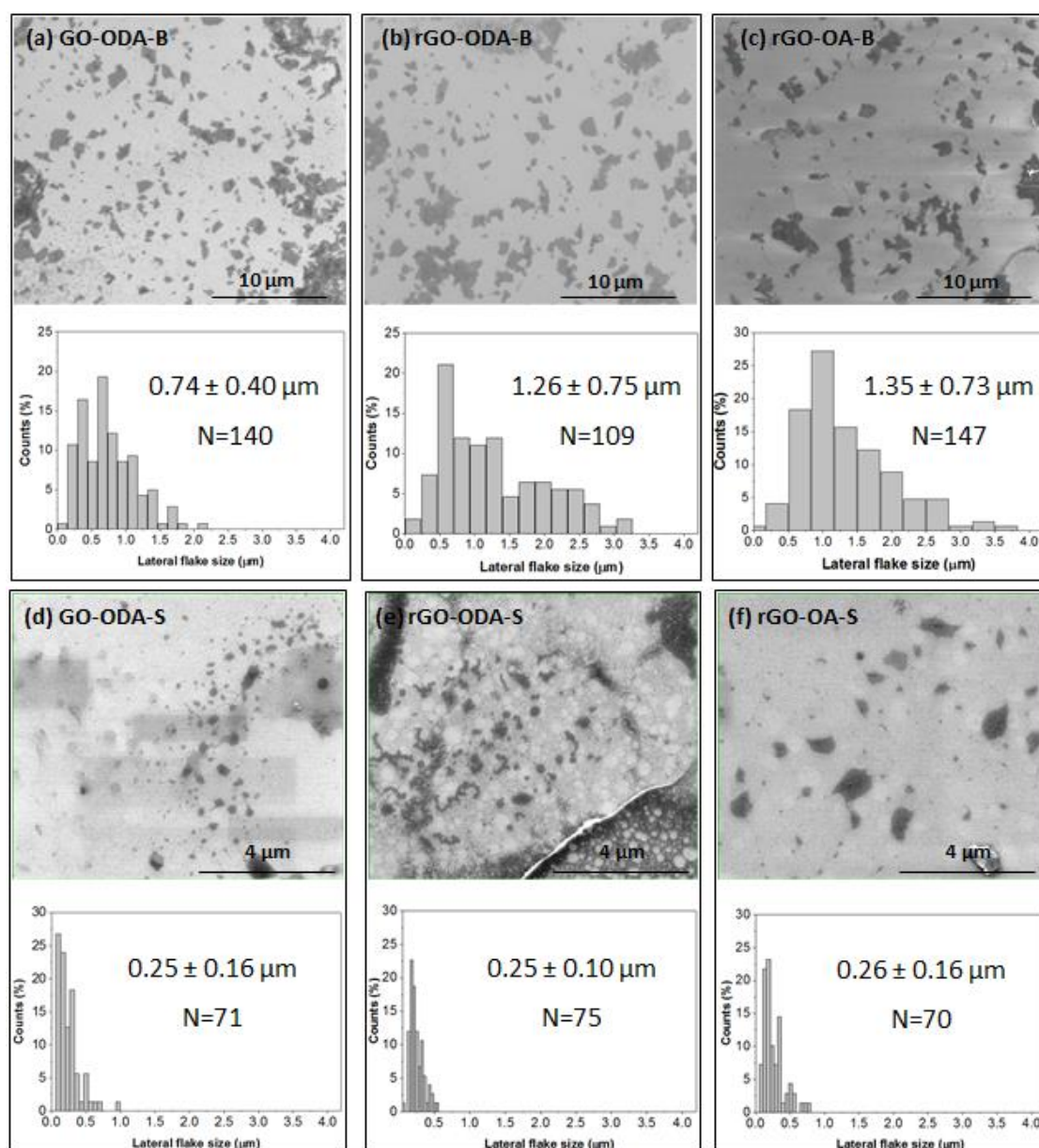
Figure 39: SEM images of graphene-like nanosheets probe sonicated in chloroform for 10 min (a) GO-ODA-B, (b) rGO-ODA-B and (c) rGO-OA10-B, and flakes probe sonicated in chloroform for 8 h (d) GO-ODA-S, (e) rGO-ODA-S and (f) rGO-OA-S. Distributions of the lateral sizes are shown below each micrograph. *N* corresponds to the number of flakes that were analyzed.

5.4.2. Characterisation of PVDF membrane supports

The surface and cross-section of the PVDF membrane support used for the TFN membrane preparation is shown in Figure 40. Phosphoric acid was added to the casting solution in order to enhance the surface porosity and decrease the average pore size of the polymer supports. This is desirable for the formation of defect-free

TFN membranes with sufficiently high flux values, as previously reported.[47] From the analysis of the SEM images, the surface porosity and average pore size obtained were in the range 4.2-11.7% and 64 ± 31 nm, respectively. Since non-conductive samples require the deposition of a conductive coating for SEM analysis, pore size and surface porosity can be underestimated using this technique. Thus, capillary flow porometry (CFP) was carried out to obtain more reliable information on the pore structure of the support – namely, the MFP size, the bubble point pore size, smallest pore size and the pore size distribution. Figure 41a shows the N_2 flow rate through the substrate versus the applied pressure on its upstream side while Figure 41b depicts the pore size flow distribution of three PVDF samples tested. The values obtained for the BP pore size, the MFP and the smallest pore size were 329 ± 22, 285 ± 11 and 192 ± 6 nm, respectively, which are comparatively larger than those calculated through micrographs. One possible explanation is that CFP only investigates connected pores that span the entire thickness of the membrane, whereas, SEM accounts for all the pores on the surface, whether they are open, blind or closed ones. Moreover, the scan areas analyzed by SEM and CFP are quite different, approximately $3x10^{-6}$ and 3 cm^2, respectively, which clearly suggests that CFP values are more representative of the bulk support. Since CFP is a widely used method that takes into account the whole membrane structure (and not only the surface), this technique gives valuable information on the pores that contribute to flow.
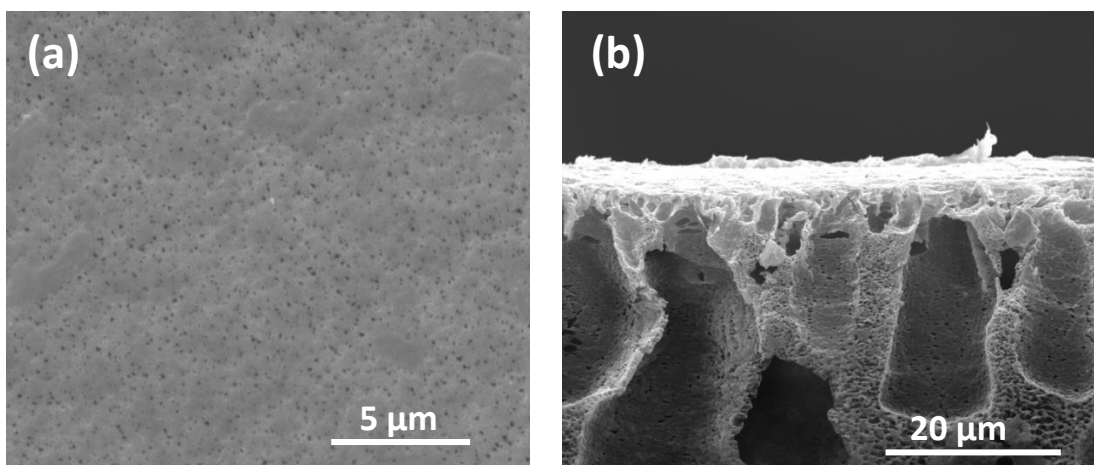
Figure 40: (a) Surface and (b) cross-section SEM images of a PVDF membrane support.
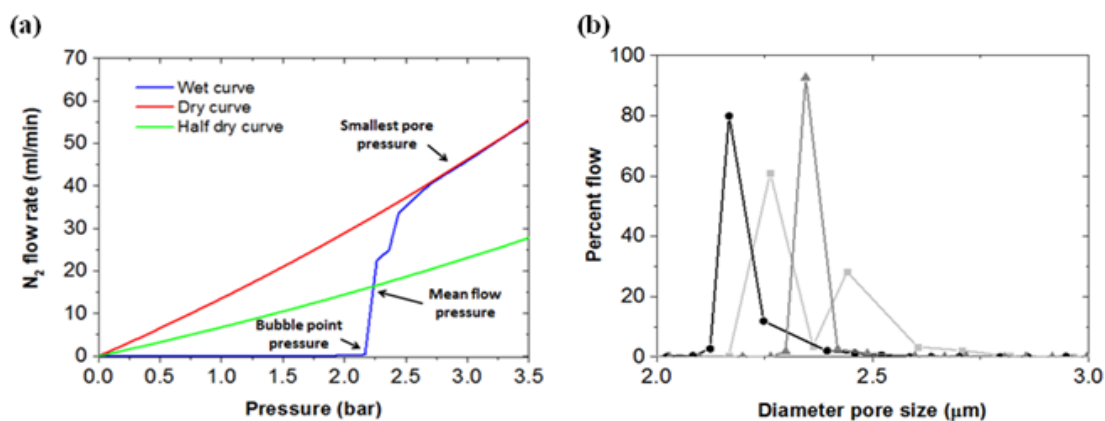
Figure 41: (a) N$_2$ flow rate as a function of pressure applied on wet and dry PVDF18 membrane, (b) Pore size flow distribution of three different samples tested.

The surface topology of the PVDF membrane support was also investigated through AFM (Figure 42). Areas of 30×30 µm were examined and the roughness parameters were calculated; the average roughness profile (R_a) value was 35.4 ± 1.2 nm, whereas the average root mean square roughness (R_q) value was 44.9 ± 1.6 nm, in accordance to reported values.[47]
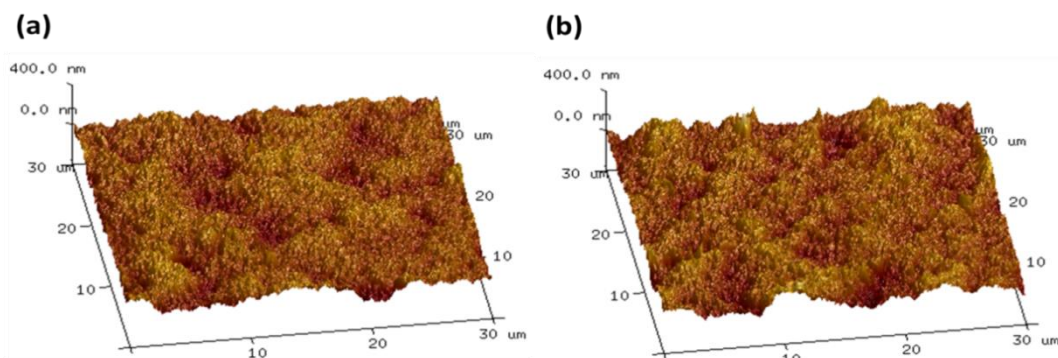
Figure 42: Tapping mode 3-Dimensional AFM images of the PVDF membrane support; (a) and (b) are two areas of the same surface sample.

5.4.3. TFN membranes

The concentrations of filler in the membranes were determined through UV-Vis spectroscopy and are presented in Table 12. The code for each membrane is given by the loading and type of filler (GO-ODA, rGO-ODA or rGO-OA) followed by either *B* or *S*, depending on the lateral size of the filler; *B* for big nanosheets (probe sonicated for 10 min), and *S* for small ones (probe sonicated for 8 h). According to these results, the values obtained from UV-Vis spectroscopy are in line with those

calculated on the basis of the weighed amounts and concentrations used for the coating process.

Table 12: TFN PIM-1/graphene membranes prepared via dip coating on PVDF porous supports and their composition. *B* and *S* in the membrane code stands for big and small, respectively. At least three UV-Vis measurements were performed in order to obtain the wt% filler in the re-dissolved membranes.

Membrane code	Filler	Sonication time	wt.% filler from composition of coating solution	wt.% filler from UV -Vis
PIM-1	-	-	-	-
0.05GO-ODA–B			0.05	0.039 ± 0.024
0.1GO-ODA–B	GO-ODA		0.1	0.072 ± 0.003
0.25GO-ODA–B			0.25	0.187 ± 0.034
0.05rGO-ODA–B			0.05	0.057 ± 0.011
0.1rGO-ODA–B	rGO-ODA	10 min	0.1	0.081 ± 0.010
0.25rGO-ODA–B			0.25	0.229 ± 0.003
0.05rGO-OA–B			0.05	0.034 ± -0.029
0.1rGO-OA–B	rGO-OA		0.1	0.102 ± 0.006
0.25rGO-OA–B			0.25	0.350 ± 0.002
0.01GO-ODA–S			0.01	0.019 ± 0.007
0.05GO-ODA–S	GO-ODA		0.05	0.052 ± 0.016
0.1GO-ODA–S			0.1	0.084 ± 0.024
0.01rGO-ODA–S			0.01	0.013 ± 0.005
0.05rGO-ODA–S	rGO-ODA	8 h	0.05	0.077 ± 0.27
0.1rGO-ODA–S			0.1	0.089 ± 0.032
0.01rGO-OA–S			0.01	0.023 ± 0.003
0.05rGO-OA–S	rGO-OA		0.05	0.032 ± 0.001
0.1rGO-OA–S			0.1	0.052 ± 0.001

Cross-sections of PIM-1-graphene TFN membranes containing 0.1 wt% of filler, as calculated for the coating solutions, are shown in Figure 43 and confirm the successful preparation of homogenous thin layers on top of PVDF porous substrates through the dip-coating technique. Active layer thicknesses were in the range 1 - 1.5 µm, although it should be mentioned that these values refer only to the apparent thickness, i.e. the layer formed on top of PVDF supports, not taking into account any polymer that has penetrated down the pores and has solidified during the coating process thus increasing the effective thickness for the separation. SEM images reveal a homogeneous distribution of the filler in the polymeric matrix with no agglomerates.
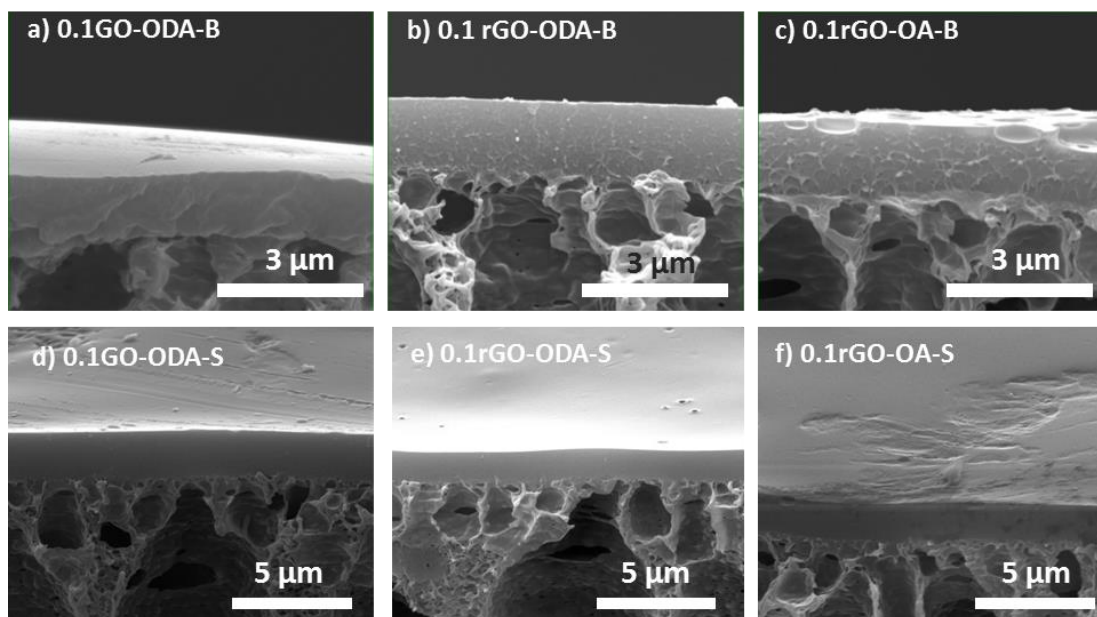
Figure 43: Cross-sectional SEM images of TFN membrane prepared with graphene-like nanosheets of lateral sizes in the micrometer range: (a) 0.1GO-ODA-B, (b) 0.1rGO-ODA-B, (c) 0.1rGO-OA-B, and TFN membranes containing fillers whose lateral size falls in the nanometer range: (d) 0.1GO-ODA-S, (e) 0.1rGO-ODA-S, (f) 0.1rGO-OA-S.

Cross sectional TEM measurements have been performed to characterize the TFN membranes produced in this work. Figure 44 shows a 80 nm thin cross section of the TFN membrane 0.1rGO-OA-S and structure analysis, such as high resolution bright field scanning transmission electron microscopy (BF-STEM) and electron diffraction (ED) to demonstrate the presence of the graphene based nanosheet. Figure 44a shows a BF-STEM image nanosheet and the corresponding ED pattern is displayed and compared to the ED pattern of a PIM only area in Figure 44b. PIM has an amorphous structure, which provides diffuse rings in the ED pattern. The graphene based nanosheet is a crystalline material from which we would expect sharper feature -rings, or spots, depending on the geometry. Functionalized rGO nanosheets are known to have higher degree of disorder than highly crystalline graphene flakes, that will make the features observed in the ED pattern more diffuse than in case of bare graphene. On top of that, the ED is probing an area significantly larger than the nanosheet itself and the main contribution to the ED pattern still comes from the amorphous PIM materials. This results in slightly more sharper ring in the ED pattern (inset of Figure 44b) and a small peak around 4.7 nm^{-1} ({1010} graphene lattice spacing) on the top of the PIM diffuse contribution, as measured in the intensity profile of the ED pattern (Figure 44b). The high

resolution BF-STEM image (inset of Figure 44a) confirms this observation by showing rGO interlayer lattice imaging corresponding to the (0001) graphene lattice spacing of the nanosheet, which means that the nanosheet is observed edge on. Form the BF STEM in Figure 44a, it can also be observed that no pore are formed between the filler and the PIM, from which it can be inferred that a good quality interface is formed between both.
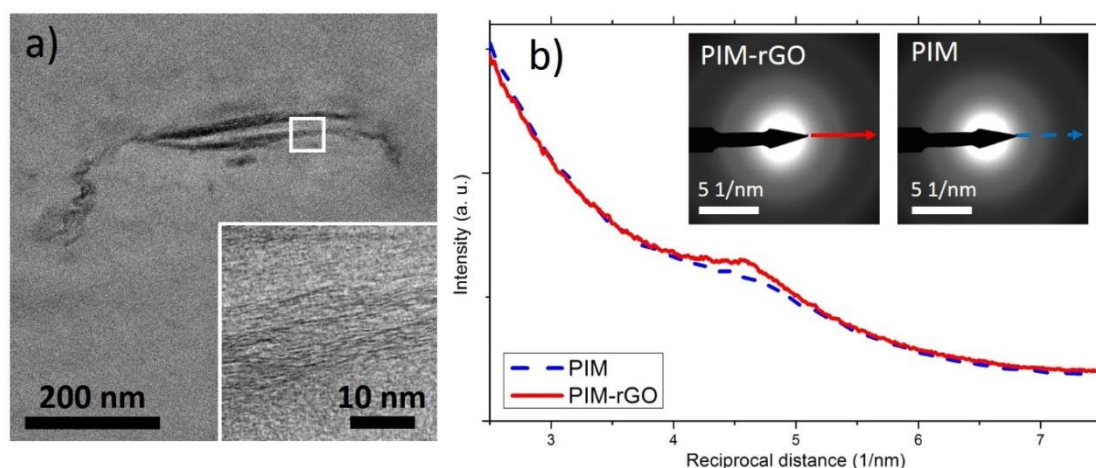
Figure 44: (a) Cross sectional BF-STEM images showing a rGO-OA-S flake in the TFN membrane 0.1rGO-OA-S. The high resolution BF-STEM image taken from the area marked by white square in (a) is displayed in the inset and shows lattice imaging corresponding to the rGO-OA interlayer spacing. (b) Intensity profile of electron diffraction pattern taken from a PIM-rGO-OA-S area (solid red line) and PIM only (dash blue line) areas. The corresponding electron diffraction patterns are shown in inset.

The hydrophobicity of the membranes was evaluated by measuring their surface water contact angles. Figure 45 shows the values obtained for a range of TFN membranes containing the three types of alkyl-functionalized graphene materials (GO-ODA, rGO-ODA, rGO-OA) of lateral sizes in the micrometer range (membrane codes ending -*B*) and in the nanometer range (membrane codes ending -*S*). Pure PIM-1 TFC membranes revealed a contact angle of 92 ± 4°, while the value of the PVDF support on which the thin films were cast was 77 ± 3°, confirming the successful formation of a homogeneous PIM-1 layer. There was not much difference between the contact angles of membranes with big and small fillers, ranging 89 - 100°, although they are slightly higher than those reported in our previous study on freestanding membranes.[260] This might be a consequence of the increased surface roughness of TFN membranes due to the PVDF substrate underneath, as per Wenzel's law. This states that the effect of increased surface

roughness is to amplify the intrinsic property of the material which, in this case, is hydrophobicity.
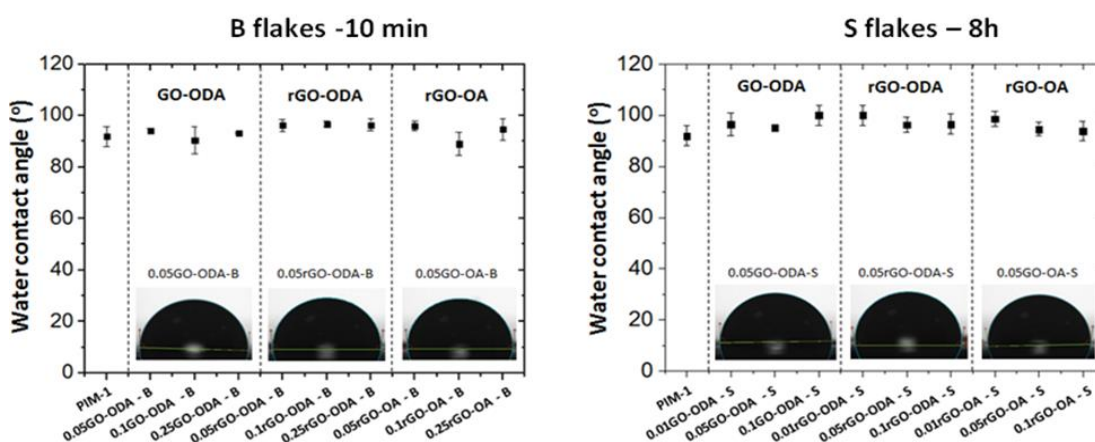
Figure 45: Water contact angle for PIM-1/graphene membranes containing micrometer- and nanometer-scale flakes, membranes (codes ending –B and –S, respectively). The average values resulted from at least three measurements on different locations of each membrane.

5.4.5. Pervaporation performance of TFN membranes

The TFN membranes were tested for *n*-BtOH removal from aqueous solutions via PV at 65 °C using a solution containing 5 wt% of *n*-BtOH as feed. The separation performance is evaluated using two parameters: (i) the total flux of feed solution permeating through the composite membrane, *J,* in units of kg m^{-2} h^{-1}, and (ii) the dimensionless separation factor *β*. *J* accounts for the production rate of the concentrated alcohol solution that is able to go through the membrane per unit area and unit time. *β* represents the weight ratio of alcohol to water in the permeate over the weight ratio in the feed, so higher values of *β* mean higher output of alcohol in the permeate and a more effective separation. Figure 46 depicts *J* and *β* when micrometer-sized graphene-like materials (probe sonicated for shorter times of 10 min) are used. The same parameters are plotted in Figure 47 for TFN membranes made with nanometer-sized graphene-like materials (probe sonicated for longer times of 8 h, and therefore smaller). In our previous study, the thickness-normalized total flux for freestanding PIM-1 membranes tested under the same conditions was ~ 70 μm kg m^{-2} h^{-1}.[260] Considering only the apparent thickness of the layers formed on top of the PVDF support (~ 1 μm), one would expected a flux of *ca.* 70 kg m^{-2} h^{-1} for the thin composite membranes prepared in this work. However, an average flux one order of magnitude smaller of 4.3 ± 1.0 kg

m^{-2} h^{-1} is obtained for pure PIM-1 TFC membranes, in good agreement with values reported for these type of membranes of about the same thickness.[47] This suggests that the coating solutions penetrate into the PVDF supports during the fabrication process, partially blocking the pore structure, and therefore increasing the overall effective thicknesses. On the other hand, the average separation factors reported for freestanding PIM-1 membrane (13.5)[260] and PIM-1 TFC membranes in this work (12.7) are very similar.

The incorporation of graphene nanosheets with lateral sizes in the micrometer-scale decreased the *n*-BtOH separation factor as compared to pure PIM-1 thin film membranes. Considering the thickness of the selective PIM-1-based layers in the TFN membranes and the size of the fillers, it is quite likely that some of them might span the entire thickness of the membrane. Moreover, the expected alignment of the polymer segments with the graphene flakes tends to become more difficult if big graphene flakes are used.[275] If non-selective voids at the polymer-filler interface are created, the performance of the membranes can be compromised. Generally when this happens the separation factor decreases and the flux through the membrane increases. This trend was observed for the majority of the membranes, although for a few of them whose content of filler was in the higher range the flux remained about the same. For the latter the presence of defects might have led to the observed decrease in the average separation factor; the impermeability of the graphene-like flakes (i.e. higher tortuosity) in conjunction with a higher flux through non-selective gaps being responsible for the unchanged flux. In our previous study on freestanding membranes, the incorporation of these materials with lateral sizes in the micrometer range led to an enhancement of separation factor to a great extent, reaching an average of 32.9 for a ~ 60 µm thick PIM-1 membrane containing 0.1 wt% rGO-OA.[260]

In contrast, when nanometer-sized flakes were incorporated into the polymer thin matrices, the overall performance of the membranes is suggested to be improved (Figure 47). Even though the error bars of the separation factors and total flux overlap, this assumption is based on their average values obtained. This may be attributed to a better polymer-filler interface, and therefore, fewer voids being

created.[275] Similarly to our results, Kudasheva *et al.* observed an enhancement in the performance of membranes of the polyimide Matrimid® incorporating smaller (0.53 µm) ordered mesoporous MCM-41 silica spheres, compared to larger (3.1 µm) particles, for water/EtOH separation.[35] They hypothesized this enhancement as an increase in area/volume ratio for smaller particles and a consequent better polymer-filler interface and dispersion. This explanation may also apply to the results in this work for the nanometer-sized fillers containing MMMs. Taking a further look at the available literature, Wang *et al.*[34] and Rodenas *et al.*[33] also reported enhanced membrane performance when smaller fillers were incorporated in polyimide matrices. Wang and co-workers justified the enhancement by a better compatibility of smaller silicalite-1 with the PDMS matrix.[34] On the other hand, Rodenas *et al.* observed a uniform distribution of CuBTC (BTC = 1,3,5-benzenetricarboxylate) nanosheets across the whole membrane, eliminating possible non-selective pathways, as compared to CuBTC crystals.[33] Nonetheless, higher filler loading compromised the overall membrane performance, possibly due to filler aggregation, as also seen by Kudasheva *et al.*[35] In this work the best average separation performance is obtained for the 0.05rGO-OA-S membrane (nanometer-sized fillers) with an average total flux and separation factor of 5.8 ± 0.6 kg m^{-2} h^{-1} and 17.0 ± 2.4, respectively. These higher values as compared to a pristine PIM-1 TFC membrane can be explained by an increase of the *n*-BtOH content in the permeate due to a higher affinity of the rGO-OA filler towards this solvent, thus hindering the water sorption.[260]

PERVAP® membranes were tested in order to obtain a benchmark value and compare the performance of the thin film nanocomposites fabricated in this study against commercially available films. PERVAP® membranes presented an average total flux and separation factor of 3.8 ± 0.9 kg m^{-2} h^{-1} and 16.4 ± 1.3, respectively. Consequently, the best membrane fabricated in this work (0.05rGO-OA-S) presents similar separation performance with a *ca.* 53% enhancement in yield.
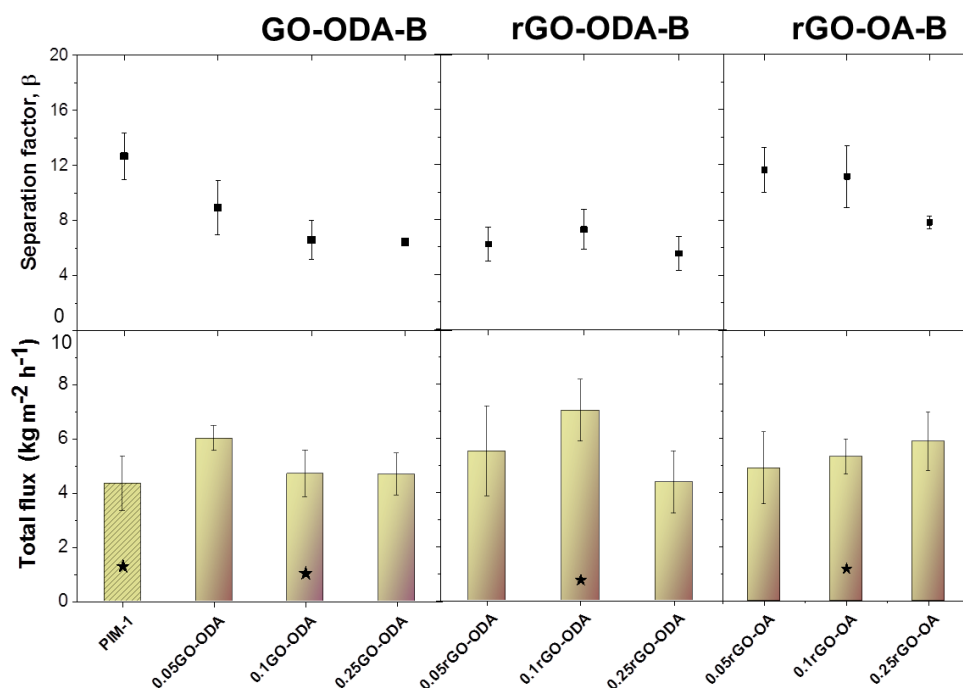
Figure 46: PV performance of TFN PIM-1/graphene-like membranes with graphene-like flakes of lateral size in the micrometer range (probe sonication time of 10min). Membranes were all tested at 65 °C using a feed composition 5 wt% *n*-BtOH/water, under a downstream pressure of 10 mbar. Separation factors for *n*-BtOH (β) are displayed in the top graphs, whereas the bars at the bottom represent values of total flux (*J*). Values of *J* and β for pure PIM-1 TFC membranes are also included in the graph (patterned bar and point above it). Stars indicate the value of flux obtained for freestanding membranes in our previous publication.[260]
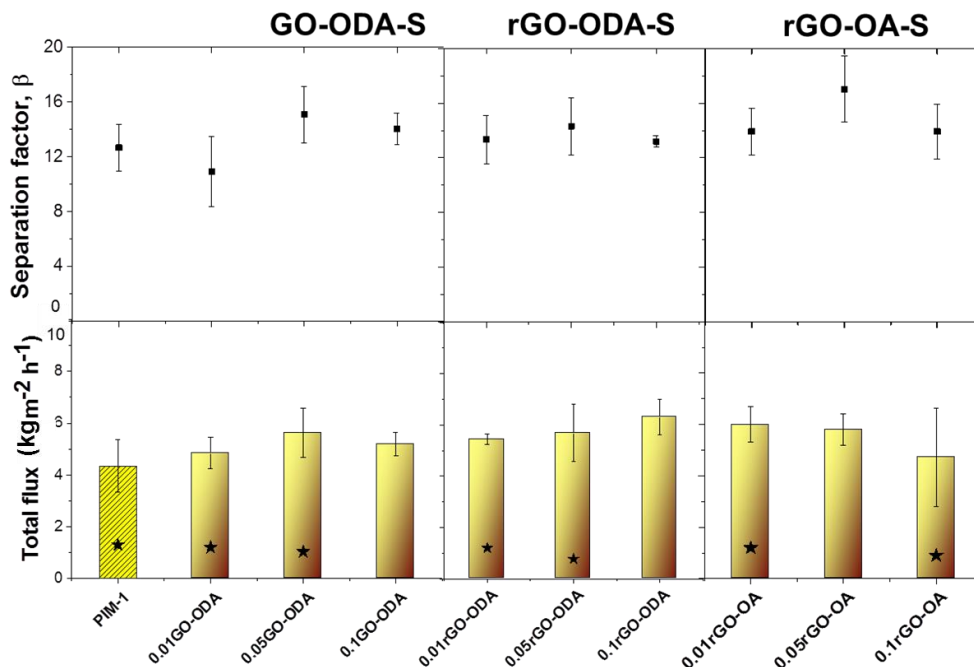
Figure 47: PV performance of TFN PIM-1/graphene-like membranes with graphene-like flakes of lateral size in the micrometer range (probe sonication time of 10min). Membranes were all tested at 65 °C using a feed composition 5 wt% *n*-BtOH/water, under a downstream pressure of 10 mbar. Separation factors for *n*-BtOH (β) are displayed in the top graphs, whereas the bars at the bottom represent values of total flux (*J*). Values of *J* and β for pure PIM-1 TFC membranes are also included in the graph (patterned bar and point above it). Stars indicate the value of flux obtained for freestanding membranes in our previous publication.[260]

5.4.6. Effect of the feed composition on the pervaporation performance

Membranes containing 0.05 wt% of the nanometer-scale fillers were chosen to study the effect of feed concentration and operating temperature on the overall membrane performance. Figure 48 shows the effect of feed composition on the PV performance of PIM-1, 0.05GO-ODA-S, 0.05rGO-ODA-S and 0.05rGO-OA-S TFN membranes at 65 °C. Aqueous solutions with n-BtOH concentrations in the range 2 - 5 wt.% were used. All membranes show an increase in both flux and separation factor with the increase in n-BtOH content in the feed. First of all, the organophilic nature of the membranes makes their interaction with n-BtOH favorable over water, as reported in our previous publication.[260] Furthermore, the membrane swelling degree increases with the n-BtOH content in the feed, adding free volume and leading consequently to the enhancement of the total flux as also observed in the work by Fouad $et\ al.$[97] In addition, the progressive increase of flux with the increase in n-BtOH feed content can be due to the enhancement of the driving force across the membrane.[28, 80] The increase in n-BtOH feed content also had a positive effect on the n-BtOH separation factor. Although both water and n-BtOH fluxes are enhanced with increasing n-BtOH feed content, the increase in separation factor is due to the increase in n-BtOH content in the permeate at a greater extent than water. However, the 0.05rGO-OA-S membrane shows different behavior; despite the increase in n-BtOH flux, the high separation factor of 17.0 ± 2.4 shown by this membrane at an n-BtOH feed concentration of 5 wt.% is due to the decrease in water flux.
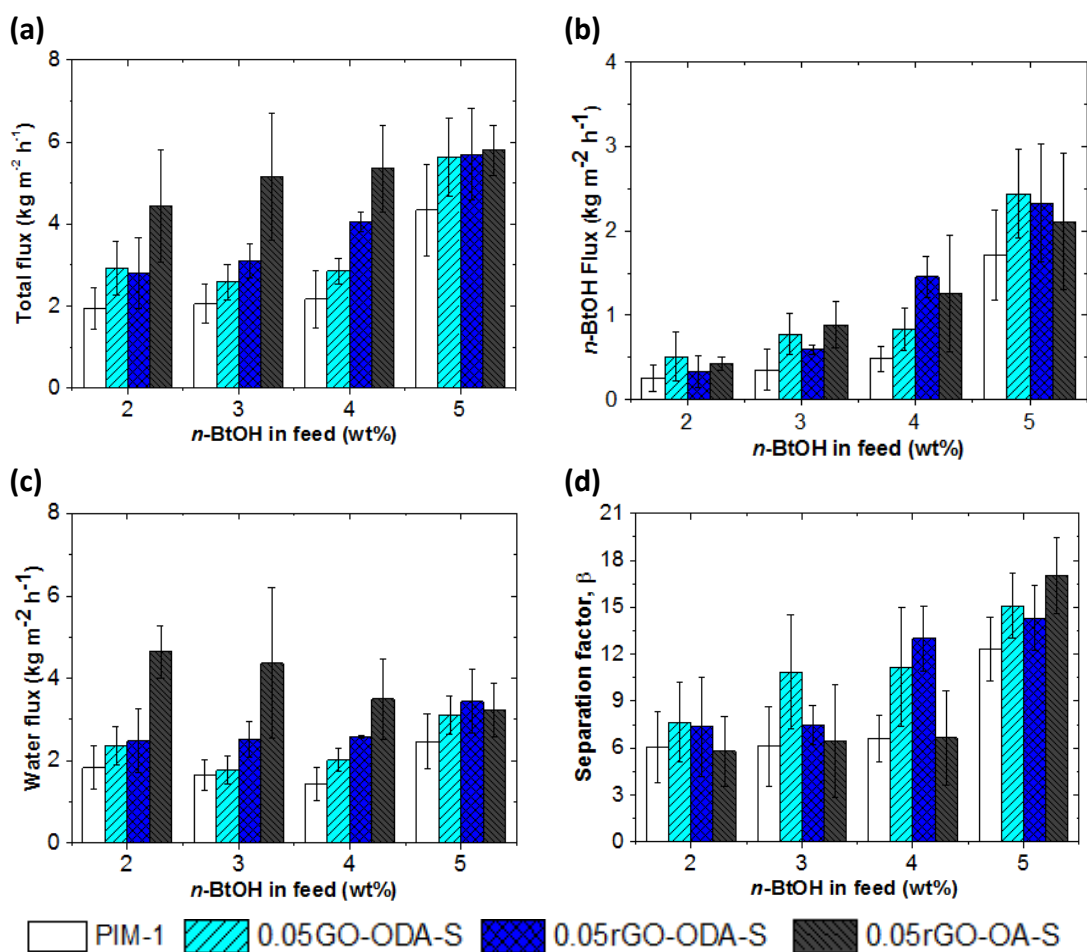
Figure 48: Effect of the feed composition on the (a) total, (b) *n*-BtOH and (c) water fluxes, and (d) separation factor of PIM-1, 0.05GO-ODA-S, 0.05rGO-ODA-S and 0.05rGO-OA-S TFN membranes. All membranes were tested at 65 °C.

5.4.7. Effect of the operating temperature on the pervaporation performance

The effect of temperature on the membrane performance was also investigated, as shown in Figure 49. Operating temperatures were in the range 35 - 65 °C and a 5 wt% *n*-BtOH aqueous solution was used as the feed. All membranes show an increase in total flux as well as partial water and *n*-BtOH fluxes when the operating temperature is increased. This can be explained by the fact that the increase in temperature leads to an increase in polymer chain mobility, enlarging the diffusive free volume of the membranes and consequently enhancing their flux.[80] Besides that, the increase in total flux can also be caused by an up to 4-fold increase in difference in vapor pressure which results in higher partial vapor pressure and, therefore, a greater driving force.[80] Moreover, the separation factor is also improved by elevating the operating temperature. Even though an increase of both

water and n-BtOH permeate fluxes is registered, the increase in separation factor is due to an even greater sorption and diffusion of n-BtOH over water at higher temperatures.[276] The temperature dependence of the permeate flux can be described through the Arrhenius equation (14), as follows:

$$J = J_0 \, exp\left(-\frac{E_a}{RT}\right) \tag{14}$$

where J, J_0, R, T and E_a are the permeation flux (kg m^{-2} h^{-1}), the pre-exponential factor, gas constant (8.314x10^{-3} kJ mol^{-1} K^{-1}), absolute feed temperature (K) and apparent activation energy (kJ mol^{-1}) of the specific compound, respectively. According to that, n-BtOH and water apparent activation energy can be determined by plotting the natural log of the permeation flux of one of the components versus the inverse of the temperature for different operating conditions (Figure 50). The slope for each curve is -E_a/R. The water and n-BtOH apparent activation energy values for PIM-1, 0.05GO-ODA, 0.05rGO-ODA and 0.05rGO-OA membranes are given in Table 13. The calculated apparent activation energies are always higher for n-BtOH, which indicates that the n-BtOH flux is more sensitive to the temperature variation.[28] Therefore, the average separation factor of all membranes increased with the increase in temperature. The 0.05rGO-OA-S membrane achieved the highest separation at 65 °C as it presents the lowest water activation energy among all.
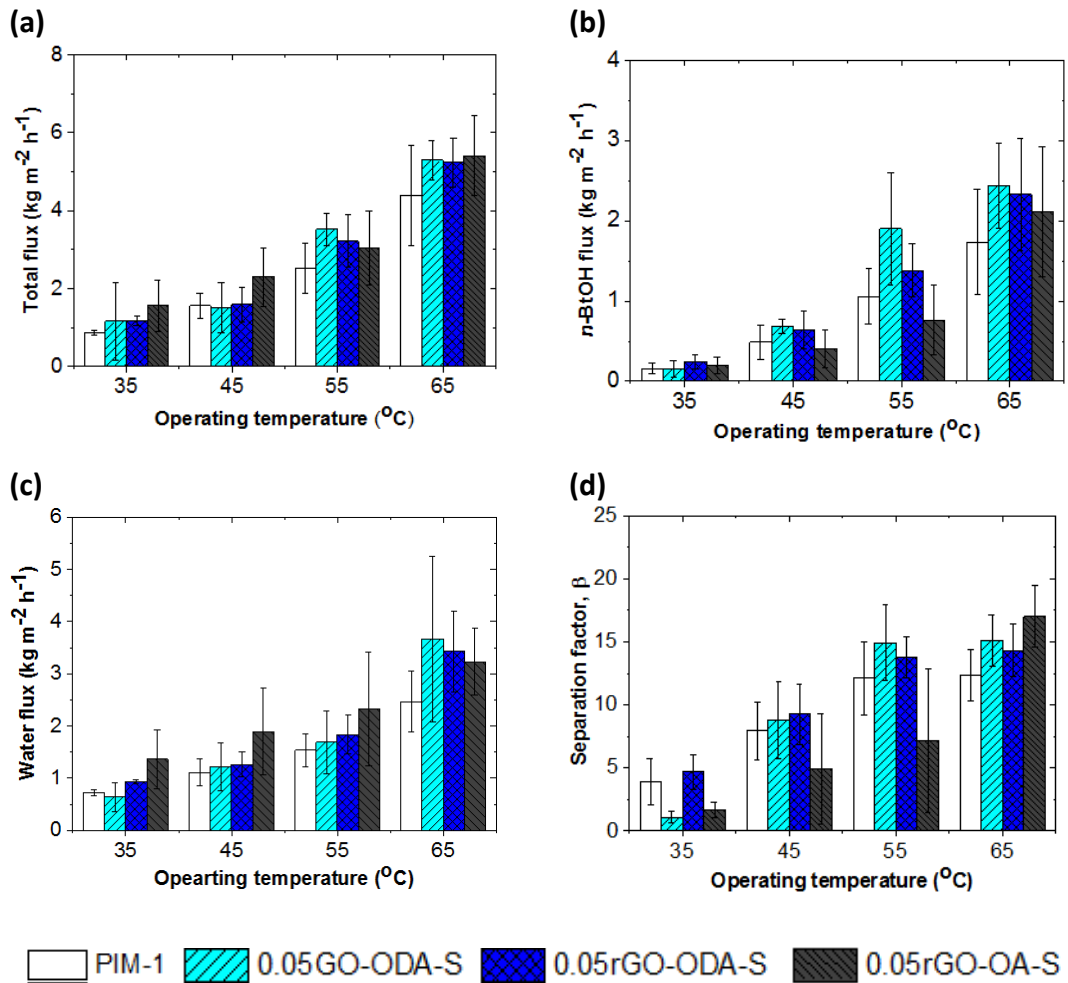
Figure 49: Effect of the operating temperature on the (a) total, (b) *n*-BtOH and (c) water fluxes, and (d) separation factor of PIM-1, 0.05GO-ODA-S, 0.05rGO-ODA-S and 0.05rGO-OA-S TFN membranes. Membranes were tested at 35, 45, 55 and 65 °C using a 5wt% *n*-BtOH aqueous solution as feed.
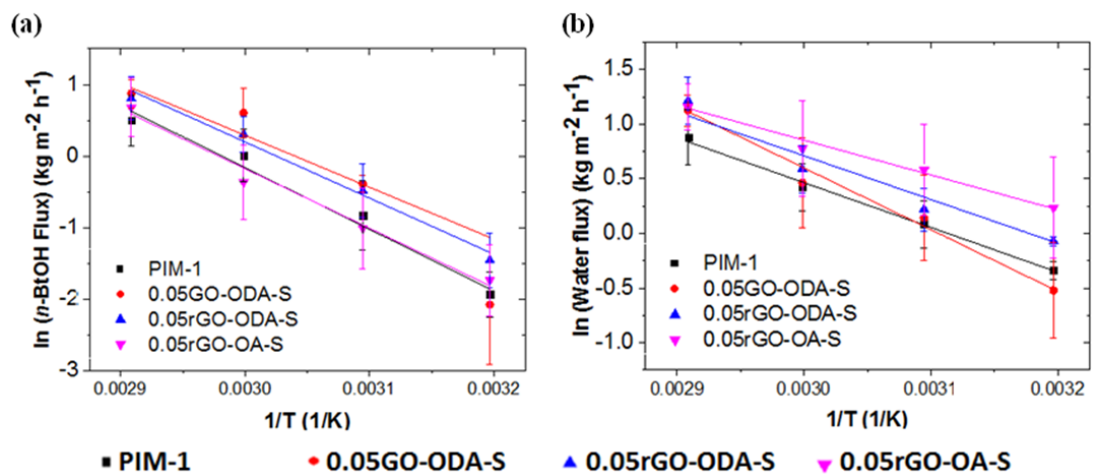
Figure 50: Arrhenius plots of *n*-BtOH (a) and water (b) permeation for PIM-1, and TFN membranes containing small-sized graphene oxide nanosheets: 0.05GO-OD-S, 0.05rGO-ODA-S and 0.05rGO-OA-S membranes. Membranes were tested at 35, 45, 55 and 65 °C using a 5wt% n-BtOH aqueous solution as the feed.

Table 13: Water and *n*-BtOH permeation activation energy values for PIM-1, 0.05GO-ODA, 0.05rGO-ODA and 0.05rGO-OA thin film membranes

Membranes	$E_{a, \text{water}}$ (kJ mol^{-1})	$E_{a, \text{n-BtOH}}$ (kJ mol^{-1})
PIM-1	34.5	70.6
0.05GO-ODA–S	45.5	85.9
0.05rGO-ODA–S	36.4	65.9
0.05rGO-OA–S	25.6	68.0

5.5.   Conclusions

In this study, thin film nanocomposite membranes of PIM-1 and functionalized graphene-like fillers were successfully fabricated for *n*-BtOH recovery from aqueous solutions. Micrometer- and nanometer- sized GO-ODA, rGO-ODA and rGO-OA flakes were used as fillers; in all cases the flux increased by at least 190% as compared to freestanding membranes of ~ 60 μm in thickness. The use of nanometer-sized flakes led to an enhancement in the separation performance, whereas the incorporation of micrometer-sized ones led to a reduced selectivity towards *n*-BtOH as compared to pure PIM-1 membranes. This suggests that the filler-polymer interface plays an important role in the overall PV performance; when micrometer-sized flakes are used, voids between the polymer and graphene are created, while the use of smaller flakes facilitate their alignment with the polymer segments, decreasing therefore the chance of creating large and non-selective voids at their interface. Despite that, the performance of TFN membranes with small flakes seems to be compromised when filler loadings are higher than 0.1 wt%, which can be explained by the effect of agglomeration as the content of filler increases. According to the results obtained, the best separation performance is achieved by a membrane containing 0.05 wt% octyl-functionalized GO of lateral size in the nanometer range. The separation factor reached by this membrane is 17.0 ± 2.4, which represents an. improvement of *ca.* 34% as compared to a pristine PIM-1 thin film composite membrane. In addition, the effects of feed composition and operating temperature were also studied and showed an increase in *n*-BtOH flux and separation factor with higher contents of *n*-BtOH in the feed and increased operating temperatures.

In summary, our work demonstrates that PIM-1 based TFN membranes containing alkyl-functionalized GO nanosheets are promising candidates for *n*-BtOH recovery from aqueous solutions with a *ca.* 53% enhancement in pervaporative flux as compared to commercial membranes.

Chapter 6 – Impeded physical aging in PIM-1 membranes containing graphene-like fillers

Monica Alberto[a], Rupesh Bhavsar[b], Jose Miguel Luque-Alled[a], Aravind Vijayaraghavan[c], Peter M. Budd[b], Patricia Gorgojo[a]

[a] School of Chemical Engineering and Analytical Science, The University of Manchester, United Kingdom

[b] School of Chemistry, The University of Manchester, United Kingdom

[c] School of Materials, The University of Manchester, United Kingdom

Keywords: CO_2 separation, gas separation; graphene; mixed matrix membranes; physical aging; polymer of intrinsic microporosity, PIM-1

6.1. Motivation

PIM-1 shows great potential use as a membrane material for CO_2 separation due to its high CO_2 permeability as compared to other gases. However, it suffers from physical aging which is one of the obstacles that prevents its use in commercial applications.

The main motivation behind this work was the combined molecular simulations and experimental study conducted by Gonciaruk *et al.* that suggested that the packing of PIM-1 chains might be affected by the presence of graphene, which might help to control the physical aging. [241] It is believed this improvement is caused by the alignment between graphene flakes and fragment of the PIM-1 chains, leading to a reduction of mobility of the polymer chains. Moreover, a good interface between PIM-1 and graphene is also expected. Regarding the experimental results, the presence of graphene seems not to have a significant effect on the membrane affinity towards CO_2 due to the similarity between the CO_2 adsorption isotherms of PIM-1 and PIM-1/graphene composite membranes. [241] The results presented in this chapter have been submitted to *Journal of Membrane Science*.

6.2. Highlights

- Physical aging of mixed matrix membranes (MMMs) composed of PIM-1 and graphene-like materials was investigated.

- A binary CO_2/CH_4 (50:50 vol.%) gas mixtures was used.

- Physical aging was reduced by the incorporation of reduced alkyl-functionalized graphene oxide nanosheets into PIM-1 matrices.

- Low filler loading led to higher reduction in physical aging.

6.3. Abstract

Physical aging of polymer of intrinsic microporosity PIM-1 is one of the major obstacles for its application as a commercial membrane material for gas separation. In this work, physical aging of PIM-1 and matrices of this same polymer containing graphene-like materials were studied. Graphene-like fillers resulted from the functionalization of graphene oxide (GO) with two alkyl chains of different lengths, using octylamine (OA) and octadecylamine (ODA), and further chemical reduction. Extents of membrane aging were evaluated through changes in gas permeability over time; the separation of gas mixtures comprising carbon dioxide and methane, which are of great interest for industrial applications such as the production of biogas or the purification of natural gas, was carried out. 50:50 vol. % CO_2/CH_4 mixtures were used as feed and separation performance analysed for fresh membranes and at intervals of approximately a month up to 155 days. At the end of this testing period, aged PIM-1 membranes showed a CO_2 permeability of $(2.0\pm 0.7) \times 10^3$ Barrer, which corresponds to a CO_2 permeability reduction of 68 % from the value obtained right after their fabrication. The addition of alkyl-functionalized GO is shown to be an efficient strategy to retard the physical aging of PIM-1 membranes; filler loadings as low as 0.05 wt.% of reduced octyl-functionalized GO showed a CO_2 permeability of $(3.5 \pm 0.6) \times 10^3$ Barrer after 5 months, which is almost three quarters higher than that of pure PIM-1 membrane aged for the same time period and represents a reduction of just 39% from its initial value. Moreover, the addition of graphene-like materials to PIM-1 does not affect its mechanical properties.

6.4. Graphical abstract

Figure 51 shows the graphical abstract that summarizes the main findings in this work.
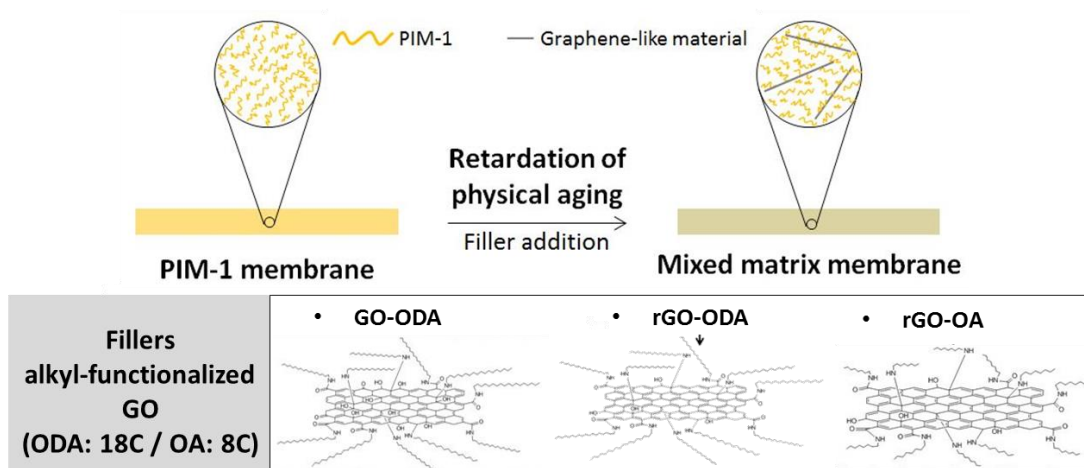
Figure 51: Graphical abstract.

6.5. Introduction

In recent years capture of carbon dioxide (CO_2) has been a subject of intense research due to its potential contribution in the prevention of global climate change. CO_2 is inevitably emitted into the atmosphere from naturally-occurring processes such as decomposition, ocean release, respiration or the degassing of magma in volcanic areas. However, human activities, including the burning of fossil fuels, deforestation and the livestock sector, are responsible for almost all the increase in CO_2 emissions over the past few decades. A recent report released by the World Meteorological Organization identified the atmospheric CO_2 concentration as the highest in 800,000 years and it is expected to rise in the coming decades [100].

In the light of these discouraging predictions and the fact that fossil fuels are finite energy sources, an increase in the use of renewable energy resources must be a global priority. Biogas is an alternative to fossil fuels. It is produced from anaerobic digestion of organic wastes and agricultural by-products and reduces CO_2 emissions by completing the carbon cycle. It is mainly composed of methane (CH_4) and CO_2 with small amounts of hydrogen sulphide, and as in natural gas the presence of CO_2

and other acid gases reduces its calorific value and causes pipeline corrosion, which makes its handling, transport and storage difficult and expensive [102, 103].

The development of economic and effective techniques to separate CO_2 from other gases such as CH_4 has attracted great interest over the past few years. Cryogenic separation and amine scrubbing technologies are conventional operations for such purpose. However, these methods are characterized by their high energy requirements, complex equipment and operation and high capital investment [102, 104]. Other techniques, including membrane-based separations are seen as potential alternatives which feature low energy demand, little maintenance cost, and ease of operation and scale-up [102].

Among all materials currently available for the fabrication of CO_2-selective membranes, polymers of intrinsic microporosity (PIMs) have received great attention since the publication of the first PIM-based membrane [3]. PIM-1 is by far the most investigated PIM since it is soluble in certain common organic solvents such as chloroform and tetrahydrofuran, which allows the fabrication of membranes through conventional solution-processing techniques [44, 47, 54]. In addition, it features high free volume as a result of frustrated packing of polymer chains due to spiro-sites of contortion in the rigid ladder polymer chain that give rise to a randomly contorted structure [17, 39, 40]. Due to its high free volume PIM-1 is highly CO_2 permeable, and it is CO_2-selective and shows good chemical, mechanical and thermal stability [39].

Despite being a promising polymer for gas separation applications, PIM-1 presents pronounced physical aging in addition to the well-known trade-off between membrane permeability and selectivity common to all polymeric membranes, therefore hindering its commercialization [142]. Physical aging occurs in non-equilibrium glassy polymers and leads to the loss of free volume and consequent decline in permeability with time due to the segmental rearrangements approaching an equilibrium state [139, 140]. This phenomenon is less pronounced over time as the excess free volume within the membranes, which is the driving force for physical aging, gradually decreases [139]. Because of the intense loss in

membrane performance over time, long-term stability represents a major challenge in the application of glassy polymer membranes in successful commercial gas separation technologies[148].

Studies have shown that physical aging is dependent on the film thickness, [148, 150, 234, 277], temperature [149], storage conditions (e.g. temperature, atmosphere and pressure) [150] and membrane treatment [39, 48, 49, 151, 152]. In addition, the experimental testing methodology (i.e. continuous or momentary) can also lead to different results [153]. Several strategies have been developed, aiming at the retardation of the physical aging of polymeric membranes including UV-treatment [144] UV photo-oxidation [145], surface modification [146], cross-linking [145, 147] and the addition of fillers to obtain a hybrid membranes, typically referred to as mixed matrix membranes (MMMs) [49, 141-143].

Graphene has been applied with great success in numerous fields, including membrane-based separation processes [260]. CO_2 sorption of PIM-1/graphene membranes was studied previously by Gonciaruk *et. al.* [241]; no significant change in CO_2 sorption was found in this work, however it has been previously reported that graphene can disrupt the polymer chains and therefore, enhance the membrane permeability without affecting its selectivity [195]. In addition, it is suggested there is an alignment between the PIM-1 polymer segments and graphene flakes which may also prevent the mobility of the polymer chains and therefore the physical aging of the membrane.

Driven by this hypothesis, in this paper the physical aging of PIM-1/graphene MMMs was investigated. Pure PIM-1 membranes and MMMs containing graphene-like materials were prepared and their gas separation performance for CO_2/CH_4 mixtures monitored over 155 days. Fillers included graphene oxide (GO) functionalized with two types of alkyl chains of different lengths, using octylamine (OA) and octadecylamine (ODA), and further chemical reduction. These graphene-based fillers were used due to their good dispersion and stability in chloroform as shown in our previous study [31]. The mechanical stability of the hybrid membranes was also investigated.

6.6. Experimental

6.6.1. Materials

Chloroform, ethanol (EtOH) and methanol were purchased from Sigma Aldrich (UK). Research grade CO_2 and CH_4 were used.

4.8.1. Synthesis of PIM-1

The synthesis of PIM-1 is described in section 3.2. PIM-1 from Batch 2 was used in this study.

4.8.2. Synthesis of graphene-like materials

The synthesis of graphene-like materials used in this work is described in section 3.3 and includes alkyl-functionalized graphene oxide with octadecylamine (GO-ODA), alkyl-functionalized reduced graphene oxide with octadecylamine (rGO-ODA), and alkyl-functionalized reduced graphene oxide with Octylamine (rGO-OA).

6.6.2. Membrane preparation

The alkyl-functionalized GO materials were dispersed in chloroform by means of a probe sonicator (Cole-Parmer, 750 W, 20 kHz, amplitude 22% - Cole-Parmer Instrument, USA) for 10 min in discontinuous mode (pulse on for 9 s and pulse off for 9 s). These dispersions were then added to a PIM-1 solution (4 wt.% of polymer) in chloroform and were magnetically stirred for 1 h before casting. Different loadings of rGO-OA, rGO-ODA and GO-ODA (0.01 wt.%, 0.05 wt.%, 0.1 wt.% and 0.25 wt.% with regards to the mass of the polymer) were used in the membrane preparation as indicated in Table 14.

Casting solutions were poured into glass petri dishes, covered with their lids and were left in an in-house made cabinet under continuous flow of nitrogen for 3 days. After that, membranes were soaked in methanol for 1day and then put in the oven overnight at 80 °C in order to remove any trapped residual solvents.

Table 14: Fabricated membranes with theoretical and experimental (obtained through UV analysis of redissolved membranes) filler loadings, and thickness after methanol treatment and vacuum.

Membrane code	Filler	wt.% of filler Theoretical values	wt.% of filler Experimental values	Membrane thickness (µm)
PIM-1	-	-	-	40 ± 10
0.01GO-ODA	GO-ODA	0.01	0.030 ± 0.015	52 ± 3
0.05GO-ODA		0.05	0.067 ± 0.004	45 ± 9
0.1GO-ODA		0.1	0.140 ± 0.050	52 ± 2
0.25GO-ODA		0.25	0.220 ± 0.080	51 ± 7
0.01rGO-ODA	rGO-ODA	0.01	0.009 ± 0.001	41 ± 4
0.05rGO-ODA		0.05	0.052 ± 0.004	43 ± 9
0.1rGO-ODA		0.1	0.110 ± 0.0075	36 ± 6
0.25rGO-ODA		0.25	0.366 ± 0.086	42 ± 11
0.01rGO-OA	rGO-OA	0.01	0.034 ± 0.002	46 ± 2
0.05rGO-OA		0.05	0.126 ± 0.027	53 ± 4
0.1rGO-OA		0.1	0.184 ± 0.010	48 ± 10
0.25rGO-OA		0.25	0.408 ± 0.023	62 ± 5

6.6.3. Characterization of the fillers and membranes

The loadings of graphene-based materials into the polymer matrices were examined through ultraviolet visible (UV-Vis) spectroscopy (Genesys 10 S UV–Vis spectrophotometer, Thermo Scientific, United Kingdom). Membranes were cut into small pieces and re-dissolved in chloroform and the absorbance of such solutions was registered at a wavelength of 660 nm. The concentration was determined using the Beer-Lambert law; the extinction coefficients used for GO-ODA, rGO-ODA, and rGO-OA were 4.939, 15.256, and 7.556 mL mg^{-1} cm^{-1} (Appendix A, Figure A1), respectively [260].

Membrane morphology was studied by scanning electron microscopy (SEM) with a FEG Quanta 250 FEG instrument (FEI, USA) at 15 kV. All samples were prepared by immersing them firstly in EtOH for 30 s and then transferring them into liquid nitrogen for another 30 s, before being snapped. Platinum (Pt) sputter coating (MTM 10 Thickness Monitor (Cressington, USA)) was applied onto all samples before imaging. The thickness of the membranes was measured using a digital micrometer screw gauge (Mitutoyo IP65 Coolant Proof, UK) with an accuracy of ±0.5 µm and verified under SEM. The membrane thickness resulted from the average of at least 5 points on each membrane.

Mechanical properties of membranes were determined by performing uniaxial tensile tests utilizing an Instron 5542 tensiometer (Instron, USA), equipped with Bluehill 3 software and a 10 N loading cell. The initial gauge length and width were 15 mm and 3 mm, respectively. A contact elongation rate of 1 mm min^{-1} was set. Tensile tests were performed at ambient temperature. Samples were cut with scissors, and five different samples for each type of membrane were tested under the same conditions in order to ensure reproducibility. Membranes were approximately 2 months old when tested. Elongation at break, ultimate tensile strength (UTS) and young's modulus were calculated from the stress-strain curve obtained. Elongation at break, $\varepsilon_{\text{breakage}}$, refers to the ratio between the change in length and the initial length of the specimen at breakage and is calculated with equation ((15) as follows:

$$\varepsilon_{\text{breakage}} = \frac{l_{\varepsilon_{\text{breakage}}} - l_0}{l_0} \times 100\% \tag{15}$$

Where l_0 and $l_{\varepsilon_{\text{breakage}}}$ are the initial and length and breakage lengths, respectively. UTS is defined as the maximum stress withstood by the material. Finally, the Young's modulus measures the stiffness of the material and is defined as the gradient between the stress applied to the strain in the elastic region of the deformation.

Gas permeation measurements were done at 25 $^\circ$C using a CO_2/CH_4 binary gas mixture in a volume ratio of 50:50 vol.% as feed (flowrate of 25 mL min^{-1} for each gas). A schematic diagram of the apparatus used for the gas permeation measurements is shown in Figure 52; a pressurized binary mixture (at approximately 3 bar) was applied to the upstream side of the membrane cell, and sweep gas He at a flowrate of 25 mL min^{-1} was passed on the downstream side of the membrane at atmospheric pressure. The composition of permeate was analysed using a 490 micro gas chromatography system (Agilent, USA). Gas permeability was recorded once steady-state was reached. Membranes were tested fresh right after their preparation and methanol treatment (day 0) and at days 35,

63, 92, 128 and 155 using the same gas composition, temperature and transmembrane pressures.
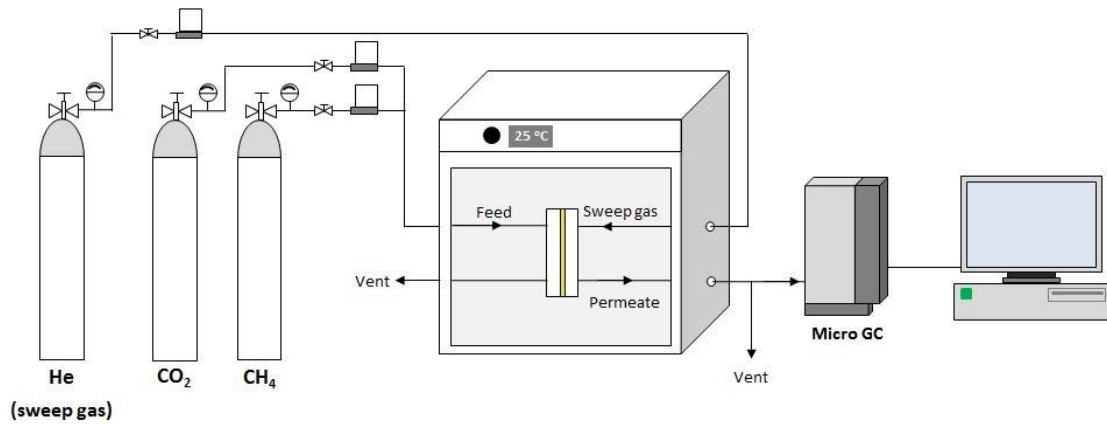
Figure 52: Schematic diagram of the setup used for gas permeation measurements.

Due to the nature of the experimental work, where the same membrane had to be tested several times and stored in between gas separation experiments, fabricated MMMs were mounted on aluminium discs using epoxy resin to seal. The effective areas of the membranes were in the range 0.09 - 0.56 cm^2.

The gas permeability was calculated using equation ((16):

$$P = \frac{Q\,l}{A\,\Delta p} \tag{16}$$

Where P is the permeability in Barrer (1 Barrer = 10^{-10} cm^3[STP] cm cm^{-2} s^{-1} cmHg^{-1}), Q is the permeate gas flow rate (cm^3(STP) s^{-1}), l is the membrane thickness (cm), A is the effective membrane area (cm^2) and Δp is the pressure difference across the membrane (cmHg). In SI units 1 Barrer is equal to 3.34×10^{-16} mol m m^{-2} s^{-1} Pa^{-1}. The selectivity for the gas pair A and B ($\alpha_{A/B}$) is given by the equation (17):

$$\alpha_{A/B} = \frac{P_A}{P_B} \tag{17}$$

Where P_A and P_B are the permeability coefficients for gases A and B, respectively.

6.7. Results and discussion

The filler loading for each cast membrane was analysed through UV-Vis, as shown in Table 14. The experimental filler loadings (i.e. real concentrations in the dried membranes) were within the same order of magnitude of those calculated for the preparation of casting solutions, with 2-3 fold differences in some cases possibly due to solvent evaporation during UV sample preparation and analysis.

SEM images of cross sections and surfaces of the membranes are shown in Figure 53b and Figure B1a-f (Appendix B) also reveal continuous films in which agglomerates are not observed. The incorporation of fillers might affect the morphology of polymeric membranes; however MMMs in this work preserve the typical dense structure of pure PIM-1, possibly as a result of the very low concentrations, with fillers not exceeding 0.25 wt.% [260]. Similarly to pure PIM-1 membranes, MMMs show a smooth surface; however, some nanoholes with an average diameter of 0.37 μm are observed and are indicated with arrows on the micrographs in Figure 53 and Figure B1 (appendix B). These nanoholes are likely formed due to evaporation of chloroform during membrane formation and are only observed on the very surface; it is evident from the cross-section SEM images that the holes do not span the entire thickness, hence membrane performance should not be undermined. However, their presence should be evaluated more extensively in thin film composite membranes where selective PIM-1 layers are reduced to a few micrometers or even few tens or hundreds of nanometres.
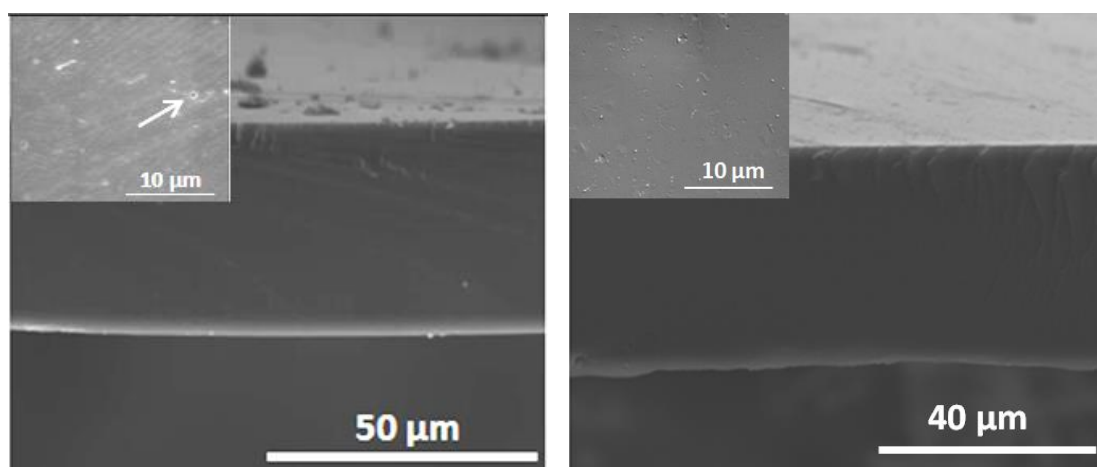
Figure 53: Cross section and surface (insets) SEM images of (a) PIM-1 and (b) 0.1GO-ODA membranes. Arrows indicates superficial holes on the membranes.

Uniaxial tensile tests were performed on all the membranes in order to investigate their mechanical properties by assessing the Young's modulus (MPa), UTS (MPa) and elongation at break (%). Obtained values for pristine PIM-1 and MMMs are shown in Table 15. Pure PIM-1 membranes have a Young's modulus of 1.00 ± 0.21 GPa, a UTS of 41.7 ± 7.1 MPa and an elongation at break of 7.0 ± 1.7 %, which are in good agreement with values for pure PIM-1 freestanding membranes found in the literature [113, 239].

Furthermore, MMMs prepared in this work present similar mechanical properties than bare PIM-1 membranes, as seen in Table 15. Some improvements can be inferred from the obtained data, but caution has to be taken given the spread in the values. This might be due to the variability in the materials properties such as the random orientation flakes within the polymer matrix. Figure B2 (Appendix B) contains stress-strain curves obtained for PIM-1, 0.05GO-ODA, 0.05rGO-ODA and 0.05rGO-OA. The maximum increase in Young's modulus of 35% was achieved by a membrane containing 0.1 wt.% rGO-ODA. As an example, the membrane with code 0.1GO-ODA (0.1 wt.% octadecyl-functioinalized GO) presented an average UTS of 46.2 ± 3.3 MPa, which represents an increase of approximately 7% over pristine PIM-1 membranes. The enhancement in the mechanical properties observed for some of the MMMs can be attributed to the good dispersion and compatibility between the fillers and the PIM-1 polymer matrix. This consequently leads to a successful load-transfer between the continuous and the dispersed phases of the membranes [278-280]. In addition, the increase in elongation at break at lower alkyl-functionalized GO loading might be due to the intrinsic mechanical properties of graphene [163]. Further increase of concentrations in the PIM-1 polymer matrix (0.25 wt.%) suggests a decline of the mechanical properties of the membranes. As seen in previous studies, this phenomenon can be attributed to filler agglomeration, and consequent reduction of effective interaction between the filler and the polymer matrix, leading to an inefficient stress transfer from matrix to filler [280-282].

Table 15: Summary of the mechanical properties of pristine PIM-1 and MMMs.

Membrane	Young's Modulus (GPa)	Ultimate tensile strength (MPa)	Elongation at break (%)
PIM-1	1.01 ± 0.21	41.7 ± 7.1	7.0 ± 1.7
0.01GO-ODA	1.02 ± 0.13	40.7 ± 6.2	10.8 ± 6.5
0.05GO-ODA	1.09 ± 0.10	44.2 ± 4.6	10.1 ± 4.1
0.1GO-ODA	1.20 ± 0.28	46.2 ± 3.3	7.4 ± 2.9
0.25GO-ODA	0.93 ± 0.30	40.2 ± 8.3	6.6 ± 1.5
0.01rGO-ODA	1.14 ± 0.08	40.2 ± 2.6	6.9 ± 1.9
0.05rGO-ODA	1.01 ± 0.13	43.5 ± 3.2	10.1 ± 2.8
0.1rGO-ODA	1.36 ± 0.46	38.4 ± 6.6	6.7 ± 3.1
0.25rGO-ODA	1.19 ± 0.28	44.4 ± 4.6	7.7 ± 1.7
0.01rGO-OA	1.08 ± 0.01	44.0 ± 7.1	7.8 ± 3.9
0.05rGO-OA	0.96 ± 0.03	45.2 ± 2.0	7.3 ± 1.3
0.1rGO-OA	1.05 ± 0.12	44.4 ± 5.1	9.5 ± 2.2
0.25rGO-OA	1.05 ± 0.17	39.6 ± 6.7	6.4 ± 2.6

Gas permeation measurements were carried out to evaluate the physical aging in pristine PIM-1 membranes and MMMs up to 155 days with permeability data for days 0 (fresh membranes right after preparation and methanol treatment), 35, 63, 92, 128 and 155. Binary CO_2/CH_4 gas mixtures at 25 °C with a transmembrane pressure of 2 bar were used. Figure 54 shows the CO_2 and CH_4 permeabilities for membranes containing different fillers in the polymer matrix. Tables B1, B2 and B3 in Appendix B show CO_2 and CH_4 permeability values and CO_2/CH_4 selectivities for all the membranes represented in Figure 54. Values of percentage permeability reduction for CO2 and CH4 for all membranes from day 35 are shown in Tables B4 and B5 (Appendix B).

Prepared freestanding pure PIM-1 membranes showed initial (day 0) CO_2 and CH_4 permeabilities and selectivity of $(6.4 ± 1.3) × 10^3$ and $(3.3 ± 1.3) × 10^2$ Barrer and 20.3 ± 3.5, respectively. These values are in good agreement with others found in the literature for PIM-1 [39, 49, 141]. Compared with values for MMMs also at day 0, it is observed that the addition of graphene-like nanosheets into the PIM-1 polymer matrix leads to a decrease in permeability which, in general, is more evident as the filler concentration increases; the presence of such non-porous fillers increases the tortuosity so that gas molecules have to diffuse across longer distances in the membrane. This behaviour does not support the results previously reported on PIM-1 MMMs containing few-layer graphene [195], where more than a

two-fold increase in CO2 permeability was achieved with a graphene loading of ~ 0.001 wt.% (0.05 vol.%) as a consequence of the disruption of polymer chains. This discrepancy can be due to differences in the nature of the fillers as well as in membrane preparation and testing.

As expected, CO_2 and CH_4 permeabilities of freestanding pure PIM-1 and MMMs decreased progressively over the period tested. The CO_2 permeability of pristine polymeric membranes dropped approximately by half after a 2-month period (from $(6.4 \pm 1.3) \times 10^3$ down to $(3.5 \pm 1.1) \times 10^3$ Barrer), and gradually decreased after that down to $(2.0 \pm 0.7) \times 10^3$ Barrer (value obtained at day 155). Similar behaviour of PIM-1 membranes is reported in the literature [39, 49]. MMMs also aged with time and gas permeabilities decreased for such membranes; however, the reduction after 155 days was in all cases lower than that of PIM-1 without fillers (i.e. lower than 68 %), which suggests retardation of the physical aging due to the incorporation of alkyl-functionalized GO nanosheets into the polymer matrices. After 155 days, CO_2 permeability values for 0.05GO-ODA, 0.05rGO-ODA and 0.05rGO-OA were $(3.0 \pm 0.2) \times 10^3$, $(2.4 \pm 0.6) \times 10^3$ and $(3.5 \pm 0.6) \times 10^3$ Barrer, respectively, which correspond to a lower reduction of 46, 49 and 39 %. That is, the CO_2 permeability of the aged 0.05rGO-OA was approximately 73% higher than that of pure PIM-1 membrane aged for 155 days.

This behaviour confirms the results presented by Gonciaruk *et al*. [241], in which the potential reduction of physical aging was attributed to the constriction of polymer chain motion due to alignment of graphene sheets and polymer segments [241]. According to our results, all MMMs still suffer from aging to some extent; however, their CO_2 permeability reduction is always lower than that of pristine PIM-1 membranes. Plots with the fraction of initial permeability as a function of time for PIM-1 and MMMs containing GO-ODA, rGO-ODA and rGO-OA are shown in Figures B3, B4 and B5 in Appendix B, respectively. Exceptionally, membranes 0.25GO-ODA and 0.25rGO-ODA, both presented a reduction in CO_2 permeability of 62 %, which is very close to that of PIM-1 without fillers after the same period of 155 days. As anticipated, the initial CO_2 permeabilities for these membrane $((4.5 \pm 1.0) \times 10^3$ and $(5.5 \pm 1.1) \times 10^3$ Barrer) was lower than the permeability of a pure PIM-1 membrane

$(6.4 \pm 1.3) \times 10^3$ Barrer) due to the increased tortuosity of the hybrid material. However, the drop in permeability after 92 days of aging is as pronounced as that of pure PIM-1 for the MMM containing 0.25 wt.% of filler GO-ODA (Figure B3, Appendix B), or even more pronounced for the MMM containing 0.25 wt.% of rGO-ODA (Figure B4, Appendix B). The latter presents a fraction of initial CO_2 permeability below that for pure PIM-1 even after 35 days of aging. This behaviour at higher loadings of functionalised GO fillers suggests higher disruption of the polymer chains at the polymer-graphene interface, which can lead to the formation of voids or higher free volume surrounding the nanosheets. This is thus more noticeable as the concentration of filler in the polymer matrix increases, adding extra volume that can be lost over time.

The permeability of CH_4 also decreased over time following a similar trend to CO_2. After 155 days, the permeability of CH_4 decreased by 79 %, 61 %, 65 % and 60 % in PIM-1, 0.05GO-ODA, 0.05rGO-ODA and 0.05rGO-OA membranes, respectively. The higher reduction in permeability of CH_4 for PIM-1 membranes and MMMs was anticipated as diffusion of bigger gas molecules are affected to a greater extent by the reduction of free volume.

Regarding the CO_2/CH_4 selectivity for all the tested membranes, values increased as membranes aged with time. Figure 55 shows the changes in CO_2/CH_4 selectivity up to 155 days. Pristine PIM-1 membranes initially showed the highest CO_2/CH_4 selectivity when compared to MMMs, possibly due to non-selective voids at the polymer-graphene interface that might be created during membrane formation. After 5 months of aging, pristine PIM-1 membranes presented a CO_2/CH_4 selectivity of 30.0 ± 4.7, and 0.05GO-ODA, 0.05rGO-ODA and 0.05rGO-OA membranes had a CO_2/CH_4 selectivity of, 23.7 ± 1.6, 29.1 ± 3.2 and 22.9 ± 1.1, respectively. After the same test period of 155 days, MMMs presented higher CO_2 permeabilities ($(2.0 \pm 0.7) \times 10^3$ Barrer for pure PIM-1 vs $(3.0 \pm 0.2) \times 10^3$, $(2.4 \pm 0.6) \times 10^3$ and $(3.5 \pm 0.6) \times 10^3$ Barrer for 0.05GO-ODA, 0.05rGO-ODA and 0.05rGO-OA membranes, respectively).This can also explained the lower CO_2/CH_4 selectivity presented by the MMMs; the higher the permeability of CO_2, the greater the tendency of PIM-1 to be

plasticized, swelling the polymer matrix and thus resulting in increased CH_4 permeability [113].

Robeson's diagrams, log-log plots of selectivity versus permeability of the more permeable gas for binary gas mixtures, are commonly used for evaluating the performance of membranes for gas separation processes. Robeson introduced in 1991 the concept of an "upper bound" relation [114] to represent the performance trade-off of polymeric membranes. The upper bound for different gas mixtures was revisited by Robeson in 2008, as new type of membrane materials including PIM-1 started to emerge, and the limits were pushed forward [115]. According to the results obtained in this work, all membranes' performance lay above the 2008 Robeson upper bound and move parallel to it over time in the direction of lower permeability and higher selectivity, as seen in Figure 56. This behaviour is also reported by Williams *et.al.* [283], and suggests that the molecular transport is governed by the polymer matrix. Moreover, the performance of all aged MMMs lay on the right hand side of the aged PIM-1 membrane on the line parallel to the upper bound, despite having lower CO2 permeability than pristine PIM-1 when fresh (tested at day 0). Thus, suggesting that the incorporation of graphene-based fillers into PIM-1 lowers the rate of physical aging. It is worth mentioning that one possible explanation for having the pure PIM-1 membrane in this work above the 2008 upper bound might be the use of mixed gas feed; early PIM-1 data, which helped to define the 2008 upper bound, were based on single gas measurements (i.e. ideal gas selectivity values). In addition, the selectivity depends on the operating conditions such as temperature and pressure, and these are rarely the same between studies.
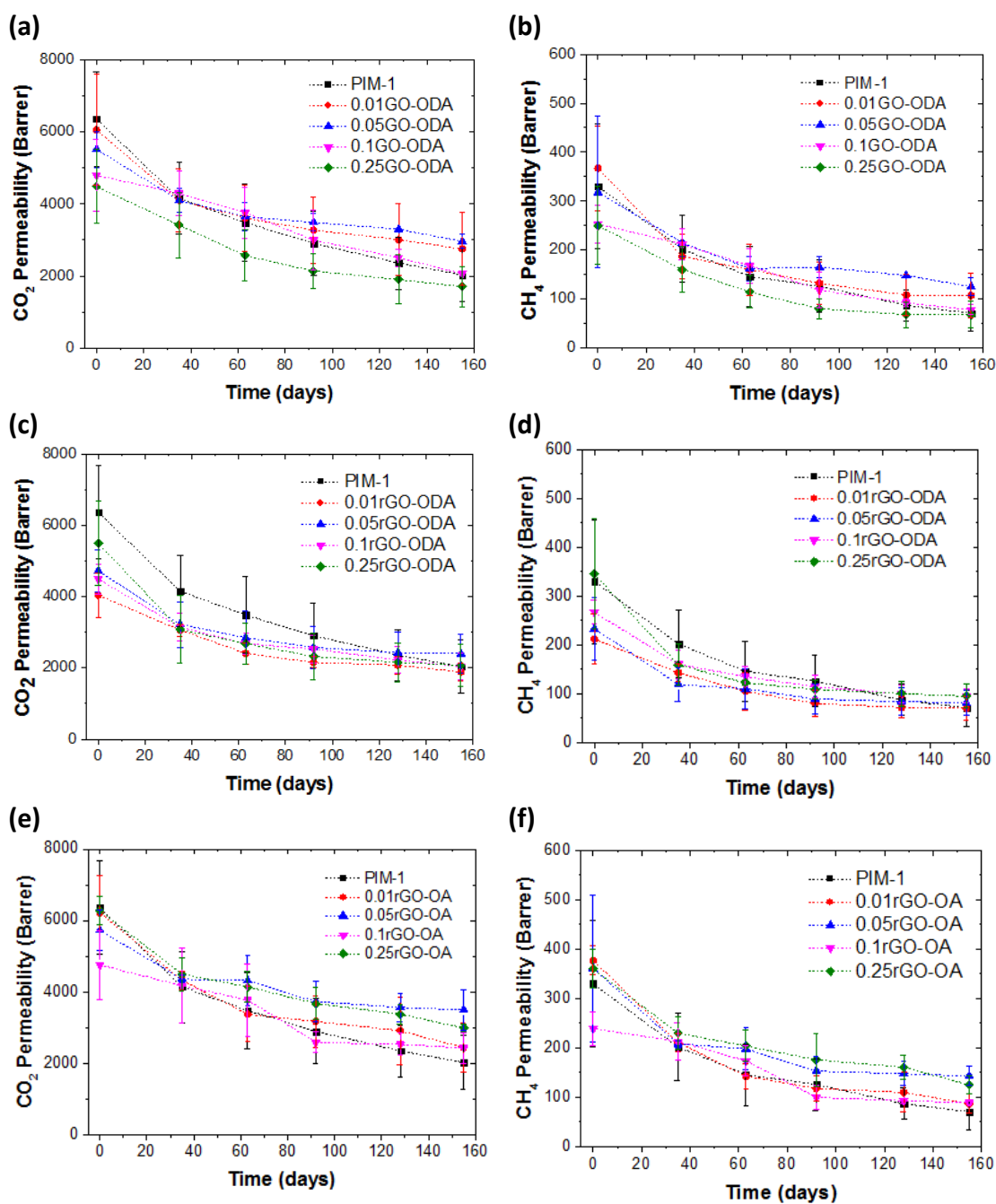
Figure 54: CO₂ and CH₄ permeabilities of PIM-1 and MMMs with (a) (b) GO-ODA, (c) (d) rGO-ODA and (e) (f) rGO-OA incorporated into the polymer matrix. A 50:50 vol.% CO₂ and CH₄ gas mixture was used as feed. Membranes were tested at 25 °C, under a transmembrane pressure 2 bar. At least two membranes of each type were tested. The error bars correspond to the standard deviation.

(a)

(b)

(c)
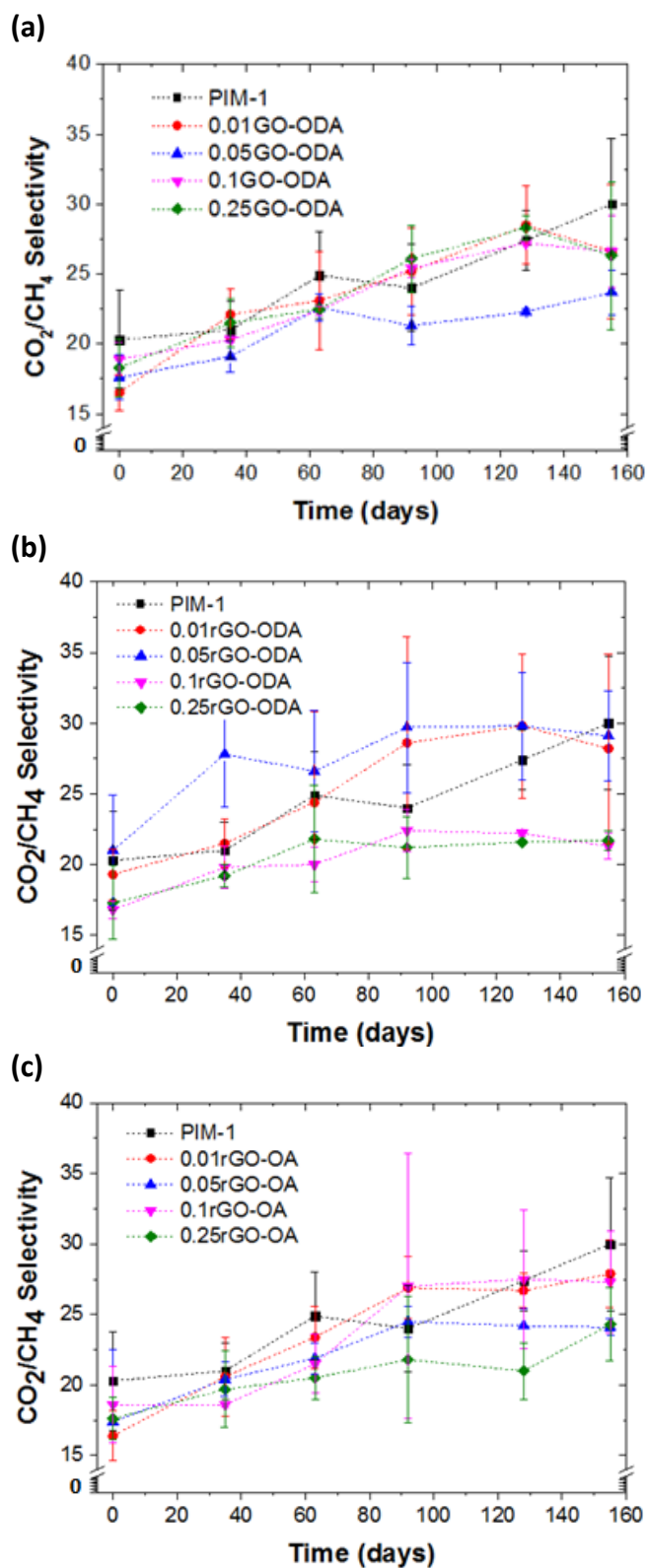
Figure 55: CO_2/CH_4 selectivity of pristine PIM-1 membranes and MMMs filled with (a) GO-ODA, (b) rGO-Oda and (c) rGO-OA. At least two membranes of each type were tested and the error bars correspond to the standard deviation.
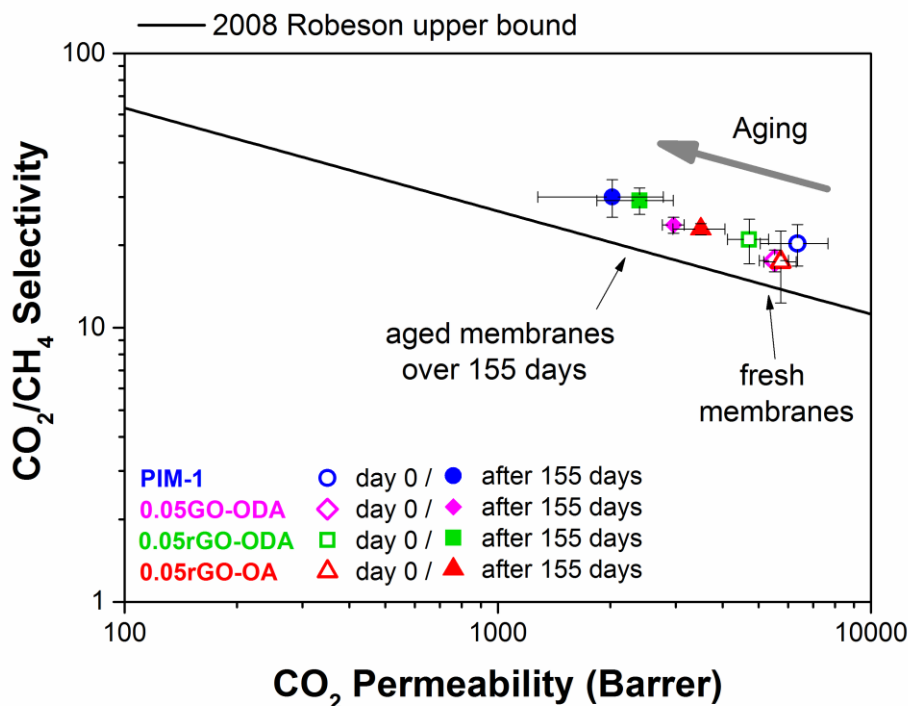
Figure 56: CO_2/CH_4 selectivity vs CO_2 permeability for pure PIM-1 and MMMs containing 0.05 wt.% of graphene-based fillers. Values represent the average of at least two membranes and error bars correspond to the standard deviation obtained. Robeson's 2008 upper bound is also plotted. Open and solid symbols correspond to the performance of membranes on day 0 (fresh membranes) and after 155 days (aged membranes), respectively.

For comparison, representative data from the literature are presented in Table 16. The gas separation performance of aged pristine PIM-1 membranes developed in this study is comparable to values reported in the literature [39, 49, 141]. Small discrepancies might be found, possibly due to differences in operating temperature, feed composition and transmembrane pressures during testing, and variations in the PIM-1 itself. Moreover, the addition of fillers into polymer matrices can lead to the retardation of the physical aging. The incorporation of PAF-1-Li_6C_{60} (10 wt.%) into PTMSP, a super glass polymer, slowed physical aging as well as enhanced gas permeabilities, due to an increase in CO_2 sorption [30]. Mitra *et al.* reported the use of crosslinked fillers (HCP) as a potential strategy to slow physical aging [49]. Therein, not only membranes aged at lower rate but also permeabilities were enhanced. More recently, Kinoshita *et al.* investigated the effect of physical aging on MMMs containing polyhedral oligomeric silsesquioxane (POSS) fillers dispersed in PIM-1 [141]. Their results showed that the addition of 5 wt.% of amino-

functionalized POSS particles could effectively retard physical aging, potentially caused by the rigidification of the polymer matrix.

It is worth mentioning that in the present study small loadings of graphene-like materials into PIM-1 membranes (as little as 0.05 wt.%) are sufficient to see effective reductions in aging, as compared to typical values of filler concentrations found in the literature and shown in Table 16.

Table 16: Comparison of data obtained in this work with other data found in the literature.

Membrane	Day	Permeability (Barrer)		CO_2/CH_4 Selectivity	Ref.
		CO_2	CH_4		
PIM-1	0	$(6.4 \pm 1.3) \times 10^3$	$(3.3 \pm 1.3) \times 10^2$	20.3 ± 3.5	This work
PIM-1	155	$(2.0 \pm 0.7) \times 10^3$	$(0.7 \pm 0.4) \times 10^2$	30 ± 4.7	
0.05GO-ODA	0	$(5.5 \pm 0.5) \times 10^3$	$(3.2 \pm 1.6) \times 10^2$	17.6 ± 1.6	
0.05GO-ODA	155	$(3.0 \pm 0.2) \times 10^3$	$(1.3 \pm 0.2) \times 10^2$	23.7 ± 1.6	
0.05rGO-ODA	0	$(4.7 \pm 0.6) \times 10^3$	$(2.3 \pm 0.7) \times 10^2$	21.0 ± 3.9	
0.05rGO-ODA	155	$(2.4 \pm 0.6) \times 10^3$	$(0.8 \pm 0.3) \times 10^2$	29.1 ± 3.2	
0.05rGO-OA	0	$(5.7 \pm 0.6) \times 10^3$	$(3.6 \pm 1.5) \times 10^2$	17.4 ± 5.1	
0.05rGO-OA	155	$(3.5 \pm 0.6) \times 10^3$	$(1.4 \pm 0.2) \times 10^2$	24.1 ± 0.6	
PTMSP	0	29000	13000	2.2	[30]
PTMSP	365	7000	1200	5.8	
10 wt.% PAF-1-Li_6C_{60}/PTMSP	0	53000	14000	3.6	
10 wt.% PAF-1-Li_6C_{60}/PTMSP	365	50600	14000	3.6	
PIM-1	0	8221			[21]
PIM-1	150	2767			
16.67 wt.% HCP/PIM-1	0	19086			
16.67 wt.% HCP/PIM-1	150	9972			
PIM-1	0	13300	1150	11.6*	[10]
PIM-1	1200	2840	159	17.8*	
PIM-1	0	4087	335	12.2*	[29]
PIM-1	90	2000	118	16.9*	
5 wt.% OAPS/PIM-1	0	3266	157	16.2*	
5 wt.% OAPS/PIM-1	90	2400	130	18.5*	
TR	0	105	4.4	23.8*	[12]
TR	150	94			
0.5 wt.% TR+CNT	0	126	4.9	25.8*	
0.5 wt.% TR+CNT	145	110			

6.8. Conclusions

In summary, the strategy of incorporating graphene-like materials into a PIM-1 polymer matrix is, indeed, an effective approach to retard the physical aging of PIM-1 membranes, and therefore, to develop high performance gas separation membranes. From our study on gas permeability, the best improvements regarding

the impediment of physical aging were achieved by the MMMs with low loadings of graphene-like materials; 0.05GO-ODA, 0.05rGO-ODA and 0.05rGO-OA registered a decrease in CO_2 permeability of 46 %, 49 % and 39 %, respectively, after 155 days. On the other hand, CO_2 permeability of PIM-1 membranes decreased 68 % after the same period of time. Moreover, 0.05rGO-OA presented the highest CO_2 permeability after 155 days of testing, $(3.5 \pm 0.6) \times 10^3$ Barrer, which was 73% higher than pristine PIM-1 membranes.

While the results obtained in this study are promising, continuous testing should be carried out in order to evaluate the performance of membranes under similar conditions to those under industrial operations. Moreover, flux could be potentially increased if the hybrid PIM-1/graphene-like materials were presented as thin film composite membranes, making them more competitive for industrial applications. However, aging should be evaluated as it is highly dependent on the film thickness.

Chapter 7 - Final Conclusions and future work

7.1.   Final conclusions

As the title of this thesis implies, this work aimed to study 2D materials, particularly graphene, for improved membrane technology. Two different membrane applications were investigated: removal of alcohols (EtOH and *n*-BtOH) from aqueous solutions through pervaporation (PV), and CO_2/CH_4 separation.

The most studied polymer of intrinsic microporosity, PIM-1, was used in both applications due to its intrinsic properties. The polymer material was fully characterized using a wide range of different techniques, including gel permeation chromatography (GPC), nitrogen sorption analysis, thermogravimetric analysis (TGA), attenuated total reflection- Fourier-transform infrared spectroscopy (ATR-FTIR) and nuclear magnetic resonance (NMR).

Graphene-like materials dispersed in chloroform were successfully prepared by alkyl-functionalization and reduction of GO. These were characterised with different techniques including TGA, ATR-FTIR, atomic force microscopy (AFM), Raman spectroscopy, X-ray photoelectron spectroscopy (XPS) and scanning electron microscopy (SEM).

Freestanding PIM-1 and mixed matrix membranes (MMMs) of approximately 60 μm in thickness were prepared via solvent evaporation and investigated for $EtOH/H_2O$ and *n*-$BtOH/H_2O$ separation through PV, with feed solutions containing 5wt.% alcohol. . Under these conditions, the total flux of pristine PIM-1 membranes when tested for EtOH/water and *n*-BtOH/water were 0.73 kg m^{-2} h^{-1} and 1.25 kg m^{-2} h^{-1}, respectively. In terms of the intrinsic properties of PIM-1, the average separation factor of PIM-1 membranes for $EtOH/H_2O$ was 3.1, whereas they presented an average factor of 13.5 for *n*-$BtOH/H_2O$. Similarity to pristine PIM-1 membranes, all MMMs also showed better separation performance for *n*-$BtOH/H_2O$ than for $EtOH/H_2O$. The addition of graphene-like fillers into PIM-1 polymer matrix was an efficient way to improve the PV performance of membranes, especially at loading as low as 0.1 wt.%. The best average value of separation factor of 32.9 was

achieved by a membrane containing 0.1 wt.% of functionalized reduced graphene oxide with octylamine (rGO-OA). Following that, 0.1 wt.% of functionalized reduced graphene oxide with octadecylamine (rGO-ODA) presented a separation factor of 26.9. Moreover, the total fluxes of MMMs for n-BtOH/H_2O separations were in the range of 0.93–1.36 kg m^{-2} h^{-1} (normalized flux 40–60 µm kg m^{-2} h^{-1}). The results obtained are based on the preferential chemical affinity and sorption for butanol > ethanol > water shown by all membranes. The sorption towards alcohol was improved by incorporating graphene-like materials in the PIM-1 matrices. At the same time, the sorption of water was hindered when rGO-ODA and rGO-OA were used due to the enhancement of hydrophobicity degree.

As shown previously, the incorporation of hydrophobic graphene-like fillers, is an effective way of improving the separation performance of PV membranes for n-BtOH recovery. In order to improve the productivity of membranes, thin film nanocomposite (TFN) membranes were fabricated through dip-coating technique. The active layer of the TFNs was composed of PIM-1 and graphene-like materials supported on porous polyvinylidene fluoride (PVDF) membranes. The PVDF supports were prepared through phase inversion, and were characterized through SEM, capillary flow porometry (CFP), AFM and water contact angle. The thicknesses of the active layer are in the range 1 -1.5 µm. As expected, the reduction in membrane thickness led to an increase in total flux of TFN membranes as compared to 60 µm freestanding thick membranes. The use of micrometer- and nanometer-sized fillers in the active layer of TFN membranes on the overall PV performance was investigated. The results obtained suggested that voids at the polymer-filler interface are created when micrometer-sized fillers are added to the PIM-1 polymer matrix. On the other hand, the use of nanometer-sized fillers facilitates their alignment with the polymer segments, therefore decreasing the chance of creating large and non-selective voids at their interface. Similarly to MMMs, the best separation performance was achieved using the filler rGO-OA. In TFN membranes, membrane containing nanometer-sized 0.05 wt.% of rGO-OA reached an average separation factor of 17. This represents an improvement of 34% as compared to a pristine PIM-1 TFC membrane (12.7). The effects of feed composition and operating

temperature on the PV performance were also investigated. The increase of both *n*-BtOH feed concentration and operating temperature led to an increase of both separation factor and *n*- *n*-BtOH flux. As seen in MMMs, the PV performance of TFN membranes was compromised when higher filler loadings were used, caused by filler agglomeration.

Physical aging phenomenon is a major drawback for commercial application of membranes. With regard to that, freestanding PIM-1 and MMMs containing graphene-like materials were fabricated through solvent evaporation to study the retardation of physical aging. Physical aging was investigated by measuring the momentary permeability of those membranes using 50:50 vol.% CO_2/CH_4 binary feed mixtures, over a period of 155 days. After 155 days, the average CO_2 permeability of pristine PIM-1 freestanding membranes reached 2027 Barrer, corresponding to a reduction in 68% relative to day 0. On the other hand, the results of MMMs suggest that the incorporation of low loadings of graphene-like materials is an effective way to retard their physical aging. After 155 days, the losses of CO_2 permeabilities of 0.05GO-ODA, 0.05rGO-ODA and 0.05rGO-OA were 46 % ($(3.0 \pm 0.2) \times 10^3$ Barrer), 49 % ($(2.4 \pm 0.6) \times 10^3$ Barrer) and 39 % ($(3.5 \pm 0.6) \times 10^3$ Barrer)), respectively. The hindrance of physical aging is suggested to happen due to the constriction of polymer chain by the graphene-like flakes as predicted previously [241].

7.2. Future work

Based on the results obtained, the incorporation of graphene-like materials led to an improvement of the overall PV performance of membranes; however, there is still potential for further improvement. Further optimization of membrane supports (surface pore size and porosity) and the use of other hydrophobic fillers can be explored in order to favour the transport of butanol across the membrane as well as to control the swelling of the membrane. Since graphene has poor solubility and strong aggregation in organic solvents, stable dispersions in chloroform are required in order to produce MMMs. Herein, alkyl-functionalized GO and rGO were studied; however, other functionalizations (e.g. didodecyldimethylammonium

bromide [284]) can also be studied in order to improve the adsorption and diffusion of the alcohol molecules through the membrane.

The long term stability of the membrane is also an issue for the commercial application of membranes. Therefore, tests for longer running periods are required to study the PV performance stability of the membranes.

Our study only included the use of binary feed solutions; however, as a next step, model aceteno-butanol-ethanol (ABE) model feed solutions can also be used to simulate a feed composition of the fermentation broth.

Although the results obtained from the gas separation study are promising, continuous testing should be carried out in order to accurately replicate what happens in industry. Membranes with higher permeabilities or produced as thinner films are also required in order to reduce the effective area of the membrane. Similarly to the work done for butanol separations from aqueous solutions-, TFN membranes could be explored. For that, optimization of the membrane support and the active layer is also recommended in order to obtain the best results possible.

Besides CO_2/CH_4 separation, PIM-1 membranes have shown great potential for other gases separation such as CO_2/N_2, O_2/N_2 separations. Therefore, detailed study to examine the performance of MMMs containing graphene-like materials can be also performed. CO_2-induced plasticization is another issue that affects the performance of membranes. Reduction of the selectivity and increase of gas permeability with feed pressure are evidence of the plasticization effect. Therefore, the plasticization behaviour of pristine PIM-1 membranes and MMMs can be also studied.

The application of graphene-like materials based in PIM-1/based MMMs can be extended to other applications such as organic solvent nanofiltration (OSN).

References

1.	Ong, Y.K., et al., *Recent membrane development for pervaporation processes.* Progress in Polymer Science, 2016. **57**: p. 1-31.
2.	Budd, P.M., et al., *Polymers of intrinsic microporosity (PIMs): robust, solution-processable, organic nanoporous materials.* Chemical Communications, 2004(2): p. 230-231.
3.	Budd, P.M., et al., *Solution-Processed, Organophilic Membrane Derived from a Polymer of Intrinsic Microporosity.* Advanced Materials, 2004. **16**(5): p. 456-459.
4.	Žák, M., et al., *Selective removal of butanol from aqueous solution by pervaporation with a PIM-1 membrane and membrane aging.* Separation and Purification Technology, 2015. **151**: p. 108-114.
5.	Swaidan, R., et al., *Pure- and mixed-gas CO2/CH4 separation properties of PIM-1 and an amidoxime-functionalized PIM-1.* Journal of Membrane Science, 2014. **457**(Supplement C): p. 95-102.
6.	Lonsdale, H.K., *Editorial.* Journal of Membrane Science, 1987. **34**(2): p. 125-126.
7.	Baker, R.W., *Membrane Technology and Applications*. 2nd ed. 2004: John Wiley & Sons, Ltd.
8.	Mulder, J., *Basic Principles of Membrane Technology*. 2nd ed. 1996: Springer.
9.	Baker, R.W., *Membrane Technology and Applications.* 2012: John Wiley & Sons, Ltd. 1-14.
10.	Strathmann, H.G., L.; Drioli, E., *An Introduction to Membrane Science and Technology*. 2006: Institute on Membrane Technology, CNR-ITM - Consiglio Nazionale delle Ricerche.
11.	Agrawal, K.V., L.W. Drahushuk, and M.S. Strano, *Observation and analysis of the Coulter effect through carbon nanotube and graphene nanopores.* Philosophical Transactions of the Royal Society A: Mathematical,
	Physical and Engineering Sciences, 2016. **374**(2060).
12.	Noble, R.D., Stern S.A, *Membrane Separations Technology: Principles and Applications*. 1995: Elsevier Science B.V. .
13.	Gorgojo, P., *Transport through porous & dense membranes (Lecture)*, T.U.o. Manchester, Editor. 2017.
14.	Atsonios, K., et al., *Palladium Membrane Technology for Hydrogen Production, Carbon Capture and Other Applications*. 2015: Woodhead Publishing. 1-21.
15.	Jyoti, G., A. Keshav, and J. Anandkumar, *Review on Pervaporation: Theory, Membrane Performance, and Application to Intensification of Esterification Reaction.* Journal of Engineering, 2015. **2015**: p. 24.
16.	Strathmann, H., *Ullmann's Encyclopedia of Industrial Chemistry*. 2000: Wiley-VCH Verlag GmbH & Co. KGaA.
17.	Budd, P.M., et al., *Gas separation membranes from polymers of intrinsic microporosity.* Journal of Membrane Science, 2005. **251**(1–2): p. 263-269.
18.	Liu, G., W. Wei, and W. Jin, *Pervaporation Membranes for Biobutanol Production.* ACS Sustainable Chemistry & Engineering, 2014. **2**(4): p. 546-560.
19.	Ismail, A.F., et al., *Transport and separation properties of carbon nanotube-mixed matrix membrane.* Separation and Purification Technology, 2009. **70**(1): p. 12-26.
20.	Xue, C., et al., *A carbon nanotube filled polydimethylsiloxane hybrid membrane for enhanced butanol recovery.* Scientific Reports, 2014. **4**: p. 5925.
21.	Liu, S., et al., *Hydrophobic-ZIF-71 filled PEBA mixed matrix membranes for recovery of biobutanol via pervaporation.* Journal of Membrane Science, 2013. **446**: p. 181-188.

22. Mason, C.R., et al., *New organophilic mixed matrix membranes derived from a polymer of intrinsic microporosity and silicalite-1.* Polymer, 2013. **54**(9): p. 2222-2230.

23. Abdel-Karim, A., et al., *High flux and fouling resistant flat sheet polyethersulfone membranes incorporated with graphene oxide for ultrafiltration applications.* Chemical Engineering Journal, 2018. **334**: p. 789-799.

24. Davood Abadi Farahani, M.H., D. Hua, and T.-S. Chung, *Cross-linked mixed matrix membranes (MMMs) consisting of amine-functionalized multi-walled carbon nanotubes and P84 polyimide for organic solvent nanofiltration (OSN) with enhanced flux.* Journal of Membrane Science, 2018. **548**: p. 319-331.

25. Park, H.M., K.Y. Jee, and Y.T. Lee, *Preparation and characterization of a thin-film composite reverse osmosis membrane using a polysulfone membrane including metal-organic frameworks.* Journal of Membrane Science, 2017. **541**: p. 510-518.

26. González-Guisasola, C. and A. Ribes-Greus, *Dielectric relaxations and conductivity of cross-linked PVA/SSA/GO composite membranes for fuel cells.* Polymer Testing, 2018. **67**: p. 55-67.

27. Adams, R.Z., J.; Lively, R.; Dai, Y.; Esekhile, O.; Liu, J.; Koros, W., *Mixed-matrix membranes*, in *Encyclopedia of Membrane Science and Technology*. 2013, John Wiley & Sons, Inc.

28. Wang, X., et al., *ZIF-7/PDMS mixed matrix membranes for pervaporation recovery of butanol from aqueous solution.* Separation and Purification Technology, 2016. **163**: p. 39-47.

29. Nasir, R., et al., *Material Advancements in Fabrication of Mixed-Matrix Membranes.* Chemical Engineering & Technology, 2013. **36**(5): p. 717-727.

30. Sabetghadam, A., et al., *Metal Organic Framework Crystals in Mixed-Matrix Membranes: Impact of the Filler Morphology on the Gas Separation Performance.* Advanced Functional Materials, 2016. **26**(18): p. 3154-3163.

31. Yin, H., et al., *Effect of ZIF-71 Particle Size on Free-Standing ZIF-71/PDMS Composite Membrane Performances for Ethanol and 1-Butanol Removal from Water through Pervaporation.* Industrial & Engineering Chemistry Research, 2017. **56**(32): p. 9167-9176.

32. Tantekin-Ersolmaz, Ş.B., et al., *Effect of zeolite particle size on the performance of polymer–zeolite mixed matrix membranes.* Journal of Membrane Science, 2000. **175**(2): p. 285-288.

33. Rodenas, T., et al., *Metal–organic framework nanosheets in polymer composite materials for gas separation.* Nat Mater, 2015. **14**(1): p. 48-55.

34. Wang, N., et al., *Tuning properties of silicalite-1 for enhanced ethanol/water pervaporation separation in its PDMS hybrid membrane.* Microporous and Mesoporous Materials, 2015. **201**: p. 35-42.

35. Kudasheva, A., et al., *Pervaporation of water/ethanol mixtures through polyimide based mixed matrix membranes containing ZIF-8, ordered mesoporous silica and ZIF-8-silica core-shell spheres.* Journal of Chemical Technology & Biotechnology, 2015. **90**(4): p. 669-677.

36. Klaysom, C., et al., *The Influence of Inorganic Filler Particle Size on Composite Ion-Exchange Membranes for Desalination.* The Journal of Physical Chemistry C, 2011. **115**(31): p. 15124-15132.

37. McKeown, N.B. and P.M. Budd, *Polymers of Intrinsic Microporosity*, in *Encyclopedia of Polymer Science and Technology*. 2002, John Wiley & Sons, Inc.

38. Emmler, T., et al., *Free Volume Investigation of Polymers of Intrinsic Microporosity (PIMs): PIM-1 and PIM1 Copolymers Incorporating Ethanoanthracene Units.* Macromolecules, 2010. **43**(14): p. 6075-6084.

39.   Bernardo, P., et al., *Effect of physical aging on the gas transport and sorption in PIM-1 membranes.* Polymer, 2017. **113**(Supplement C): p. 283-294.

40.   Budd, P.M., *Polymer with Intrinsic Microporosity (PIM)*, in *Encyclopedia of Membranes*, E. Drioli and L. Giorno, Editors. 2016, Springer Berlin Heidelberg: Berlin, Heidelberg. p. 1606-1607.

41.   Bushell, A.F., et al., *Gas permeation parameters of mixed matrix membranes based on the polymer of intrinsic microporosity PIM-1 and the zeolitic imidazolate framework ZIF-8.* Journal of Membrane Science, 2013. **427**(0): p. 48-62.

42.   Ahn, J., et al., *Gas transport behavior of mixed-matrix membranes composed of silica nanoparticles in a polymer of intrinsic microporosity (PIM-1).* Journal of Membrane Science, 2010. **346**(2): p. 280-287.

43.   McKeown, N.B. and P.M. Budd, *Polymers of intrinsic microporosity (PIMs): organic materials for membrane separations, heterogeneous catalysis and hydrogen storage.* Chemical Society Reviews, 2006. **35**(8): p. 675-683.

44.   Gorgojo, P., et al., *Ultrathin Polymer Films with Intrinsic Microporosity: Anomalous Solvent Permeation and High Flux Membranes.* Advanced Functional Materials, 2014. **24**(30): p. 4729-4737.

45.   Fritsch, D., et al., *High performance organic solvent nanofiltration membranes: Development and thorough testing of thin film composite membranes made of polymers of intrinsic microporosity (PIMs).* Journal of Membrane Science, 2012. **401-402**: p. 222-231.

46.   Adymkanov, S.V., et al., *Pervaporation of alcohols through highly permeable PIM-1 polymer films.* Polymer Science Series A, 2008. **50**(4): p. 444-450.

47.   Gao, L., et al., *High-flux PIM-1/PVDF thin film composite membranes for 1-butanol/water pervaporation.* Journal of Membrane Science, 2017. **529**: p. 207-214.

48.   Budd, P.M., et al., *Gas permeation parameters and other physicochemical properties of a polymer of intrinsic microporosity: Polybenzodioxane PIM-1.* Journal of Membrane Science, 2008. **325**(2): p. 851-860.

49.   Mitra, T., et al., *PIM-1 mixed matrix membranes for gas separations using cost-effective hypercrosslinked nanoparticle fillers.* Chemical Communications, 2016. **52**(32): p. 5581-5584.

50.   Thomas, J.C., et al., *Optical Sensor for Diverse Organic Vapors at ppm Concentration Ranges.* Sensors, 2011. **11**(3): p. 3267.

51.   Hong, J. and Y. He, *Effects of nano sized zinc oxide on the performance of PVDF microfiltration membranes.* Desalination, 2012. **302**: p. 71-79.

52.   Jimenez-Solomon, M.F., et al., *Beneath the surface: Influence of supports on thin film composite membranes by interfacial polymerization for organic solvent nanofiltration.* Journal of Membrane Science, 2013. **448**: p. 102-113.

53.   Zhang, Y., et al., *The performance of integrally skinned polyetherimide asymmetric nanofiltration membranes with organic solvents.* Journal of Membrane Science, 2017. **544**: p. 119-125.

54.   Jue, M.L., V. Breedveld, and R.P. Lively, *Defect-free PIM-1 hollow fiber membranes.* Journal of Membrane Science, 2017. **530**: p. 33-41.

55.   Ren, J. and R. Wang, *Preparation of Polymeric Membranes*, in *Membrane and Desalination Technologies*, L.K. Wang, et al., Editors. 2011, Humana Press: Totowa, NJ. p. 47-100.

56.   Ismail, A.F., K. Khulbe, and T. Matsuura, *Gas Separation Membranes - Polymeric and Inorganic*. 2015: Springer.

57.   Hwang, J., et al., *Effect of Withdrawal Speed on Film Thickness and Hexagonal Pore-Array Dimensions of SBA-15 Mesoporous Silica Thin Film.* Langmuir, 2014. **30**(51): p. 15550-15559.

58.   Tiwari, R., *Global Membranes Market Forecast to Grow at 9.47% CAGR to 2020*. 2015, PR Newswire.

59.   Research, T.M., *Membrane Separation Systems Market - Global Industry Analysis, Size, Share, Growth, Trends, and Forecast 2017 - 2025*. 2017.

60.   *Membrane Technology for Liquid and Gas Separations*. November 2016, BCC Research.

61.   Freedonia, *Membrane Separation Technologies*, in *Membrane Separation Technologies - Demand and Sales Forecasts, Market Share, Market Size, Market Leaders*. 2014, Freedonia Group, Inc.

62.   PR Newswire, *Global Markets and Technologies for Nanofiltration 2014*. 2014, ReportBuyer.

63.   British Petroleum, *BP Energy Outlook 2035.* 2017.

64.   US Energy Information Administration, *International Energy Outlook 2016*. 2016.

65.   European Commission *The 2020 climate and energy package. Climate Action - EU Action 2014*. 2015 [cited 2015 12 May]; Available from: http://ec.europa.eu/clima/policies/package/index_en.htm.

66.   Azapagic, A. and H. Stichnothe, *Sustainability Assessment of Biofuels*, in *Sustainable Development in Practice*. 2010.

67.   Li, J., et al., *Continuous Acetone–Butanol–Ethanol (ABE) Fermentation with in Situ Solvent Recovery by Silicalite-1 Filled PDMS/PAN Composite Membrane.* Energy & Fuels, 2013. **28**(1): p. 555-562.

68.   Liu, G., et al., *PDMS/ceramic composite membrane for pervaporation separation of acetone–butanol–ethanol (ABE) aqueous solutions and its application in intensification of ABE fermentation process.* Chemical Engineering and Processing: Process Intensification, 2014. **86**(0): p. 162-172.

69.   Tan, H., Y. Wu, and T. Li, *Pervaporation of n-butanol aqueous solution through ZSM-5-PEBA composite membranes.* Journal of Applied Polymer Science, 2013. **129**(1): p. 105-112.

70.   Kim, Y.K., et al., *Preparation and characterization of thermally crosslinked chlorine resistant thin film composite polyamide membranes for reverse osmosis.* Desalination, 2010. **250**(2): p. 865-867.

71.   Shi, G.M., T. Yang, and T.S. Chung, *Polybenzimidazole (PBI)/zeolitic imidazolate frameworks (ZIF-8) mixed matrix membranes for pervaporation dehydration of alcohols.* Journal of Membrane Science, 2012. **415–416**(0): p. 577-586.

72.   Kujawska, A., et al., *ABE fermentation products recovery methods—A review.* Renewable and Sustainable Energy Reviews, 2015. **48**: p. 648-661.

73.   Norkobilov, A., D. Gorri, and I. Ortiz, *Process flowsheet analysis of pervaporation-based hybrid processes in the production of ethyl tert-butyl ether.* Journal of Chemical Technology & Biotechnology, 2017. **92**(6): p. 1167-1177.

74.   González, B. and I. Ortiz, *Modelling and simulation of a hybrid process (pervaporation–distillation) for the separation of azeotropic mixtures of alcohol–ether.* Journal of Chemical Technology & Biotechnology, 2002. **77**(1): p. 29-42.

75.   Verhoef, A., et al., *Simulation of a hybrid pervaporation–distillation process.* Computers & Chemical Engineering, 2008. **32**(6): p. 1135-1146.

76.   Matsumura, M., et al., *Energy saving effect of pervaporation using oleyl alcohol liquid membrane in butanol purification.* Bioprocess Engineering, 1988. **3**(2): p. 93-100.

77. Rom, A., et al., *Energy saving potential of hybrid membrane and distillation process in butanol purification: Experiments, modelling and simulation.* Chemical Engineering and Processing: Process Intensification, 2016. **104**: p. 201-211.

78. Friedl, A., *Downstream process options for the ABE fermentation.* FEMS Microbiology Letters, 2016. **363**(9): p. fnw073-fnw073.

79. Van Hoof, V., et al., *Economic comparison between azeotropic distillation and different hybrid systems combining distillation with pervaporation for the dehydration of isopropanol.* Separation and Purification Technology, 2004. **37**(1): p. 33-49.

80. Zhuang, X., et al., *Improved performance of PDMS/silicalite-1 pervaporation membranes via designing new silicalite-1 particles.* Journal of Membrane Science, 2015. **493**: p. 37-45.

81. Dutta, B.K. and S.K. Sikdar, *Separation of azeotropic organic liquid mixtures by pervaporation.* AIChE Journal, 1991. **37**(4): p. 581-588.

82. Hyder, M.N., R.Y.M. Huang, and P. Chen, *Effect of selective layer thickness on pervaporation of composite poly(vinyl alcohol)–poly(sulfone) membranes.* Journal of Membrane Science, 2008. **318**(1–2): p. 387-396.

83. Villaluenga, J.P.G., et al., *Analysis of the membrane thickness effect on the pervaporation separation of methanol/methyl tertiary butyl ether mixtures.* Separation and Purification Technology, 2005. **47**(1–2): p. 80-87.

84. Huang, R.Y.M. and V.J.C. Lin, *Separation of liquid mixtures by using polymer membranes. I. Permeation of binary organic liquid mixtures through polyethylene.* Journal of Applied Polymer Science, 1968. **12**(12): p. 2615-2631.

85. Huang, J. and M.M. Meagher, *Pervaporative recovery of n-butanol from aqueous solutions and ABE fermentation broth using thin-film silicalite-filled silicone composite membranes.* Journal of Membrane Science, 2001. **192**(1–2): p. 231-242.

86. Niemistö, J., W. Kujawski, and R.L. Keiski, *Pervaporation performance of composite poly(dimethyl siloxane) membrane for butanol recovery from model solutions.* Journal of Membrane Science, 2013. **434**(0): p. 55-64.

87. González-Marcos, J.A., C. López-Dehesa, and J.R. González-Velasco, *Effect of operation conditions in the pervaporation of ethanol–water mixtures with poly(1-trimethylsilyl-1-propyne) membranes.* Journal of Applied Polymer Science, 2004. **94**(4): p. 1395-1403.

88. Claes, S., et al., *High flux composite PTMSP-silica nanohybrid membranes for the pervaporation of ethanol/water mixtures.* Journal of Membrane Science, 2010. **351**(1–2): p. 160-167.

89. Claes, S., et al., *Preparation and benchmarking of thin film supported PTMSP-silica pervaporation membranes.* Journal of Membrane Science, 2012. **389**: p. 265-271.

90. Fadeev, A.G., et al., *Extraction of butanol from aqueous solutions by pervaporation through poly(1-trimethylsilyl-1-propyne).* Journal of Membrane Science, 2001. **186**(2): p. 205-217.

91. González-Velasco, J.R., J.A. González-Marcos, and C. López-Dehesa, *Pervaporation of ethanol—water mixtures through poly(1-trimethylsilyl-1-propyne) (PTMSP) membranes.* Desalination, 2002. **149**(1): p. 61-65.

92. López-Dehesa, C., J.A. González-Marcos, and J.R. González-Velasco, *Pervaporation of 50 wt % ethanol–water mixtures with poly(1-trimethylsilyl-1-propyne) membranes at high temperatures.* Journal of Applied Polymer Science, 2007. **103**(5): p. 2843-2848.

93. Zhan, X., et al., *Mixed matrix membranes with HF acid etched ZSM-5 for ethanol/water separation: Preparation and pervaporation performance.* Applied Surface Science, 2012. **259**: p. 547-556.

94.   Vankelecom, I.F.J., et al., *Influence of zeolites in PDMS membranes. Pervaporation of water/alcohol mixtures.* Journal of physical chemistry, 1995. **99**(35): p. 13193-13197.

95.   Fouad, E.A. and X. Feng, *Pervaporative separation of n-butanol from dilute aqueous solutions using silicalite-filled poly(dimethyl siloxane) membranes.* Journal of Membrane Science, 2009. **339**(1–2): p. 120-125.

96.   Le, N.L., Y. Wang, and T.-S. Chung, *Pebax/POSS mixed matrix membranes for ethanol recovery from aqueous solutions via pervaporation.* Journal of Membrane Science, 2011. **379**(1): p. 174-183.

97.   Fouad, E.A. and X. Feng, *Use of pervaporation to separate butanol from dilute aqueous solutions: Effects of operating conditions and concentration polarization.* Journal of Membrane Science, 2008. **323**(2): p. 428-435.

98.   Jee, K.Y., N. Kim, and Y.T. Lee, *The effect of metal complex on pervaporation performance of composite membrane for separation of n-butanol/water mixture.* Journal of Industrial and Engineering Chemistry, 2016. **44**: p. 155-163.

99.   Li, Y., et al., *PEBA/ceramic hollow fiber composite membrane for high-efficiency recovery of bio-butanol via pervaporation.* Journal of Membrane Science, 2016. **510**: p. 338-347.

100.   Organization, W.M., *World Meteorological Organization's Greenhouse Gas Bulletin.* 2017.

101.   Virginie Marchal, et al., *OECD Environmental Outlook to 2050 - Climate Change Chapter*. 2011.

102.   Zhang, Y., et al., *Current status and development of membranes for CO2/CH4 separation: A review.* International Journal of Greenhouse Gas Control, 2013. **12**(Supplement C): p. 84-107.

103.   Alcheikhhamdon, Y. and M. Hoorfar, *Natural gas purification from acid gases using membranes: A review of the history, features, techno-commercial challenges, and process intensification of commercial membranes.* Chemical Engineering and Processing: Process Intensification, 2017. **120**(Supplement C): p. 105-113.

104.   Cheng, Y., et al., *Ultrathin mixed matrix membranes containing two-dimensional metal-organic framework nanosheets for efficient CO2/CH4 separation.* Journal of Membrane Science, 2017. **539**(Supplement C): p. 213-223.

105.   Yang, H., et al., *Economic Comparison of Three Gas Separation Technologies for CO2 Capture from Power Plant Flue Gas.* Chinese Journal of Chemical Engineering, 2011. **19**(4): p. 615-620.

106.   Merkel, T.C., et al., *Power plant post-combustion carbon dioxide capture: An opportunity for membranes.* Journal of Membrane Science, 2010. **359**(1): p. 126-139.

107.   Scholes, C.A., *CHAPTER 8 Cost Competitive Membrane Processes for Carbon Capture*, in *Membrane Engineering for the Treatment of Gases: Volume 1: Gas-separation Issues with Membranes (2)*. 2018, The Royal Society of Chemistry. p. 216-241.

108.   Eric M. V. Hoek and V.V. Tarabara, *Encyclopedia of Membrane Science and Technology*. Vol. 3 Volume Set. 2013: Weley.

109.   He, X., T.-J. Kim, and M.-B. Hägg, *Hybrid fixed-site-carrier membranes for CO2 removal from high pressure natural gas: Membrane optimization and process condition investigation.* Journal of Membrane Science, 2014. **470**: p. 266-274.

110.   Eltahir Mustafa, S.G.E., et al., *Synthesis, characterization, and performance evaluation of PES/EDA-functionalized TiO2 mixed matrix membranes for CO2/CH4 separation.* Journal of Applied Polymer Science, 2017. **134**(39): p. 45346-n/a.

111.   Şen, D., H. Kalıpçılar, and L. Yilmaz, *Development of polycarbonate based zeolite 4A filled mixed matrix gas separation membranes.* Journal of Membrane Science, 2007. **303**(1): p. 194-203.

112.   Olivieri, L., et al., *Effect of Graphene and Graphene Oxide Nanoplatelets on the Gas Permselectivity and Aging Behavior of Poly(trimethylsilyl propyne) (PTMSP).* Industrial & Engineering Chemistry Research, 2015. **54**(44): p. 11199-11211.

113.   Wu, X., et al., *Nanoporous ZIF-67 embedded polymers of intrinsic microporosity membranes with enhanced gas separation performance.* Journal of Membrane Science, 2018. **548**(Supplement C): p. 309-318.

114.   Robeson, L.M., *Correlation of separation factor versus permeability for polymeric membranes.* Journal of Membrane Science, 1991. **62**(2): p. 165-185.

115.   Robeson, L.M., *The upper bound revisited.* Journal of Membrane Science, 2008. **320**(1–2): p. 390-400.

116.   Bastani, D., N. Esmaeili, and M. Asadollahi, *Polymeric mixed matrix membranes containing zeolites as a filler for gas separation applications: A review.* Journal of Industrial and Engineering Chemistry, 2013. **19**(2): p. 375-393.

117.   Pechar, T.W., et al., *Fabrication and characterization of polyimide–zeolite L mixed matrix membranes for gas separations.* Journal of Membrane Science, 2006. **277**(1): p. 195-202.

118.   Jusoh, N., et al., *Fabrication of silanated zeolite T/6FDA-durene composite membranes for CO2/CH4 separation.* Journal of Cleaner Production, 2017. **166**: p. 1043-1058.

119.   Vu, D.Q., W.J. Koros, and S.J. Miller, *Mixed matrix membranes using carbon molecular sieves: I. Preparation and experimental results.* Journal of Membrane Science, 2003. **211**(2): p. 311-334.

120.   Weng, T.-H., H.-H. Tseng, and M.-Y. Wey, *Fabrication and characterization of poly(phenylene oxide)/SBA-15/carbon molecule sieve multilayer mixed matrix membrane for gas separation.* International Journal of Hydrogen Energy, 2010. **35**(13): p. 6971-6983.

121.   Rafizah, W.A.W. and A.F. Ismail, *Effect of carbon molecular sieve sizing with poly(vinyl pyrrolidone) K-15 on carbon molecular sieve–polysulfone mixed matrix membrane.* Journal of Membrane Science, 2008. **307**(1): p. 53-61.

122.   Li, T., et al., *Carbon dioxide selective mixed matrix composite membrane containing ZIF-7 nano-fillers.* Journal of Membrane Science, 2013. **425-426**: p. 235-242.

123.   Basu, S., A. Cano-Odena, and I.F.J. Vankelecom, *MOF-containing mixed-matrix membranes for CO2/CH4 and CO2/N2 binary gas mixture separations.* Separation and Purification Technology, 2011. **81**(1): p. 31-40.

124.   Dorosti, F., M. Omidkhah, and R. Abedini, *Fabrication and characterization of Matrimid/MIL-53 mixed matrix membrane for CO2/CH4 separation.* Chemical Engineering Research and Design, 2014. **92**(11): p. 2439-2448.

125.   Chen, X.Y., et al., *Amine-Functionalized MIL-53 Metal–Organic Framework in Polyimide Mixed Matrix Membranes for CO2/CH4 Separation.* Industrial & Engineering Chemistry Research, 2012. **51**(19): p. 6895-6906.

126.   Sun, H., et al., *Fabrication of polyimide and functionalized multi-walled carbon nanotubes mixed matrix membranes by in-situ polymerization for CO2 separation.* Separation and Purification Technology, 2017. **177**: p. 327-336.

127.   Weng, T.H., H.H. Tseng, and M.Y. Wey, *Preparation and characterization of multi-walled carbon nanotube/PBNPI nanocomposite membrane for H2/CH4 separation.* Int J Hydrogen Energy, 2009. **34**.

128.   Ge, L., et al., *Investigation of Gas Permeability in Carbon Nanotube (CNT)–Polymer Matrix Membranes via Modifying CNTs with Functional Groups/Metals and*

Controlling Modification Location. The Journal of Physical Chemistry C, 2011. **115**(14): p. 6661-6670.

129.   Ge, L., Z. Zhu, and V. Rudolph, *Enhanced gas permeability by fabricating functionalized multi-walled carbon nanotubes and polyethersulfone nanocomposite membrane.* Separation and Purification Technology, 2011. **78**(1): p. 76-82.

130.   Zornoza, B., et al., *Mesoporous Silica Sphere–Polysulfone Mixed Matrix Membranes for Gas Separation.* Langmuir, 2009. **25**(10): p. 5903-5909.

131.   Shen, J., et al., *Size effects of graphene oxide on mixed matrix membranes for CO2 separation.* AIChE Journal, 2016. **62**(8): p. 2843-2852.

132.   Matteucci, S., et al., *Gas transport in TiO2 nanoparticle-filled poly(1-trimethylsilyl-1-propyne).* Journal of Membrane Science, 2008. **307**(2): p. 196-217.

133.   Hasanajili, S., M. Latifzadeh, and M. Bahmani, *Permeation properties of CO2 and CH4 in asymmetric polyethersulfone/polyesterurethane and polyethersulfone/polyetherurethane blend membranes.* Chinese Journal of Chemical Engineering, 2017. **25**(12): p. 1750-1759.

134.   Khan, M.M., et al., *Cross-linking of Polymer of Intrinsic Microporosity (PIM-1) via nitrene reaction and its effect on gas transport property.* European Polymer Journal, 2013. **49**(12): p. 4157-4166.

135.   Dong, G., H. Li, and V. Chen, *Plasticization mechanisms and effects of thermal annealing of Matrimid hollow fiber membranes for CO2 removal.* Journal of Membrane Science, 2011. **369**(1): p. 206-220.

136.   Carreon, M.L., S. Li, and M.A. Carreon, *AlPO-18 membranes for CO2/CH4 separation.* Chemical Communications, 2012. **48**(17): p. 2310-2312.

137.   Yoshimune, M. and K. Haraya, *CO2/CH4 Mixed Gas Separation Using Carbon Hollow Fiber Membranes.* Energy Procedia, 2013. **37**(Supplement C): p. 1109-1116.

138.   Steel, K.M. and W.J. Koros, *Investigation of porosity of carbon materials and related effects on gas separation properties.* Carbon, 2003. **41**(2): p. 253-266.

139.   Shamsabadi, A.A., et al., *Physical aging of polyetherimide membranes.* Journal of Natural Gas Science and Engineering, 2015. **27**(Part 2): p. 651-660.

140.   Xu, L., et al., *Physical aging in carbon molecular sieve membranes.* Carbon, 2014. **80**(Supplement C): p. 155-166.

141.   Kinoshita, Y., et al., *Enhanced PIM-1 membrane gas separation selectivity through efficient dispersion of functionalized POSS fillers.* Journal of Membrane Science, 2017. **539**(Supplement C): p. 178-186.

142.   Brunetti, A., et al., *Thermally rearranged mixed matrix membranes for CO2 separation: An aging study.* International Journal of Greenhouse Gas Control, 2017. **61**(Supplement C): p. 16-26.

143.   Lau, C.H., et al., *Tailoring Physical Aging in Super Glassy Polymers with Functionalized Porous Aromatic Frameworks for CO2 Capture.* Chemistry of Materials, 2015. **27**(13): p. 4756-4762.

144.   Li, F.Y., et al., *High-Performance Thermally Self-Cross-Linked Polymer of Intrinsic Microporosity (PIM-1) Membranes for Energy Development.* Macromolecules, 2012. **45**(3): p. 1427-1437.

145.   Song, Q., et al., *Controlled thermal oxidative crosslinking of polymers of intrinsic microporosity towards tunable molecular sieve membranes.* Nat Commun, 2014. **5**.

146.   Ghalei, B., et al., *Surface functionalization of high free-volume polymers as a route to efficient hydrogen separation membranes.* Journal of Materials Chemistry A, 2017. **5**(9): p. 4686-4694.

147.   Kelman, S.D., et al., *Crosslinking poly[1-(trimethylsilyl)-1-propyne] and its effect on physical stability.* Journal of Membrane Science, 2008. **320**(1): p. 123-134.

148. Huang, Y. and D.R. Paul, *Effect of Film Thickness on the Gas-Permeation Characteristics of Glassy Polymer Membranes.* Industrial & Engineering Chemistry Research, 2007. **46**(8): p. 2342-2347.

149. Huang, Y. and D.R. Paul, *Effect of Temperature on Physical Aging of Thin Glassy Polymer Films.* Macromolecules, 2005. **38**(24): p. 10148-10154.

150. Nagai, K. and T. Nakagawa, *Effects of aging on the gas permeability and solubility in poly(1-trimethylsilyl-1-propyne) membranes synthesized with various catalysts.* Journal of Membrane Science, 1995. **105**(3): p. 261-272.

151. Nagai, K., A. Higuchi, and T. Nakagawa, *Gas permeability and stability of poly(1-trimethylsilyl-1-propyne-co-1-phenyl-1-propyne) membranes.* Journal of Polymer Science Part B: Polymer Physics, 1995. **33**(2): p. 289-298.

152. Shamsipur, H., et al., *Thermally Rearrangeable PIM-Polyimides for Gas Separation Membranes.* Macromolecules, 2014. **47**(16): p. 5595-5606.

153. Pilnáček, K., et al., *Aging of polymers of intrinsic microporosity tracked by methanol vapour permeation.* Journal of Membrane Science, 2016. **520**(Supplement C): p. 895-906.

154. Swaidan, R., et al., *Physical Aging, Plasticization and Their Effects on Gas Permeation in "Rigid" Polymers of Intrinsic Microporosity.* Macromolecules, 2015. **48**(18): p. 6553-6561.

155. Tiwari, R.R., et al., *Physical aging, CO2 sorption and plasticization in thin films of polymer with intrinsic microporosity (PIM-1).* Journal of Membrane Science, 2017. **537**: p. 362-371.

156. Kim, K.-J., et al., *CO2 separation performances of composite membranes of 6FDA-based polyimides with a polar group.* Journal of Membrane Science, 2003. **211**(1): p. 41-49.

157. José, N.M., L.A.S.A. Prado, and I.V.P. Yoshida, *Synthesis, characterization, and permeability evaluation of hybrid organic–inorganic films.* Journal of Polymer Science Part B: Polymer Physics, 2004. **42**(23): p. 4281-4292.

158. Dong, G., H. Li, and V. Chen, *Factors affect defect-free Matrimid® hollow fiber gas separation performance in natural gas purification.* Journal of Membrane Science, 2010. **353**(1): p. 17-27.

159. Geim, A. and K. Novoselov, *The rise of graphene.* Nat Mater, 2007. **6**: p. 183 - 191.

160. Balandin, A.A., et al., *Superior Thermal Conductivity of Single-Layer Graphene.* Nano Letters, 2008. **8**(3): p. 902-907.

161. Castro Neto, A.H., et al., *The electronic properties of graphene.* Reviews of Modern Physics, 2009. **81**(1): p. 109-162.

162. Du, X., et al., *Approaching ballistic transport in suspended graphene.* Nature Nanotechnology, 2008. **3**: p. 491.

163. Lee, C., et al., *Measurement of the Elastic Properties and Intrinsic Strength of Monolayer Graphene.* Science, 2008. **321**(5887): p. 385-388.

164. Novoselov, K.S., et al., *Electric Field Effect in Atomically Thin Carbon Films.* Science, 2004. **306**(5696): p. 666-669.

165. Lin, Y.-M., et al., *100-GHz Transistors from Wafer-Scale Epitaxial Graphene.* Science, 2010. **327**(5966): p. 662-662.

166. El-Kady, M.F., Y. Shao, and R.B. Kaner, *Graphene for batteries, supercapacitors and beyond.* Nature Reviews Materials, 2016. **1**: p. 16033.

167. Bae, S., et al., *Roll-to-roll production of 30-inch graphene films for transparent electrodes.* Nature Nanotechnology, 2010. **5**: p. 574.

168. Wang, L., et al., *Graphene-copper composite with micro-layered grains and ultrahigh strength.* Scientific Reports, 2017. **7**: p. 41896.

169. Bhuyan, M.S.A., et al., *Synthesis of graphene.* International Nano Letters, 2016. **6**(2): p. 65-83.

170. Eigler, S., *Graphene Synthesis*, in *Graphene Technology*. 2016, Wiley-VCH Verlag GmbH & Co. KGaA. p. 19-61.

171. Novoselov, K.S., et al., *A roadmap for graphene.* Nature, 2012. **490**: p. 192.

172. Bunch, J.S., et al., *Impermeable Atomic Membranes from Graphene Sheets.* Nano Letters, 2008. **8**(8): p. 2458-2462.

173. Cohen-Tanugi, D. and J.C. Grossman, *Water permeability of nanoporous graphene at realistic pressures for reverse osmosis desalination.* J Chem Phys, 2014. **141**(7): p. 074704.

174. Schrier, J., *Helium Separation Using Porous Graphene Membranes.* The Journal of Physical Chemistry Letters, 2010. **1**(15): p. 2284-2287.

175. Sun, C., et al., *Mechanisms of Molecular Permeation through Nanoporous Graphene Membranes.* Langmuir, 2014. **30**(2): p. 675-682.

176. Koenig, S.P., et al., *Selective molecular sieving through porous graphene.* Nature Nanotechnology, 2012. **7**: p. 728.

177. Celebi, K., et al., *Ultimate Permeation Across Atomically Thin Porous Graphene.* Science, 2014. **344**(6181): p. 289-292.

178. Pastrana-Martínez, L.M., et al., *Graphene-Based Membranes for Separation Engineering*, in *Graphene Technology*. 2016, Wiley-VCH Verlag GmbH & Co. KGaA. p. 133-154.

179. Nair, R.R., et al., *Unimpeded Permeation of Water Through Helium-Leak–Tight Graphene-Based Membranes.* Science, 2012. **335**(6067): p. 442-444.

180. Tang, Y.P., D.R. Paul, and T.S. Chung, *Free-standing graphene oxide thin films assembled by a pressurized ultrafiltration method for dehydration of ethanol.* Journal of Membrane Science, 2014. **458**: p. 199-208.

181. Huang, K., et al., *A Graphene Oxide Membrane with Highly Selective Molecular Separation of Aqueous Organic Solution.* Angewandte Chemie International Edition, 2014. **53**(27): p. 6929-6932.

182. Joshi, R.K., et al., *Precise and Ultrafast Molecular Sieving Through Graphene Oxide Membranes.* Science, 2014. **343**(6172): p. 752-754.

183. Dikin, D.A., et al., *Preparation and characterization of graphene oxide paper.* Nature, 2007. **448**: p. 457.

184. Hung, W.-S., et al., *Pressure-assisted self-assembly technique for fabricating composite membranes consisting of highly ordered selective laminate layers of amphiphilic graphene oxide.* Carbon, 2014. **68**(0): p. 670-677.

185. Wang, J., et al., *Graphene Oxide as an Effective Barrier on a Porous Nanofibrous Membrane for Water Treatment.* ACS Applied Materials & Interfaces, 2016. **8**(9): p. 6211-6218.

186. Chengmeng, C., et al., *Self-Assembled Free-Standing Graphite Oxide Membrane.* Advanced Materials, 2009. **21**(29): p. 3007-3011.

187. Abraham, J., et al., *Tunable sieving of ions using graphene oxide membranes.* Nature Nanotechnology, 2017. **12**: p. 546.

188. Su, Y., et al., *Impermeable barrier films and protective coatings based on reduced graphene oxide.* Nat Commun, 2014. **5**.

189. Sun, P., et al., *Highly efficient quasi-static water desalination using monolayer graphene oxide/titania hybrid laminates.* Npg Asia Materials, 2015. **7**: p. e162.

190. Pei, J., et al., *Fabrication of reduced graphene oxide membranes for highly efficient water desalination.* RSC Advances, 2016. **6**(104): p. 101948-101952.

191. Li, H., et al., *Ultrathin, Molecular-Sieving Graphene Oxide Membranes for Selective Hydrogen Separation.* Science, 2013. **342**(6154): p. 95-98.

192. Xin, Q., et al., *Enhancing the CO2 separation performance of composite membranes by the incorporation of amino acid-functionalized graphene oxide.* Journal of Materials Chemistry A, 2015. **3**(12): p. 6629-6641.

193. Li, X., et al., *Efficient CO2 Capture by Functionalized Graphene Oxide Nanosheets as Fillers To Fabricate Multi-Permselective Mixed Matrix Membranes.* ACS Applied Materials & Interfaces, 2015. **7**(9): p. 5528-5537.

194. Li, X., et al., *Synergistic effect of combining carbon nanotubes and graphene oxide in mixed matrix membranes for efficient CO2 separation.* Journal of Membrane Science, 2015. **479**(0): p. 1-10.

195. Althumayri, K., et al., *The influence of few-layer graphene on the gas permeability of the high-free-volume polymer PIM-1.* Philosophical Transactions of the Royal Society A: Mathematical, Physical and Engineering Sciences, 2016. **374**(2060).

196. Cao, K., et al., *Enhanced water permeation through sodium alginate membranes by incorporating graphene oxides.* Journal of Membrane Science, 2014. **469**(0): p. 272-283.

197. Yeh, T.-M., et al., *High flux ethanol dehydration using nanofibrous membranes containing graphene oxide barrier layers.* Journal of Materials Chemistry A, 2013. **1**(41): p. 12998-13003.

198. Wang, N., et al., *Poly(vinyl alcohol)–graphene oxide nanohybrid "pore-filling" membrane for pervaporation of toluene/n-heptane mixtures.* Journal of Membrane Science, 2014. **455**: p. 113-120.

199. Rourke, J.P., et al., *The Real Graphene Oxide Revealed: Stripping the Oxidative Debris from the Graphene-like Sheets.* Angewandte Chemie International Edition, 2011. **50**(14): p. 3173-3177.

200. Hou, Y., et al., *Positive piezoresistive behavior of electrically conductive alkyl-functionalized graphene/polydimethylsilicone nanocomposites.* Journal of Materials Chemistry C, 2013. **1**(3): p. 515-521.

201. Hernandez, N., et al., *Carbonization of polymers of intrinsic microporosity to microporous heterocarbon: Capacitive pH measurements.* Applied Materials Today, 2017. **9**(Supplement C): p. 136-144.

202. Khan, M.M., et al., *Synthesis, characterization and gas permeation properties of anthracene maleimide-based polymers of intrinsic microporosity.* RSC Advances, 2014. **4**(61): p. 32148-32160.

203. Li, P., T.S. Chung, and D.R. Paul, *Gas sorption and permeation in PIM-1.* Journal of Membrane Science, 2013. **432**: p. 50-57.

204. Heuchel, M., et al., *Atomistic packing model and free volume distribution of a polymer with intrinsic microporosity (PIM-1).* Journal of Membrane Science, 2008. **318**(1): p. 84-99.

205. Al Kutubi, H., et al., *Polymers of intrinsic microporosity as high temperature templates for the formation of nanofibrous oxides.* RSC Advances, 2015. **5**(89): p. 73323-73326.

206. Hao, L., K.-S. Liao, and T.-S. Chung, *Photo-oxidative PIM-1 based mixed matrix membranes with superior gas separation performance.* Journal of Materials Chemistry A, 2015. **3**(33): p. 17273-17281.

207. Satilmis, B. and P.M. Budd, *Base-catalysed hydrolysis of PIM-1: amide versus carboxylate formation.* RSC Advances, 2014. **4**(94): p. 52189-52198.

208. Satilmis, B., M.N. Alnajrani, and P.M. Budd, *Hydroxyalkylaminoalkylamide PIMs: Selective Adsorption by Ethanolamine- and Diethanolamine-Modified PIM-1.* Macromolecules, 2015. **48**(16): p. 5663-5669.

209. Jang, J., et al., *Dispersibility of reduced alkylamine-functionalized graphene oxides in organic solvents.* J Colloid Interface Sci, 2014. **424**: p. 62 - 66.

210. Yang, X., et al., *Synthesis and characterization of alkylamine-functionalized graphene for polyolefin-based nanocomposites.* Applied Surface Science, 2014. **305**(0): p. 725-731.

211. Zhang, J., et al., *Reduction of graphene oxide vial-ascorbic acid.* Chemical Communications, 2010. **46**(7): p. 1112-1114.

212. Dresselhaus, M.S., et al., *Defect characterization in graphene and carbon nanotubes using Raman spectroscopy*. Vol. 368. 2010. 5355-5377.

213. Lucchese, M.M., et al., *Quantifying ion-induced defects and Raman relaxation length in graphene.* Carbon, 2010. **48**(5): p. 1592-1597.

214. Lin, Z., Y. Liu, and C.-p. Wong, *Facile Fabrication of Superhydrophobic Octadecylamine-Functionalized Graphite Oxide Film.* Langmuir, 2010. **26**(20): p. 16110-16114.

215. Vane, L.M., *A review of pervaporation for product recovery from biomass fermentation processes.* Journal of Chemical Technology & Biotechnology, 2005. **80**(6): p. 603-629.

216. Vrana, D.L., et al., *Pervaporation of Model Acetone-Butanol-Ethanol Fermentation Product Solutions Using Polytetrafluoroethylene Membranes.* Separation Science and Technology, 1993. **28**(13-14): p. 2167-2178.

217. Dobrak, A., et al., *Performance of PDMS membranes in pervaporation: Effect of silicalite fillers and comparison with SBS membranes.* Journal of Colloid and Interface Science, 2010. **346**(1): p. 254-264.

218. Liu, S., et al., *Hydrophobic-ZIF-71 filled PEBA mixed matrix membranes for recovery of biobutanol via pervaporation.* Journal of Membrane Science, 2013. **446**(0): p. 181-188.

219. Liu, X.-L., et al., *An Organophilic Pervaporation Membrane Derived from Metal–Organic Framework Nanoparticles for Efficient Recovery of Bio-Alcohols.* Angewandte Chemie International Edition, 2011. **50**(45): p. 10636-10639.

220. Hua, D., et al., *ZIF-90/P84 mixed matrix membranes for pervaporation dehydration of isopropanol.* Journal of Membrane Science, 2014. **453**(0): p. 155-167.

221. Liu, G., et al., *Improved performance of PDMS/ceramic composite pervaporation membranes by ZSM-5 homogeneously dispersed in PDMS via a surface graft/coating approach.* Chemical Engineering Journal, 2011. **174**(2–3): p. 495-503.

222. Yen, H.-W., Z.-H. Chen, and I.K. Yang, *Use of the composite membrane of poly(ether-block-amide) and carbon nanotubes (CNTs) in a pervaporation system incorporated with fermentation for butanol production by Clostridium acetobutylicum.* Bioresource Technology, 2012. **109**(0): p. 105-109.

223. Rubio, C.Z., B.; Gorgojo, P.; Tellez, C.; Coronas, J., *Separation of H2 and CO2 Containing Mixtures with Mixed Matrix Membranes Based on Layered Materials.* Current Organic Chemistry, 2014. **18**(18): p. 2351-2363(13).

224. Kim, W.-g., et al., *Nanoporous layered silicate AMH-3/cellulose acetate nanocomposite membranes for gas separations.* Journal of Membrane Science, 2013. **441**: p. 129-136.

225. Jeong, H.-K., et al., *Fabrication of Polymer/Selective-Flake Nanocomposite Membranes and Their Use in Gas Separation.* Chemistry of Materials, 2004. **16**(20): p. 3838-3845.

226. Choi, S., et al., *Layered Silicates by Swelling of AMH-3 and Nanocomposite Membranes.* Angewandte Chemie International Edition, 2008. **47**(3): p. 552-555.

227. Gorgojo, P., et al., *Exfoliated zeolite Nu-6(2) as filler for 6FDA-based copolyimide mixed matrix membranes.* Journal of Membrane Science, 2012. **411–412**: p. 146-152.

228. Cohen-Tanugi, D. and J.C. Grossman, *Water Desalination across Nanoporous Graphene.* Nano Letters, 2012. **12**(7): p. 3602-3608.

229. Dharupaneedi, S.P., et al., *Functionalized Graphene Sheets Embedded in Chitosan Nanocomposite Membranes for Ethanol and Isopropanol Dehydration via Pervaporation.* Industrial & Engineering Chemistry Research, 2014. **53**(37): p. 14474-14484.

230. Suhas, D.P., et al., *Graphene-loaded sodium alginate nanocomposite membranes with enhanced isopropanol dehydration performance via a pervaporation technique.* RSC Advances, 2013. **3**(38): p. 17120-17130.

231. Ganesh, B.M., A.M. Isloor, and A.F. Ismail, *Enhanced hydrophilicity and salt rejection study of graphene oxide-polysulfone mixed matrix membrane.* Desalination, 2013. **313**(0): p. 199-207.

232. Ghanbari, M., et al., *Synthesis and characterization of novel thin film nanocomposite reverse osmosis membranes with improved organic fouling properties for water desalination.* RSC Advances, 2015. **5**(27): p. 21268-21276.

233. Wu, X.M., et al., *Pervaporation removal of volatile organic compounds from aqueous solutions using the highly permeable PIM-1 membrane.* AIChE Journal, 2016. **62**(3): p. 842-851.

234. Harms, S., et al., *Aging and Free Volume in a Polymer of Intrinsic Microporosity (PIM-1).* The Journal of Adhesion, 2012. **88**(7): p. 608-619.

235. Huang, Y. and D.R. Paul, *Experimental methods for tracking physical aging of thin glassy polymer films by gas permeation.* Journal of Membrane Science, 2004. **244**(1–2): p. 167-178.

236. Huang, Y. and D.R. Paul, *Physical aging of thin glassy polymer films monitored by gas permeability.* Polymer, 2004. **45**(25): p. 8377-8393.

237. Song, Q., et al., *Nanofiller-tuned microporous polymer molecular sieves for energy and environmental processes.* Journal of Materials Chemistry A, 2016. **4**(1): p. 270-279.

238. De Angelis, M.G., R. Gaddoni, and G.C. Sarti, *Gas Solubility, Diffusivity, Permeability, and Selectivity in Mixed Matrix Membranes Based on PIM-1 and Fumed Silica.* Industrial & Engineering Chemistry Research, 2013. **52**(31): p. 10506-10520.

239. Tien-Binh, N., et al., *Crosslinked MOF-polymer to enhance gas separation of mixed matrix membranes.* Journal of Membrane Science, 2016. **520**: p. 941-950.

240. Khan, M., et al., *Functionalized carbon nanotubes mixed matrix membranes of polymers of intrinsic microporosity for gas separation.* Nanoscale Research Letters, 2012. **7**(1): p. 1-12.

241. Gonciaruk, A., et al., *PIM-1/graphene composite: A combined experimental and molecular simulation study.* Microporous and Mesoporous Materials, 2015. **209**(0): p. 126-134.

242. Shin, Y., et al., *Synthesis and characterization of composite membranes made of graphene and polymers of intrinsic microporosity.* Carbon, 2016. **102**: p. 357-366.

243. Kujawski, J., et al., *Pervaporative removal of acetone, butanol and ethanol from binary and multicomponent aqueous mixtures.* Separation and Purification Technology, 2014. **132**: p. 422-429.

244. Li, S.-Y., R. Srivastava, and R.S. Parnas, *Separation of 1-butanol by pervaporation using a novel tri-layer PDMS composite membrane.* Journal of Membrane Science, 2010. **363**(1–2): p. 287-294.

245. Liu, S., et al., *Fabrication of MOFs/PEBA mixed matrix membranes and their application in bio-butanol production.* Separation and Purification Technology, 2014. **133**: p. 40-47.

246. Varoon, K., et al., *Dispersible Exfoliated Zeolite Nanosheets and Their Application as a Selective Membrane.* Science, 2011. **334**(6052): p. 72-75.

247. Karan, S., et al., *Ultrafast Viscous Permeation of Organic Solvents Through Diamond-Like Carbon Nanosheets.* Science, 2012. **335**(6067): p. 444-447.

248. Nair, R.R., et al., *Unimpeded Permeation of Water Through Helium-Leak-Tight Graphene-Based Membranes.* Science, 2012. **335**(6067): p. 442-444.

249. Abraham, J., et al., *Tunable sieving of ions using graphene oxide membranes.* Nature Nanotechnology, 2017. **12**(6): p. 546-+.

250. Kim, H.W., et al., *Selective Gas Transport Through Few-Layered Graphene and Graphene Oxide Membranes.* Science, 2013. **342**(6154): p. 91-95.

251. Li, H., et al., *Ultrathin, Molecular-Sieving Graphene Oxide Membranes for Selective Hydrogen Separation.* Science, 2013. **342**(6154): p. 95-98.

252. Yang, Q., et al., *Ultrathin graphene-based membrane with precise molecular sieving and ultrafast solvent permeation.* Nature Materials, 2017. **16**: p. 1198.

253. Hu, Y., et al., *Zeolitic Imidazolate Framework/Graphene Oxide Hybrid Nanosheets as Seeds for the Growth of Ultrathin Molecular Sieving Membranes.* Angewandte Chemie International Edition, 2016. **55**(6): p. 2048-2052.

254. Han, Y., Z. Xu, and C. Gao, *Ultrathin Graphene Nanofiltration Membrane for Water Purification.* Advanced Functional Materials, 2013. **23**(29): p. 3693-3700.

255. Goh, K., et al., *All-Carbon Nanoarchitectures as High-Performance Separation Membranes with Superior Stability.* Advanced Functional Materials, 2015. **25**(47): p. 7348-7359.

256. Liu, H., H. Wang, and X. Zhang, *Facile Fabrication of Freestanding Ultrathin Reduced Graphene Oxide Membranes for Water Purification.* Advanced Materials, 2015. **27**(2): p. 249-254.

257. Huang, L., et al., *Reduced Graphene Oxide Membranes for Ultrafast Organic Solvent Nanofiltration.* Advanced Materials, 2016. **28**(39): p. 8669-8674.

258. Sorribas, S., et al., *Pervaporation and membrane reactor performance of polyimide based mixed matrix membranes containing MOF HKUST-1.* Chemical Engineering Science, 2015. **124**(Supplement C): p. 37-44.

259. Khan, M.M., et al., *Functionalized carbon nanotubes mixed matrix membranes of polymers of intrinsic microporosity for gas separation.* Nanoscale Research Letters, 2012. **7**(1): p. 504.

260. Alberto, M., et al., *Enhanced organophilic separations with mixed matrix membranes of polymers of intrinsic microporosity and graphene-like fillers.* Journal of Membrane Science, 2017. **526**: p. 437-449.

261. Zhang, Q.G., et al., *Sub-10 nm Wide Cellulose Nanofibers for Ultrathin Nanoporous Membranes with High Organic Permeation.* Advanced Functional Materials, 2016. **26**(5): p. 792-800.

262. Karan, S., Z.W. Jiang, and A.G. Livingston, *Sub-10 nm polyamide nanofilms with ultrafast solvent transport for molecular separation.* Science, 2015. **348**(6241): p. 1347-1351.

263. Jimenez-Solomon, M.F., et al., *Polymer nanofilms with enhanced microporosity by interfacial polymerization.* Nature Materials, 2016. **15**(7): p. 760-+.

264. Sorribas, S., et al., *High Flux Thin Film Nanocomposite Membranes Based on Metal-Organic Frameworks for Organic Solvent Nanofiltration.* Journal of the American Chemical Society, 2013. **135**(40): p. 15201-15208.

265. Zhu, J.Y., et al., *Elevated Performance of Thin Film Nanocomposite Membranes Enabled by Modified Hydrophilic MOFs for Nanofiltration.* ACS Applied Materials & Interfaces, 2017. **9**(2): p. 1975-1986.

266. Ma, D., et al., *Thin-Film Nanocomposite (TFN) Membranes Incorporated with Super-Hydrophilic Metal–Organic Framework (MOF) UiO-66: Toward Enhancement of Water Flux and Salt Rejection.* ACS Applied Materials & Interfaces, 2017. **9**(8): p. 7523-7534.

267. Wang, J., et al., *Zeolitic Imidazolate Framework/Graphene Oxide Hybrid Nanosheets Functionalized Thin Film Nanocomposite Membrane for Enhanced Antimicrobial Performance.* ACS Applied Materials & Interfaces, 2016. **8**(38): p. 25508-25519.

268. Kim, S.G., et al., *Novel thin nanocomposite RO membranes for chlorine resistance.* Desalination and Water Treatment, 2013. **51**(31-33): p. 6338-6345.

269. Shen, L., S. Xiong, and Y. Wang, *Graphene oxide incorporated thin-film composite membranes for forward osmosis applications.* Chemical Engineering Science, 2016. **143**: p. 194-205.

270. Hung, W.-S., et al., *A study on high-performance composite membranes comprising heterogeneous polyamide layers on an electrospun substrate for ethanol dehydration.* Journal of Membrane Science, 2014. **470**: p. 513-523.

271. Wu, D., et al., *Thin film composite membranes comprising of polyamide and polydopamine for dehydration of ethylene glycol by pervaporation.* Journal of Membrane Science, 2015. **493**: p. 622-635.

272. Niemistö, J., W. Kujawski, and R.L. Keiski, *Pervaporation performance of composite poly(dimethyl siloxane) membrane for butanol recovery from model solutions.* Journal of Membrane Science, 2013. **434**: p. 55-64.

273. Fritsch, D., et al., *High performance organic solvent nanofiltration membranes: Development and thorough testing of thin film composite membranes made of polymers of intrinsic microporosity (PIMs).* Journal of Membrane Science, 2012. **401**: p. 222-231.

274. Sorribas, S., M. Tamaddondar, and P.M. Budd, *1.9 Membranes Made of Polymers of Intrinsic Microporosity (PIMs)*, in *Comprehensive Membrane Science and Engineering (Second Edition)*. 2017, Elsevier: Oxford. p. 216-235.

275. Gonciaruk, A., et al., *PIM-1/graphene composite: A combined experimental and molecular simulation study.* Microporous and Mesoporous Materials, 2015. **209**: p. 126-134.

276. Hu, M., et al., *High-performance interpenetrating polymer network polyurethane pervaporation membranes for butanol recovery.* Journal of Chemical Technology & Biotechnology, 2015. **90**(12): p. 2195-2207.

277. Tiwari, R.R., et al., *Physical aging, CO2 sorption and plasticization in thin films of polymer with intrinsic microporosity (PIM-1).* Journal of Membrane Science, 2017. **537**(Supplement C): p. 362-371.

278. Shen, B., et al., *Chemical functionalization of graphene oxide toward the tailoring of the interface in polymer composites.* Composites Science and Technology, 2013. **77**: p. 87-94.

279. Tian, Z., et al., *Enhanced gas separation performance of mixed matrix membranes from graphitic carbon nitride nanosheets and polymers of intrinsic microporosity.* Journal of Membrane Science, 2016. **514**(Supplement C): p. 15-24.

280. Wang, X., et al., *Mechanical properties of polymer composites reinforced by functionalized graphene prepared via direct exfoliation of graphite flakes in styrene.* RSC Advances, 2016. **6**(113): p. 112486-112492.

281. Ebrahimzadeh, S., B. Ghanbarzadeh, and H. Hamishehkar, *Physical properties of carboxymethyl cellulose based nano-biocomposites with Graphene nano-platelets.* International Journal of Biological Macromolecules, 2016. **84**: p. 16-23.

282. Kumar, A., et al., *Graphene-like nanocarbon: An effective nanofiller for improving the mechanical and thermal properties of polymer at low weight fractions.* Composites Science and Technology, 2016. **127**(Supplement C): p. 79-87.

283. Williams, R., et al., *A highly rigid and gas selective methanopentacene-based polymer of intrinsic microporosity derived from Troger's base polymerization.* Journal of Materials Chemistry A, 2018. **6**(14): p. 5661-5667.

284. Liang, Y., et al., *Dispersion of graphene sheets in organic solvent supported by ionic interactions.* Adv Mater, 2009. **21**: p. 1679 - 1683.

285. Leaper, S., et al., *Flux-enhanced PVDF mixed matrix membranes incorporating APTS-functionalized graphene oxide for membrane distillation.* Journal of Membrane Science, 2018. **554**: p. 309-323.

Appendix A - Ultraviolet-visible spectroscopy: Calibration

Calibration of the UV-Vis spectrophotometer for the three graphene-like materials: GO-ODA, rGO-ODA and rGO-OA (Figure A1).

(a)

(b)

(c)
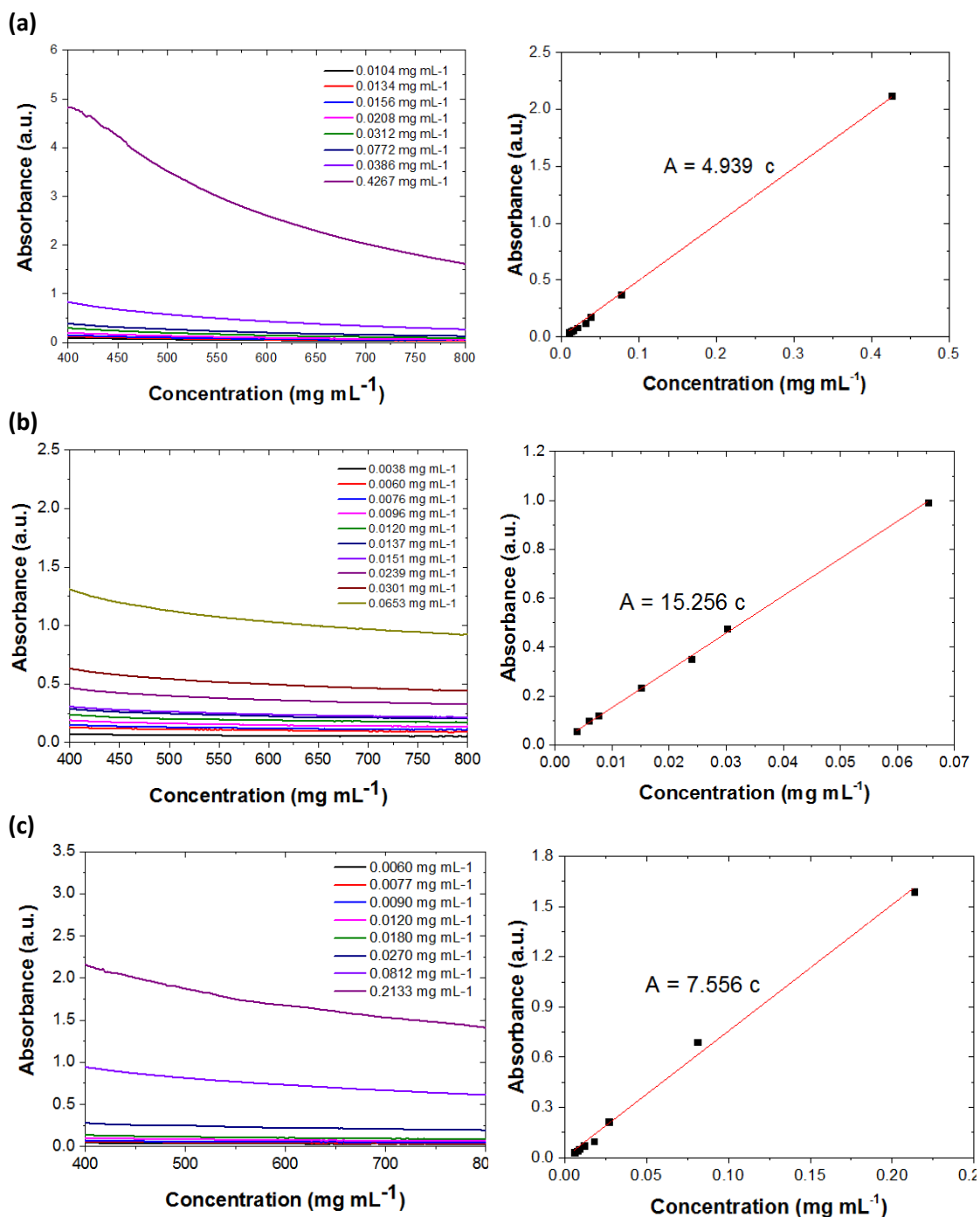
Figure A1: UV-Vis spectra of graphene-based fillers dispersed in chloroform at a range of concentrations and their respective calibration curves (a) GO-ODA, (b) rGO-ODA and (c) rGO-OA. A and c represent the absorbance and the filler graphene-based filler concentration, respectively.

Appendix B - Impeded physical aging in PIM-1 membranes containing graphene-like fillers
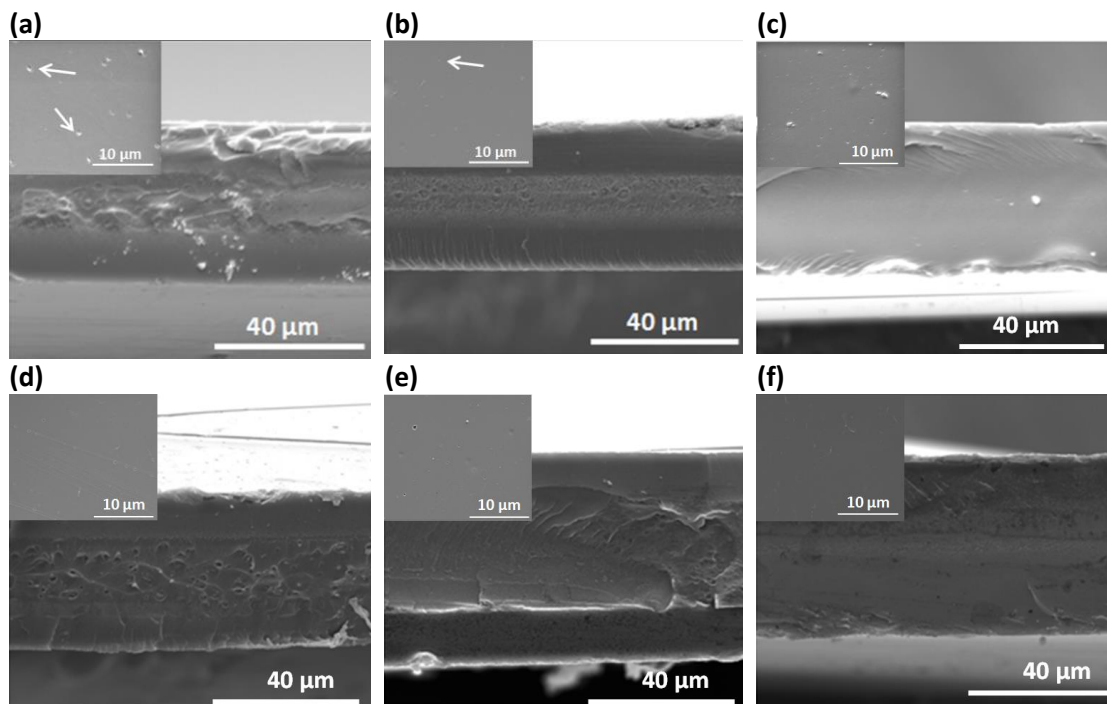
Figure B1: Cross sections and surface (inset) SEM images of (a) 0.01rGO-OA, (b) 0.05rGO-OA, (c) 0.1rGO-OA, (d) 0.25rGO-OA, (e) 0.05GO-ODA and (f) 0.05rGO-ODA membranes. Arrows indicates superficial holes on the membranes.
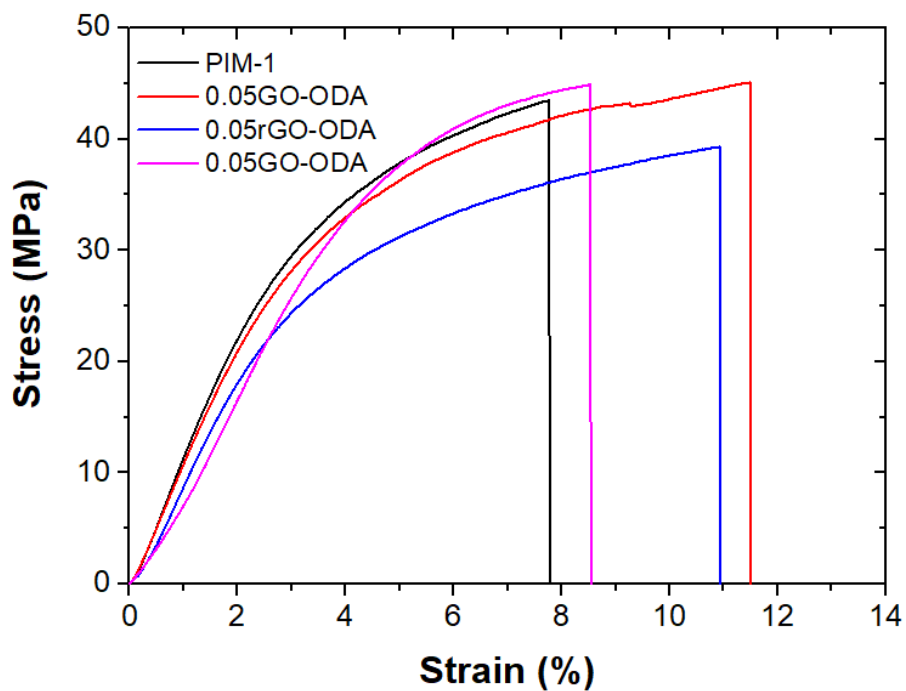
Figure B2: Stress-strain curves for membranes PIM-1, 0.05GO-ODA, 0.05rGO-ODA and 0.05rGO-OA.

Figures B3, B4 and B5 contain plots with the fraction of initial permeability as a function of time for PIM-1 and MMMs containing GO-ODA, rGO-ODA and rGO-OA, respectively. Table B1 and Table B2 show CO_2 and CH_4 permeabilities of pristine PIM-1 membranes and MMMs. CO_2/CH_4 selectivities are presented in Table B3. The reduction in CO_2 and CH_4 permeabilities of all membranes tested is shown in Table B4 and Table B5, respectively.
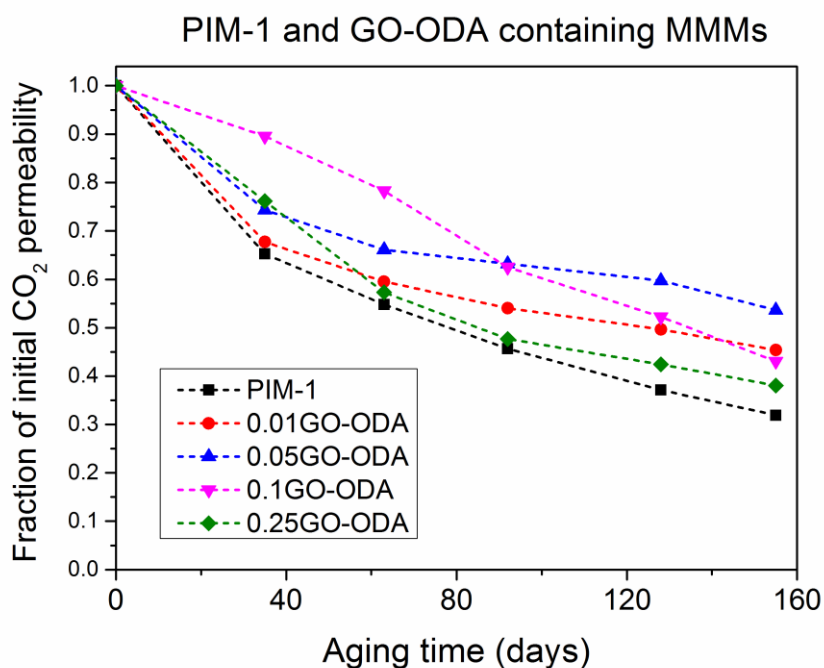
Figure B3: Fraction of initial permeability as a function of time for PIM-1 and MMMs containing GO-ODA. The fraction of initial permeability has been calculated with the average CO2 permeability values obtained for at least two membranes of each type. Standard deviations are shown in Table B1.
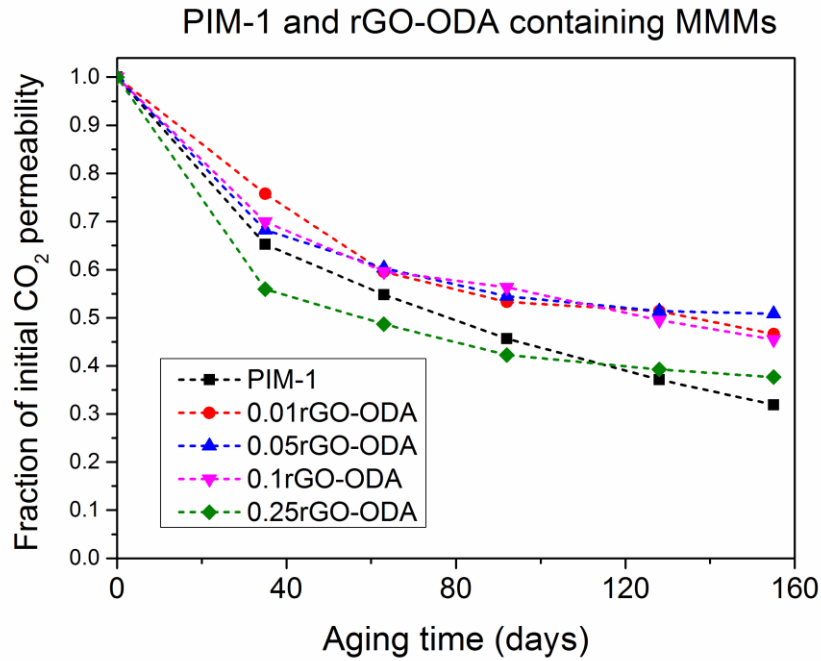
Figure B4: Fraction of initial permeability as a function of time for PIM-1 and MMMs containing rGO-ODA. The fraction of initial permeability has been calculated with the average CO2 permeability values obtained for at least two membranes of each type. Standard deviations are shown in Table B1.
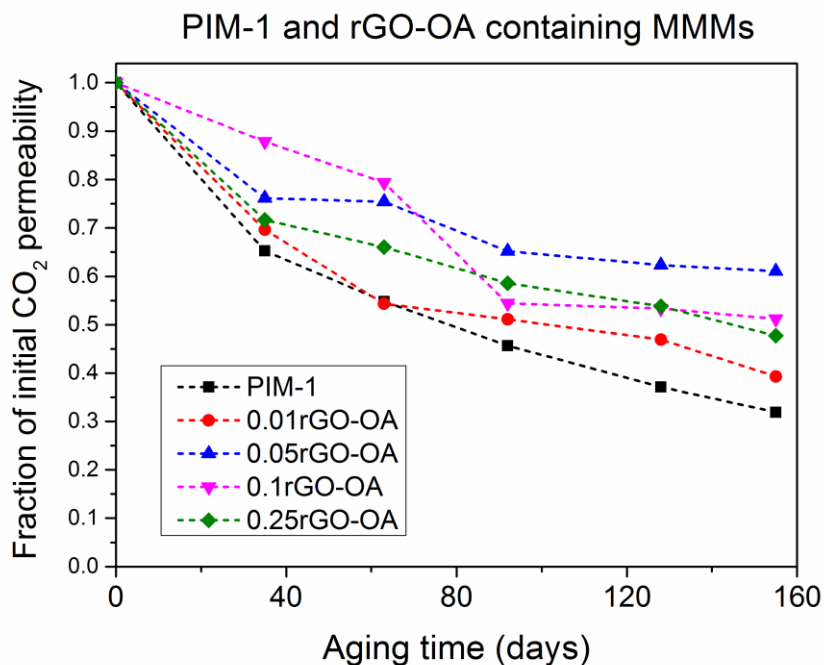
Figure B5: Fraction of initial permeability as a function of time for PIM-1 and MMMs containing rGO-OA. The fraction of initial permeability has been calculated with the average CO2 permeability values obtained for at least two membranes of each type. Standard deviations are shown in Table B1.

Table B1: CO_2 permeabilities of pristine PIM-1 membranes and MMMs over 155 days: (a) GO-ODA, (b) rGO-ODA and (c) rGO-OA. 1 Barrer = 3.34×10^{-16} mol m m^{-2} s^{-1} Pa^{-1}.

(a)

| Day	CO_2 Permeability ($\times 10^3$, Barrer)				
	PIM-1	0.01GO-ODA	0.05GO-ODA	0.1GO-ODA	0.25GO-ODA
0	6.4± 1.3	6.1 ± 1.5	5.5 ± 0.5	4.8 ± 1.0	4.5 ± 1.0
35	4.1 ± 1.0	4.1 ± 0.9	4.1 ± 0.3	4.3 ± 0.6	3.4 ± 0.9
63	3.5 ± 1.0	3.6 ± 0.9	3.6 ± 0.4	3.8 ± 0.7	2.6 ± 0.7
92	2.9 ± 0.9	3.3 ± 0.9	3.5 ± 0.2	3.0 ± 0.8	2.1 ± 0.5
128	2.4 ± 0.7	3.0 ± 1.0	3.3 ± 0.0	2.5 ± 0.2	1.9 ± 0.7
155	2.0 ± 0.7	2.7 ± 1.0	3.0 ± 0.2	2.0 ± 0.1	1.7 ± 0.6

(b)

Day	CO_2 Permeability ($\times 10^3$, Barrer)				
	PIM-1	0.01rGO-ODA	0.05rGO-ODA	0.1rGO-ODA	0.25rGO-ODA
0	6.4 ± 1.3	4.0 ± 0.6	4.7± 0.6	4.5 ± 0.4	5.5 ± 1.2
35	4.1 ± 1.0	3.1 ± 0.2	3.2 ± 0.6	3.1 ± 0.4	3.0 ± 0.9
63	3.5 ± 1.0	2.4 ± 0.3	2.8 ± 0.8	2.7 ± 0.3	2.7 ± 0.6
92	2.9 ± 0.9	2.2 ± 0.2	2.6 ± 0.6	2.5 ± 0.4	2.3 ± 0.6
128	2.4 ± 0.77	2.1 ± 0.2	2.4 ± 0.6	2.2 ± 0.4	2.2 ± 0.6
155	2.0 ± 0.7	1.9 ± 0.2	2.4 ± 0.6	2.0 ± 0.4	2.1 ± 0.7

(c)

Day	CO_2 Permeability ($\times 10^3$, Barrer)				
	PIM-1	0.01rGO-OA	0.05rGO-OA	0.1rGO-OA	0.25rGO-OA
0	6.4 ± 1.3	6.2 ± 1.1	5.7 ± 0.6	4.8 ± 1.0	6.3 ± 0.4
35	4.1 ± 1.0	4.3 ± 0.3	4.8 ± 0.7	4.2 ± 1.0	4.5 ± 0.5
63	3.5 ± 1.1	3.4 ± 0.8	4.3 ± 0.7	3.8 ± 1.0	4.1 ± 0.4
92	2.9 ± 0.9	3.2 ± 0.7	3.7 ± 0.6	2.6 ± 0.3	3.7 ± 0.5
128	2.4 ± 0.7	2.9 ± 0.9	3.6 ± 0.6	2.5 ± 0.3	3.4 ± 0.3
155	2.0 ± 0.7	2.4 ± 0.7	3.5 ± 0.6	2.4± 0.4	3.0 ± 0.1

Table B2: CH$_4$ permeabilities of pristine PIM-1 membranes and MMMs over 155 days: (a) GO-ODA, (b) rGO-ODA and (c) rGO-OA. 1 Barrer = 3.34 × 10^{-16} mol m m^{-2} s^{-1} Pa^{-1}.

(a)

Day	CH$_4$ Permeability (× 10^2, Barrer)				
	PIM-1	0.01GO-ODA	0.05GO-ODA	0.1GO-ODA	0.25GO-ODA
0	3.3 ± 1.3	4.4 ± 0.9	3.2 ± 1.6	2.5 ± 0.4	2.5 ± 0.8
35	2.0 ± 0.7	1.9 ± 0.5	2.2 ± 0.3	2.1 ± 0.3	1.6 ± 0.5
63	1.5 ± 0.6	1.6 ± 0.5	1.6 ± 0.3	1.7 ± 0.4	1.2 ± 0.3
92	1.3 ± 0.5	1.3 ± 0.4	1.7 ± 0.2	1.2 ± 0.4	0.8 ± 0.2
128	1.0 ± 0.3	1.1 ± 0.4	1.5 ± 0.0	0.9 ± 0.1	0.7 ± 0.3
155	0.7 ± 0.4	1.1 ± 0.5	1.3 ± 0.2	0.8 ± 0.1	0.7 ± 0.3

(b)

Day	CH$_4$ Permeability (× 10^2, Barrer)				
	PIM-1	0.01rGO-ODA	0.05rGO-ODA	0.1rGO-ODA	0.25rGO-ODA
0	3.3 ± 1.3	2.1 ± 0.5	2.3 ± 0.7	2.7 ± 0.3	3.5 ± 1.1
35	2.0 ± 0.7	1.4 ± 0.2	1.2 ± 0.4	1.6 ± 0.2	1.6 ± 0.4
63	1.5 ± 0.6	1.1 ± 0.4	1.1 ± 0.4	1.4 ± 0.2	1.2 ± 0.1
92	1.3 ± 0.5	0.8 ± 0.3	0.9 ± 0.3	1.1 ± 0.2	1.1 ± 0.2
128	1.0 ± 0.3	0.7 ± 0.2	0.8 ± 0.3	1.0 ± 0.2	1.0 ± 0.3
155	0.7 ± 0.4	0.7 ± 0.2	0.8 ± 0.3	1.0 ± .01	1.0 ± 0.2

(c)

Day	CH$_4$ Permeability (× 10^2,Barrer)				
	PIM-1	0.01rGO-OA	0.05rGO-OA	0.1rGO-OA	0.25rGO-OA
0	3.3 ± 1.3	3.8 ± 0.3	3.6 ± 1.5	3.2 ± 1.1	3.6 ± 0.4
35	2.0 ± 0.7	2.1 ± 0.2	2.1 ± 0.1	2.1 ± 0.4	2.3 ± 0.3
63	1.5 ± 0.6	1.4 ± 20.3	2.0 ± 0.4	1.7 ± 0.3	2.0 ± 0.3
92	1.3 ± 0.5	1.2 ± 0.3	1.5 ± 0.3	1.0 ± 0.3	1.8 ± 0.5
128	1.0 ± 0.3	1.1 ± 0.4	1.5 ± 0.2	0.9 ± 0.1	1.6 ± 0.2
155	0.7 ± 0.4	0.9 ± 0.2	1.4 ± 0.2	0.9 ± 0.0	1.3 ± 0.2

Table B3: CO_2/CH_4 selectivity of pristine PIM-1 membranes and MMMs over 155 days: (a) GO-ODA, (b) rGO-ODA and (c) rGO-OA.

(a)

Day	CO₂/CH₄ Selectivity				
	PIM-1	0.01GO-ODA	0.05GO-ODA	0.1GO-ODA	0.25GO-ODA
0	20.3 ± 3.5	16.5 ± 1.3	17.6 ± 1.6	18.9 ± 1.2	18.3 ± 2.1
35	21.0 ± 2	22.1 ± 1.8	19.1 ± 1.1	20.3 ± 0.2	21.5 ± 1.7
63	24.9 ± 3.1	23.1 ± 3.5	22.6 ± 1.0	22.4 ± 0.3	22.5 ± 0.3
92	24.0 ± 3.1	25.2 ± 3.1	21.3 ± 1.4	25.4 ± 0.7	26.1 ± 2.4
128	27.4 ± 2.1	28.5 ± 2.8	22.3 ± 0.2	27.2 ± 0.2	28.3 ± 0.9
155	30.0 ± 4.7	26.6 ± 4.8	23.7 ± 1.6	26.6 ± 2.6	26.3 ± 5.3

(b)

Day	CO₂/CH₄ Selectivity				
	PIM-1	0.01rGO-ODA	0.05rGO-ODA	0.1rGO-ODA	0.25rGO-ODA
0	20.3 ± 3.5	19.3 ± 1.8	21.0 ± 3.9	16.8 ± 0.6	17.3 ± 2.6
35	21.0 ± 2	21.5 ± 1.7	27.8 ± 3.7	19.8 ± 1.5	19.2 ± 0.8
63	24.9 ± 3.1	24.4 ± 6.4	26.6 ± 4.3	20.0 ± 1.2	21.8 ± 3.8
92	24.0 ± 3.1	28.6 ± 7.5	29.7 ± 4.6	22.4 ± 1.5	21.2 ± 2.2
128	27.4 ± 2.1	29.8 ± 5.1	29.8 ± 3.8	22.2 ± 0.2	21.5 ± 0.1
155	30.0 ± 4.7	28.2 ± 6.7	29.1 ± 3.2	21.3 ± 0.9	21.7 ± 0.7

(c)

Day	CO₂/CH₄ Selectivity				
	PIM-1	0.01rGO-OA	0.05rGO-OA	0.1rGO-OA	0.25rGO-OA
0	20.3 ± 3.5	16.4 ± 1.8	17.4 ± 5.1	18.6 ± 2.7	17.6 ± 1.5
35	21.0 ± 2	20.6 ± 2.8	21.3 ± 1.1	18.6 ± 0.2	19.7 ± 2.7
63	24.9 ± 3.1	23.4 ± 2.2	21.9 ± 1.1	22.6 ± 3.7	20.5 ± 1.5
92	24.0 ± 3.1	26.9 ± 2.2	24.5 ± 1.1	27.0 ± 9.4	21.8 ± 4.5
128	27.4 ± 2.1	26.7 ± 1.2	23.5 ± 1.6	27.5 ± 4.9	21.0 ± 2.0
155	30.0 ± 4.7	27.9 ± 2.4	22.9 ± 1.1	27.3 ± 3.6	24.3 ± 2.6

Table B4: Reduction in CO_2 permeability (%) over time: (a) GO-ODA, (b) rGO-ODA and (c) rGO-OA.

(a)

Day	Reduction in CO_2 permeability (%)				
	PIM-1	0.01GO-ODA	0.05GO-ODA	0.1GO-ODA	0.25GO-ODA
0	-	-	-	-	-
35	−35	−32	−26	−10	−24
63	−45	−41	−34	−22	−43
92	−54	−46	−37	−38	−52
128	−63	−50	−40	−48	−58
155	−68	−55	−46	−57	−62

(b)

Day	Reduction in CO_2 permeability (%)				
	PIM-1	0.01rGO-ODA	0.05rGO-ODA	0.1rGO-ODA	0.25rGO-ODA
0	-	-	-	-	-
35	−35	−24	−32	−30	−44
63	−45	−41	−40	−40	−51
92	−54	−47	−46	−44	−58
128	−63	−49	−49	−51	−61
155	−68	−53	−49	−55	−62

(c)

Day	Reduction in CO_2 permeability (%)				
	PIM-1	0.01rGO-OA	0.05rGO-OA	0.1rGO-OA	0.25rGO-OA
0	-	-	-	-	-
35	−35	−30	−24	−12	−28
63	−45	−46	−25	−21	−34
92	−54	−49	−35	−46	−41
128	−63	−53	−38	−47	−46
155	−68	−61	−39	−49	−52

Table B5: Reduction in CH$_4$ permeability (%) over time: (a) GO-ODA, (b) rGO-ODA and (c) rGO-OA.

(a)

Day	Reduction in CH$_4$ permeability (%)				
	PIM-1	0.01GO-ODA	0.05GO-ODA	0.1GO-ODA	0.25GO-ODA
0	-	-	-	-	-
35	−39	−49	−32	−16	−36
63	−56	−56	−49	−34	−54
92	−62	−64	−48	−54	−68
128	−74	−71	−54	−64	−73
155	−79	−71	−61	−69	−73

(b)

Day	Reduction in CH$_4$ permeability (%)				
	PIM-1	0.01rGO-ODA	0.05rGO-ODA	0.1rGO-ODA	0.25rGO-ODA
0	-	-	-	-	-
35	−39	−33	−49	−40	−54
63	−56	−51	−53	−49	−65
92	−62	−62	−62	−57	−68
128	−74	−66	−64	−63	−71
155	−79	−67	−65	−64	−73

(c)

Day	Reduction in CH$_4$ permeability (%)				
	PIM-1	0.01rGO-OA	0.05rGO-OA	0.1rGO-OA	0.25rGO-OA
0	-	-	-	-	-
35	−39	−44	−42	−11	−36
63	−56	−62	−45	−27	−43
92	−62	−69	−58	−58	−51
128	−74	−71	−59	−61	−55
155	−79	−77	−60	−63	−65

Appendix C – Side contributions

This chapter is dedicated to my contribution to side works that resulted in three scientific publications.

(1) "High flux and fouling resistant flat sheet polyethersulfone membranes incorporated with graphene oxide for ultrafiltration applications"

Human population growth, agricultural production, livestock and energy production are the main factors for the increase in fresh water consumption. As a result, two-thirds of the world population is predicted to live under water stress conditions by 2025. Along with other applications studied, membrane technology offers a great potential for production of fresh water.

In this work, mixed matrix membranes (MMMs) containing graphene oxide (GO) flakes and polyethersulfone (PES) were studied for wastewater treatment. Three different pore forming agents were investigated: poly(vinylpyrrolidinone (PVP), reverse triblock Pluronic (P31R1), and poloxamine Tetronic (T904). The results obtained showed an increase of water flux from 2 to 13 L m^{-2} h^{-1} and a rejection of bovine serum albumin (BSA) from 89.2 to 97% when 0.5 wt.% of GO was added to the PES polymer matrix. Similar results were obtained when a pore forming agent T904 was added to the dope solution. Herein, the maximum water flux, BSA and acridine orange rejections reached 245 L m^{-2} h^{-1}, 93.3 % and 48.3%, respectively. Apart from that, improvements in terms of anti-fouling properties were also registered in MMMs. Figure C1 shows the graphical abstract referring this work.

In summary, the incorporation of GO flakes and pore forming agents into PES polymer matrix was an effective way to enhance the membrane performance for ultrafiltration processes.

In this paper, I was involved in the characterization of materials and membranes. I have characterized GO through attenuated total reflection Fourier-transform infrared spectroscopy (ATR-FTIR). With regard to the characterization of membranes, I have performed the following techniques: ATR-FTIR, Raman spectroscopy, water contact angle and atomic force microscopy (AFM).
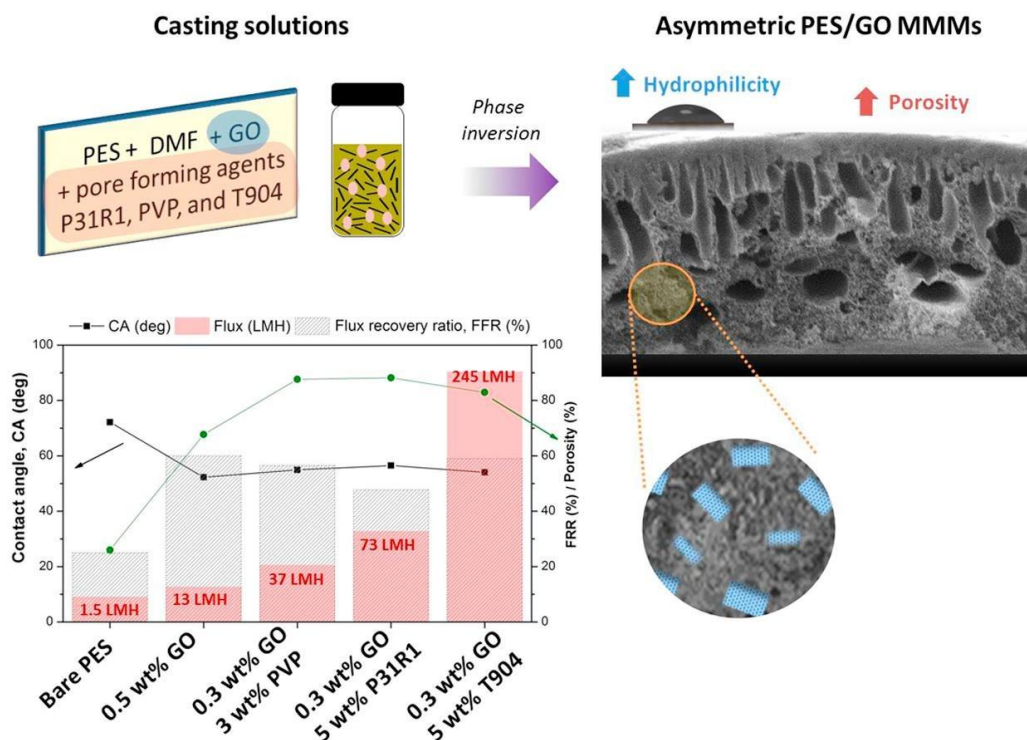
Figure C1: Graphical abstract [23].

(2) *"Flux-enhanced PVDF mixed matrix membranes incorporating APTS-functionalized graphene oxide for membrane distillation"*

The work developed in this project aimed to address, similarly to the previous project (1), the scarcity of fresh water in the world. Herein, air gap membrane distillation (AGMD) was explored for the production of fresh water through the purification of artificial sea water.

MMMs were fabricated via phase inversion method, using dope solution containing GO and GO-3-(aminopropyl)triethoxysilane (APTS) imbedded into PVDF polymer matrix. It was found that the incorporation of both GO and GO-APTS led to an enhancement of water flux, maintaining high salt rejection. The membrane containing 0.5 wt.% GO in its structure showed a water flux of 5.0 L m^{-2} h^{-1}, 52% higher than a pristine PVDF membrane, and a salt rejection of 99.7 %. With regard to GO-APTS as filler in PVDF membranes, the best performing membrane contained a loading of 0.3 wt.%. This membrane, 0.3 wt.% GO-APTS, showed a water flux and salt rejection of 6.2 L m^{-2} h^{-1} (86% higher than pristine PVDF membranes) and 99.8%, respectively. Figure C2 shows the graphical abstract referring this work.

As a conclusion, the results obtained suggested the potential application of blended GO and GO-APTS in PVDF polymer membrane for membrane distillation applications.

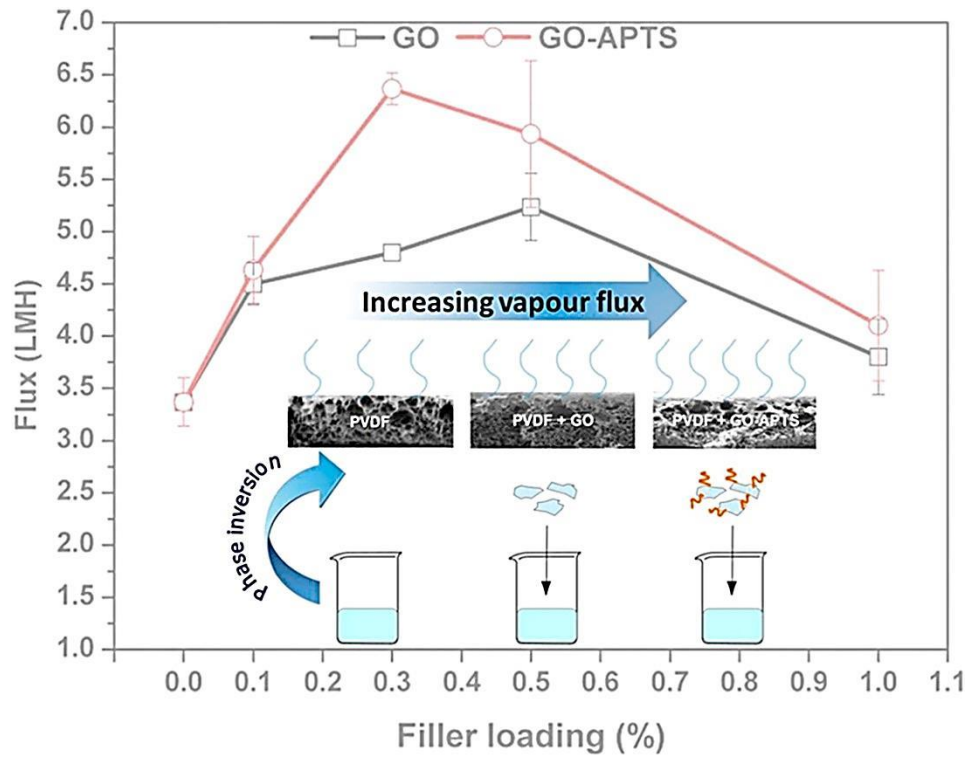In this paper, I was involved in the characterization of membranes through AFM.

Figure C2: Graphical abstract [285].